
Global Alignment of Single-Wall Carbon Nanotubes via Dead-End Filtration

Globale Ausrichtung von einwandigen Kohlenstoffnanoröhren mittels Sackgassenfiltration

Zur Erlangung des Grades eines Doktors der Naturwissenschaften (Dr. rer. nat.)

Genehmigte Dissertation von Christian Rust aus Bietigheim-Bissingen

Tag der Einreichung: 16.02.23, Tag der Prüfung: 30.03.23

1. Gutachten: Prof. Dr. Krupke

2. Gutachten: Prof. Dr. Stark

Darmstadt, Technische Universität Darmstadt



TECHNISCHE
UNIVERSITÄT
DARMSTADT

Materials- and Geosciences
Molecular Nanostructures

Global Alignment of Single-Wall Carbon Nanotubes via Dead-End Filtration
Globale Ausrichtung von einwandigen Kohlenstoffnanoröhren mittels Sackgassenfiltration

Accepted doctoral thesis by Christian Rust

Date of submission: 16.02.23

Date of thesis defense: 30.03.23

Darmstadt, Technische Universität Darmstadt

Bitte zitieren Sie dieses Dokument als:

URN: urn:nbn:de:tuda-tuprints-236568

URL: <http://tuprints.ulb.tu-darmstadt.de/23656>

Jahr der Veröffentlichung auf TUprints: 2023

Dieses Dokument wird bereitgestellt von tuprints,

E-Publishing-Service der TU Darmstadt

<http://tuprints.ulb.tu-darmstadt.de>

tuprints@ulb.tu-darmstadt.de

Veröffentlicht unter CC BY-SA 4.0 International - Creative Commons , Namensnennung

<https://creativecommons.org/licenses/>

Licensed under CC BY-SA 4.0 International - Creative Commons , Attribution

<https://creativecommons.org/licenses/>

Erklärungen laut Promotionsordnung

§ 8 Abs. 1 lit. c PromO

Ich versichere hiermit, dass die elektronische Version meiner Dissertation mit der schriftlichen Version übereinstimmt.

§ 8 Abs. 1 lit. d PromO

Ich versichere hiermit, dass zu einem vorherigen Zeitpunkt noch keine Promotion versucht wurde. In diesem Fall sind nähere Angaben über Zeitpunkt, Hochschule, Dissertationsthema und Ergebnis dieses Versuchs mitzuteilen.

§ 9 Abs. 1 PromO

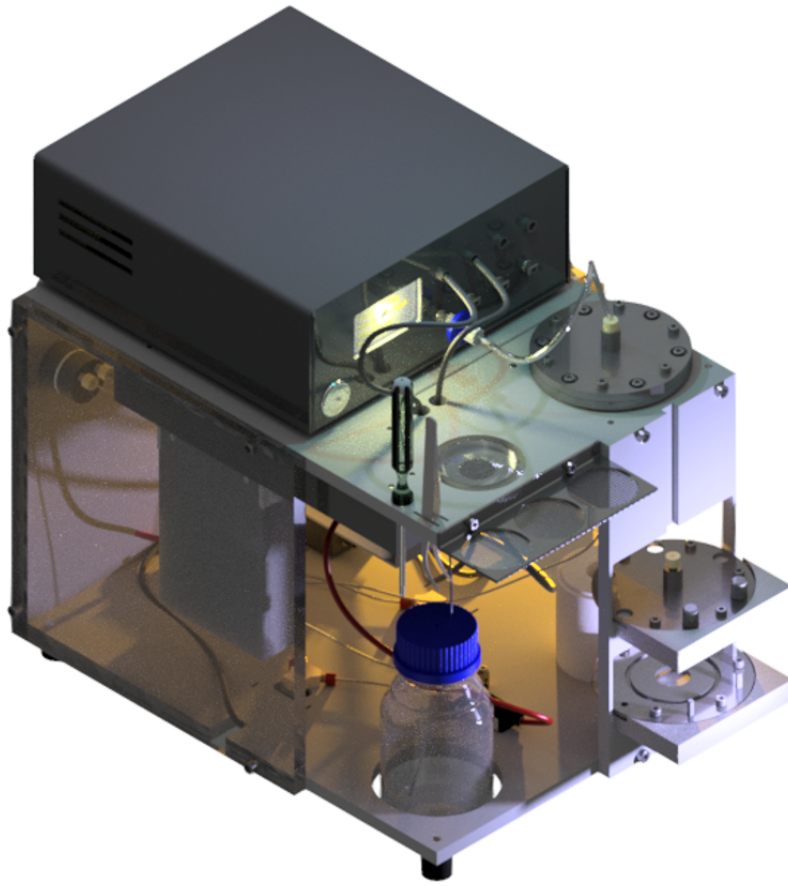
Ich versichere hiermit, dass die vorliegende Dissertation selbstständig und nur unter Verwendung der angegebenen Quellen verfasst wurde.

§ 9 Abs. 2 PromO

Die Arbeit hat bisher noch nicht zu Prüfungszwecken gedient.

Darmstadt, 16.02.23

C. Rust



"You have power over your mind – not outside events. Realize this, and you will find strength."

—Marc Aurel, *Meditations*

Curriculum Vitae

Akademische Ausbildung

12/2018–jetzt **Promotion in der Materialwissenschaft** TU Darmstadt

Project: *Carbon Nanotubes for Energy*

5 Veröffentlichungen, 3 als Erstautor, 1 Cover-Page

1 Application Note: Elveflow

Konstruktion und Programmierung mehrerer Versuchsaufbauten

1 Betreuung einer Bachelorarbeit, (Note 1.0)

2 Invited Talks Electrochemical Society Conference 07/2022 and 05/2021

03/2016–09/2018 **Master of Science in Materialwissenschaft Ø1.23** TU Darmstadt

Masterarbeit: *Entwicklung eines frequenzmodulierten Rasterkraftmikroskopieaufbaus*

zur hochauflösenden Abbildung von Tensidstrukturen auf

Kohlenstoffnanoröhren in Flüssigkeiten, (Note 1.0)

10/2011–03/2016 **Bachelor of Science Materialwissenschaft Ø1.87** TU Darmstadt

Bachelorarbeit: *Untersuchung von lanthandotierten $\text{Bi}_{1/2}\text{Na}_{1/2}\text{TiO}_3$ – $\text{Bi}_{1/2}\text{K}_{1/2}\text{TiO}_3$*

-Relaxoren mittels Piezoresponse-Kraftmikroskopie, (Note 1.0)

Schulbildung

08/2001-07/2010 **Abitur** Martin-Luther-Schule Rimbach

Leistungskurse: Mathematik, Englisch

Berufserfahrung

- 11/2015-02/2016 Umicore NV/SA Wolfgang-Hanau**
Praktikum für die Entwicklung neuer Kontaktwerkstoffe und Modellierung
von Werkstoffeigenschaften. Rasterelektronenmikroskopie von Plattierungen.
- 11/2013-07/2014 Wissenschaftlicher Mitarbeiter TU Darmstadt**
Studentische Hilfskraft in der Arbeitsgruppe Nicht-Metallische Anorganische
Werkstoffe für Lasermikroskopie und Datenverarbeitung.
- 06/2011-08/2011 Freudenberg Gruppe Weinheim**
Studentische Hilfskraft im Rohmischwerk
- 08/2010-02/2011 Universitätsklinikum Mannheim Mannheim**
Zivildienst in der Patientenlogistik

Zusammenfassung

Seit ihrer Entdeckung durch Iijima im Jahr 1991 wird erwartet, dass Kohlenstoff-Nanoröhren sämtliche neue Technologien ermöglichen werden. Da ihre Bandlücke durch ihren Durchmesser definiert ist, können sie als Halbleiter mit scharfen Absorptionsbanden im Infrarot- und UV-VIS-Bereich verwendet werden, was sie für die Optik und Photonik sehr interessant macht. Darüber hinaus weisen sie eine der größten bekannten intrinsischen Ladungs- und Phononenmobilitäten auf, wodurch sie sich wiederum als metallische Verbindungselemente in der Elektronik oder als Wärmemanagementsysteme für Hochleistungselektronik anbieten. Dank der Fortschritte bei der Synthese und den Sortierverfahren sind immer weitere Typen von Kohlenstoffnanoröhren in größeren Mengen verfügbar. Dennoch besteht weiterhin eine große Herausforderung darin, ihre Position und Ausrichtung in Anwendungsfällen zu kontrollieren. Daher konzentrieren sich viele Forschungsarbeiten heutzutage auf die Ausrichtung von Kohlenstoffnanoröhren in dünnen Filmen, was auch das Thema dieser Arbeit darstellt. Vor nicht allzu langer Zeit (2016) hat eine neue Methode zur Ausrichtung von einwandigen Kohlenstoffnanoröhren für Aufsehen gesorgt, da sie die Herstellung großflächiger hochausgerichteter Filme ermöglicht, welche sich über mehrere Quadratzentimeter erstrecken. Die so genannte Filtrationsmethode, die aus einem sehr langsamen Sackgassen-Filtrationsprozess besteht, erfordert scheinbar nur eine gewöhnliche Laborausrüstung und mäßige praktische Fähigkeiten, aber dennoch berichten viele Gruppen, dass sie nicht in der Lage sind, die erstaunlichen Ergebnisse von He et al. zu reproduzieren, was zur Schlussfolgerung führt, dass viele Faktoren, die diese Ausrichtung ermöglichen, unbekannt sein könnten.

Um die Mechanismen hinter dieser Methode zu erforschen und die Fläche, die Qualität der Ausrichtung, die verwendbaren Kohlenstoffnanoröhren und die Reproduzierbarkeit zu verbessern, zielt diese Arbeit darauf ab, einige dieser Faktoren zu erörtern. Hierbei wird versucht, diese Faktoren zu isolieren und die Ergebnisse mit Hilfe eines selbstgebauten mikrofluidischen Filtrationsaufbaus anzuwenden. Zunächst werden die üblicherweise verwendeten Polycarbonat-Membranen anhand des Filtrationswiderstandes und des Zeta-Potentials eingeordnet und Experimente mit unterschiedlicher Ionenstärke und Tensidkonzentration durchgeführt, um ein grundlegendes Verständnis der Membranladungen zu erlangen. Ähnlich wie bei den Membranen, werden auch die Zeta-Potentiale der Kohlenstoffnanoröhren-Dispersionen für verschiedene Tenside und deren Konzentrationen gemessen, um deren Stabilität zu bestimmen. Im nächsten Schritt werden die präzisen Fluss- und Druckmessungen des maßgeschneiderten Aufbaus zur Optimierung der Filtrationsbedingungen verwendet, die aus einem anfänglichen langsamen und einem abschließenden schnellen Filtrationsschritt bestehen. Diese Daten werden anfänglich nur mit einem Typ von einwandigen Kohlenstoffnanoröhren erhoben, der sich laut Literatur besser ausrichten lässt als andere. Für die Bewertung der Ausrichtung werden die Kohlenstoffnanoröhren-Filme auf der Membrane und Substraten mittels Kreuzpolarisationsmikroskopie und Rasterelektronenmikroskopie detailliert analysiert. Der Einfluss der langsamen Volumenrate auf die Größe und Morphologie der Kohlenstoffnanoröhrenkristalle (Domänen), wird hierbei auch mit einem Algorithmus zur Formerkennung gemessen, welcher mit Hilfe des maschinellen Lernens zuverlässig große Datensätze generieren konnte. Im Gegensatz zum langsamen Filtrationsschritt, konnte beim schnellen Filtrations-

schritt festgestellt werden, dass er keinen Einfluss auf die tatsächliche Ausrichtung hat, sondern zur Bildung von Trocknungsringen führt, die anhand von Fotos gemessen werden. Daraufhin werden auch die Abhängigkeit der Ausrichtung von der abgelagerten Masse sowie die entsprechenden Konzentrationen unter Beibehaltung der optimierten Filtrationsparametern untersucht, was schließlich zu einem großflächig ausgerichteten Film führt. Nachdem die Ausrichtung auf unbehandelten Membranen realisiert worden ist, werden mittels Heißprägen in Verbindung mit speziell angefertigten Prägescheiben uni-axiale und radiale Muster in die Membranen eingepreßt. Dabei wird der Stegabstand und Breite der uni-axialen Muster variiert, um die benötigten Mustergeometrien und Prägekraft zu untersuchen. Darüber hinaus werden radial ausgerichtete Filme mit radialsymmetrischen Lichtmustern belichtet, um eine mögliche Verwendung als optische Bauelemente zu untersuchen und Zwei-Klemmen-Widerstandsmessungen durchgeführt, um die Auswirkungen der Ausrichtung der Nanoröhren auf den elektrischen Widerstand zu beurteilen. Nachdem der Einfluss von Membranmodifizierungen auf die Ausrichtung untersucht worden ist, besteht der nächste Schritt in der Reproduktion der Ausrichtung mit längensortierten einwandigen Kohlenstoffnanoröhren mit unterschiedlichen durchschnittlichen Durchmessern. Eine umfassende Charakterisierung mit verschiedenen makroskopische und nanoskopische Methoden wird erneut verwendet, um Trends zur Verbesserung der Ausrichtung anhand der abgelagerten Masse zu ermitteln. Um die Vergleichbarkeit mit anderen Forschungsgruppen, welche auf diesem Gebiet arbeiten, zu gewährleisten, werden die am besten ausgerichteten Filme in dieser Arbeit zusätzlich mit Raman-Spektroskopie vermessen und durch Berechnung des zweidimensionalen Ordnungsparameters S_{2D} nach Bestimmung des wellenlängenabhängigen dichroitischen Verhältnisses bewertet.

Daraufhin wird eine auf Kohlenstoffnanoröhren maßgeschneiderte Derjaguin, Landau, Verwey und Overbeek Analyse mittels der Zetapotenziale, der geometrischen Daten sowohl der Kohlenstoffnanoröhren als auch der Membranen und der vorliegenden experimentellen Daten verwendet, um Modelle für die Ausrichtungsmechanismen zu erörtern, welche durch die Oberflächenmodifikation der Membran und das Vorzeichen der Ladung der Kohlenstoffnanoröhre differenziert werden. Außerdem kann mit dieser Analyse auch ein Zusammenhang zwischen dem Durchmesser und der erforderlichen Länge der Kohlenstoffnanoröhren hergestellt werden, sodass die abschließende Diskussion weitere neue Anwendungsfälle und Verbesserungen dieser vielversprechenden Methode erörtert, welche sich aus dieser Arbeit ergeben könnten.

Abstract

Carbon nanotubes have been envisioned to open up new pathways for many applications since their discovery by Iijima in 1991. Their band gap being defined by their diameter allows to use them as semiconductors with sharp absorption bands in the infrared and UV-VIS making them often interesting for optics and photonics. Additionally, they exhibit one of the largest intrinsic charge and phonon mobilities known for any material, which in turn sparks the interest of using them as metal interconnects in electronics or heat-management systems for high-performance electronics. As the combined advances in synthesis and sorting processes are making a lot of carbon nanotubes species accessible in larger quantities, a challenge still remains to control their location and orientation in device architectures. Thus, a lot of research nowadays focuses on the alignment of carbon nanotubes in thin films and this is where the efforts made in this work are focused at. Just recently in 2016, a new method of alignment single wall carbon nanotubes has gathered a lot of attention, as it allows for large scale films, spanning over several cm^2 , while maintaining very high order-parameters. The so-called filtration method, which comprises of a very slow dead-end filtration process, is seemingly just needing basic lab equipment and moderate practical skills, but anecdotal reports of many groups being unable to reproduce the astonishing results of He *et al.* come to the conclusion, that many factors making this alignment possible may be unknown.

In order to investigate the mechanisms behind that method and improve the area, quality of alignment, usable carbon nanotubes species and reproducibility, this thesis aims at working out some of those factors by trying to isolate them one by one and applying the findings to a custom-made microfluidic filtration setup. At first the common used polycarbonate track-etched membranes are evaluated by means of filtration resistance and zeta-potential and experiments with varying ionic strength and surfactant concentration are conducted in order to establish a basic understanding of the membrane charges. Similar to the membranes, the zeta-potentials of the carbon nanotubes dispersions are measured for different surfactants and their concentrations as well, defining their stability. In the next step, the precise volume-rate and pressure readings of the custom-made setup are used to optimize the filtration conditions, comprising of an initial slow- and a final fast-filtration step. This data is gathered by only using a single type of single wall carbon nanotube, that has been deemed to align better than others as stated by researchers in the field. The data gained from the setup is then compared to the carbon nanotube thin films being still on the membrane and after transfer to several substrates, allowing for detailed analysis by cross-polarization microscopy and scanning electron microscopy. The domains of carbon nanotube crystals formed at various volume-rates are also measured by a shape-identifying machine learning algorithm, providing large data-sets, that are then used to quantify the impact of the slow-filtration conditions on the size and morphology. However, the fast filtration step has been found not to impact the actual alignment, but result in drying rings formed, which are measured by photographs. Eventually the dependence on deposited mass, as well as appropriate concentrations are investigated under the given filtration parameters, which then finally lead to globally aligned films. Having realized the alignment on pristine membranes, hot-embossing in conjunction with custom made shims is utilized to imprint uni-axial and

radial patterns into the membranes. Thereby the bar-spacing of the former is varied to study the needed width and imprinting force. Additionally, radial symmetric patterns are designed and the resulting films were exposed to radial symmetric light patterns, to evaluate their possible use as optical elements, while terminal two-probe measurements in conjunction with custom-made flexible printed circuit boards are conducted to quantify the effect of nanotube alignment on electrical resistance. After investigating the effects on alignment from the perspective of the membranes, length-sorted single wall carbon nanotubes with different average diameters are used to reproduce the global alignment obtained before, using similar conditions. Comprehensive characterization comprising of various methods, covering the macroscopic and nanoscopic alignment under the influence of changing deposited mass are used again to determine trends of improving alignment. In order to warrant comparability to other research groups investigating this method, all champion films throughout this work are additionally mapped with Raman spectroscopy and quantified by calculating the two-dimensional order parameter S_{2D} after determining the wavelength dependent dichroic-ratio obtained from absorption spectroscopy.

With the zeta-potentials, geometric data measured of both, the carbon nanotubes and membranes and the experimental data at hand, Derjaguin, Landau, Verwey, Overbeek analysis tailored for an individual single wall carbon nanotube is used to propose models for the alignment mechanisms, which were differentiated by the surface modification of the membrane and the sign of charge of the carbon nanotube. Eventually, this analysis also allows to establish a connection between carbon nanotube diameter and required length, and thus the conclusion given in the end, explores several new use cases and improvements, that might come from this work.

Acknowledgment

First of all I would like to express my gratitude to Prof. Dr. Ralph Krupke and Prof. Dr. Robert Stark for evaluating this dissertation as referee and co-referee, respectively. Additionally, I would like to thank Prof. Dr. Ralph Krupke, who wholeheartedly welcomed me to his group and has always been supportive by providing assistance with difficult scientific questions, technical details, as well as thought-provoking discussions.

Furthermore I want to mention Dr. Benjamin S. Flavel, who I was always grateful to call my supervisor over the last couple years. There was never a time, I could not count on his support and without his scientific expertise and advice, this would not have been possible.

However, many results shown in this work, were realised with the help and combined efforts of many other colleagues and collaborators, that I appreciate to have had during this scientific journey. Without them, many of the ambitious projects would not have come to fruition, so I want to mention them here:

First and foremost, I want to thank the wonderful people of the Institute of Nanotechnology (INT) and especially the Krupke and Flavel group, I was able to work with and learn from. This involves Dr. Han Li, who always provided me with scientific insights and carbon nanotube material, from which a lot of the films shown in this work have been created with. Laura Wieland, who has been always a pleasant company in the shared office and fellow PhD-student and I had the opportunity to also collaborate with. I also want to thank Simone Dehm, who took a lot of the administrative workload and assisted me in the lab, wherever needed. And last, but not least, I am appreciative of Elias Schill's fantastic work on the radial alignment during his Bachelors thesis.

I also want to acknowledge the other groups and facilities on Campus South and North of the Karlsruhe Institut of Technology (KIT). Thereby the workshop lead by Michael Hesselschwerdt always offered me their expertise and services for all sorts of handy work. Here, I also want to mention Andreas Leiser, who double-checked my construction plans of my various ideas and made them become a reality. This is also true for my good friend, Manuel Spari, who helped me out with the Arduino Controller, which runs to this day like a charm.

Another big help were the staff of the Institute of Microstructure Technology (IMT) and the support of the Karlsruhe Nano Micro Facility (KNMF), Dr. Markus Guttman, Marc Schneider and Andreas Bacher, who enabled me to hot-emboss the membranes with my custom shim-designs and thus collaborated with me on all of my publications.

At this point, I want to comment on the assistance I experienced from the kind people of the Water Chemistry, namely Dr. Florencia Saravia and Dr. Ali Sayegh, who helped me to do a lot of membrane related measurments at their institute at difficult times and also mention Qihao Jin from the Lichttechnisches Institut (LTI), who heped me out with dichroic ratio measurments on short notice.

Additionally, I also want to thank my collaborators from the FU Berlin, Prof. Dr. Stephanie Reich, Oisín Garrity and Dr. Georgy Gordeev and the kind people from the National Institute of Standards and Technology (NIST), Dr. Jeffrey

A. Fagan, Dr. Pavel Shapturenka, Dr. Ming Zheng, Dr. Tehseen Adel, Dr. Angela R. Hight Walker, who contributed with numerous Raman measurements, provided the length-sorted carbon nanotubes as well as fruitful discussions and scientific insights, that I learned and benefited from.

With the last words of this section, I also want to thank my friends and family for their everlasting support and love over the years and especially my brother, who spent some time with me, squashing bugs in my python scripts.

Contents

Zusammenfassung	1
Abstract	3
Acknowledgment	5
List of Acronyms	11
Author Contributions and Reuse of published Content	13
1. Introduction	15
1.1. Motivation	15
1.2. Carbon Nanotubes	16
1.2.1. Synthesis of Carbon Nanotubes	21
1.2.2. Suspensions of Carbon Nanotubes	23
1.3. Alignment of Carbon Nanotubes	24
1.3.1. Applications of Aligned Films	28
1.3.2. Alignment of Single-Wall Carbon Nanotubes using Dead-End Filtration	30
1.4. Principles of Filtration	33
1.4.1. Concentration Polarization, Fouling and Blocking Laws	34
1.4.2. Derjaguin, Landau, Verwey, Overbeek Theory	37
1.4.3. Zeta potentials of Membranes and SWCNTs	44
1.5. Characterization of Aligned Carbon Nanotube Films	49
1.5.1. Direct Characterization	49
1.5.2. Indirect Characterization	50
2. Methods	55
2.1. Construction and Programming of the Custom Filtration Setup	55
2.2. Operation of the Setup	57
2.2.1. Pressure Sensor Calibration	57
2.2.2. Precision of the Coriolis flow-sensor	57
2.2.3. FOPDT Method for Flow Control	59
2.2.4. Loading a Membrane and Release of Excess Pressure under the Membrane	59
2.2.5. Cleaning and Maintaining the Filtration Setup	60
2.3. Dispersions of SWCNTs	60
2.3.1. Unsorted EA-SWCNTs dispersed in DOC and CTAB	60

2.3.2.	Length-Sorting of EA-SWCNTs and CoMoCAT-SWCNTs	60
2.3.3.	Chirality pure (6,5)-SWCNTs	61
2.3.4.	Concentrating the Dispersions with Ultra-Filtration	61
2.3.5.	UV-VIS Measurements for Concentration Determination	61
2.3.6.	AFM Length Determination	61
2.4.	Polycarbonate Track-Etched Membranes	62
2.4.1.	Modification of Membranes	62
2.4.2.	Shim Production: Axial and Radial Shims	62
2.4.3.	Hot-Embossing	63
2.5.	Transfer to Substrates	63
2.5.1.	Transfer to Silicon Wafers and Glass	63
2.5.2.	Transfer to Flexible Printed Circuit Boards	63
2.6.	Characterization Of Aligned Films	64
2.6.1.	Determination of the Dichroic Ratio	64
2.6.2.	Two-dimensional Order Parameter Evaluation with Raman Measurements	65
2.6.3.	Scanning Electron Microscopy	65
2.6.4.	Light Microscopy and Cross Polarized Microscopy	65
2.6.5.	Atomic Force Microscopy	66
2.7.	Two-Probe Resistance Measurements	66
2.8.	Transmission Experiments	66
2.9.	Derjaguin, Landau, Verwey, Overbeek Analysis with Python	67
2.9.1.	Zeta Potential of Membranes:	67
2.9.2.	Zeta Potential of SWCNT Dispersions	68
3.	Results	69
3.1.	Resistance and Zeta-Potential of Membranes	69
3.2.	Zeta-Potential and Concentration of Dispersions made with Unsorted EA-SWCNTs	70
3.3.	Optimization of the Slow Volume-Rate for unsorted EA-SWCNTs	72
3.4.	Optimization of the Fast Volume-Rate for Unsorted EA-SWCNTs	77
3.5.	Influence of Deposited Mass on the Alignment of Unsorted EA-SWCNTs	79
3.6.	Hot-Embossing of Membranes with Axial Patterns	81
3.7.	Two-Dimensional Order Parameter of Axial Aligned EA-SWCNTs	84
3.8.	Radial Alignment of Unsorted EA-SWCNTs via Hot-Embossing	85
3.9.	Characterization of Radial Aligned Films	89
3.10.	Length Sorting of EA- and CoMoCat-SWCNTs	92
3.11.	Filtration of Length-Sorted EA-SWCNTs	95



3.12. Alignment of Length-Sorted CoMoCAT-SWCNTs 99

3.13. Evaluation of the Two-Dimensional Order Parameter for Length-Sorted EA- and CoMoCAT-SWCNTs 103

3.14. Derjaguin, Landau, Verwey, Overbeek for Unsorted EA-SWCNTs Dispersed in DOC and CTAB 104

3.15. Derivation of the Relationship between SWCNT Length and Diameter using DLVO-Theory 106

4. Discussion and Outlook 111

A. Appendix 115

A.1. Resistance and Zeta-Potential of Membranes 115

A.2. Determination of Suitable Slow Volume-Rate for EA-SWCNTs 119

A.3. Hot-Embossing of Membranes with Axial Patterns 132

A.4. Raman Analysis of Aligned EA-SWCNT-films 135

A.5. Hot-Embossing of Membranes with Radial Patterns 136

A.6. Length-Sorting of EA- and CoMoCAT-SWCNTs 142

A.7. Derjaguin, Landau, Verwey, Overbeek Calculations for Unsorted SWCNTs 166

A.8. Derjaguin, Landau, Verwey, Overbeek Calculations for Sorted SWCNTs 169

A.9. Construction plans: Frame of the Microfluidic Filtration Setup 172

- This page is left blank intentionally. -

List of Acronyms

SWCNT	single-wall carbon nanotube
DWCNT	double-wall carbon nanotube
MWCNT	multi-wall carbon nanotube
CVD	chemical vapor deposition
AFM	atomic force microscopy
SDS	sodium dodecyl sulfate)
CMC	critical micelle concentration
CVD	chemical vapour deposition
LCP	liquid crystalline polymer
LCE	liquid crystalline elastomer
IR	infrared
DCE	1,2-dichloroethane
GO	graphene oxide
EISA	evaporation-induced self-assembly
SDS	sodium dodecyl sulfate
PFO-BPy	Poly[(9,9-dioctylfluorenyl-2,7-diyl)-alt-(6,6'-2,2'-bipyridine)]
PEG-DA	polyethylene glycol diacrylate
PDMS	polydimethylsiloxane
FESA	floating evaporative self-assembly
DLVO-theory	Derjaguin, Landau, Verwey, Overbeek theory
CP	concentration polarization
CF	critical flux
CFV	critical fouling volume
PVP	polyvinylpyrrolidone
PCTE	polycarbonate track-etched
DA	Derjaguin approximation
DH	Debye Hückel-model
CMC	critical micelle concentration
SEI	surface element integration
IHP	inner Helmholtz plane

OHP outer Helmholtz plane
IEP isoelectric point
PZC point of zero charge
ELS electrophoretic light scattering
PALS phase analysis light scattering
CTAB Cetyltrimethylammoniumbromid
SEM scanning electron microscope
DOS density of states
vHS van Hove singularities
DNA Deoxyribonucleic acid
ATPE aqueous two-phase extraction
DOC sodium deoxycholate
PEG-DA Poly-(ethylenglykol)-diacrylat
PDMS Polydimethylsiloxan
UC uncoated
SCPM scanning cross-polarized microscopy
FOPDT first order plus dead time
SEC size-exclusion chromatography
RZ rate-zonal
PMMA Polymethylmethacrylat
fPCB flexible printed circuit board
SP spoke
CA cake
HB herringbone
OD optical density
HiPco high pressured carbon monoxide
MCE mixed cellulose ester
EA-SWCNTs electric arc synthesis method SWCNTs
CoMoCAT-SWCNTs cobalt-molybdenum catalyst synthesis method SWCNTs
ELS electrophoretic light scattering
DLS dynamic light scattering

Author Contributions and Reuse of published Content

Below is a list of the published articles by the author of this dissertation as first [1–3] and co-author [4, 5], as well as the Bachelor-thesis of Elias Schill [6], which he has supervised.

- ¹C. Rust, H. Li, G. Gordeev, M. Spari, M. Guttman, Q. Jin, S. Reich, and B. S. Flavel, “Global alignment of carbon nanotubes via high precision microfluidic dead-end filtration”, *Advanced Functional Materials* **32**, 2107411 (2022).
- ²C. Rust, E. Schill, O. Garrity, M. Spari, H. Li, A. Bacher, M. Guttman, S. Reich, and B. S. Flavel, “Radial alignment of carbon nanotubes via dead-end filtration”, *Small* (2023).
- ³C. Rust, P. Shapturenka, M. Spari, Q. Jin, H. Li, A. Bacher, M. Guttman, M. Zheng, T. Adel, A. R. H. Walker, J. A. Fagan, and B. S. Flavel, “The impact of carbon nanotube length and diameter on their global alignment by dead-end filtration”, *Small* **1**, 2206774 (2023).
- ⁴L. Wieland, H. Li, C. Rust, J. Chen, and B. S. Flavel, “Carbon nanotubes for photovoltaics: from lab to industry”, *Advanced Energy Materials* **11**, 2002880 (2021).
- ⁵L. Wieland, C. Rust, H. Li, M. Jakoby, I. Howard, F. Li, J. Shi, J. Chen, and B. Flavel, “The potential of swcnts to extend the ir-absorption of silicon solar cells”, *Carbon* **184**, 828–835 (2021).
- ⁶E. Schill, “Impact of carbon nanotube film structure on strain sensing”, Bachelor’s Thesis (Karlsruhe Institute of Technology, 2022).

Partial content (text and figures) of this work have been previously published in the listed publications shown above [1–3]. The permission for reproduction was granted by Wiley-VCH GmbH under the creative commons agreement, which allows for reproduction by adequate citation of the contents. Partial data from the Bachelor-thesis of Elias Schill [6] is reused with his personal permission as well. Figures reused are additionally labeled as such.

Content of [1] will be reused in the sections and chapters:

1.3.2, 1.4, 1.4.1, 2, 3.1 - 3.7, 3.14; and appendices A.1- A.4, A.7.

Content of [2] will be found again in the following sections and chapters:

2, 3.8 - 3.9; and appendix A.5.

Finally, content of [3] will be reused in the sections and chapters:

1.3.2, 2, 3.10 - 3.13, 3.15; and appendices A.6, A.8.

Additionally, figures of other authors are reproduced under the license of the respective publisher and will be denoted by footnotes according to the publishers guidelines.

- This page is left blank intentionally. -

1. Introduction

In the following sections of this chapter a motivation is given, as to why aligned carbon nanotubes hold many keys of improving a plethora of device applications as well as unlocking new ones. Thereby a special emphasis is put on the newly developed dead-end filtration method, which is a promising contender for large aligned single-wall carbon nanotube (SWCNT) films stemming from SWCNT dispersions. In order to equip the reader with a solid theoretical foundation, a basic description of carbon nanotubes and their synthesis is given in the beginning followed by their use in dispersions. Then a short literature review of other alignment techniques and applications is given in order to classify the capabilities and shortcomings of the dead-end filtration method. The method itself is then put into a theoretical framework by introducing basic concepts of filtration and the Derjaguin, Landau, Verwey, Overbeek theory (DLVO-theory) and eventually, several routes of quantifying the alignment of the obtained films are discussed.

1.1. Motivation

Single-wall carbon nanotubes (SWCNTs) have been envisioned to change our every day lives for more than three decades,[7] as this quasi 1-dimensional allotrope of carbon exhibits several outstanding material properties interfacing optics, thermal transport as well as electronics and mechanics.[8–10] Additionally, their diameter, described by the chiral indices (n,m) , defines whether they act as semiconductor (s) or metal (m), which in turn also defines the position of their sharp absorption bands, ranging from the infrared to the ultra-violet spectral regions.[11–13] Their size and shape being the source of their desirable properties is also causing great challenges for researchers investigating possible device architectures. In order to tap into their anisotropic properties it often appears to be most beneficial to create thin films of aligned carbon nanotubes that provide performance enhancements [14, 15] and in some cases even establish new material properties not seen in their disordered counterparts [16] which eventually lead to terahertz polarizers,[17, 18] air-stable n-type transistors [19] or heat management systems.[20] This prospect leads to many efforts of tailoring SWCNT thin films using as-grown carbon nanotubes,[21, 22] matrix-materials [23, 24] and lastly dispersion-based methods.[25, 26] The latter category is often seen as the most promising as it can be used in conjunction with selective separation techniques which provide precise control of the diameter,[27] length,[28] wall-number,[29, 30] electronic properties,[31–33] chirality, [34–36] and enantiomeric type[37, 38] without the need for elaborate removal of matrices.[39] As of today there is not a single technique available, that offers large area films with a high degree of alignment suitable for a wide range of nanotube diameters. Recently, He *et al.* introduced a filtration-based method, that promises to reach those goals.[40] However, despite of many anecdotal reports of efforts made to reproduce those results, only a few groups are able to do so, but have not been able to generate sufficient data on suitable conditions.[1, 41] In order to advance this method to be a reliable source of aligned thin films, it is important to examine the alignment mechanism as well as identifying crucial parameters of the SWCNTs and membranes alike.

1.2. Carbon Nanotubes

Carbon is a fundamental element of the fourth group in the periodic table and has six electrons, which occupy the 1s, 2s, and 2p atomic orbitals. It forms covalent bonds with its weakly bound electrons located in the $2s^2$ and $2p^2$ orbitals, leading to hybridization states (sp^1 , sp^2 and sp^3), which are essential for many organic compounds and its extraordinary allotropes.[10, 42] Naturally occurring three-dimensional (3D) allotropes of carbon comprise of diamond (sp^3) and graphite (sp^2), which exhibit very dissimilar mechanical, thermal and electrical material properties. The discovery of the zero-dimensional Buckminsterfullerene C_{60} in 1985 by the group of Smalley happened then by chance as they vaporized graphite rods in order to investigate the formation of long-chain carbon molecules in interstellar space.[43] This sparked a novel research field, which we nowadays term as "nanotechnology". Carbon Nanotubes being a one dimensional allotrope of carbon, were first discovered by Iijima in 1991 [7] and consist of rolled-up sheets of two-dimensional graphene which was unambiguously produced and identified by Geim and Novoselov in 2004.[44] Carbon nanotubes themselves are first and foremost distinguished by the amount of cylinders they consists of which conventionally leads to the groups of single (SWCNT), double (DWCNT) and multi-wall carbon nanotubes (MWCNT). The distance of those walls is thereby comparable to the interlayer distance of graphite (0.341 nm).[45] Since the repeating elements of C_{60} , Carbon Nanotubes and graphite can be derived from the so-called honeycomb structure found in graphene,[46] the latter is often used to describe the properties of the other allotropes.[47] The covalent sp^2 -bonds found in graphene have a bond length of $a_{C-C} = 0.142$ nm [48] and form a triangular lattice with a primitive unit cell consisting of two carbon atoms, A and B, providing two π -electrons.[10] This cell is defined by the basis vectors a_1 and a_2 , that have length of $|a_1| = |a_2| = a_0 = 0.246$ nm and from an angle of 60° . [49] Unlike graphene, the electronic states in a single-wall carbon nanotube are confined by its circumference C with n and m being positive integers and $n \geq m$, as represented in equation 1.1

$$C = na_1 + ma_2 \quad (1.1)$$

The chiral indices (n,m) can thereby used to calculate the value ν (eq. 1.2, which defines if the SWCNT is metallic ($\nu = 0$) or semiconducting ($\nu = 1, 2$):[47]

$$\nu = (n - m) \mod 3 \quad (1.2)$$

The bandgap of the semiconducting nanotubes, thereby scales with the diameter of the SWCNT d_t ($\approx 0.7 \frac{eV}{d_t}$). But it has to be noted that only SWCNT with $n = m$ are truly metallic, while other species have a curvature induced bandgap scaling with $\frac{1}{d_t^2}$. [50] The SWCNT diameter d_t can be calculated by inserting the chiral indices and the basis

¹ Reprinted from "Advances in tailoring the electronic properties of single-wall carbon nanotubes" Vol 77, p. 125-211, Kharlamova., April 2016, with permission from Elsevier.

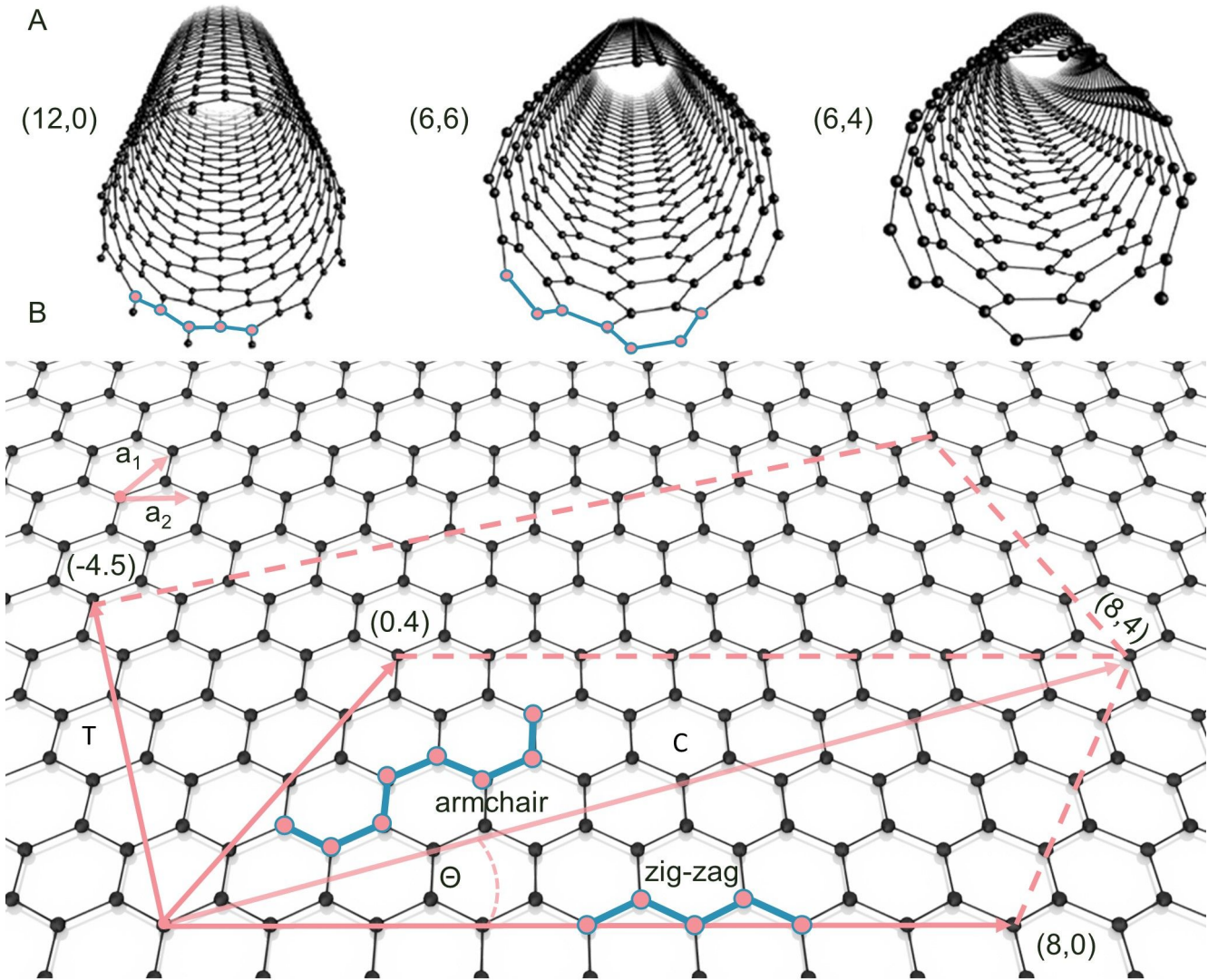


Figure 1.1.: (A) Schematic representations of a zig-zag, armchair, and chiral SWCNT.¹ (B) Graphical reconstruction of the circumference C and the translational vector T of an (8,4) SWCNT in real-space, which define the primitive unit cell according to Reich et al..[45] The type of SWCNTs can also be described by their chiral angle Θ , which is formed between c and the vector part of n .

vector length a_0 into eq. 1.3, shown below:[51]

$$d_t = \frac{|c|}{\pi} = \frac{a_0}{\pi} \sqrt{(n^2 + m^2 + nm)} \quad (1.3)$$

SWCNTs are also often distinguished by the appearance of the carbon atoms forming the end of the cylinder, which can be interpreted as an armchair ($n = m$), zig-zag pattern ($n, 0$) or a mixed, chiral type (n, m). This distinction can also be made with the chiral angle Θ , which forms between a_1 and the circumference C . In this case, zig-zag

SWCNTs exhibit a chiral angle of 0° , armchair SWCNTs are found at $\Theta = 30^\circ$ and chiral SWCNTs can be found in between. It should be noted, that higher chiral angles are represented in this interval as well due to the six fold rotational symmetry of graphene.[45] A schematic representation of C , the indices n, m , the chiral angle Θ and types of SWCNTs (armchair, zig-zag and chiral) on a two dimensional sheet of graphene is shown in Figure 1.1 in the case of an (8,4) SWCNT. In order to define the primitive unit cell, that can then be repeated in z -direction building a carbon nanotube, one must also determine the translational period $T = (t_1, t_2)$, that is defined by the smallest lattice vector perpendicular to C . In the case shown, T would be defined by the vector (-4,5). In order to determine the amount of carbon atoms in the unit cell n_c , one has to form the ratio q of the area of the unit cell of the cylinder surface $S_t = TC$ and the area of the graphene unit cell S_g :

$$q = \frac{S_t}{S_g} = \frac{2(n^2 + nm + m^2)}{n\nu_0} \quad (1.4)$$

Thereby ν_0 is set as 3, if $\nu = 0$ (eq. 1.2) and otherwise it is set to 1. As one unit cell of graphene q is occupied by two carbon atoms, one can simply compute the amount of carbon atoms of a SWCNT unit cell to be $n_{SWCNT} = 2q$. In the reciprocal space defined by $k_{x,y}$ (Figure 1.2), the primitive vectors $a_{1,2}$ are transformed to $b_{1,2}$, which also define a triangular lattice with the center of the Brillouin zone being denoted by Γ and high symmetry points as M and K :

$$b_1 = \left(\frac{1}{\sqrt{3}}, 1\right) \frac{2\pi}{a_0}, b_2 = \left(\frac{1}{\sqrt{3}}, -1\right) \frac{2\pi}{a_0} \quad (1.5)$$

The corresponding vectors of the circumference C and translational vector T can be written as K_1 and K_2 , respectively by following the Kronecker delta relationship between the real-space and frequency-space vectors $R_i K_j = 2\pi\delta_{ij}$ leading to: [52]

$$K_1 = \frac{1}{q}(-t_2 b_1 + t_1 b_2), K_2 = \frac{1}{q}(m b_1 + n b_2), \quad (1.6)$$

Because of the one-dimensional appearance of a SWCNT, only K_2 is continuous, while K_1 is quantized, due to the periodic boundary condition. This can be rationalized by considering a wave function of a quasi-particle (electron or phonon), as the wavelength λ has to have a phase shift of 2π preventing it from vanishing due to interference. This results then into:

$$\mu\lambda = |c| = \pi d, K_1 = \frac{2\pi}{\lambda} = \frac{2\mu}{d} \quad (1.7)$$

So there are q wave vectors with μK_1 with $\mu = -q/2+1, \dots, 0, \dots, 1, q/2$, which correspond to q discrete one-dimensional k vectors. Another viewpoint can be achieved by looking at $K_1 q = (-t_2 b_1 + t_1 b_2)$ being a reciprocal lattice vector and thus wave vectors with $q K_1$ are equivalent. So the first Brillouin zone of a carbon Nanotube is described by eq.1.8:

$$K = \frac{k K_2}{|K_2|} + \mu K_1 \quad (1.8)$$

with $|K_1| = 2/d_t$ and $|K_2| = 2\pi/|T| = 2d_R/\sqrt{3}d_t$, as it can be seen in Figure 1.3. This means that with increasing diameter the number of lines increases but the distance decreases. The number of energy bands then corresponds to

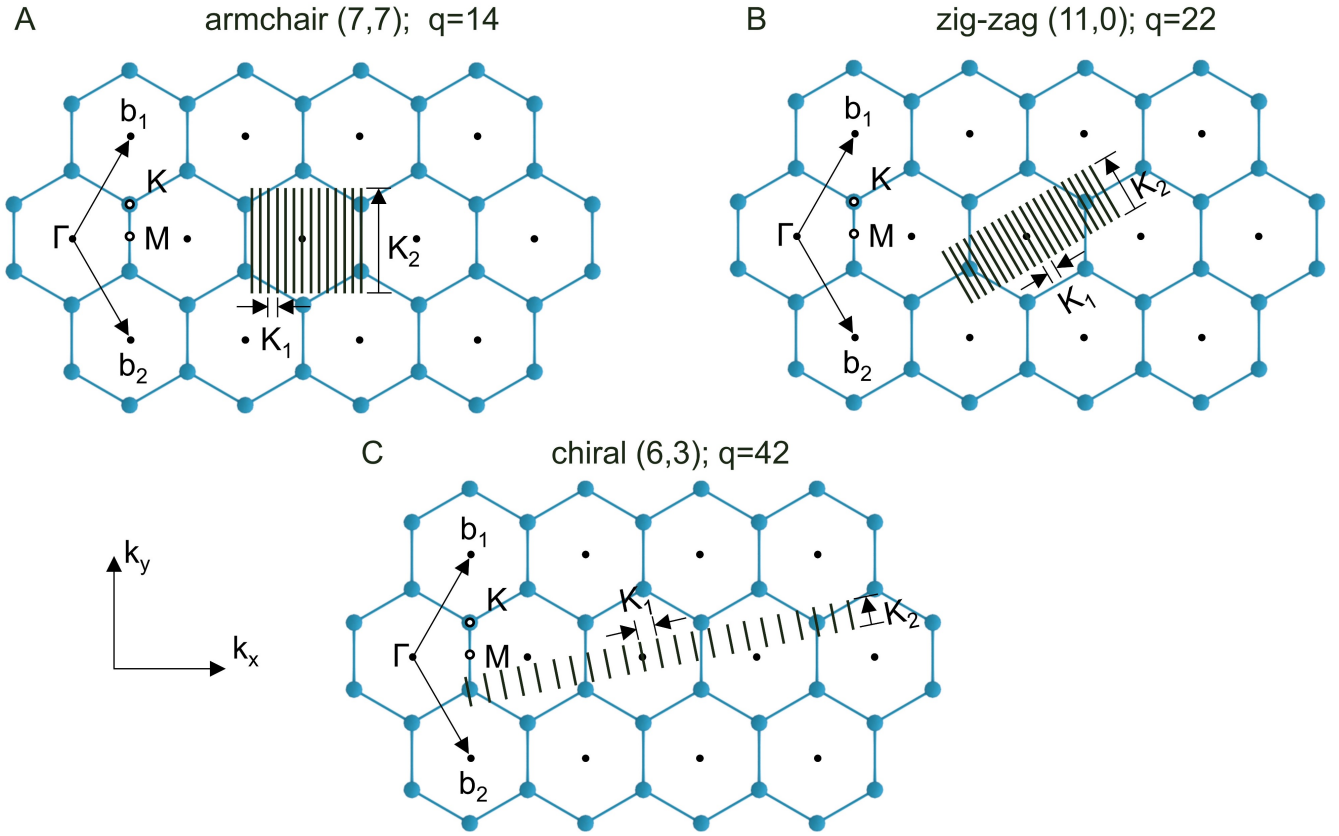


Figure 1.2.: Representation of the vectors K_1, K_2 for an armchair (A), zig-zag (B) and chiral (C) SWCNT in the first Brillouin zone (k_x, k_y) of a graphene lattice. The number of quantized vectors and thus electronic bands, can be calculated by the number of primitive unit cells q in real-space. The center of the cells (Γ) are connected by the vectors b_1, b_2 and the high symmetry points are denoted by K and M . The graphic was made according to the review of Kharlamova.[52]

the number of unit cells present using the zone-folding approximation, which commonly neglects the influence of the curvature of a carbon nanotube and thus should be handled with care. Therefore the energy dispersion of graphene E_{g2D}^\pm is calculated using the tight binding model, which gives the energy bands of the last valence (binding π) and first conduction (antibonding π^*) bands that are energetically the lowest and meet at the K point as shown in Figure 1.3 (A) and eq.1.9 :

$$E_{g2D}^\pm(k_x, k_y) = \gamma_0 \sqrt{1 + 4 \cos\left(\frac{\sqrt{3}k_x a}{2}\right) \cos\left(\frac{k_y a}{2}\right) + 4 \cos^2\left(\frac{k_y a}{2}\right)} \quad (1.9)$$

with $\gamma_0 = 3.033 \text{ eV}$ being the interaction energy between two neighboring carbon atoms in a graphene lattice. Combining the energy dispersion of graphene with the wave vector of the first Brillouin zone of a SWCNT results then in:

$$E_{1D}^\pm = E_{g2D}^\pm \frac{kK_2}{|K_2|} + \mu K_1 \quad (1.10)$$

² Reproduced from “Science and applications of wafer-scale crystalline carbon nanotube films prepared through controlled vacuum filtration” V 6, 3, March 2019, under Creative Commons license agreement from Royal Society publishing.

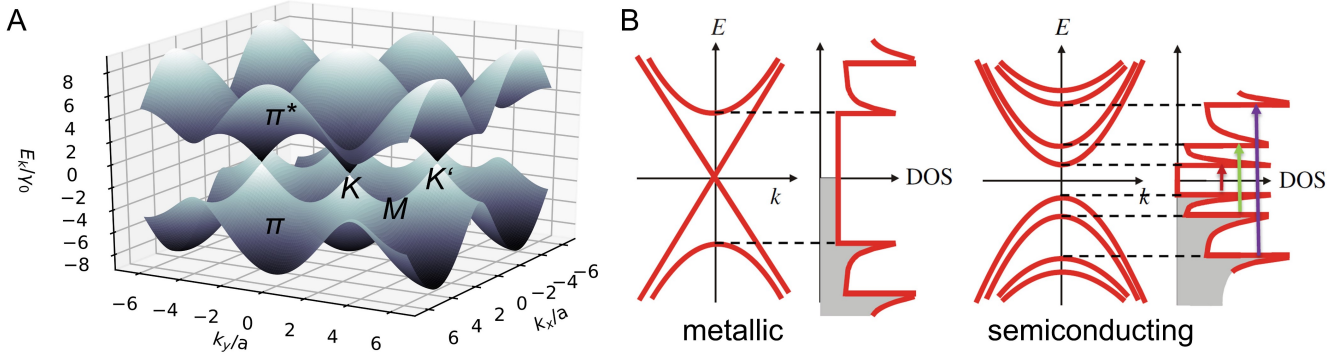


Figure 1.3.: (A) Energy dispersion E_{g2D}^{\pm} of graphene according to Castro et al..[53] The conduction and valence band are touching at the high symmetry point K . (B) DOS of a metallic and semiconducting SWCNT derived from the band structure. At every maxima or minima of the bands, a van Hove singularity can be found in the DOS, which mark the the energy levels for the transitions between both bands.²

In order to determine whether the SWCNT is now metallic or semiconducting, one has to consider if the quantized vector of the SWCNT is cutting the K point of graphene or not. As mentioned above, due to geometric reasons, the rule shown in eq. 1.2 can be used to determine the electronic properties if the chiral vectors are known. In order to derive the density of states (DOS), one has to calculate the number of states Z per energy interval from E to $E + \partial E$, leading to:

$$D(E) = \frac{dZ}{dE} \quad (1.11)$$

It can be seen, that every time the energy dispersion is going through a maxima or minima, a "spike" appears in the DOS, Figure 1.3 (B). These are called van Hove singularities (vHS) and are symmetrically arranged in the conduction and valence band [54]. Conventionally, they are counted by integer numbers relative to their position to the Fermi energy E_F . Due to the selection rules, the dominant parallel polarized optical transitions can only occur between symmetrically spaced vHS. The first transitions for a semiconducting E_{11}^S and metallic E_{11}^M SWCNT between the lowest vHS in the conduction and highest vHS in the valence band,[55] can then be described as:

$$E_{11}^S = \frac{2a_{C-C}\gamma_0}{d_t}, E_{11}^M = \frac{6a_{C-C}\gamma_0}{d_t} \quad (1.12)$$

where γ_0 is the nearest neighbor interaction energy between two carbon atoms from the tight binding model. Those transitions are than often plotted in a so-called Kataura plot,[56] where the diameter d_t is connected to the expected transition energies. Thereby the transition energy decreases inversely proportional to the diameter of the nanotube. Optical absorption and resonant Raman spectra can then be used to identify the species present after synthesis.[56]

1.2.1. Synthesis of Carbon Nanotubes

As of today, the synthesis of carbon nanotubes can be split into three main categories: electric arc discharge, laser ablation and chemical vapour deposition (CVD).[57] All methods in turn are thereby relying on three main ingredients: (i) a carbon source, (ii) nanocatalysts and (iii) an energy input.[58] These factors mainly determine the wall-number and diameter of the majority of the obtained carbon nanotubes. The first method ever used, is the evaporation of carbon atoms by applying a bias between two graphite rods forming a plasma at very high temperatures ($3200\text{ }^{\circ}\text{C}$) and inert gas atmosphere. The carbon atoms are then migrating to the colder zone of the reaction chamber, resulting in a growth of CNTs on the cathode and carbon soot, consisting of amorphous carbon and fullerenes on the reactor walls. However, if the anode does not contain any catalysts, this process will mainly yield MWCNTs.[58] In order to facilitate the growth of SWCNTs over MWCNTs, catalysts are embedded into the anode and the temperature of the reaction chamber has to be maintained below $2000\text{ }^{\circ}\text{C}$, which then yields SWCNTs with a diameter ranging between 1.2 and 1.7 nm.[59] This method has been modified later, by using a focused solar beam instead of a pulsed or continuous laser source, which initially yielded fullerenes and later carbon nanotubes.[60, 61] However, by using an electrical furnace under inert conditions and combining it with laser ablation of graphite target, Smalley's group was able to achieve an even smaller diameter range.[62] Thereby graphite is sublimated with a laser and subsequently transported to a cooled copper surface, where the nanotubes that nucleated in the vapor phase are collected. And again, pure SWCNTs can only be obtained by adding catalysts to the graphite target.[58] In 1996, one year after the introduction of the laser ablation synthesis method, the same group reported a very narrow distribution of diameters around $1.4 \pm 0.2\text{ nm}$ by adding cobalt and nickel as catalysts to the target and keeping the temperature at $1200\text{ }^{\circ}\text{C}$. Smaller diameters can only be obtained using CVD, by which hydrocarbon vapor is passed through a tubular reactor, that is heated to $600\text{-}1200\text{ }^{\circ}\text{C}$ in order to decompose the constituents of the vapor. The nanocatalysts present in the reactor coating are then seeding the growth of the CNTs, which can be collected after cooling the system to room-temperature. The sources for the hydro carbon can be either organic liquids like benzene and alcohol, which are transported to the reactor after evaporation using inert gases, or sublimating solids like camphor or naphthalene.[63] The size of the catalysts determine whether MWCNT or SWCNT are growing on the substrate.[64] The most widely-accepted growth mechanism involves the hydrocarbon being decomposed at the catalysts-sites, with the hydrogen being evaporated and the carbon dissolving into the metal. The carbon is then reaching the limits of its solubility in the metal and precipitates out, crystallizing into a carbon nanotube without dangling bonds. The balance between hydrocarbon decomposition (exothermic) and crystallization (endothermic) is than sustaining the growth, which can be split into two cases. If the catalyst-substrate interaction is weak, the solved carbon will push out the catalysts particle until it is covered in excess carbon and diffusion to the bottom stops (tip-growth).[65] On the contrary, if the interaction between catalyst and substrate is strong, the particle will remain on the substrate and a dome and subsequent cylinder is pushed out from the base, hence it is called the base-growth model, Figure 1.4.[65] By exchanging the hydro carbon to high pressured carbon monoxide (HiPco) being sourced from $\text{Fe}(\text{CO})_5$, again Smalley's group has been able to grow SWCNTs with diameters being closer to

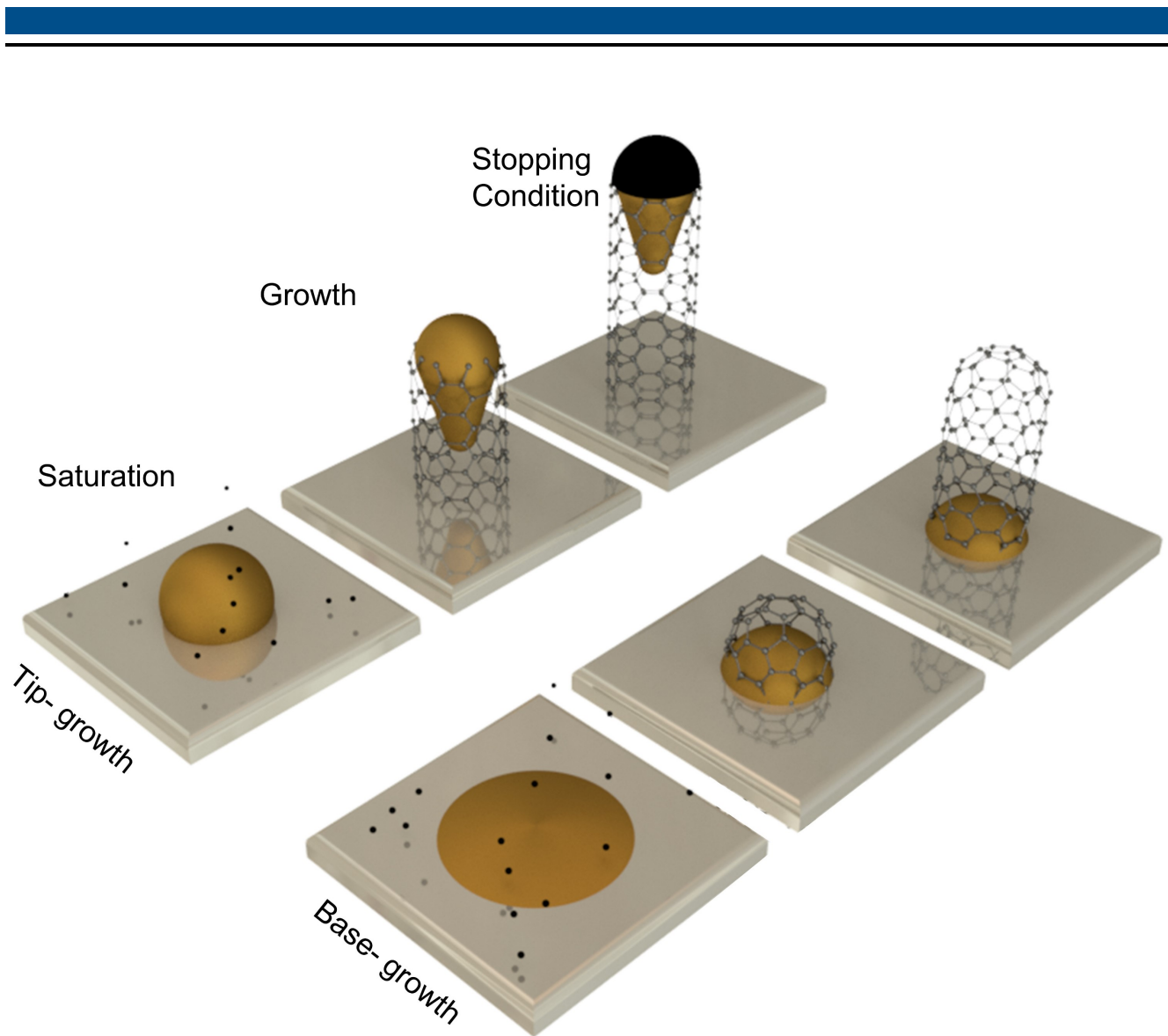


Figure 1.4.: Schematic of tip-growth and base-growth according to Kumar *et al.* [63]. The former will be observed, when the interaction between catalysts and substrate is low and vice versa. The Stopping conditions can be distinguished by the catalyst surface being either saturated or the chemical activity of carbon dropping off significantly.

1 nm. [66] Resasco *et al.* then introduced the use of cobalt and molybdenum catalyst particles to the HiPco method nowadays known as the CoMoCAT-synthesis method, which results in very small diameter (0.78 nm) SWCNTs with an increased amount of (6,5) and (7,5). [67] Efforts to further increase the single chirality output of carbon nanotubes also involve a combination of the base growth mechanism with seeding caps of a targeted species (eg. (6,6)). [68] A comprehensive review on the growth of targeted species can be found here. [69] Despite all the efforts on directly growing long, chirality pure SWCNTs with low defect rates, most techniques to date still offer only low yields or need further sorting and purification steps as well.

1.2.2. Suspensions of Carbon Nanotubes

A dispersion is defined as a system, in which particles are intermixed in a continuous phase of another state.[70] A further distinction is made between the sizes of the particles, which leads to the common terms of "solution" for particles being in the range of several nanometers in size and below, or "colloidal solutions" for particles being in between nanometers and micrometers.[71] The latter is then further separated into suspensions (carbon nanotube dispersions) and emulsions (cow milk), depending on the particles being solid or liquid. Since there is no objective parameter by which a dispersion can be objectively measured researchers often qualitatively evaluate their dispersions of carbon nanotubes using photographs.[36, 72] In order to achieve a homogeneous dispersion of carbon nanotubes mainly three groups of approaches can be determined, which all aim at modifying the surface walls of the carbon nanotube. As an example of the mechanical modification, ball-milling is often used to introduce defect sites, which are then used in combination with a reactant (eg. Deoxyribonucleic acid (DNA) [73] or KOH adding hydroxy groups [74]), that modifies the carbon nanotube surface hindering agglomeration. This route is still rather unfavorable, as it significantly shortens the carbon nanotubes, which draw many of their properties from their high aspect ratio and also the defect sites can limit their properties.[75] This is also true for the second category using irradiation in the form of plasma [76] or an electron beam,[77] breaking up the bond between the carbon atoms and concurrently use the defect sites for reactions. The physiochemical method can then be differentiated between covalent (e.g. acids [78, 79], sodium ions [80]) or non-covalent (e.g. polymers or surfactants) modifications of the side-walls. As covalent modifications also result in the partial disruption of the sp^2 hybridization system, they also degrade the electronic performance of the nanotubes.[81] The dispersion are then often stabilized by the formation of carboxylic acid groups on the CNT surface, increasing the solubility in common organic and inorganic solvents.[82] Therefore the last category, the non-covalent modification of carbon nanotubes is most often preferred for applications. This includes polymers "wrapping" the carbon nanotubes by adsorbing due to strong $\pi - \pi$ interactions and consequently decreasing the inter-tube van der Waals forces.[83] However, since conjugated polymers and also the wrapped CNTs have a limited solubility in aqueous solutions, they are often prepared with organic solvents like toluene.[84] Another advantage of this method is, that it allows for the sorting of electronic type [35] as well as certain chiral species like (6,5) and (7,5) in a two-step process, comprising of sonication or shear-force mixing and subsequent centrifugation.[84–87] The second-step is thereby used for the removal of unwrapped nanotubes, agglomerates and unreacted catalysts.[84] Additionally, this method is also able to facilitate dispersions with comparably long SWCNTs (eg. $1.8 \mu\text{m}$).[85] Potential drawbacks of polymer wrapped SWCNTs are the low yield ($\approx 0.35\%$) and high cost of the polymers ($\approx 50000 \frac{\text{€}}{\text{g}}$) [11], as well as the subsequent difficult removal of such [88, 89], which is needed for certain applications like solar cells as the polymers shorten the exciton life-time.[90] By contrast, aqueous suspensions are using surfactants, that encapsulate the SWCNTs with the hydrophobic part of their micelles, while the structure formed on the carbon nanotube is still a matter of debate.[9, 91] A great advantage of the aqueous sorting methods over the organic ones is the greater accessibility of different species (33 vs. 5 as of today [11]), which also include metallic species [31–33], enantiomers [37, 38, 92] and can also sort for length [29, 30] and wall-number.[28]

Especially the aqueous two-phase extraction (ATPE) method developed by Khiripin *et al.* has proven to be rapid and effective in accessing the most species of all techniques by being eight times cheaper than the organic route.[11, 33, 36] However, the obtainable SWCNTs are shorter (0.6-1.1 μm) compared to their polymer wrapped counterparts and the sorting methods are significantly more complex. SWCNTs from ATPE are often obtained dispersed in sodium deoxycholate (DOC), which has proven to stabilize SWCNTs over long time periods, even at very low concentrations (0.04 wt%) and can also be used to enrich the dispersions to very high carbon nanotube concentrations ($800 \mu\text{g mL}^{-1}$), which is imperative in order to reach the aforementioned low DOC concentration.[1, 40] Recently, Zhang *et al.* synthesized a surfactant that is closely related to DOC by replacing the sodium ion with an ammonium group and thus making it possible to remove the surfactant completely by pyrolysis.[93] Most of the surfactants used to date are known to be negatively charged, but also positively charged surfactants like Cetyltrimethylammoniumbromid (CTAB) have shown to be effective in dispersing carbon nanotubes.[94]

1.3. Alignment of Carbon Nanotubes

Tailoring the morphology of SWCNT thin-films has been a long standing challenge, as it constitutes the next line of influencing an applications performance, regardless of the SWCNTs themselves. Therefore initial devices have been created using disordered, unaligned films, which are not able to harness the highly anisotropic properties of the SWCNTs. These involve simple filtration [95], spin coating [96], dip coating [97] and the use of as-grown CNTs [98], resulting in compressed sheets of CNTs, the so-called CNT buckypapers [20]. On the other hand, some applications are in need of extremely high entropy films and need the SWCNTs also to be disordered in three dimensions, which can be achieved by the fabrication of aerogels. Those films are interesting for light absorbers, as well as thermoelectric elements, as their voids are inhibiting thermal transport, while maintaining the electrical conductance of a SWCNT film leading to higher thermal gradients and thus higher Seebeck coefficients.[99] However, when ordering of the SWCNTs is needed, one can distinguish between three main groups of manipulation: (1) Manipulation of as-grown CNTs, (2) Matrix assisted alignment (3) dispersion based techniques. For the first category, as-grown CNT forests made with CVD are aligned with the so-called 'dominio pushing' method, which is achieved by rolling a membrane onto the CNT-array, causing the SWCNTs to exhibit a common direction over rather large areas, Figure 1.5 (A).[21] Another representative technique, is the use of faceted nanosteps realized by a miscut sapphire ($\alpha\text{-Al}_2\text{O}_3$) [100] or Quartz,[22] which enable a controlled growth of SWCNTs again using CVD, Figure 1.5 (B). While all of these techniques offer alignment over large areas, they cannot influence the constitution of the SWCNTs (length, diameter, chirality and enantiomeric type) and as of today the removal of metallic SWCNTs from those films is often accompanied by a degradation of the performance of the device. The low density of SWCNTs generated result in a low current output, compared to silicon based counterparts.[25] The second category involves the fabrication of polymer-based composites comprising of a carbon nanotube suspended in chloroform and a thermoplastic polymer.

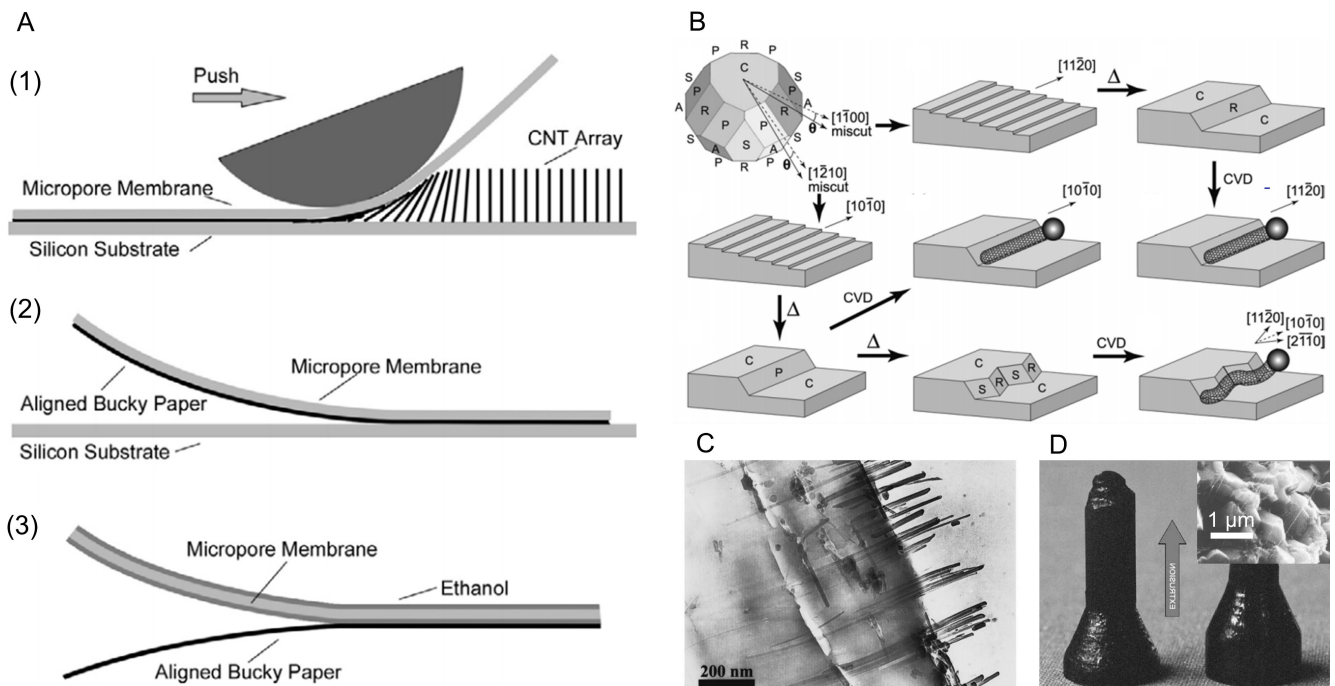


Figure 1.5.: Alignment methods of carbon-nanotubes using direct growth or as-grown SWCNTs and matrix-assisted methods. (A) Schematic representation of the "Domino Pushing"-method consisting of the push (1), lift-off from the substrate (2) and removal of the buckypaper (3).³ (B) Direct CVD growth on miscut-sapphire along the thermally grown grooves (denoted by Δ). Depending on the crystallographic faces created, the SWCNTs can also adopt a so called "saw-tooth" shape.⁴ (C) Alignment due to polymer-stretching, observed with a TEM.⁵ (D) Extrusion of metall-oxides containing carbon nanotubes, which align during the process. The insert shows the orientated nanotubes.⁶

A uni-axial loading is then applied to the polymer-matrix under elevated temperatures (100 °C), aligning the trapped SWCNTs, which keep their order even after the external stress is removed, Figure 1.5 (C).[39] Another method involves a dry mix of CNTs and metal-oxides (eg. $\text{Fe-Al}_2\text{O}_3$ and $\text{Fe/Co-MgAl}_2\text{O}_4$) in order to align the carbon nanotubes during an extrusion process under high temperature (1730 °C) forming a ceramic composite with aligned tubes, Figure 1.5 (D).[24] Ultimately, SWCNTs can be aligned by wrapping them in thermotropic liquid crystalline polymer (LCP) and dispersing them in a liquid crystalline elastomer (LCE) matrix. The alignment of the SWCNTs can be facilitated by again applying mechanical strain or using infrared (IR) light driving an actuation not possible with the pristine LCE system.[101] Other methods involving LCE systems use an filtration process to enrich

³ Used with permission of IOP Publishing from "Highly oriented carbon nanotube papers made of aligned carbon nanotubes", Wang et al., 19, 075609 and 2008; permission conveyed through Copyright Clearance Center, Inc.

⁴ Reprinted (adapted) with permission from "Carbon Nanotube Graphoepitaxy: Highly Oriented Growth by Faceted Nanosteps", 127, 33, 11554–11555, Ismach et al., Aug 1, 2005, American Chemical Society.

⁵ Reprinted from "Alignment of carbon nanotubes in a polymer matrix by mechanical stretching", Vol. 73, 119, Jin et al. October 1998 with the permission of AIP Publishing.

⁶ Reprinted from "Aligned carbon nanotubes in ceramic-matrix nanocomposites prepared by high-temperature extrusion" Vol 352, p. 20-25, Peigney et al., Jan 24, 2002, with permission from Elsevier.

the SWCNTs on the surface before alignment. Electric and magnetic fields mainly influencing the LCs can be used to notch the SWCNTs into alignment, as well as grooves in the membrane with sizes comparable to the LCs.[23] The alignment achieved with those methods is often lacking compared to other options outlined in this section, but it might be still sufficient to enhance mechanical, thermal or even optical properties of the host-material. However, the removal of the used matrix often poses an extra challenge and has to be considered, when the focus lies on the SWCNTs themselves. Ultimately, dispersion based methods, like the one discussed in this thesis, offer a variety of different approaches and are also compatible with solution-based separation techniques and thus offer several advantages over the ones mentioned above. An overview over all methods discussed below is shown in Figure 1.6. The Langmuir-Schaefer or Langmuir-Blodgett is commonly used to align 1D objects (eg. nanowires or nanotubes) [102] and utilizes an oil layer, where the SWCNTs suspended in 1,2-dichloroethane (DCE) are floating on top of an aqueous bath. The oil phase (DCE) is then evaporated, leaving behind an isotropic phase, with the SWCNTs floating on a two-dimensional air/water interface.

Alignment can be achieved by decreasing the space between two mobile barriers, effectively increasing the concentration and alignment until the film is about to crack, which can be avoided by monitoring the isotherm surface pressure. The difference in the methods is defined by the orientation of the substrate the film is transferred to (horizontal, Langmuir-Schaefer or vertical, Langmuir-Blodgett). In order to increase the covered substrate surface, the latter has been used in combination with roll-to-roll fabrication style methods for the alignment of graphene oxide (GO), but in generally this method is prone to reproducibility issues and can only produce small aligned areas.[103] In contrary to the method outlined above, evaporation-induced self-assembly (EISA) actually utilizes the evaporation of an aqueous nanotube suspension as the main alignment mechanism. Thereby a receding meniscus is formed by trapping the suspension between two microscope slides and creating a capillary flow transporting the SWCNTs to the liquid-air interface by lifting the slide on the top.[104] This method has been shown to work with (n, m) -pure SWCNTs in aqueous solutions using sodium dodecyl sulfate (SDS),[104, 105] as well as organic solutions by wrapping the SWCNTs in Poly[(9,9-dioctylfluorenyl-2,7-diyl)-alt-(6,6'-2,2'-bipyridine)] (PFO-BPy),[106, 107] but is lacking in the size covered ($\approx 20 \mu\text{m}$). [104] Until recently, researchers believed that its mechanism would be coherent with floating evaporative self-assembly (FESA), contributing to its name given. For this technique a substrate immersed in water is pulled out steadily, while droplets of the organic dispersion are carefully placed on top of the water/air surface. The SWCNTs are then gathering at the organic/air/water interface and can be deposited onto the wafer by

⁷ Reproduced from “Arrays of single-walled carbon nanotubes with full surface coverage for high-performance electronics”, Vol 8, p. 180-186, Cao et al., January 2013 with permission from Springer Nature.

⁸ Reprinted (adapted) with permission from “Nanotube Alignment Mechanism in Floating Evaporative Self-Assembly”, 33, 46, 13407–13414, Jinkins et al., October 2017, American Chemical Society.

⁹ Reprinted (adapted) with permission from “Aligned Carbon Nanotube Thin Films from Liquid Crystal Polyelectrolyte Inks”, 7, 46, 25857–25864, Tune et al., October 2015, American Chemical Society.

¹⁰ Reprinted (adapted) with permission from “Substrate-Wide Confined Shear Alignment of Carbon Nanotubes for Thin Film Transistors”, 5, 2, p9, Jinkins et al., November 2018, Wiley-VCH

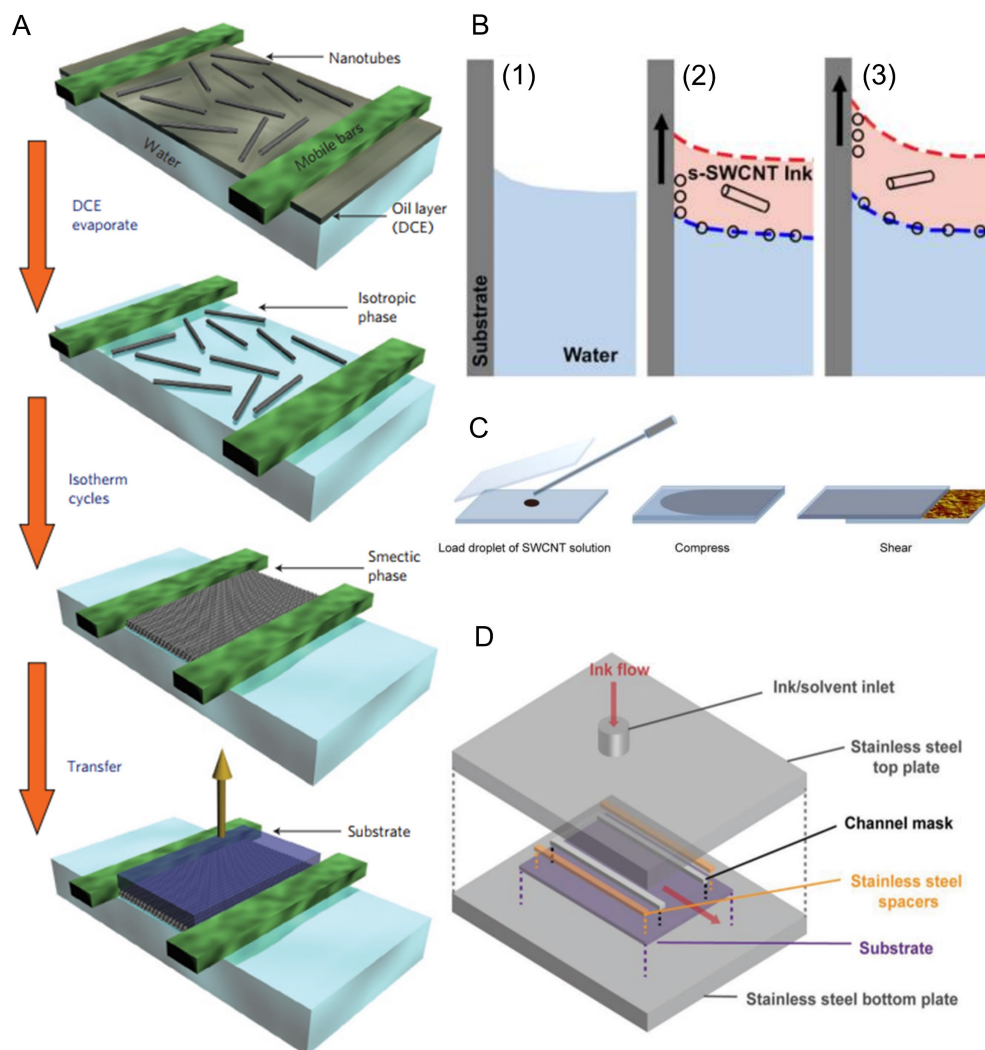


Figure 1.6.: Overview of dispersion based alignment methods: (A) Langmuir-Schaefer method as used by Cao *et al.*⁷ (B) Floating evaporative self-assembly according to Jinkins *et al.*⁸ (C) Alignment of highly concentrated SWCNT inks by shear.⁹ (D) Usage of confined shear flow by Jinkins *et al.* to coat a large surface (up to 100 cm²) with a single layer of aligned SWCNTs.¹⁰

pulling it carefully horizontally. Even though the organic solvent is evaporating at a fast rate, it gets steadily replaced by new droplets and thus Jinkins *et al.* stated, that the alignment depends on the interface interactions rather than the evaporation of the solvent.[108] Similar to the LC-based methods shown above, Krupke *et al.* have shown that HiPco SWCNTs suspended in SDS can be sorted by electronic type and aligned directly using electrical fields applied in a small capacitor over a substrate.[109] Another set of approaches utilizes high concentrated SWCNT inks (≈ 4.5 mg/mL), where the SWCNTs are commonly dispersed by super-acids (eg. chloro sulfonic acid, HSO₃Cl), [26] sodium ions [80] or even forming liquid crystals from the SWCNTs suspended by DNA.[110] A small droplet of the ink is then sandwiched between two microscope slide, which are displaced in a rapid motion to facilitate the shear

Alignment method	Area Covered	Layers and Density	deposition time or velocity	CNT Material used
Domino Pushing [21]	79 cm ²	ML, HD	-	as-grown SWCNTs
Growth on faceted nanosteps [22, 100]	2 mm ²	SL, LD	5- 10 h	precursor material (CVD)
Polymer matrix stretching [39]	15 mm ²	ML, LD	-	MWCNTs dispersed in chloroform
Metal oxide extrusion [24]	1470 mm ²	ML, LD	200 μm min ⁻¹	MWCNTs (powder)
Liquid crystal assisted alignment [23]	0.5 mm ²	SL, LD	-	SWCNTs and MWCNTs dispersed in LCs
Langmuir-Shaefer/ Langmuir-Blodgett[25]	1 mm ²	ML, HD	2 h	SWCNTs (s) in (DCE)
Evaporation-induced self-assembly [104, 107]	10 mm ²	SL, MD	12 μm min ⁻¹	SWCNTs aq. (SDS) and organic (PFO-BPy)
Floating evaporative self-assembly [108]	6.25 cm ²	SL, MD	10 μm min ⁻¹	SWCNTs (s), organic (PFO-BPy)
Dielectrophoresis (electric field) [109]	6000 μm ²	SL, MD	-	SWCNTs aq. (SDS)
chlorosulfonic acid, mechanical shear[26]	9 mm ²	ML, HD	-	SWCNTs in HSO ₃ Cl
nanotubides, mechanical shear[80]	18.75 m ²	ML, HD	-	SWCNTs in sodium DMA
Nanochannel, mechanical shear[111]	24 cm ²	ML, HD	-	SWCNTs aq. (SDS)
Constrained channel, shear flow [113]	100 cm ²	SL, MD	-	SWCNTs (PFO-BPy)
Dead-End filtration [1, 40, 41]	6.25 mm ²	ML, HD	2 h	SWCNTs aq. (DOC, CTAB, SDBS)

Table 1.1.: Summary of different carbon nanotube alignment methods. The methods are additionally differentiated by the amount of layers they produce (SL: single layer, ML: multi layer) and the density of the films obtained (LD: low density, MD: medium density, HD: high density). Following the categories given above, they are further separated by the conditions of the SWCNT material used.

needed for alignment of ≈ 40 nm thick films. The high concentration of charges present on the SWCNTs often pose a challenge for device applications, which led researchers to apply mechanical shear also to lesser concentrated SWCNT (SDS) dispersion, involving the use of nanochannels made from Poly-(ethylenglykol)-diacrylat (PEG-DA) [111] or Polydimethylsiloxan (PDMS) [112], which are then moved over a substrate (eg. silicon). The shear force needed can also be provided by a fast flow through a channel using again concentrated inks of SWCNTs (Chloroform, PFO-BPy), as shown recently by Jinkins *et al.* The channel used in this approach is rather wide (10 cm) and allows for large scale surface coverage (100 cm²). [113] Finally, the dead-end filtration method also discussed in this thesis, gathered its attention in the community in 2016, when He *et al.* reported large scale alignment of SWCNTs on a membrane spanning over ≈ 25 mm, while alignment measured by the two dimensional order parameter S_{2D} is almost reaching one and is discussed in further detail below. All methods outlined above are summarized in Table 1.1.

1.3.1. Applications of Aligned Films

Regardless of the scientific interest in aligning carbon nanotubes, there are also novel and existing applications that are expected to benefit from them. Aligned films are anticipated to provide performance enhancements as the anisotropic physical properties of one-dimensional nanoobjects cannot be harnessed in disordered films. [14] This involves the electronic transport, [40] heat transfer, [114] and polarization dependent optical properties, [17] as exemplified by Figure 1.7. Additionally, aligned films would minimize device variations while not requiring to position individual carbon nanotubes over large areas. [47] Random-networks of undoped carbon nanotube thin-films typically reach conductivities in the range of several hundreds of S cm⁻¹ [115, 116] and are falling thereby one

order of magnitude short compared to dense aligned films ($\sigma = 2500 \text{ S cm}^{-1}$).^[40] It should be mentioned, that the density of the films also plays an important role in the electronic transport as electrons have to be passed between the nanotubes, which in turn leads to low conductivities in low density, but aligned CVD films ($\sigma \approx 10 \text{ S cm}^{-1}$). Thereby high performance electronics utilizing the high conductivities of aligned carbon nanotubes have already been demonstrated by Kang *et al.* and would also be of interest for bendable electronics/optoelectronics,^[117] which also involve transparent electrodes suitable for security applications and back-lit displays.^[118] For SWCNT transistors

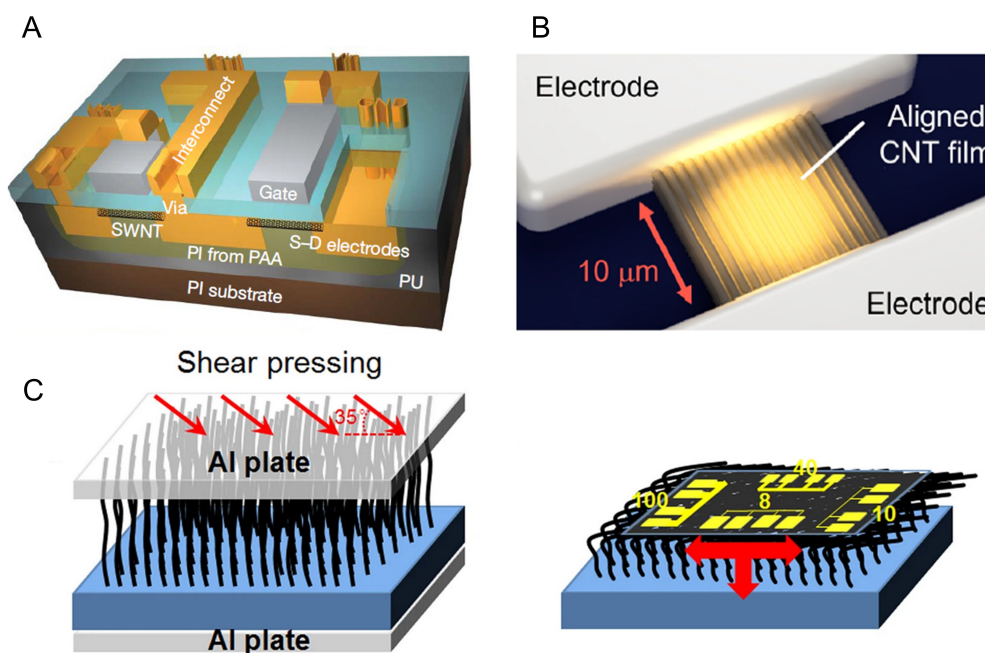


Figure 1.7.: Several applications of aligned carbon nanotubes, covering electronics, optics and heat transfer: (A) flexible electronics design from Cao *et al.*¹¹ (B) Polarized light emitter from Matano *et al.*¹² Heat transfer capability of shear-aligned MWCNTs probed with Au-microsensors with various sizes (C).¹³

the carrier mobility and achievable On/Off ratio are mainly dependent on the semiconducting purity of the SWCNTs used and their alignment. While the highest mobility and On/Off ratio is still observed for individual SWCNTs ($\mu_m = 10\,000 \text{ cm}^2/\text{Vs}$, 10^6), transistors made with semiconducting SWCNTs reach mobilities of $\approx 1000 \text{ cm}^2/\text{Vs}$ with On/Off ratios of 100, which still surpass their disordered counterparts by one magnitude for each value.^[119] This tendency can also be observed for the thermal conductivity,^[120] as peak performance to date has been observed for aligned bucky papers ($766 \text{ W m}^{-1} \text{ K}$),^[20] while lower density arrays are dropping off significantly and only reach

¹¹ A) Reproduced from “Medium-scale carbon nanotube thin-film integrated circuits on flexible plastic substrates”, 454, p. 495–500, Cao *et al.*, July 2008 with permission from Springer Nature

¹² B) Reprinted (adapted) with permission from “Electrical Generation of Polarized Broadband Radiation from an On-Chip Aligned Carbon Nanotube Film” 4, 4, 626–633, Matano *et al.*, March 2022, American Chemical Society.”

¹³ C) Reproduced from “Remarkably enhanced thermal transport based on a flexible horizontally-aligned carbon nanotube array film.” *Sci Rep* 6, 21014, Qiu *et al.*, February 2016 with permission from Springer Nature under Creative Commons

thermal conductivities below $1 \text{ W m}^{-1} \text{ K}$ [121] or up to $270 \text{ W m}^{-1} \text{ K}$. [122] Heat transfer in carbon nanotubes is mainly governed by phonon conduction, which is even true for metallic carbon nanotubes. [123] However, the mean free path of phonons in films is expected to be much shorter than in individual CNTs (0.5 to 1.5 μm) [124–126] and so besides mechanical compression, [20] acid treatment and decreasing the defect density, [127] there is also alignment of the carbon nanotubes in order to achieve better performing devices. [20] As an application, heat management is getting more attention, as three-dimensional integrated electronics require efficient heat dissipation, [123] which lead also to the involvement of industrial research. [128] In the optical research field, linear polarizers made of carbon nanotubes for the fast growing field of terahertz spectroscopy [18] are considered a viable alternative for the inflexible, brittle wire grid polarizers, which require high precision fabrication processes [129, 130] and are exhibiting low extinction ratios compared to their infrared/Vis counterparts. Recently, Baydin et al. showed the existence of a “magic” angle (30°) between the THz pulse and an aligned SWCNT thin film ($t \approx 45 \text{ nm}$) made with the filtration method, which rotated the polarization by exactly 90° , due to the high anisotropy of the optical constants of the film and SWCNTs. [17] In other wavelength ranges, radial aligned SWCNTs could find use cases as optical limiters for sensors and eyesight against radial polarized lasers, [131] due to their high absorption in the infrared/VIS range, ($\lambda \approx 400\text{--}800 \text{ nm}$) as well as photomasks in the extreme UV wavelength range ($\lambda \approx 10 \text{ nm}$). [132] Other applications involve the detection of polarized light via a p-n junction made from undoped and doped SWCNTs, which would be suitable for flexible and planar devices, [133] or emitters of polarized light as shown recently by Matano et al. [134]

1.3.2. Alignment of Single-Wall Carbon Nanotubes using Dead-End Filtration

The following chapter focuses on the discovery and development of the filtration technique used for the global alignment of carbon nanotubes and the challenges, that still have to be addressed in order to increase the impact it could have on the design of novel applications. The literature documenting the development of the filtration technique is summed up in Figure 1.8. In 1998 Shaffer et al. [135] recognized that enrichment of carbon nanotubes at the membrane surface can result in the formation of a nematic phase and self-ordered domains of multi-wall CNTs. The concentrations of SWCNTs needed to form liquid crystals and thus nematic ordering have been determined to be ($\approx 3.8 \text{ mg mL}^{-1}$ [136]) and following the Onsager theory, Lagerwall et al. suggested for a typical SWCNT with a length and diameter ratio of $\frac{l_t}{d_t} = 1 \times 10^3$ a concentration of ($\approx 1.5 \text{ g mL}^{-1}$ [137]). The controlled use of dead-end filtration

¹⁴ Reprinted (adapted) with permission from “Nematic-Like Alignment in SWNT Thin Films from Aqueous Colloidal Suspensions” 51, 30, 10232–10237, Dan et al., June 2012, American Chemical Society.

¹⁵ Reproduced from “Wafer-scale monodomain films of spontaneously aligned single-walled carbon nanotubes”, 11, p. 633–638, He et al., Apr 2016 with permission from Springer Nature

¹⁶ Reprinted (adapted) with permission from “Groove-Assisted Global Spontaneous Alignment of Carbon Nanotubes in Vacuum Filtration” 20, 4, 2332–2338, Komatsu et al., February 2020, American Chemical Society.

¹⁷ Reprinted (adapted) with permission from “Global Alignment of Solution-Based Single-Wall Carbon Nanotube Films via Machine-Vision Controlled Filtration” 19, 10, 7256–7264, Walker et al., September 2019, American Chemical Society.

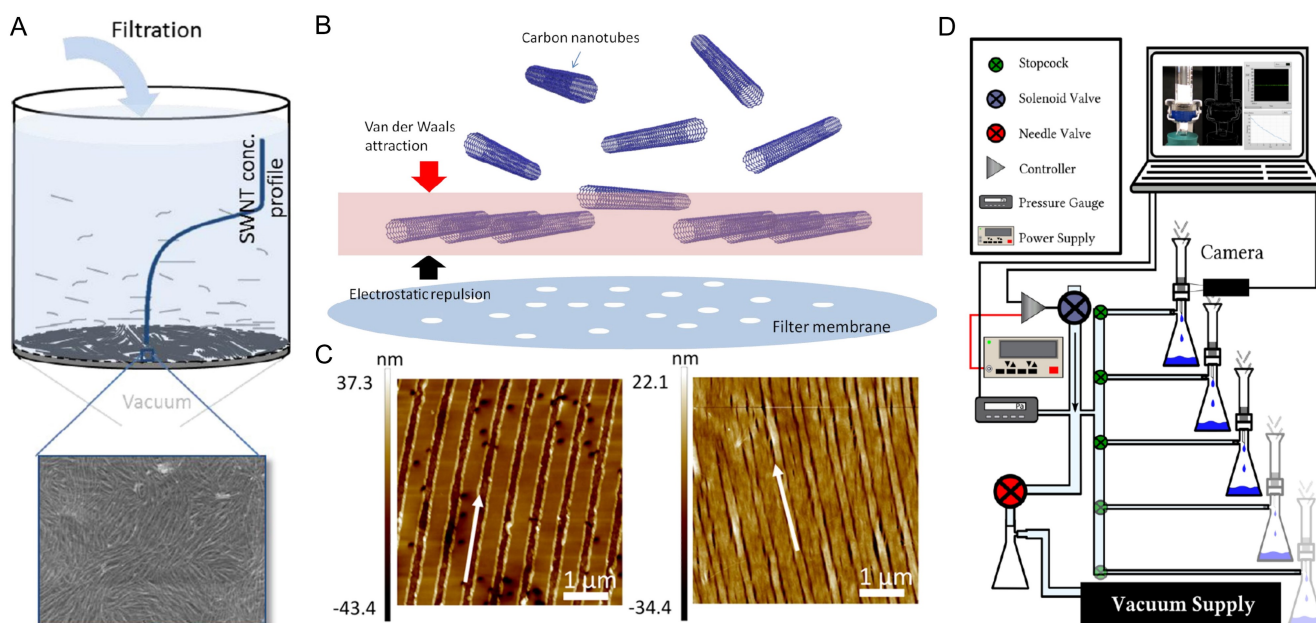


Figure 1.8.: Overview of the development of the filtration method to date: (A) Nematicially aligned SWCNTs achieved by slow vacuum filtration by Dan *et al.*¹⁴ (B) Model proposed by He *et al.* in 2016,¹⁵ consisting of the SWCNTs gathering in a two-dimensional plane above the membrane and spontaneously aligning without an exterior direction, contrary to the alignment by artificial grooves facilitated by Komatsu *et al.* four years later (C).¹⁶ (D) Parallel vacuum bench filtration setup by Walker *et al.*. The flow rate is controlled by monitoring the meniscus of the dispersion in the funnel with machine vision.¹⁷

to obtain nematicially ordered films of SWCNTs began with Dan *et al.* [95] and King and Panchapakesan,[138] who observed the formation of single domains (several μm^2 in size) when aqueous dispersions of SWCNTs were slowly filtered onto polycarbonate track-etched (PCTE) and mixed cellulose ester (MCE) membranes, and this despite the use of SWCNT concentrations (45 and 0.01 mg mL^{-1}) that are well below the concentrations stated above. This has been later rationalized to warrant the required rotation time for an unaligned CNT to orientate itself approaching the surface. Then He *et al.* [40] made the remarkable discovery, that under very specific filtration conditions it was possible to create a single, globally aligned domain of SWCNTs. Despite the efforts of the authors to provide complete experimental information, the filtration technique remains challenging to reproduce, as most research groups anecdotally only reported to achieve local instead of global ordering. The difficulty can be primarily attributed to the experimental sophistication required to control the flow rate with high precision, and until recently,[1] it has also been unclear how narrow the set of flow conditions are. As of now, global alignment has been demonstrated for polyvinylpyrrolidone (PVP) coated PCTE membranes with a pore size of 80 nm or 200 nm and a filtration diameter of 15 , 22 and 25 mm . [1, 40, 41, 139, 140] In most cases, the SWCNTs were dispersed by negatively charged surfactants such as sodium deoxycholate (DOC) or sodium dodecylbenzenesulfonate (SDBS) and at a concentration ($0.004 - 0.03 \text{ wt}\%$) well below the critical micelle concentration ($0.24 \text{ wt}\%$ for DOC [40] and $0.13 \text{ wt}\%$ for SDBS [141]) of the surfactant. In the first studies, a total volume of $4 - 5 \text{ mL}$ with a SWCNT concentration of $\approx 8 - 15 \mu\text{g mL}^{-1}$ [40,

41, 139, 142] was then carefully filtered using conventional bench-top filtration apparatus, as He et al. stress the importance of a "slow and well-controlled" flux, right from the beginning of the filtration. This required a careful adjustment of the pressure series of steps from zero to a gentle pressure at the beginning of filtration such that volume rates of $1 - 2.5 \text{ mL h}^{-1}$ are obtained, followed by a reduction to even 0.5 mL h^{-1} as the SWCNTs begin to enrich. A final ramp to $\approx 10 \text{ mL h}^{-1}$, which is applied when the meniscus of the solution is 3 – 5 mm above the membrane surface, is finally applied in order to push the aligned film onto the membrane and consequently dry it. While He et al. emphasized the importance of the initial phase of the filtration, Komatsu et al. later stated that also the pushing step had to be optimized in order for the nanotubes to globally align, but unfortunately both were not able to provide data on the precision of control needed.[40, 139]

These issues are further complicated by the desire to widen the diameter range of the CNTs used, as well as the tendency of authors only showing champion alignment, while the mechanism behind the transition from local to global order is still up to debate. As an example, He et al. [143] report large diameter ($d_t \approx 1.4 \text{ nm}$) SWCNTs to align better than their small diameter ($d_t \approx 0.73 \text{ nm}$ to 1 nm) counterparts, but it is unclear why and which experimental parameter(s) would lead to an improvement. This is also reflected by the amount of studies on aligning large diameter electric arc synthesis method SWCNTs (EA-SWCNTs) [17, 41, 139, 144–147], while only a few studies can be found on small diameter cobalt-molybdenum catalyst synthesis method SWCNTs (CoMoCAT-SWCNTs). [40, 148] To acquire data on the flow-rates needed, Walker et al. introduced the first custom-built setup, comprising of a bench-top filtration apparatus treated with hydrophobic silane coating and a camera monitoring the level of the meniscus over time, in order to measure the flow-rate.[41] A feedback loop was then deployed, steering the vacuum source under the membrane, in order to ensure a constant flow-rate until the final pushing ramp was triggered. While the authors, were able to reproduce the global alignment and measure an increase in filtration resistance, the precision did not allow for an analysis of the mode of fouling. Also the initial flow-rate could not be lowered indefinitely due to the gravity pull acting on the dispersion and the final flow-rate could only be estimated due to the disappearance of the meniscus. As one of their findings, Walker et al. also reported an enhancement of the alignment after tribo-charging the membrane, which lead them to the conclusion, that the alignment was a consequence of the SWCNTs being orientated by directional charges present on the membrane. Alternatively, Komatsu et al. have shown that the global alignment direction is closely correlated macro- and micro-grooves found in the PCTE membrane, which are caused by the roll-to-roll manufacturing process. This could also lead ambiguously to the directional charges mentioned before.[139] Correspondingly, the authors later intentionally modified their membranes by embossing a series of periodically spaced grooves [139] using a diffraction grating and showing that there is an enhancement in alignment as well. Those mechanisms stand in contrast to the explanation given by He et al., stating that the carbon nanotubes self-orientate in a 2-dimensional plane of minimum potential above the surface of the membrane. This plane of minimum potential is a consequence of attractive van-der Waals potentials ϕ_{VDW} and repulsive electric double-layer potentials ϕ_{EDL} being superimposed and resulting in ϕ_{TOT} , which can be commonly described by DLVO-theory. Nevertheless, it is commonly agreed upon that alignment occurs close to, but not directly on the membrane surface,

which would require deeper knowledge of the filtration process used.[40, 41, 138, 139] Consequently the following section 1.4 is providing a basic understanding of filtration, in order to provide a framework for interpreting the obtained films and the filtration resistances measured.

1.4. Principles of Filtration

Filtration can be described in simple terms, as a separation technique in which a solute (eg. SWCNTs) are separated from the solvent (eg. water) by means of retention of a membrane. During the process, several transport mechanisms have to be considered, that cause the solvated species to either be collected on the membrane surface, forming a retentate or getting conveyed to the feed solution, enriching it, which is shown in Figure 1.9. Therefore for a single

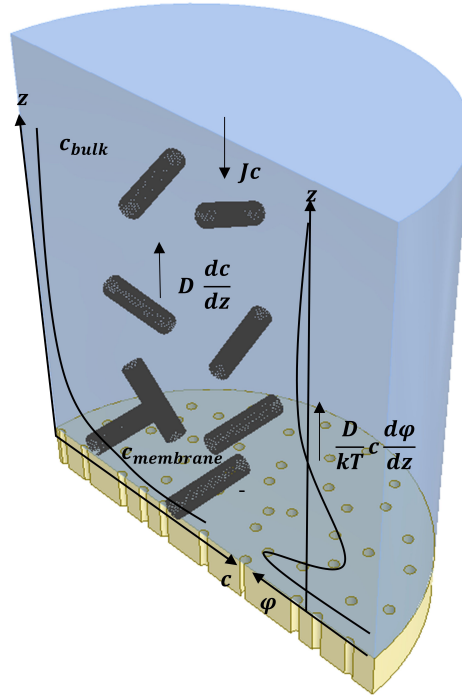


Figure 1.9.: Transport mechanisms occurring during filtration, according to the particle stream balance provided by Bachhin et al.,[149] shown in equation 1.13. The concentration of the solvated species (SWCNTs) is increasing at the membrane during filtration, leading to a diffusive back-transport $D \frac{\partial c}{\partial z}$ into the feed, counteracting the convective flux Jc . The vector, derived from the interaction potential ϕ is also defined to be opposing the convection, but can turn its direction depending on the distance to the surface z .

colloid (a single SWCNT), one can describe the mechanisms by an effective flux of particles N : [149]

$$N = Jc - D \frac{\partial c}{\partial z} - \frac{D}{kT} c \frac{\partial \phi}{\partial z} \quad (1.13)$$

The first part of the equation covers the convective flux J of the particles towards the membrane actuated by a vacuum suction under the membrane, gravity or even positive pressure applied to the feed and is also dependent on the concentration of the solute in the feed, also termed bulk c_{bulk} . Conventionally, J is thereby defined by the volume-rate \dot{v} divided by the effective area of the membrane A_{mem} . The second part is governed by the diffusion and depends on the concentration gradient $\frac{\partial c}{\partial z}$, that builds up during the filtration. The diffusion coefficient D is also found in the last part, which inherits the thermal energy kT and the interaction potential ϕ between the solute and the membrane, which can be derived by DLVO-theory. While the diffusion driven by the concentration gradient between the concentration at the membrane $c_{membrane}$ and c_{bulk} is always counteracting the convective transport, the flux vector driven by the interaction potential can point either towards or away from the membrane depending on the SWCNTs being repulsed or attracted by the electric double layer forces, which will be discussed in detail later. Equation 1.13 offers basically two possible outcomes for the filtration process. If the effective flux $N = 0$ or even becomes negative, the solute will remain dispersed in the feed solution, which should happen for slow flux J towards the membrane and is commonly described as concentration polarization (CP). Alternatively, fouling occurs if $N > 0$ causing the species to deposit onto the membrane and lowering its permeability. In practical terms, concentration polarization leads to an increase of solute concentration above the membrane and can be removed by rinsing the membrane or back-flushing, while fouling results in an irreversible solid blocking layer.[150] CP is further defined by the geometry of the filtration setup itself. In cross-flow filtration, the feed solution is driven parallel to the membrane surface, leading to only a partial flow actually permeating the membrane, while in dead-end filtration the flux vector is directly pointing at the membrane. In the former case, a critical flux (CF) can be found, under which CP occurs, but no fouling can be observed. On the contrary, using a dead-end geometry always leads to fouling, eventually, resulting in a flux-dependent critical fouling volume (CFV) before fouling occurs.[151] Therefore CP is probed differently for both setups: In cross-flow setups, researchers and engineers are conventionally using the so-called "flux-stepping" consisting of incremental full increases and halved decreases of fluxes to determine the CF, without the need of exchanging the membrane,[152, 153] opposing to dead-end filtration setups, where several fluxes have to be tested with a pristine membrane.[151] Since SWCNTs are aligned using a dead-end filtration setup in this thesis, all following aspects of fouling and CP are discussed in terms of this filtration geometry.

1.4.1. Concentration Polarization, Fouling and Blocking Laws

In order to distinguish between concentration polarization and fouling, the change in filtration resistance R_{total} with permeated volume has to be determined. Given that the viscosity of the solvent is known ($\mu_{H_2O, T=298K} = 0.89 \text{ mPa}\cdot\text{s}^{-1}$ [154]), the resistance can be calculated as follows using Darcy's law, equation 1.14 :[131, 155]

$$R_{total} = \frac{p_{TMP}}{\mu \cdot J} \quad (1.14)$$

Thereby the trans-membrane pressure p_{TMP} can be evaluated by subtracting the pressure beneath the membrane p_{out} from the pressure p_{in} used to drive the liquid through it. The total resistance R_{total} itself contains all resistances occurring during the filtration and describes it as a series similar to electrical resistances (Kirchhoff's law), equation 1.15 :[1, 156]

$$R_{total} = R_{setup} + R_m + R_{cp} + R_b \quad (1.15)$$

With R_{setup} being the resistance of the setup, R_m the membrane resistance, R_{cp} the resistance due to the concentration polarization and R_b the resistance due to blocking of the membrane (fouling). The first two components are constants, that can be determined prior to an experiment and in fact R_m can also be approximated (R_{mT}), if the charges are neglected, see Figure 1.10 and equations 1.16 to 1.20:

$$J_p = \frac{\partial V_p}{A_p \partial t} = \frac{\pi r^2 \Delta p}{8 \mu l_p} \quad (1.16)$$

$$J_m = \frac{\partial V_m}{A_m \partial t} = \frac{p_{TMP}}{\mu R_m} \quad (1.17)$$

$$n \dot{v}_p = \dot{v}_m \quad (1.18)$$

$$n = \epsilon_{pore} A_m \quad (1.19)$$

Combining 1.16 to 1.19, one can calculate the theoretical membrane resistance:

$$R_{mT} = \frac{128 l_m}{\pi^2 d^4 \epsilon_{pore}} \quad (1.20)$$

As stated above, the flux J is defined as the volume rate normalized by the area the liquid passes through. For a

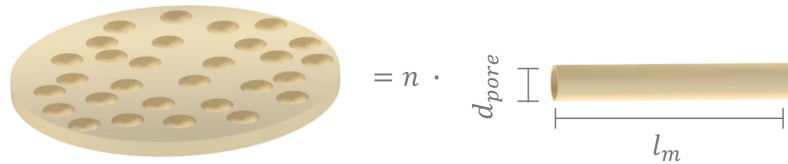


Figure 1.10.: Schematic of the theoretical calculation of theoretical membrane resistance, R_{mT} . All n pores of the membrane are considered as a set of identical cylinders with diameter d_{pore} and length l_m . The hydraulic resistance of a single pore is calculated with the Hagen-Poiseuille-law and under the assumption that the flow is split equally between all pores. Reproduced from [1]

single pore, this area is the pore area, A_p and for a membrane it is the entire membrane area, A_m . The flow inside a tube with known length, l_p can be calculated with the Hagen-Poiseuille-law, if the tube radius, r , the pressure difference, Δp which stems from the difference of the inlet and outlet pressure and the viscosity of the liquid, μ , are known. To relate the flow of a single pore to all pores of the membrane an assumption is made that the volume passing the membrane is split equally between the pores and that the pressure difference between inlet and outlet

is the same as the trans-membrane pressure, p_{TMP} . The number of pores n can be calculated by multiplying the membrane porosity ϵ_{pore} with the membrane area A_m . [1] Additionally, membranes are also defined by their ability to separate the solute from the solvent, which is usually defined by the molecular weight of the impermeable species and the membrane itself. This can also be described by the observable (equation 1.21) and intrinsic retention (equation 1.22). [157, 158] Thereby the observable retention is defined by the ratio of the concentration of the bulk c_{bulk} and the permeate $c_{permeate}$, while the intrinsic retention relies on knowledge of the enrichment of concentration close to the membrane $c_{membrane}$, which is often experimentally challenging to determine.

$$r_{obs} = 1 - \frac{c_{permeate}}{c_{bulk}} \quad (1.21)$$

$$r_{int} = 1 - \frac{c_{permeate}}{c_{membrane}} \quad (1.22)$$

The latter two parts of the total resistance can be identified by monitoring the resistance of the membrane during passage of the feed with respect to the permeated volume. Fouling is identified as a positive gradient in the resistance, while CP often manifests as a constant added resistance. [1, 159] However, analysis of the gradient of the resistance with respect to permeated volume allows for the mode of fouling to be determined, or in other words, the way in which mass accumulates on the membrane. [160] This is done by applying so called blocking laws which were first introduced by Hermans and Bredée, [161] further improved by Gonsalves and Grace [162] and were later summarized by Hermia et al. [143] in a simple power law expression. Eventually, Hlavacek and Bouchet derived these laws for constant flow rate experiments [163] depicted in Figure 1.11. Depending on the particles and membrane, the filtered species can either block the pores entirely (complete blocking), reduce the effective pore size by depositing inside the pores (pore blocking), form a film that partially blocks pores (intermediate blocking), or build up on top of pre-existing layers (cake filtration). To identify the blocking law, usually the transmembrane pressure p_{TMP} is plotted against volume v or time t and a linear fit is tested for various axis of p_{TMP} . These laws can be summarized in a single power law and are defined by viscosity (eg., Newtonian fluid), and whether the experiment is performed in constant flow, constant pressure or constant p_{TMP} mode. For the former case (constant flow rate), which is exclusively used in this thesis, all cases can be summed up by the following power laws, if p_{TMP} is plotted against the volume v (equation 1.23), [164] or time t (equation 1.24). [163]

$$\frac{\partial^2 p_{TMP}}{\partial^2 v} = k'_1 \left[\frac{\partial p_{TMP}}{\partial v} \right]^{n'_1} \quad (1.23)$$

$$\frac{\partial^2 t}{\partial^2 p_{TMP}} = k'_2 \left[\frac{\partial t}{\partial p_{TMP}} \right]^{n'_2} \quad (1.24)$$

In constant flow mode, the resistance R_b obtained by Darcy's law is proportional to the p_{TMP} , and it is possible to directly compare the slope of R_b to the volume v . While the fitting values for n are numbers ranging from 1.5 to 2, the parameters k are comprising of different filtration parameters (eg. membrane resistance R_m , constant flux J or viscosity).

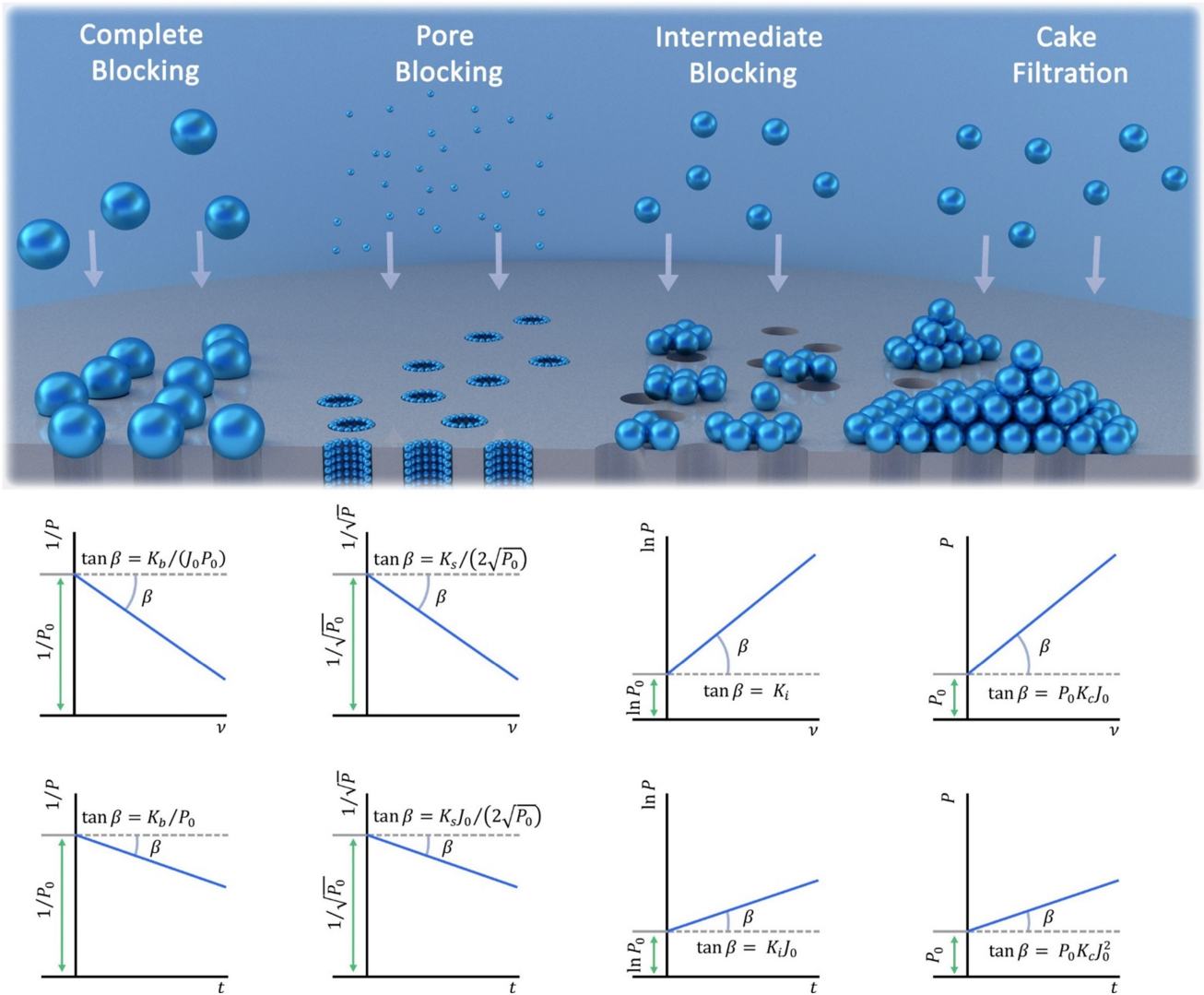


Figure 1.11.: A schematic of the four types of fouling that exist and their associated blocking laws. In each case the blocking law is derived from a generalized power law and are shown for constant flux and Newtonian fluids.[164] In this case, the pressure $P = p_{TMP}$. Figure reproduced from [1].

1.4.2. Derjaguin, Landau, Verwey, Overbeek Theory

The following part is a summary of the work of Trefalt and Borkovec [165] and as well as the textbook of Israelachvili.[166] DLVO-theory is named after the principal ideas of Boris Derjaguin [167], extended by Lev Landau [168] and later published in a book by Evert Verwey and Jan Overbeek.[169] Initially their goal was to describe the aggregation of identical particles (homoaggregation) and later on different particles (heteroaggregation) or even the deposition of particles onto a planar surface, Figure 1.12. In its simplest form, the force $F(z)$ between two particles

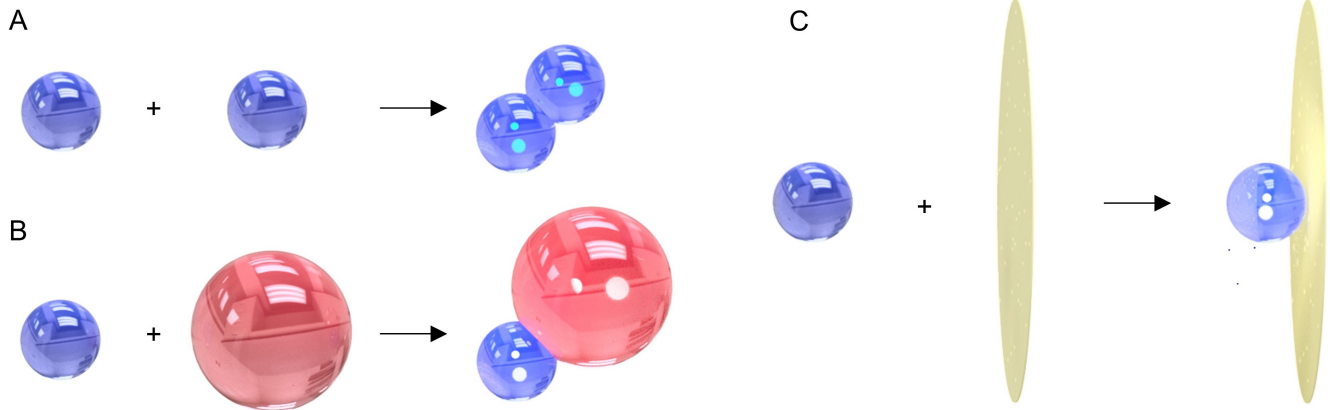


Figure 1.12.: Examples of Homo- and Hetero-aggregation as well as Deposition according to Trefalt and Borkovec.[165]

can be described by the Derjaguin approximation (DA), shown below:

$$F(z) = 2\pi r_{eff} W(z) \quad (1.25)$$

with the effective radius being:

$$r_{eff} = \frac{r_1 r_2}{r_1 + r_2} \quad (1.26)$$

with r_1 and r_2 being the radii of the different particles, and this consequently yields for identical particles $r_{eff} = \frac{r}{2}$. The interaction energy between the particles can then be calculated by integrating, as shown in equation 1.27:

$$W(z) = \int_h^{\text{inf}} F(z') \partial z \quad (1.27)$$

The total free energy $W(z)$ can then be obtained by means of the DLVO-theory in terms of superposition of the van der Wals forces and the electric double layer forces, leading to:

$$W(z) = W_{VDW}(z) + W_{edl}(z) \quad (1.28)$$

The first term can then be described with the framework of the Livshitz theory, which describes the free energy between two semi-infinite half-spaces in a non-retarding dispersion, considering microscopic length scales.[170, 171]

$$W_{VDW}(z) = -\frac{A}{12\pi z^2} \quad (1.29)$$

The evaluation of the Hamaker constant A is considering the free energy of two opposing surfaces as the sum of of the interactions between pairs of atoms located within those surfaces.[172] It is geometry independent and has typical values in the range of 10×10^{-21} to 10×10^{-19} J, which often decrease with salt content in the solvent. Experimentally it can be determined via dielectric constants or ionisation-potentials.[173] Overall Hamaker constants

can be derived with equation 1.30 and 1.31, depending on their composition being equal ("1") and separated by a medium ("2") or dissimilar/aggregating like in a deposition leading the other surface to be ("3"):

$$A_{121} = (A_{22}^{\frac{1}{2}} - A_{11}^{\frac{1}{2}})^2 \quad (1.30)$$

$$A_{123} = (A_{33}^{\frac{1}{2}} - A_{22}^{\frac{1}{2}})(A_{11}^{\frac{1}{2}} - A_{22}^{\frac{1}{2}}) \quad (1.31)$$

However, the Lifshitz theory is not favorable to use for SWCNTs, as it relies on flat boundary surfaces and SWCNTs might not be characterized sufficiently by the frequency-dependent dielectric permittivity.[174] For nanoscopic length scales (short range interactions), one can use the Lenard-Jones potential, which has been initially used by Girifalco *et al.* to describe carbon nanotubes [175] and others following his work.[176–178] It can only be used for the van der Waals forces with the attractive constant being $k_{attractive}$ or also the repulsive part $k_{repulsive}$, equation 1.32:

$$W(z) = -\frac{k_{attractive}}{z^6} + \frac{k_{repulsive}}{z^{12}} \quad (1.32)$$

The most popular method to describe the electric double layer forces is the Poisson-Boltzmann model, which in its simplest form describes two plates being immersed in an electrolyte at a distance z . The second order derivative is thereby described by the charge density ρ divided by the dielectric permittivity of the vacuum ϵ_0 and electrolyte ϵ_r , equation 1.33:[166]

$$\frac{\partial^2 W_{EDL}}{\partial z^2} = -\frac{-\rho}{\epsilon_0 \epsilon_r} \quad (1.33)$$

Therefore, the charge density can be written in terms of the concentrations of the anions c_- and cations c_+ being present in the electrolyte with equal charge q as:

$$\rho = q(c_+ - c_-) \quad (1.34)$$

The concentrations c_+ and c_- do change with the distance to the plates and are also dependent on the free energy and can approximated as the bulk concentration c_B for very low potentials or charges, or high temperatures T :

$$c_{\pm} = c_B \exp\left(\mp \frac{qW_{EDL}}{kT}\right) \quad (1.35)$$

The bulk concentration $c_B = N_A I$ is often also addressed in terms of the ionic strength I , which is a sum of the valences multiplied by the concentration of the ions found in the electrolyte:

$$I = \frac{1}{2} \sum_i z_i^2 c_i \quad (1.36)$$

Equations 1.34 and 1.35 can be combined to equation 1.37. For brevity $\frac{1}{kT}$ is often written as β :

$$\frac{\partial^2 W_{EDL}}{\partial z^2} = -\frac{qc_B}{\epsilon_0 \epsilon_r} (\exp(+\beta q W_{EDL}) - \exp(-\beta q W_{EDL})) \quad (1.37)$$

Equation 1.37 requires to be solved numerically and thus it is often exchanged for the more simple Debye Hückel-model (DH), which is valid for low charge densities q and electrical potentials W_{EDL} . The formula shown below reassembles the case, that the charged surfaces are separated over a large distance and thus are not able to perturb each other, such that the potentials can be simply superimposed, resulting in equation 1.38, which can be solved analytically.

$$W_{EDL}(z) = \frac{2\sigma_+ \sigma_-}{\epsilon_0 \epsilon_r \kappa} \exp(-\kappa z) \quad (1.38)$$

Thereby κ^{-1} being the inverse Debye length, indicates the length scale, on which the electrostatic force persists in the electrolyte:

$$\kappa^{-1} = \sqrt{\frac{kT \epsilon_0 \epsilon_r}{2q^2 c_B}} = \frac{0.3nm}{\sqrt{I}} \quad (1.39)$$

and σ_{\pm} describes the surface charge density which depends on the electric surface potential:

$$\sigma_{\pm} = \epsilon_0 \epsilon_r \kappa W_{EDL\pm} \quad (1.40)$$

The following images are taken from the Overview of Trefalt and Bokrkovec [165] and describe the symmetric situation, that is identified by particles having a constant radius of $r = 250$ nm and a typical Hamaker constant of $A = 5 \times 10^{-21}$ J, Figure 1.13 (A). The charge density of the particles is also kept constant ($\sigma = 2$ mC m⁻²), while being submersed in a monovalent salt concentration of 8 mmol. It can be seen that the van der Waals forces are predominately influencing the short and larger distances, while intermediate distances are governed by the electric double layer forces. While the primary minimum is found close to the surface, a secondary minimum can establish before the energy barrier, preventing the particles from getting into the primary minimum. The energy barrier (maximum) is thereby typically located close to the Debye length κ^{-1} .

Figure 1.13 (B) shows, how the influence of the electric double layer forces can be diminished in basically two ways. Adding salt results in the surface charge being screened, which is quite comparable to an overall decrease in charge density. In fact, both methods result in the total forces being reduced to the attractive van der Waals forces. The asymmetric situation involves only having different charge densities with opposing sign (σ_- , σ_+) or a charged and uncharged surface ($\sigma_+, \sigma_- = 0$). A change in radius is only accounted for in the DeJarguin approximation found in equation 1.25 and would not result in any new features, despite changing the magnitude of the forces. If the particles exhibit opposite charges, the electric double layer forces is just adding to the van der Waals forces as it can

¹⁸ Reprinted (adapted) with permission from “Overview of DLVO theory” <https://archive-ouverte.unige.ch/unige:148595>, Trefalt & Borkovec, 2014, under Creative Commons Agreement.

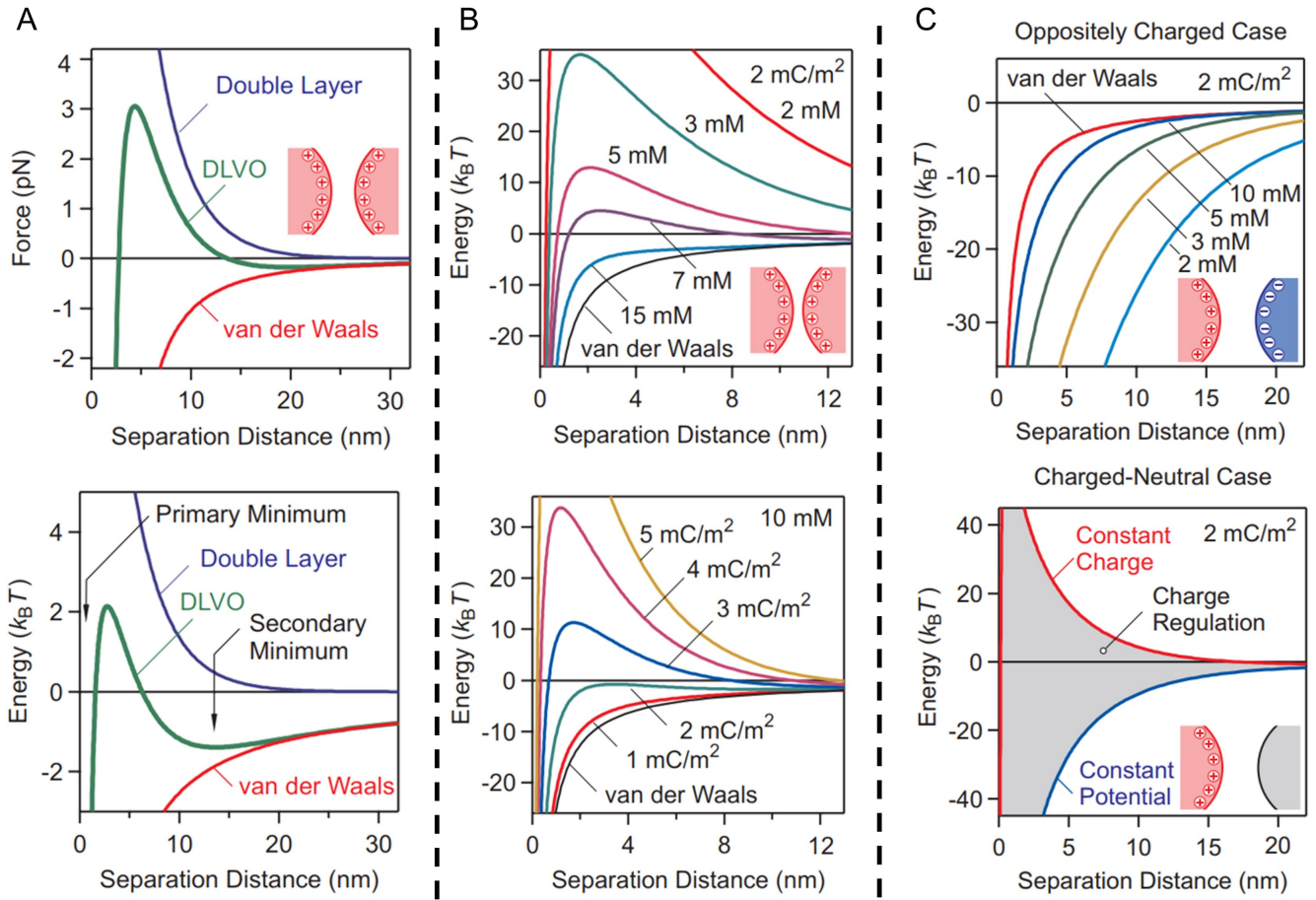


Figure 1.13.: (A) Plot of the DLVO-forces consisting of the double layer and van der Waals forces, in the case of identical charged particles. (B) Dependence on ionic strength and charge on the double layer forces. Lower ionic strength and higher charges alike lead to higher energy barriers and can sometimes not be indistinguishable. (C) Plot of the total potential with varying ionic strength for particles with opposite charging or no charge at all.¹⁸

be seen in the left plot, Figure 1.13 (C). In the charged-neutral case, one would expect, no double layer forces to be present, but in fact the compression of the diffuse layer on the charged particle, requires a change to the double layer potential shown below, equation 1.41:

$$W_{EDL}(z) = \frac{2\sigma_+^2}{\epsilon_0 \epsilon_r \kappa} (2p_- - 1) \exp(-\kappa z) \quad (1.41)$$

with p_- being the charge regulation parameter. Upon approach of the charged particle to neutral particle, either the charge density remain constant, resulting in an increase of potential (constant charge, $p_- = 1$) or the potential is kept constant, which results in a decrease of charges during the approach (constant potential, $p_- = 0$). Charge regulation is met, when $p_- = \frac{1}{2}$, which happens, when ions are adsorbed to the surface and so the superposition approximation holds true again. In fact p_- can also take arbitrary values, between the extreme cases (0,1) and can result in attractive or repulsive forces (grey area in Figure 1.13 (C)).

DLVO theory for Carbon Nanotubes Filtration and Alignment

Whether a director field is involved in the alignment of SWCNTs or not, most researchers agree upon the idea of the SWCNTs being kept in a two-dimensional plane above the membrane during filtration.[1, 40, 41] But the idea of analyzing SWCNT alignment with DLVO-theory already took hold in 2005, when McLean *et al.* reported the spontaneous alignment of DNA-wrapped carbon nanotubes on a SiO₂ wafer covered with a thin hydrophobic layer. Akin to He *et al.*, they suggested, that the spontaneous alignment occurred due to the enrichment of carbon nanotubes in the secondary minimum, forming a quasi-2D nematic phase, from which the aligned species would "hop" onto the wafer surface. In order to calculate the DLVO-forces they considered the SWCNTs and the hydrophobic coating both to be negatively charged and approximated the geometry by a line and a half-space in order to calculate the van der Waals term.[166] While the electric double layer energy was based of Manning's approach leading to:[179]

$$W_{tot} = \frac{\sigma_{surf}\sigma_{SWCNT}}{2kT} \exp(-\kappa z) - \frac{Ar_{SWCNT}t_{SWCNT}}{3z^3kT} \quad (1.42)$$

thereby the linear charge density of the carbon nanotube and surface charge of the hydrophobic coating is denoted by σ_{SWCNT} and σ_{surf} , respectively, and the geometry of the SWCNT is defined by the radius r_{SWCNT} and the thickness is defined by the layer-to-layer distance of graphene t_{SWCNT} . The authors reported a secondary minimum of 3- 4 kT, for a surface charge around 50 mV, which is shown in Figure 1.14. The approach by Manning and Lustig

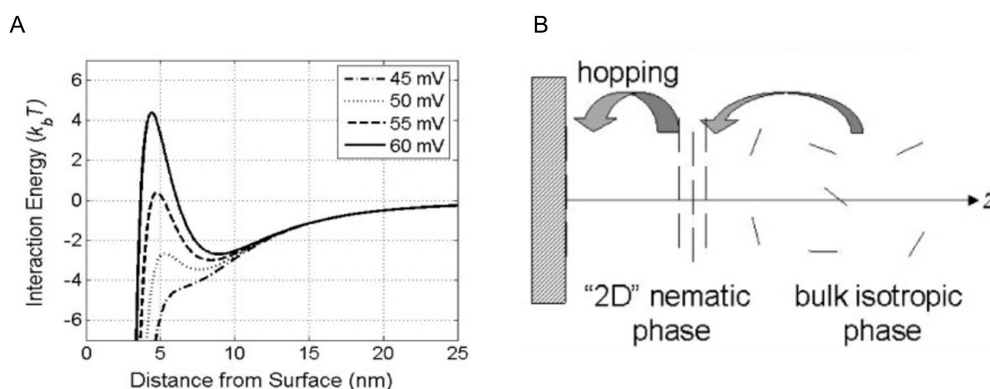


Figure 1.14.: (A) Total potential of a carbon nanotubes approximated by a line of charges being close to a Si-wafer. (B) The alignment mechanism described by McLean *et al.*, due to the SWCNTs gathering in the secondary minimum as predicted by the DLVO calculations, involves an enrichment in a two-dimensional plane above the membrane and a consequently hopping onto the surface.¹⁹

[179] considers the influence of the DNA wrapped around the SWCNT core to be greater than the SWCNT itself and might thus not be useful for SWCNTs dispersed in surfactants, especially, when the surfactant concentration is considerably lower than the critical micelle concentration (CMC) of the SWCNTs. Unfortunately, also the DA

¹⁹ Reprinted (adapted) with permission from "Controlled Two-Dimensional Pattern of Spontaneously Aligned Carbon Nanotubes" 6, 1, 55–60, Mclean *et al.*, November 2006, American Chemical Society.

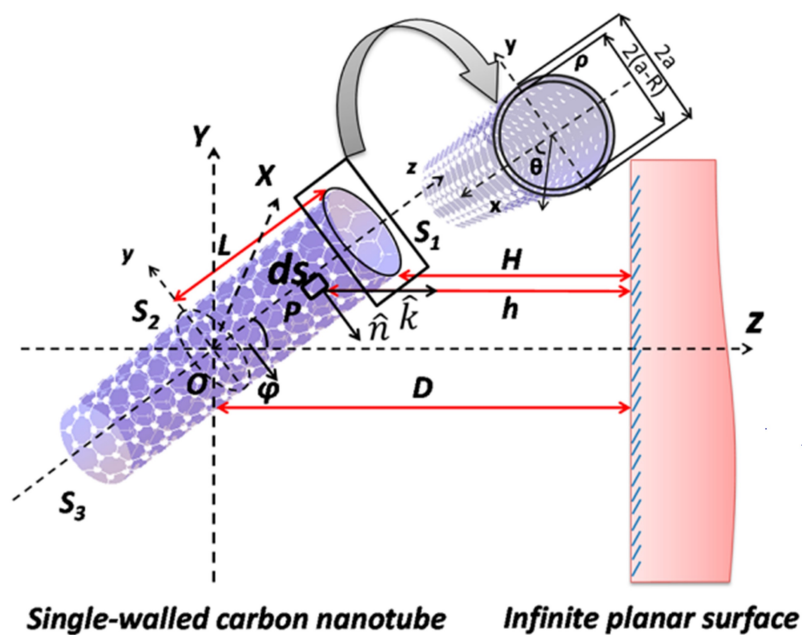


Figure 1.15.: Representation of the carbon nanotubes parameters involved in the surface element integration (SEI)-technique to derive the exact solution (eq. 1.44 and 1.45) for a SWCNT approaching an infinite planar surface at an angle ϕ . The segments are defined by the top and bottom cap (S_1 and S_3) as well as the hull (S_2).²⁰

approach discussed above is often not applicable to small nano-particles, as their reach of forces is longer, than their actual size and is especially problematic for particles with a high aspect ratio like a carbon nanotube, which can not be simply approximated by a sphere.[165, 180] But it still serves the purpose of understanding the basic principles of changing the size, charge and ionic strength strength of the particles in question. For carbon nanotubes, the SEI technique has been applied recently by Wu et al., which works especially well for very small and non-spherical particles at low ionic strength conditions, Figure 1.15.[172] Additionally, this technique is also considering the angle ϕ between the surface and the SWCNT and divides the SWCNT surface into different segments, equation 1.43:[180]

$$W(z, \phi) = \int_{S_i} \tilde{n}_{S_i} \tilde{k} E z_i dS \quad (1.43)$$

where S_i represents the surface element ($i = 1, 2, 3$ represent, top side and bottom surfaces of the SWCNT, respectively), \tilde{k} is a unit vector normal to the surface and $W(z_i)$ represents the interaction energy between the planar surface and the respective surface element S_i at a distance of z_i . The in-depth derivation is computational demanding and would also overreach the scope of this thesis, thus only the resulting equations (1.44 and 1.45) of the SWCNT

²⁰ Reprinted (adapted) with permission from "DLVO Interactions of Carbon Nanotubes with Isotropic Planar Surfaces 29, 12, 3976–3988, Wu et al., February 2013, American Chemical Society.

being parallel to the surface are shown, which yield the lowest secondary minima.[180]

$$W_{VDW}(z, \phi = \frac{\pi}{2}) = -\frac{2aAL[\sqrt{(z^2 - a^2)} + a \arctan(\frac{a}{\sqrt{(z^2 - a^2)}})]}{3\pi(z^2 + a^2)^{\frac{3}{2}}} + \frac{2(a - t_c)AL[\sqrt{z^2 - (a - t_c)^2} + (a - t_c) \arctan(\frac{(a - t_c)}{\sqrt{z^2 - (a - t_c)^2 + (a - t_c)^2}})]}{3\pi(z^2 - (a - t_c)^2)^{\frac{3}{2}}} \quad (1.44)$$

$$W_{EDL}(z, \phi = \frac{\pi}{2}) = 128\pi a L \epsilon_0 \epsilon_r \gamma_1 \gamma_2 \kappa \left(\frac{kT}{\nu e}\right)^2 \exp(-\kappa z) L_{-1}(\kappa a) \quad (1.45)$$

As those equations are used in this thesis to analyse the interaction-potential of the SWCNTs being close to the membrane surface, all parameters used are listed below: a , [nm] average SWCNT diameter

A , [J] Hamaker constant

L , [nm] length of a SWCNT

t_c , [nm] thickness of the SWCNT, estimated by graphene sheet thickness

κ^{-1} , [nm] Debye length (inverse Debye-Hückel parameter) for the ionic strength

T , [K] temperature

$\epsilon_0 \epsilon_r$ permittivity of water

$N_A = 6.022 \times 10^{23}$ Avogadro Number

$k = 1.38 \times 10^{-23}$ [J K⁻¹] Boltzmann constant

γ_1 , [C m⁻²] surface charge of the SWCNT

γ_2 , [C m⁻²] surface charge of the membrane

ν , [] valence

L_{-1} , Struve function of Order -1

The EDL interactions of the CNTs are following the superposition approach, with intermediate values chosen between the extreme cases of constant potential and constant charge, which has been considered to be the most accurate description for SWCNTs according to Gregory.[181] The Hamaker constant has been chosen for SWCNTs being separated by water from a Mica surface and the surface charges have been approximated by using the zeta potential, which will be covered in more detail in the following section.

1.4.3. Zeta potentials of Membranes and SWCNTs

The electric double layer model discussed above is used to analyze the distribution of ions being present in an electrolyte, when a charged surface is immersed in it. The electrolyte in total is charge neutral, which means that the observed charge separation is happening at the interface of the submerged charged surface and the electrolyte. Thereby the charges of the surface (electrode) can be intrinsic, due to dielectric properties or due to an external

potential.[166] The electric double layer theory mainly evolved from the Helmholtz model, to the Gouy-Chapman model and was later modified by the addition of the Stern layer, as depicted in Figure 1.16.[182] In the model

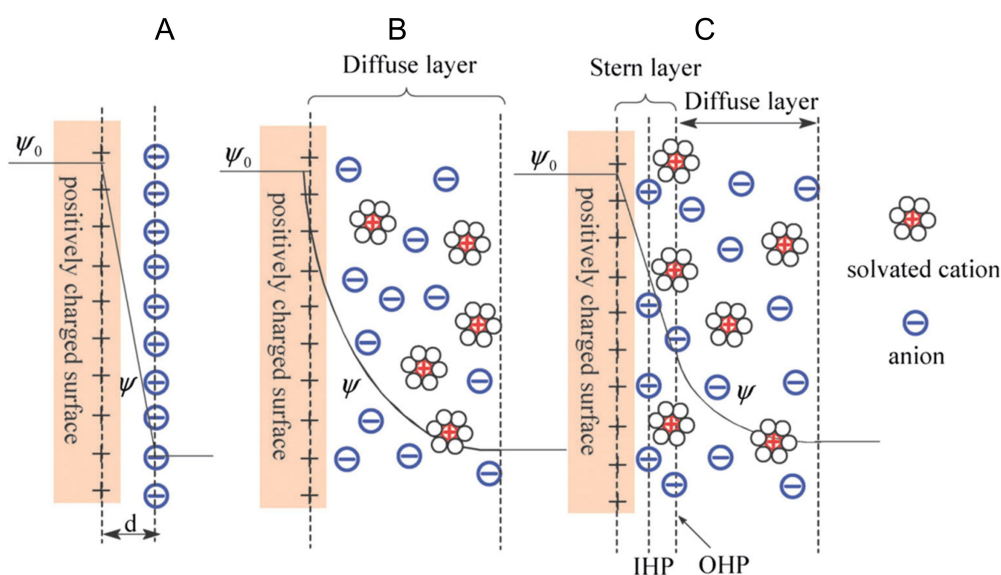


Figure 1.16.: Schematic representation of the Helmholtz-model (A), the Guoy-Chapman-model (B) and the most commonly used model to date, the Stern model (C). The inner and outer Helmholtz-plane are thereby defined at the center of the counter-ions (here anion) and identical charged ions closest to the surface (here solvated cation), while the zeta-potential is usually defined as the potential given at the slipping plane, which is close to the OHP.²¹

proposed by Helmholtz,[183] the electrode surface is covered by a rigid layer of counter-ions neutralizing its charge at a distance d followed by a diffuse layer consisting of both, negatively and positively charged ions. This could also be interpreted as a capacitor with a distance d and would result in a linear drop of electrical potential energy Ψ . Guoy and Chapman independently, doubted that the counter-ions would be held rigidly to the surface and proposed that those counter-ions would diffuse back into the liquid phase, creating a diffuse layer with the counter-ion concentration decreasing with the distance to the surface.[182] The potential drop is then described using the Poisson-Boltzmann equation outlined in eq. 1.37. Integrating this equation under appropriate limits yield the thickness of the double layer, which decreases with increasing ionic strength and is often referred to as the Debye-length κ^{-1} . However, in reality this model underestimates the thickness of the double layer, due to the negligence of the change of activity. Lastly, Stern stated that the size of the ions is finite and thus their distance to the surface had to be at least the ion radius.[184] Some of the ions would then form the so-called Stern layer, consisting of counter-ions adsorbed onto the electrode, followed by the aforementioned diffuse layer, resulting in two capacitors being between the electrode and the Stern layer and between the slipping plane and the diffuse layer. The slipping plane then separates the ions attached to the surface and the ones being mobile in the electrolyte, with its corresponding potential being defined at the outer radius of the counter-ions and being coined as ζ -potential. It is also common to divide the layer by the

²¹ Reproduced from “Electric double-layer transistors: a review of recent progress”, 50, p 5641–5673, Du et al., June 2015 with permission from Springer Nature.

inner and outer Helmholtz plane. The inner Helmholtz plane (IHP) is thereby defined by the centre of the specifically adsorbed ions, while the outer Helmholtz plane (OHP) is defined by the centre of non-specifically adsorbed ions, which are marking the begin of the diffuse layer.[182, 185] Providing additional ions via change of the pH value (H^+ or OH^-) is often used to define the isoelectric point (IEP) or point of zero charge (PZC). The former is reached, when the ζ -potential reaches zero and the latter defines the actual net charge of the surface to be zero.

Zeta Potential of Membranes

Streaming potential measurements are typically applied to macroscopic surfaces like membranes in order to determine their zeta potential. Thereby a confined flow channel is formed by attaching the membrane samples to two plates, through which an electrolyte is pushed due to a pressure drop forming between the inlet and outlet, Figure 1.17. The moving ions of the electrolyte are then shearing off the electric double layer at the membrane surface creating a

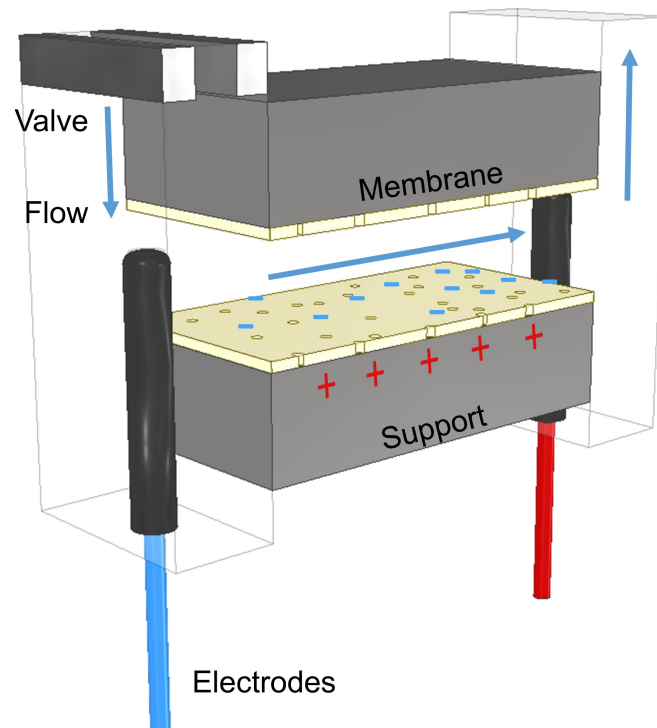


Figure 1.17.: Streaming Potential measurement conducted by inducing a flow opening the pressure gauge and subsequently shearing off the double layer attached to the sample, while measuring the potential drop at the electrodes.

streaming potential (eq. 1.46), or alternatively streaming current (eq. 1.47), which in turn can be used to evaluate the zeta potential using the corresponding Helmholtz-Smucowski equation.

$$\zeta = \frac{\partial U_{str}}{\partial \Delta p} \frac{\eta}{\epsilon_0 \epsilon_r} \kappa_{el} \quad (1.46)$$

$$\zeta = \frac{\partial I_{str}}{\partial \Delta p} \frac{\eta}{\epsilon_0 \epsilon_r} \frac{L_{ch}}{A_{ch}} \quad (1.47)$$

with $\frac{\partial U_{str}}{\partial \Delta p}$ and $\frac{\partial I_{str}}{\partial \Delta p}$ being the slope of potential or current against the differential pressure drop, η the electrolyte viscosity, κ_{el} the electrolyte conductivity and L_{ch} and A_{ch} being the length and cross-section of the streaming potential. The former equation 1.46 requires the knowledge of the electrolyte conductivity, while the latter (eq. 1.47) is only applicable for smooth surfaces like a membrane, as only then the channel can be defined well. Alternatively, the zeta potential of surfaces could also be determined via the electroosmotic flow measurement, which uses a similar geometry compared to the streaming potential, but instead of external pressure, the ions are moved with an external electrical field, which is often more practical for microfluidic channels.[186]

Zeta Potential of SWCNTs

In contrast to streaming potential, electrophoretic light scattering (ELS) is used to evaluate the zeta potential of particles with surface areas being much smaller and often not homogeneous. The technique involves an alternating electric field inducing movement into the charged particles suspended in the liquid. The electrophoretic mobility μ_E of the particles is corresponding to the ζ -Potential of the particles, consequently leading to higher electrophoretic velocities v_E in case of higher electric fields E :

$$\mu_E = \frac{v_E}{E} \quad (1.48)$$

The electrophoretic velocity can be evaluated by the frequency shift occurring between the reference (incident) laser beam and the scattered light, which is Doppler-shifted, as shown in eq. 1.49 and requires knowledge of the refractive index of the solvent n_0 and the speed a light c . [187, 188]

$$\frac{\Delta f}{\nu} \propto \frac{n_0 v_E}{c} \quad (1.49)$$

The phase changes registered are in the range of $\frac{\Delta f}{\nu} = 1 \times 10^{-11}$ and require additional instrumentation to be measured. In order to achieve the required resolution of the phase shift and determine the actual sign of the charging different techniques are deployed. The constant modulation technique is combining the incident or scattered signal with a modulated reference signal provided by moving mirrors, which is often termed as phase analysis light scattering (PALS). By subsequent comparison of both signals, one can exactly filter out the Doppler-shift stemming from the electrophoresis and from the diffusion/ Brownian motion of the particles. Any non-linearities from the mirrors are compensated as well, allowing to use large movements of the mirrors. Other geometries involve an attenuator before the detector levelling the intensity to a regime, that could be measured best by the detector,[189] or large detector areas that can resolve the phase shift precisely, due to the added distance travelled depending on the incident angle by comparing it to the initial radiation.[187] discussed before.[190] This measurement is often

²²Reprinted from "Recent applications of light scattering measurement in the biological and biopharmaceutical sciences, Analytical Biochemistry" Vol 501, p. 4-22, Minton, May, 2016, with permission from Elsevier.

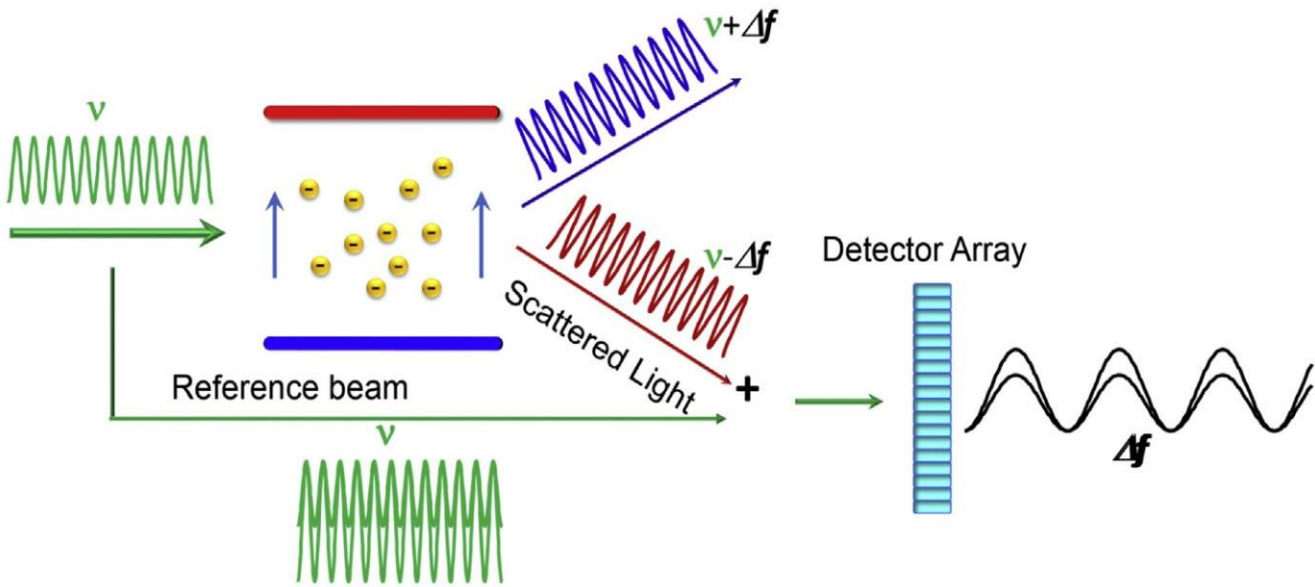


Figure 1.18.: Schematic of a typical ELS setup. In this case, suspended negatively charged particles are radiated by a light beam with known frequency ν . The light exiting the sample will be blue shifted in the direction of migration or red shifted for the opposite direction by Δf . The frequency shift Δf can be determined by evaluating the interference of the reference and the scattered light.²²

combined with dynamic light scattering (DLS), which can determine the hydrodynamic radius R_H of a particle using the Debye-Hückel-Henry relationship. If R_H is then calculated to be much larger than the thickness of the ionic double layer, Smoluchowski's equation can be used.

$$\zeta = \frac{\eta \mu E}{\epsilon_0 \epsilon_r} \quad (1.50)$$

Alternatively, if it is much smaller, then Hückel's equation applies:

$$\zeta = \frac{3\eta \mu E}{2\epsilon_0 \epsilon_r} \quad (1.51)$$

Thus, the sign of charge can eventually also be evaluated.[190] Generally, dispersions are considered to be stable, when the ζ -potential reaches ± 30 mV and are evaluated often in combination with the pH value. Depending on the surfactant used, White *et al.* reported zeta potentials, between -100 mV (Dowfax) and 80 mV (CTAB) using the method outlined above.[94] Another method of measuring the zeta potential of particles utilizes the electroacoustic effect. Unlike the procedure described above, the electrophoretic mobility is measured by probing acoustic soundwaves generated due to their movement in the solution under the influence of an external electrical field. This normally involves the fixture of transducers to the measurement cell and is particular interesting for highly absorbing samples.[191]

1.5. Characterization of Aligned Carbon Nanotube Films

In the following section different techniques of qualitatively or quantitatively evaluating the obtained films are discussed. Each of those techniques have their specific use cases and are often complemented by the others, in order to reach a conclusion about the quality of the alignment. This mainly arises from the problem, that the nano-scopic order has to be evaluated at macroscopic scales leading most often to a compromise between accuracy and adequate usage of measurement time.

1.5.1. Direct Characterization

Due to their size, direct imaging of the SWCNTs is not possible with a conventional light microscope. Therefore a scanning electron microscope (SEM) is often used, which can achieve sub-nm resolution and requires little to no sample preparation, if the sample is already electrical conductive. In order to create an image, a filament (cathode) emits electrons being accelerated with an anode, which are then collimated into an electron beam using magnetic condenser lenses. This beam is then steered with with magnetic coils and used to probe the sample, which in turn results in a so-called ionization-pear forming. Thereby several electrons exiting the sample and different types of radiation can be analyzed. Having only an energy around 50 eV, secondary electrons are having a very limited mean free path and are thus only leaving the sample, where it's thickness does not exceed ≈ 1 nm, which in turn is useful for topography scanning and as such is mainly used to image carbon nanotubes.[40, 41] The back-scattered electrons are emitted from greater depths and their exit velocity depends on the atomic number Z of the specimen making them useful for composition or density mapping. Since electrons are decelerated, X-Rays can be observed also, some of them also being a consequence of fluorescence, which can be used to map the elements involved.[192] An image of nematic ordered carbon nanotubes can be found in Figure 1.8 (A). In general, this method can be used for SWCNTs being transferred to a conductive substrate (eg. Si-wafer) and can be used to confirm alignment on a small scale (several μm), but is too time-consuming, mapping complete samples. It should be mentioned, that if axial astigmatism is not be taken care of correctly, SWCNTs can appear as homogeneous and well aligned film and thus it is mandatory to compare round features (contamination) between images in order to spot such errors. Additionally, atomic force microscopy (AFM) can also be used to image SWCNTs directly and a topography image of aligned carbon nanotubes can be seen in Figure 1.8 (B).[139] In the standard amplitude modulation method, a cantilever with a sharp tip (often just several μm in size) is excited with a piezo transducer at its harmonic resonant frequency. The movement of the tip is thereby monitored with a laser diode pointing at the back of the cantilever, which is reflected on a spatial resolved detector. Then a feedback loop is engaged, which is trying to keep the amplitude at a user-defined setpoint below the free resonant amplitude by moving the tip closer or further away to the sample surface. If the setpoint is chosen below half of the free resonant frequency, the tip is actually touching the surface and the forces minimizing the amplitude is mainly dictated by the Pauli-repulsion of the sample. Otherwise the

van-der Waals forces are acting on the tip and can be used to create an image. While the former method often can increase resolution, it also bears the risk of contaminating or blunting the tip used.[193] While AFM samples do not need to be conductive, this method can also be used to analyze the alignment on a membrane. However, even smaller images can be quite time-consuming and the results can only be evaluated qualitatively.

1.5.2. Indirect Characterization

In general, optical polarization is a consequence of polarization dependent absorption (dichroism) and birefringence, which are in turn stemming from orientation-dependent differences in refractive indices and are observed in anisotropic, non-spherical objects such as SWCNTs,[194] or structured materials like globally aligned thin films thereof.[40] Light entering a birefringent anisotropic material at an axis not coinciding with the optical axis, is split into two rays, which are vibrating in planes being perpendicular to each other, travelling with a fast and a slow velocity and different refractive indices. Thereby the refractive index of the slower (extraordinary) ray is greater than the unrefracted ordinary ray, as it is inversely proportional to its velocity.[195] However, dichroism is defined as the preferential absorption of light depending on its polarization and the anisotropic absorption properties of the material.[196] Cross polarized microscopes are conventional bright-field microscopes equipped with two polarizers, which are mutual perpendicular and can be found before the sample (polarizer) and after the light has passed the sample (analyzer), Figure 1.19. When the polarized light is exiting the sample it is split into the extraordinary and

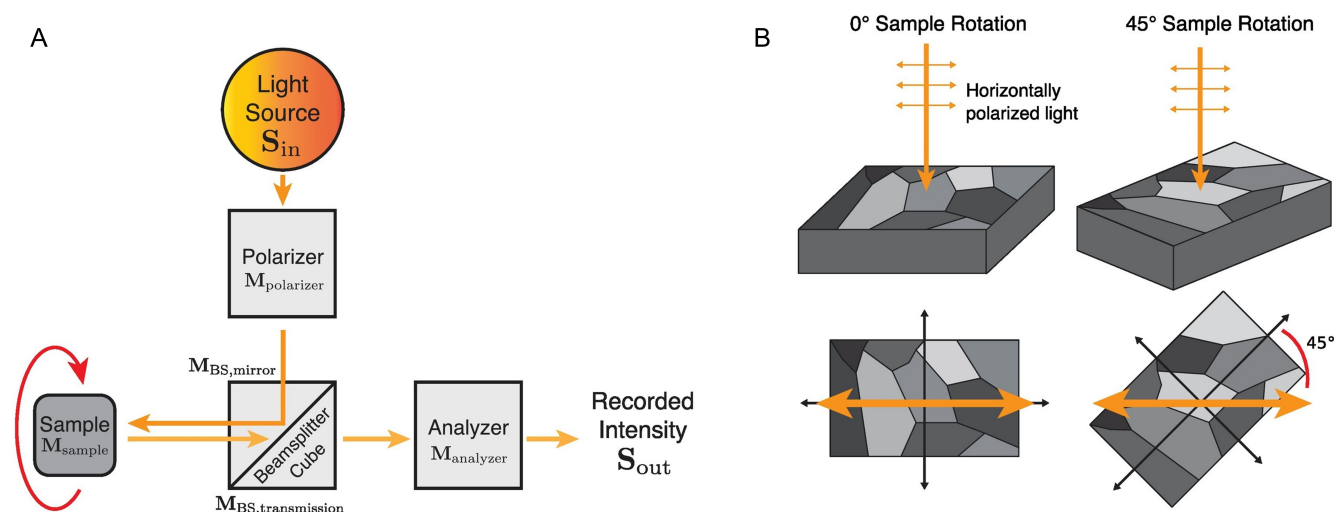


Figure 1.19.: (A) Schematic principle of a light microscope with polarizer, analyzer and rotational stage for the recording of cross-polarized images. Depending on the setup, the images are taken in transmittance, or as shown here in reflectance. (B) Resulting dark (0°) or bright (45°) images depending on the sample rotation.²³

²³ Reprinted from “c-Axis orientation determination of α -titanium using Computational Polarized Light Microscopy” Vol 167, 110503, Jin and De Graef, September, 2020, with permission from Elsevier under Creative Commons.

ordinary ray, which interfere at the analyzer and recombine. If the sample reassembling a perfect polarizer itself, has its fast axis coinciding with either the polarizer or analyzer, this will lead to destructive interference and the image will be dark. Hence, the highest brightness can be achieved if the fast axis is 45° shifted to both polarizing elements. As indicated in Figure 1.19, the microscopes are often operated in reflectance, but are sometimes also set up in transmission. This can also be explained by using Malu's law, [197] which describes how the transmitted light intensity I_1 drops in comparison to the incident intensity I_0 based on the angle ϕ between the incident polarized light and a sample acting as a perfect linear polarizer (eq. 1.52). Using the same equation again for the intensity exiting the sample I_1 and the analyzer yields equation 1.53. By inserting eq. 1.52 into eq. 1.53 one can arrive at the final equation 1.54, which has its maxima ($0.25 \times I_0$) at $\phi = \frac{\pi}{4} + n\frac{\pi}{2}$ and its minima (0) at $\phi = \frac{\pi}{2} + n\frac{\pi}{2}$ for $n \in \mathbb{N}$

$$I_1 = I_0 \cos^2(\phi) \quad (1.52)$$

$$I_2 = I_1 \cos^2\left(\frac{\pi}{2} - \phi\right) \quad (1.53)$$

$$I_2 = I_0 \cos^2(\phi) \sin^2(\phi) \quad (1.54)$$

Cross polarization microscopy measurements can be performed on transferred sample as well as films still being on the membrane. By the usage of low magnifying objectives, a large area of the film can be covered in a short time span, which allows for qualitative comparison between similar samples. Modern light microscopes also offer the ability to scan samples and stitch single images together using algorithms comparing the edges of the single images, thus making it possible to image complete membranes. It should be mentioned, that the birefringence of the substrate can easily be misinterpreted as the birefringence of the sample, so that complementary methods should always be used. Since the highest brightness can always expected with the SWCNTs aligned $\frac{\pi}{4}$ to the polarizer and analyzer and the lowest, when it's alignment coincides with one of those, this method is not able to distinguish between a sample being orientated parallel or perpendicular to one of the polarizers. Another method of quantify alignment is a four terminal probe measurement as shown in Figure 1.20. Therefore a film has to be transferred to a substrate and gold contacts are applied in a so-called Hall bar geometry. Then a current is applied between the source and drain, here being located left and right and the voltage is measured between the side contacts as indicated in Figure 1.20. Since no current is flowing through the side contacts, they can be seen as virtually without any contact-resistance, which allows to determine the sheet resistance with equation 1.55. [198] Since it is more intuitive to characterize carbon nanotubes by their conductance instead of resistance, one can convert the resistance measured to conductivity, if the length L and cross-sectional area A of the device is known with equation 1.56

$$R_s = \frac{\pi}{\ln(2)} \frac{\Delta V}{I} \quad (1.55)$$

²⁴ Reproduced from "Wafer-scale monodomain films of spontaneously aligned single-walled carbon nanotubes", 11, p. 633–638, He et al., Apr 2016 with permission from Springer Nature.

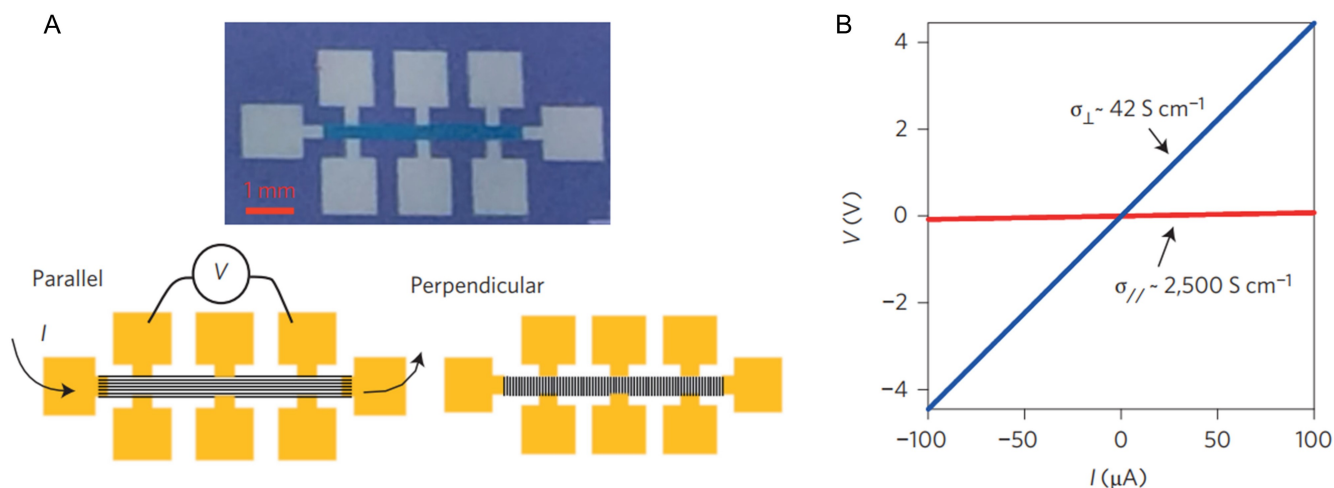


Figure 1.20.: (A) Hall-bar geometry used by He *et al.* for a terminal four probe measurement of parallel and perpendicular carbon nanotubes. (B) The I, V -curves are showing the great difference in conductance σ depending on the alignment direction of the SWCNTs.²⁴

$$\sigma = \frac{L}{R_s A} \quad (1.56)$$

Obviously, in order to make such devices, the alignment has to be identified beforehand, otherwise the values measured could not be assigned to an orientation, which requires this technique to be paired up with SEM, AFM or comparable techniques. It should also be noted that the conductivity is not solely dependent on the alignment, but also on the constitution of the SWCNTs, comprising of contamination from catalysts and surfactants or polymers, chiral type and defect density.[199, 200] One of the most common quantitative methods is the evaluation of the polarization dependent Raman vibrational modes of the carbon nanotubes. Most of the incident photons scattering by an object or molecule do so elastically (Rayleigh scattering), which result in an excitement of the object to a virtual energy state and subsequently a release of a photon with the same frequency (energy). If inelastic-scattering is taking place, the photon emitted can have a lower frequency (Stokes-Raman scattering) or higher frequency (Anti-Stokes Raman-scattering), which would have resulted in the creation or depletion of a phonon. Normally the frequency shifts observed are tiny compared to the frequency of the incident laser source, which requires to effectively block the signal of the exciting laser. This could be done using notch filters, blocking a specific frequency signal, Czerny-Turner monochromators, blocking unwanted wavelengths, or Fourier-Transform spectrometers, which are able to detect those small shifts. The so-called two-dimensional order parameter S_{2D} ranges from 0 to 1, with the latter indicating perfect alignment and the former indicating perfect disorder. The parameter introduced by Zamora-Ledezma *et al.* can be determined by evaluating the intensity of the G vibrational mode of the carbon nanotubes. Prior to calculation of the order parameter, the alignment dependent absorption ratio (dichroic ratio Δ)

²⁵ Reprinted (adapted) with permission from “Global Alignment of Solution-Based Single-Wall Carbon Nanotube Films via Machine-Vision Controlled Filtration” 19, 10, 7256–7264, Walker *et al.*, September 2019, American Chemical Society.

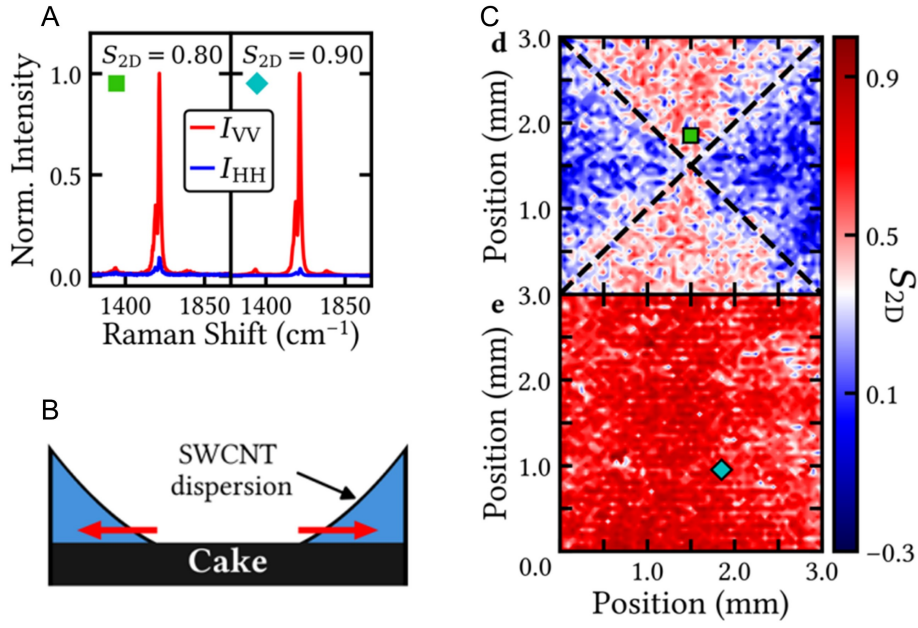


Figure 1.21.: (A) Single measurements of the vibrational G band with I_{VV} and I_{HH} at different locations of the sample, showing an increase in S_{2D} , due to the elimination of a spherulite formation, due to the hydrophilicity of the filtration funnel shown in (B). The effect on the obtained S_{2D} maps is shown in (C)²⁵

has to be determined, with a power meter or a UV-spectrometer equipped with a Glan-Taylor-Prism, as shown in equation 1.57

$$\Delta = \frac{a_{\parallel}}{a_{\perp}} \quad (1.57)$$

The incident Raman laser radiation is then linearly polarized using a half wave plate and the sample is measured in various geometric configurations: I_{VV} is the intensity measured with incident and scattered polarization being aligned with the sample, I_{HH} describes the opposite, meaning that both polarization directions are perpendicular to the sample and I_{VH} describes a mixed state, with the incident polarization coinciding with the sample and the scattered intensity being perpendicular.

$$S_{2D} = \frac{\Delta I_{VV} - \Delta I_{HH}}{\Delta I_{VV} + \Delta I_{HH}(1 + \Delta)I_{VH}} \quad (1.58)$$

In the original publication from Zamora-Ledezma *et al.*, they report order parameters between 0.1 and 0.15 for shear aligned SWCNTs.[110] Later He *et al.* reported order parameters of 0.96 for SWCNTs made with SWCNTs stemming from electric-arc discharge ($d_t = 1.4nm$, $l_t = 227nm$) and 0.75 with the use of (6,5) enriched CoMoCAT-SWCNTs ($d_t = 0.73nm$, $l_t = 420nm$), using the filtration method.[40] Walker *et al.* provided then the first Raman maps of aligned carbon nanotubes using the filtration method, spanning over $3 \times 3 \text{ mm}^2$ with S_{2D} reaching 0.9, after treating their sidewalls of the filtration funnel with silanes in order to prevent the occurrence of a spherulite as shown in Figure 1.21.

- This page is left blank intentionally. -

2. Methods

2.1. Construction and Programming of the Custom Filtration Setup

In the past global alignment of SWCNTs has been performed on membranes supported by a glass or metallic frit, to which a glass funnel is clamped from above and a rubber stopcock used to seal the setup to a Buechner flask. A vacuum pump is connected to apply a controllable under-pressure and regulate the flow rate of filtration.[40, 41, 138, 139] Despite its convenience, such a setup does not allow for a direct inline measurement of p_{TMP} and retention, nor does it provide accurate initial conditions. Even in the absence of the applied under-pressure, a capillary force and gravity still act on the feed solution to draw it into the membrane, and up to several hundred microliters may already have passed before the vacuum pump is switched on. It has been discussed before, that especially the initial phase of the filtration is key to global alignment,[40] which requires to initiate the filtration from a zero-flow state. To circumvent these issues, a custom filtration cell is designed for that purpose, allowing to install a membrane and load the dispersion without any liquid permeating the membrane. A technical drawing of the components in expanded view is shown in Figure 2.1 (A) and a cross-section of the assembled cell is shown in Figure 2.1 (B). In this design, the membrane is supported by a 300 μm fine stainless-steel mesh (Fteu) laser-welded to a 0.2 mm thick metal ring with an inner diameter of 22 mm and outer diameter matching the membranes used (47 mm). The inner diameter defines the effective filtration area (3.8 cm^2) and represents the largest to date.[40, 41, 139] Teflon blocks are pressed on the membrane and support the membrane holder, which in turn are contained by a stainless-steel sleeve and two flanges. The first (intermediate) flange fixes the membrane in place and allows for the addition of feed solution through the top, whilst the second (closing flange) makes a gas-tight seal for filtration. The assembled cell is placed inline as shown in Figure 2.1 (C) by connecting the inlet and outlet of the stainless-steel sleeve via 1/4"-28 UNF standard threads and 1/8" and 1/16" polytetrafluoroethylene (PTFE) or polyether ether ketone (PEEK) tubing with an internal diameter of 2 mm and 1 mm (Techlab), respectively. In general, gas line tubing (red) consisted solely of 1/8" PTFE tubing with an inner diameter of 1.6 mm. The fluid lines (blue) were 1/16" PTFE tubing with an inner diameter of 1 mm, except for the lines connecting the Coriolis flow sensor, which employ Swage Lock fittings and require stiffer PEEK tubing. Positive pressure is provided through the inlet by a Nitrogen gas bottle connected to an electronic pressure regulator (OB1 MK3+, Elveflow) rated to 0 –2 bar operation. In order to prevent contamination, bottled nitrogen with a purity of 99.999 % and air filters prior to the regulator was used. The outlet of the filtration cell is met by an arrangement of two 3/2 solenoid valves (type 6742, Bürkert), which can be actuated to pass the permeate either through a high- (± 2 bar), low- (± 340 mbar) pressure piezoelectric sensor (MPS1 and MPS2, Elveflow) or stop the flow completely. These are operated at 24 V with DC-relays, controlled by a custom-built Arduino UNO (Arduino). After the pressure sensors, the permeate passes into a Coriolis flow sensor (BFS 1+, Elveflow/Bronkhorst) followed by a UV-diode array detector (G2258A, Agilent) and finally into a waste container. A bubble catcher (44 μL , Elveflow) avoids artifacts in the pressure and flow measurements [201, 202]

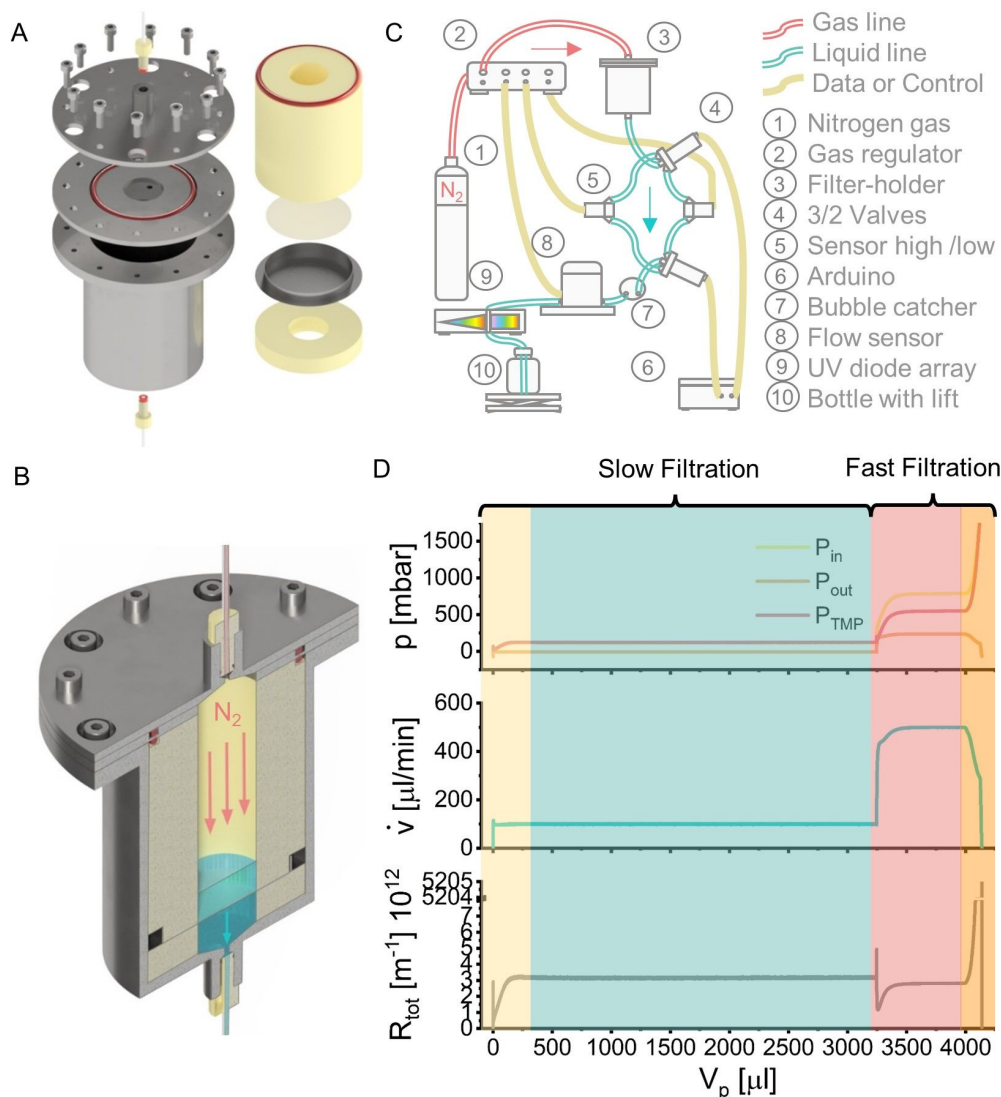


Figure 2.1.: (A) Expanded view of the filtration holder showing the internal components (right) and the stainless-steel sleeve (left). (B) Cross sectional view of the assembled holder. (C) Schematic of the complete microfluidic dead-end filtration setup. (D) Filtration data divided into color-coded regions: concentration polarization (yellow), film growth (blue), a push phase (orange) and drying (red). Reproduced from [1].

and comparison of time resolved absorption spectra with and without a membrane allow for the determination of membrane retention.[203] The gravity flow of the system without a membrane in place and with the solenoid valve open was adjusted to a constant value of $100 \mu\text{L min}^{-1}$ by raising or lowering the position of the waste container relative to the height of the filter holder. Later this feature has been removed from the setup as the variations in gravity flow were below $10 \mu\text{L min}^{-1}$ and an impact on the resulting films could not be found. The initial zero flow state was afforded by the ability to fill the dead volume under the membrane in the filtration cell, the pores of the membrane itself, and the tubing leading up to a solenoid valve (in a closed position) prior to adding SWCNTs. The

transmembrane pressure p_{TMP} was calculated as the difference between the measured pressure at the sensor in the gas regulator, p_{in} , and one of the inline piezoelectric sensors, p_{out} . As an example, Figure 2.1 (D) shows the data obtained from the setup for an entire filtration experiment. Throughout the remainder of this thesis, it will be customary to consider only specific sections of the filtration labeled as slow and fast filtration for the sake of clarity. The program code was written with Labview (National Instruments) utilizing software packages from Elveflow and open-source LyNx for the Arduino. Additional construction plans are provided in the appendix A.9.

2.2. Operation of the Setup

In the following subsections several details about the operation of the setup are discussed, which include the calibration of the pressure sensors, the achievable precision of the flow-sensor and how to load a membrane or clean it.

2.2.1. Pressure Sensor Calibration

R_{setup} is associated with the components used in the filtration setup and it is often neglected because it is minor compared to the other resistances, equation 1.15. By using the calibration discussed in this section, the output of the piezoelectric sensors is leveled by the output of the regulator, which effectively sets $p_{TMP} = 0$ for a setup absent of a membrane and filled with water. The low-pressure sensor has an absolute and relative accuracy of 6.8 mbar and 1.3 mbar, respectively, and is used for experiments with a membrane in place, whereas the high-pressure sensor is mostly used for cleaning and high flow rate experiments involving low resistive membranes, which would damage the piezo elements of the more sensitive sensor. The pressure sensor at the gas regulator can be calibrated independently with a protocol given by the manufacturer and was used to calibrate the two piezoelectric sensors. A pressure step function from 0 mbar to 100 mbar was applied by the gas regulator with no membrane in place (Figure 2.2 (A)) and a linear fit ($p_{in} = m \times p_{out} + b$) was used to correct for the offset caused by the slope of the linear part of the piezo hysteresis, the amplifier of the outlet sensor and the resistance of the filtration setup, Figure 2.2 (B).

2.2.2. Precision of the Coriolis flow-sensor

The Coriolis flow sensor operates by driving an inner tube to oscillate with a known frequency and uses the phase shift between the inlet and outlet to determine the volume rate \dot{v} , while the shift in frequency is attributed to the density of the fluid.[204] The advantages of this sensor include no need for calibration for the heat capacity of the liquid and a large measurement range ($1.6 \mu\text{L min}^{-1} - 3300 \mu\text{L min}^{-1}$) whilst still maintaining high precision, which is typically $\pm 2.5 \%$ or less of the measured volume rate depending on the range used. This was confirmed

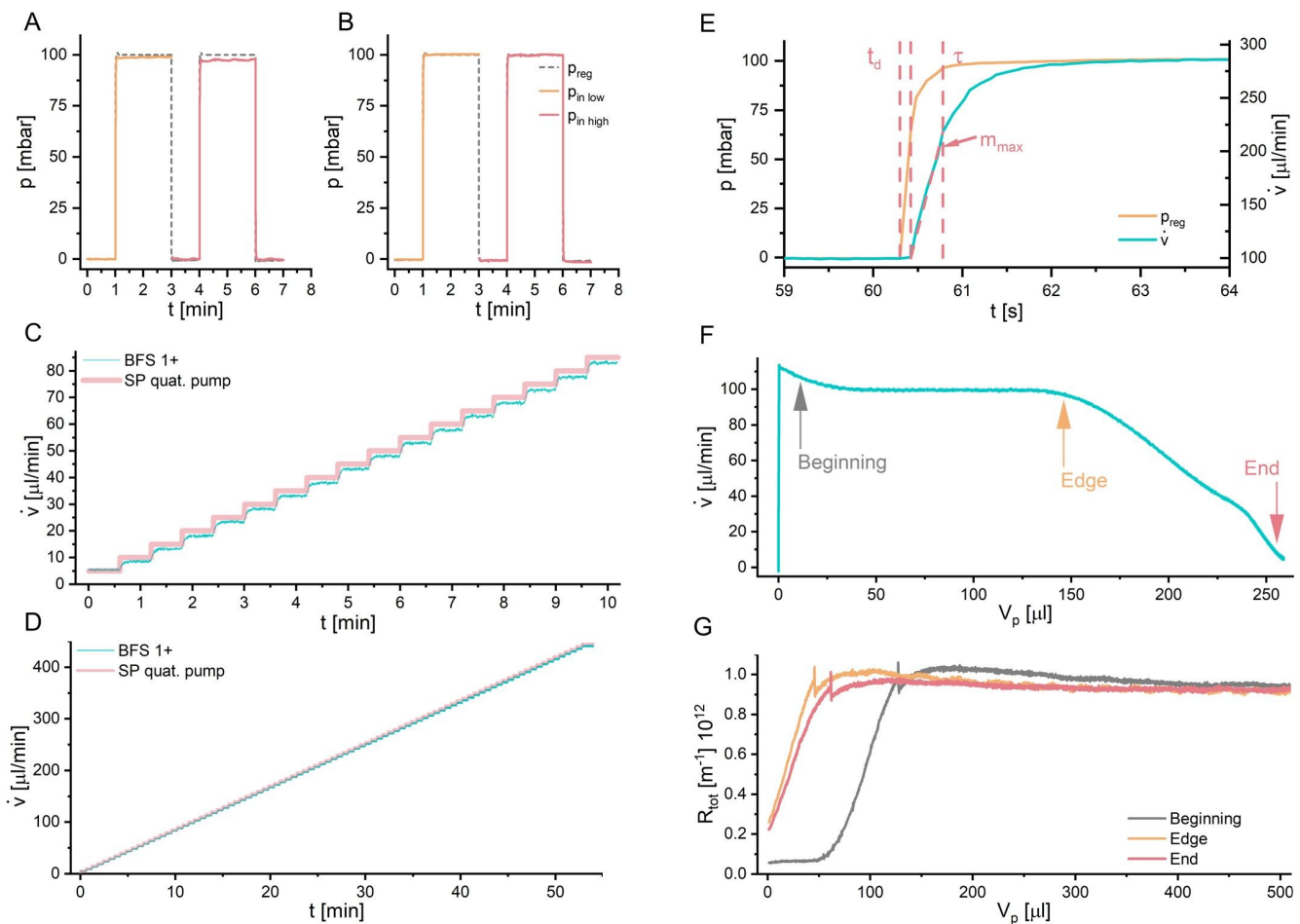


Figure 2.2.: Measurement of a pressure step function by the inline piezoelectric sensors (A) before and (B) after calibration. (C) $5 \mu\text{L min}^{-1}$ steps output by a quaternary pump and measured by the Coriolis flow sensor in the range $5 \mu\text{L min}^{-1} - 445 \mu\text{L min}^{-1}$. (D) Enlargement of the flow region $5 \mu\text{L min}^{-1} - 85 \mu\text{L min}^{-1}$. (E) Determination of the FOPDT-parameters using a pressure step function. (F) Volume rate measured for a fresh membrane and the release of water between the membrane and the valves by gravity. The arrows mark positions where the filtration in (G) was conducted. The absence of a delay for the increase in resistance indicates that water in the setup has been sufficiently equilibrated (Edge and End). Reproduced from [1].

by connecting the flow sensor directly to a quaternary pump from a gel permeation chromatography system (1260 Infinity, Agilent). Quaternary pumps are known for their highly accurate ($10 \mu\text{L min}^{-1}$ of the absolute value) flow control and deionized water was pumped with flow steps of $5 \mu\text{L min}^{-1}$ from $5 \mu\text{L min}^{-1}$ to $445 \mu\text{L min}^{-1}$ and the values output were matched almost exactly by the Coriolis sensor, Figure 2.2 (C) and (D). The average difference between the pump and the sensor was $\Delta\dot{v} = 2.6 \mu\text{L min}^{-1}$.

2.2.3. FOPDT Method for Flow Control

The pressure regulator (p_{in} , process variable) was controlled by a feedback loop minimizing the error, $e(t)$, between the actual flow and the desired flow (setpoint) from the Coriolis sensor. Suitable proportional and integrational gain values were obtained by the Ziegler and Nicholson calibration method (also known as the first order plus dead time (FOPDT) method), performed on the pressure step function used to calibrate the piezoelectric pressure sensors, Figure 2.2 (E). Calculation of the dead time, t_d , time constant, τ , taken at $(\dot{v}) (1 - e^{-1})$ and slope m was automatically performed to give optimal parameters for the controller gain, K_c , and integration time, I , using the following equations:

$$g_p = \frac{\dot{v}_{norm}}{p_{in\ norm}} \quad (2.1)$$

$$K_c = \frac{\tau}{g_p(a\tau t_d)}, I = \tau \quad (2.2)$$

Where the flow \dot{v}_{norm} and inlet pressure $p_{in\ norm}$ are the measured values normalized by the maximum output of the sensors, respectively. The parameter a was chosen to be 1 by empirical means.[205] Additionally, the setup can also be operated in constant p_{TMP} , when the process variable is exchanged for it, but in this case the parameters for the feedback-loop have to be adjusted manually. When a constant pressure p_{in} operation is needed, the in-built feedback-loop of the regulator takes over and no additional calibration is needed.

2.2.4. Loading a Membrane and Release of Excess Pressure under the Membrane

For every filtration experiment, a fresh membrane was placed onto the sieve holder and the excess water above the membrane removed with a pipette to leave it in a wetted state. The upper Teflon block was then lowered into the steel sleeve and pressed against the membrane by mounting the intermediate flange with six M4 screws sealed with a Viton ®O-ring. The excess water trapped between the membrane and lower part of the filtration cell was then released under gravity flow with the lid open. The volume flow through the Coriolis sensor during this process is shown in Figure 2.2 (F). A decrease of the volume rate \dot{v} is observed and ends at $5 \mu\text{L min}^{-1}$. The arrows indicate three possible conditions for starting a filtration experiment and these are labelled as “Beginning”, “Edge” and “End”, and refer to how close the membrane is to becoming dry during this initial step. In order to test the influence of the starting conditions, at each of these points 4 mL of EA-SWCNTs ($8 \mu\text{g mL}^{-1}$, 0.04 wt%DOC) were carefully inserted with the solenoid valve in a closed position. The lid was then closed to make an air-tight seal and bring the filtration cell into an operational state. Figure 2.2 (G) shows the total resistance measured in the slow filtration step at $100 \mu\text{L min}^{-1}$ for a 100 nm PCTE membrane for each of these possible states. When the release of the water is not sufficient, “Beginning”, the resistance curve shows a delay. This is due to the release of trapped water below the membrane before the SWCNT dispersion can enter. This can lead to inaccurate volume readings and was thus not an appropriate initial state for filtration. The “Edge” and “End” positions result in a direct increase in the total resistance which is desirable because it means that SWCNT feed enter the membrane immediately. In all experiments the “Edge”

position is used because at the “End” position the membrane is almost dry and there is a risk of introducing air in the form of bubbles into the filtration lines.

2.2.5. Cleaning and Maintaining the Filtration Setup

To clean the setup, approximately 100 mL of a 1 wt% DOC solution was used to backflush the filtration lines with a quaternary pump at 1.25 mL min^{-1} and the filtration-cell disconnected. The removal of any residues was visible as a pressure drop at the MPS2 pressure sensor. Eventually, the setup was backflushed and purged of potential air bubbles by washing 500 mL of deionized water with the same parameters. After cleaning, the filtration cell was connected under flow to ensure that no bubbles formed during connection. Since the retention of the predominantly used membranes (80 nm pore size) is close to 1 (cf. Figure A.4), cleaning of the setup can be most often avoided, by flushing the setup from time to time in forward direction with deionized water.

2.3. Dispersions of SWCNTs

2.3.1. Unsorted EA-SWCNTs dispersed in DOC and CTAB

Following previously reported protocols,[206] 40 mg of EA-P2 (lot no. 02-A011, Carbon Solutions) SWCNTs were dispersed in a 40 mL aqueous solution of either 2 % sodium deoxycholate (DOC) (20 g L^{-1} , BioXtra 98+ %) or 0.5 % CTAB (5 g L^{-1} , Sigma-Aldrich) by tip sonication for 45 min (0.9 W mL^{-1}) in an ice bath followed by centrifugation ($45,560 \text{ g}$, Beckman Optima L-80 XP, SW 40 Ti rotor) for 1 h. The top eighty percent of the supernatant was collected and used further. All dispersions were prepared with deionized water ($18.2 \text{ M}\Omega\text{cm}$, $pH = 6.93$) from an Arium pro UV (Sartorius).

2.3.2. Length-Sorting of EA-SWCNTs and CoMoCAT-SWCNTs

Prior to length sorting, soot from SWCNTs obtained by the EA and CoMoCAT synthesis methods were dispersed via tip sonication in surfactant solutions. Conventional and rate-zonal (RZ) centrifugation steps were used to remove aggregates and morphologically impure SWCNTs. The EA-SWCNTs were additionally filled with linear alkane, $\text{C}_{20}\text{H}_{42}$, by using the method previously reported by Campo *et al.* [207, 208], and subjected to ATPE after the RZ process to separate the metallic and semiconducting species from each other. [32, 209] The EA-SWCNTs have an average diameter of $\approx 1.4 \text{ nm}$. The CoMoCAT samples, however, were water-filled and contained both metallic and semiconducting species having an average SWCNT diameter of $\approx 0.78 \text{ nm}$. Length separation of the SWCNT dispersions was performed via size-exclusion chromatography (SEC) following the method described by Khripin *et al.* [210]. The SEC separation was conducted over three SEC columns (Sepax Technologies) packed with $5 \mu\text{m}$ silica

beads with nominal pore sizes of 200 nm, 100 nm, and 30 nm, using a GE ÄTKA Purifier HPLC system. SWCNTs were injected and eluted with 10 g L^{-1} DOC pumped at a flowrate of 5 mL min^{-1} and subsequently 5 mL fractions were collected. Accordingly, those fractions contain distributions of carbon nanotube lengths and their average length decreases, with the total volume being collected, resulting in later fractions yielding shorter carbon nanotubes.

2.3.3. Chirality pure (6,5)-SWCNTs

(6,5)-SWCNTs were obtained by the ATPE separation technique, which has been introduced by Fagan [209]. CoMo-Cat65i (CHASM, lot number SG65i-L58) as the raw soot was separated by a diameter sorting protocol containing the surfactants sodium deoxycholate (DOC, BioXtra) and sodium dodecyl sulfate (SDS, Sigma-Aldrich). The two-phase system was established by using dextran (MW 70 kDa, TCI) and Poly(ethylene glycol) (PEG, MW 6 kDa, Alfa Aesar). [209] The concentrations of SDS were first increased to 1.1 wt% in order to push all species with larger diameters than (6,5)-SWCNTs to the top phase and remove them, while maintaining the DOC concentration at 0.04 wt%. Then the SDS concentrations increased even further (from 1.2 % to 1.5 %) and all (6,5)-enriched fractions were collected. A more detailed protocol can be found here [211].

2.3.4. Concentrating the Dispersions with Ultra-Filtration

All SWCNT dispersion were concentrated and adjusted towards 1 wt% DOC or 0.5 wt% CTAB, respectively, by multiple filtration cycles in a pressurized ultrafiltration stirred cell (Millipore) with a 300 kDa MW cutoff membrane. The high concentrations ($\approx 800 \mu\text{g mL}^{-1}$) were necessary to facilitate low surfactant concentrations ($\approx 0.04 \text{ wt\% DOC}$ and 0.02 wt\% CTAB) needed for filtration after dilution.

2.3.5. UV-VIS Measurements for Concentration Determination

UV–VIS–NIR absorbance spectra of nanotube dispersions were collected on a Cary 500 spectrometer from 1880 nm – 200 nm in 1 nm increments through a 1 mm glass cuvette. The concentration, was then determined by comparison of the π -plasmon peaks to reference samples.

2.3.6. AFM Length Determination

For the length determination using an AFM, $30 \mu\text{L}$ of ten times diluted dispersion were spin coated onto a silicon wafer at 2000 rpm for 3 min. The details on the instrumentation are similar to the measurement of the topographies shown in section 2.6.5

2.4. Polycarbonate Track-Etched Membranes

All membranes were obtained from it4ip with a diameter of 47 mm, a pore density of $6 \times 10^8 \text{ cm}^{-2}$ and a thickness of 25 μm with pore sizes comprising of 50, 80, 100 and 200 nm. If not stated otherwise, the membranes had a hydrophilic PVP coating, otherwise they were uncoated (UC), which led them to be hydrophobic due to the polycarbonate surface.

2.4.1. Modification of Membranes

The thermo-mechanical modification used in this work, always requires the production of custom-made shims beforehand. Thus, it is first discussed in terms of the design and the production of the shims and then the actual hot-embossing process following it. Basically two types of shims have been generated: axial aligned ones and radial ones. While the hot-embossing process is mostly similar, the production of the shims slightly varies considering the current densities used to galvanize the nickel shims.

2.4.2. Shim Production: Axial and Radial Shims

All patterns for the master fabrication were designed with Klayouter, Open Source and converted into a machine-readable format by LayoutBEAMER Software from GenISYS. A Polymethylmethacrylat (PMMA) resist (AR-P 672.045; Allresist GmbH) was spin-coated at 3000 rpm for 60 s onto a non-oxidized standard silicon wafer after a substrate baking step (180 °C for 300 s), resulting in a 100 nm high film for the electron beam lithography. The structures were reproduced best with a dose of 380 $\mu\text{C}/\text{cm}^2$. After exposure, the nanostructures in PMMA were developed in a mixture of methyl isobutyl ketone (MIBK) and isopropyl alcohol (IPA) (ratio 1:3) by spray development. Chromium (7 nm) and gold (25 – 30 nm) layers were evaporated on top of the wafer and PMMA structures. The chromium layer serves as adhesive layer and the gold layer as conductive plating base for the subsequent deposition of nickel. During metallization the substrate was tilted at 30°. For the nickel deposition, the metallized nanostructured wafers were immersed in an electrolytic bath. Electroplating was carried out in a boric acid containing nickel sulphamate electrolyte (pH 3.4 to 3.6 at 52 °C) for 43 h and 48 h for the axial and radial shims, respectively. To ensure a slow growth of the nickel layer and to achieve a defect-free filling of the irradiated nanostructured areas the current density was adjusted to 0.25 A dm^{-2} (corresponding a growth speed of approximately 0.05 $\mu\text{m min}^{-1}$) at the beginning of the plating process for the axial shim and 0.1 A dm^{-2} (growth speed 0.02 $\mu\text{m min}^{-1}$) for the radial shims respectively. The current density was increased to 0.5 A dm^{-2} ($\approx 0.1 \mu\text{m min}^{-1}$) for the axial shim after 30 min and in further steps up to 1 A dm^{-2} ($\approx 0.2 \mu\text{m min}^{-1}$). However, the current density of the radial shims was increased to 0.25 A/dm^2 ($\approx 0.05 \mu\text{m min}^{-1}$) after 60 min and in further steps up to 1.0 A/dm^2 ($\approx 0.2 \mu\text{m min}^{-1}$) This ensured that the required shim thickness of at least 500 μm could be targeted. The nickel shims were separated using a simple lift-off process

and subsequently the resist was dissolved using acetone (60 s) and a final IPA cleaning step, ensured a contamination free surface (60 s, shaker). The metallization layers (gold and chromium) were not removed, as the membranes are not impacted by them.

2.4.3. Hot-Embossing

For the actual hot-embossing procedure the shim is built into a home-made retaining device, which in turn is mounted onto a vice. The vice, however, being a repurposed custom tensile test machine from Zwick und Roell, was also equipped with heating modules and thermocouples to allow for accurate temperature control. A membrane is directly placed onto the patterned area of the shim and then covered with a sheet of Polyimide (Kapton) and Teflon. The Kapton is thereby ensuring that the membrane does not adhere too firmly to the backside of the press and the Teflon piece guarantees an equal distribution of the force deployed. The setup itself is additionally depicted in Figure 3.9. Typically forces between 8 and 25 kN are used to deform the membrane with the temperature always being adjusted to the glass transition temperature of polycarbonate during the loading step 120 °C lasting 10 min. [212] After loading, the membrane is removed only after cooling down to 40 °C, in order to prevent the polycarbonate of contracting and subsequently closing the formed structures. Additional water cooling of the vice could be used, in order to decrease the time cooling down, which is needed after repeated use of the machine and subsequent heating.

2.5. Transfer to Substrates

2.5.1. Transfer to Silicon Wafers and Glass

SWCNT films were transferred either to uncoated or ITO coated glass substrates ($\text{PGO}, 20 \pm 6 \Omega \text{ m}^{-1}$, and $1.0 \pm 0.1 \text{ mm}$ thickness) or Si wafers (CrysTec, polished and etched, thickness $525 \mu\text{m}$, p-type, specific resistance $> 1 \Omega \text{ cm}$) using the method outlined by Walker *et al.* [41] Membranes adhered to the substrate-surface at 50 °C by heating the substrate with a hot-plate and subsequently dissolved with Chloroform using a syringe (99.2 % stabilized with 0.6 % ethanol, VWR chemicals).

2.5.2. Transfer to Flexible Printed Circuit Boards

After filtration, the membranes were wetted with deionized water ($18.2 \text{ M}\Omega\text{cm}$, $\text{pH} = 6.93$ from an Arium pro UV (Sartorius)) and adhered with the carbon nanotube film facing the substrate. Subsequently, the films were slightly dried on a hot plate at 50 °C to remove most of the moisture before dissolving the membrane with Chloroform (99.2 % stabilized with 0.6 % ethanol, VWR Chemicals). This was achieved by placing the substrates with the membrane facing towards the bottom of a Petri dish and carefully raising the Chloroform levels until it reaches the membrane.

As shown in Figure 2.3, a small retaining device for the flexible printed circuit board (fPCB) was used to keep the polyimide taut during this process and avoid bubbles/rupturing of the SWCNT film. The flexible printed circuit boards were custom designed using open source software KiCad EDA 5.1.12 and ordered at Multi Leiterplatten GmbH (Polyimide, contacts made of gold).

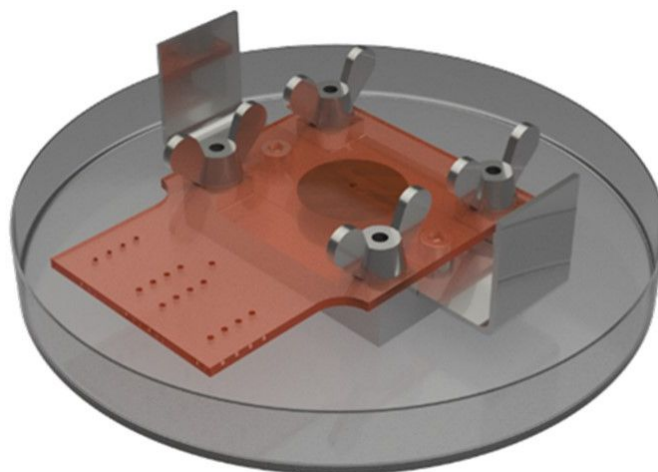


Figure 2.3.: Custom built transfer station made to hold the polyimide stretched whilst the membrane is dissolved facing downwards. The films were less likely to rupture when the chloroform was filled in carefully until it interfaced the membrane instead of using a syringe.[1, 41] In order to prevent the Chloroform from evaporating during the transfer (30 min), a larger Petri dish was used to cover the top of the holder. Reproduced from [2].

2.6. Characterization Of Aligned Films

2.6.1. Determination of the Dichroic Ratio

The dichroic ratio was determined with a Lambda 1050 spectrometer (Perkin Elmer) with an integrating sphere module, 2 mm beam spot, and Glan-Thompson polarizing prism. Raman experiments were conducted with a Horiba Xplora spectrometer, equipped with a 2.33 eV laser source. The laser was focused on the aligned nanotubes with a $100 \times$ (0.95 N.A.) objective. The laser power was 100 μ W. The backscattered light was collected with the same objective, dispersed by 1200 grooves per mm grating and detected by a silicon charge coupled device. A built-in half wave plate was used to rotate the laser polarization perpendicular or parallel to the alignment direction. In a similar manner the analyzer was set for the desired direction. Additionally, the dichroic ratio has been measured once more with a power meter of the Raman instrument (see below) by comparing the highest and lowest values obtained.

2.6.2. Two-dimensional Order Parameter Evaluation with Raman Measurements

The Raman measurements for the unsorted and radial aligned EA-SWCNTs were conducted with a Horiba Xplora spectrometer, equipped with a 2.33 eV laser source. The laser was focused on the aligned nanotubes with a $100 \times$ (0.95 N.A.) objective. The laser power was $100 \mu\text{W}$. The backscattered light was collected with the same objective, dispersed by 1200 grooves per mm grating and detected by a silicon charge coupled device. A built-in half wave plate was used to rotate the laser polarization perpendicular or parallel to the alignment direction. In a similar manner the analyzer was set for the desired direction. For the two-dimensional order parameter S_2D , the equation 1.58 from Zamora-Ledezma *et al.* (see section 1.5.2) requires the dichroic ratio at the laser wavelength (532 nm), which has been measured by the means discussed above. Depending on the size of the map, I_{HH} , I_{VV} , and I_{VH} were recorded with $2 \mu\text{m}$ intervals. The different sensitivity in the vertical and horizontal directions was calibrated by Raman signals from Benzonitrile molecules. For polarization rotation experiments, the custom built half-wave plate was introduced into the incident and scattered paths of the light. The intensity was collected for a series of incident angles (5° steps). The fit is provided by a standard equation for this phonon, where intensity varies as

$$I(\alpha) = I_{\parallel} \cos^4 \alpha + I_{\perp} \quad (2.3)$$

The length sorted samples were measured with a Horiba LabRAM HR Evolution with $\approx 1 \text{ mW}$ of 532 nm laser excitation over a spectral range of 1500 to 1650 cm^{-1} in a similar fashion.

2.6.3. Scanning Electron Microscopy

Images were taken with a Zeiss Ultra Plus with a $30 \mu\text{m}$ aperture and an acceleration voltage of 2 kV. The images were taken by collecting the secondary electrons and the contrast and brightness have been adjusted accordingly for each film, in order to account for different film thickness and slightly different distances between the cathode and the films.

2.6.4. Light Microscopy and Cross Polarized Microscopy

A Leica DMLM light microscope was used to capture images of the drying rings and make cross polarized measurements of membrane and substrate supported films. Cross polarized images were obtained in reflectance with two linear polarizers. Incident light was polarized by 90° with respect to the analyzer. To record the images for dark (0°) and bright position (45°), a rotational stage was placed on the microscope table and rotated to identify the position with maximum intensity. A Leica DM6 M light microscope was used to capture cross-polarized was used for mapping entire membranes by stitching several $5\times$ magnified images using the software provided by Leica. All images were recorded with the same brightness and exposure time. Images were analyzed with ImageJ and the open-source

extension shape logic detecting the individual grains, with two iterations performed, a minimal pixel threshold of 50 and maximal pixel threshold comprising all pixels of the image.

2.6.5. Atomic Force Microscopy

Topographies were recorded with a Dimension Icon, Bruker with NSC 19 cantilevers (μmasch) with a resonance frequency of 65 kHz and a force constant of 0.5 N m^{-1} . Imaging was performed in the repulsive regime with standard tapping mode in air and a resolution of 1024 lines. All topographies were evaluated using open-source Gwyddion.

2.7. Two-Probe Resistance Measurements

The radial films transferred to the fPCBs were connected to a multiplexer (Analog Digital, 16 channels, SparkFun electronics) controlled by an Arduino Micro and the resistances were measured by a Keithley 2400 Standard Series SMU. In order to ensure a good contact the SWCNTs interfacing the gold contacts were slightly covered with liquid silver paste (Leitsilber 200N, Hans Wolbring GmbH). The resistance of the measurement setup was determined with a reference resistance to be $\approx 60 \Omega$.

2.8. Transmission Experiments

Cross-polarized transmission measurements with linearly polarized light and transmission measurements with azimuthal and radial beam profiles were performed with a supercontinuum laser (NKT-FIU15) at 650 nm at an initial power of 0.1 mW. A linear polarized light field was obtained by placing a linear polarizer after the laser, while the structured light beams were formed by an additional Q-plate (ARCOptix). To form the structured light profiles, linearly polarized light polarized perpendicularly from the beam path, vertically for azimuthally polarized light, and horizontally for radially polarized light, were passed through the Q-plate. The beam then traveled through two achromic, convex lenses from Edmund Optics to expand the beam in order to fill the SP and CA films. The beam after the film is then shrunk with two more achromatic lenses and the beam intensity recorded with a beam profiler from Thorlabs (BC106N). A schematic of the measurement setup is displayed in Figure 2.4. The beam power (measured with a PM100d power meter and S121C photodiode power sensor from Thorlabs) just before the film was $9.1 \mu\text{W}$. The registered power fell to $8.2 \mu\text{W}$, after passing the beam through a glass substrate.

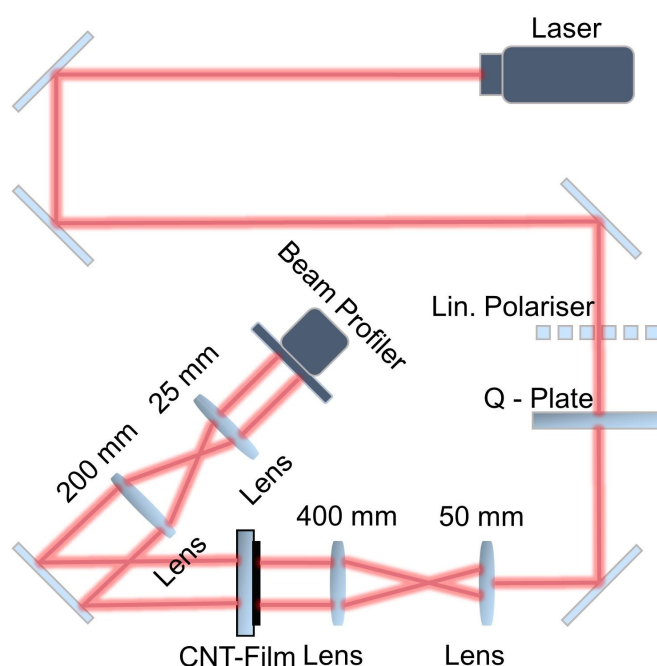


Figure 2.4.: Optical setup used to image the beam profiles shown in Figure 3.17 and Figure A.24. A supercontinuum laser was used to produce a 650 nm beam. This beam was either polarised linearly using a linear polarizer or polarised azimuthally or radially using the Q-plate. The beam was then passed through two achromatic lenses (focal length indicated above the lenses) to expand the beam to cover the entire film. Once transmitted, the beam is shrunk in order to fit the beam profiler. Reproduced from [2].

2.9. Derjaguin, Landau, Verwey, Overbeek Analysis with Python

DLVO Plots were realized with the Anaconda 3 jupyter notebook using python 3 with numpy and scipy packages. If not stated otherwise the parameters can be found in the work of Wu *et al.* [180]. Special emphasis was put onto the evaluation of the zeta-potentials of the membranes and dispersions as shown below.

2.9.1. Zeta Potential of Membranes:

All measurements were performed with a Surpass, Anton Paar. The pH and conductivity probes were calibrated with buffer solutions (pH 4, 7 and 10) and a KCl standard, respectively. The pH tested was increased in steps of 0.5 from pH 4 to pH 10 and three successive zeta potentials were measured and averaged at each value. The surface zeta potential was measured in a gap cell with a height adjusted to 100 μm . The pore zeta potential was measured in a similar fashion, albeit with a cylindrical cell and with the membrane cut to a diameter of 13 mm.

2.9.2. Zeta Potential of SWCNT Dispersions

Solution zeta potentials were measured with a Zetasizer Nano ZS, Malvern. The Smoluchowski model was used to evaluate the zeta potential from the hydrodynamic radius calculated from the auto correlation function and the electrophoretic mobility using the integrated PALS system, with the constants of pure water at 25 °C ($\nu = 0.8872 \text{ mm}^2 \text{ s}^{-1}$, $n = 1.33$ and $\epsilon_r = 78.5$).

3. Results

3.1. Resistance and Zeta-Potential of Membranes

Throughout this work, Polycarbonate track-etched membranes having pore sizes of 50, 80, 100 and 200 nm were used, uncoated (denoted as UC) and coated with a PVP layer. In order to measure R_m , 4 mL of deionized water (pH = 6.93) has been filtered through each membrane at volume rates of $40 \mu\text{L min}^{-1}$ – $150 \mu\text{L min}^{-1}$, Figure A.1 (A), and the average value taken at a permeate volume of 3.25 mL, Figure 3.1 (A). Also shown is an 80 nm membrane after hot embossing (denoted as HE) but this will be discussed later. These values were compared to the theoretical membrane resistance, R_{mT} , for membranes with a uniform pore length, l_m , and diameter, d_{pore} . A detailed derivation of R_{mT} can be found in section 1.4.1 following equations 1.16 to 1.20. It can be seen that the theoretical value is always lower than the measured value. This can be attributed to some pores not being straight and the added resistance due

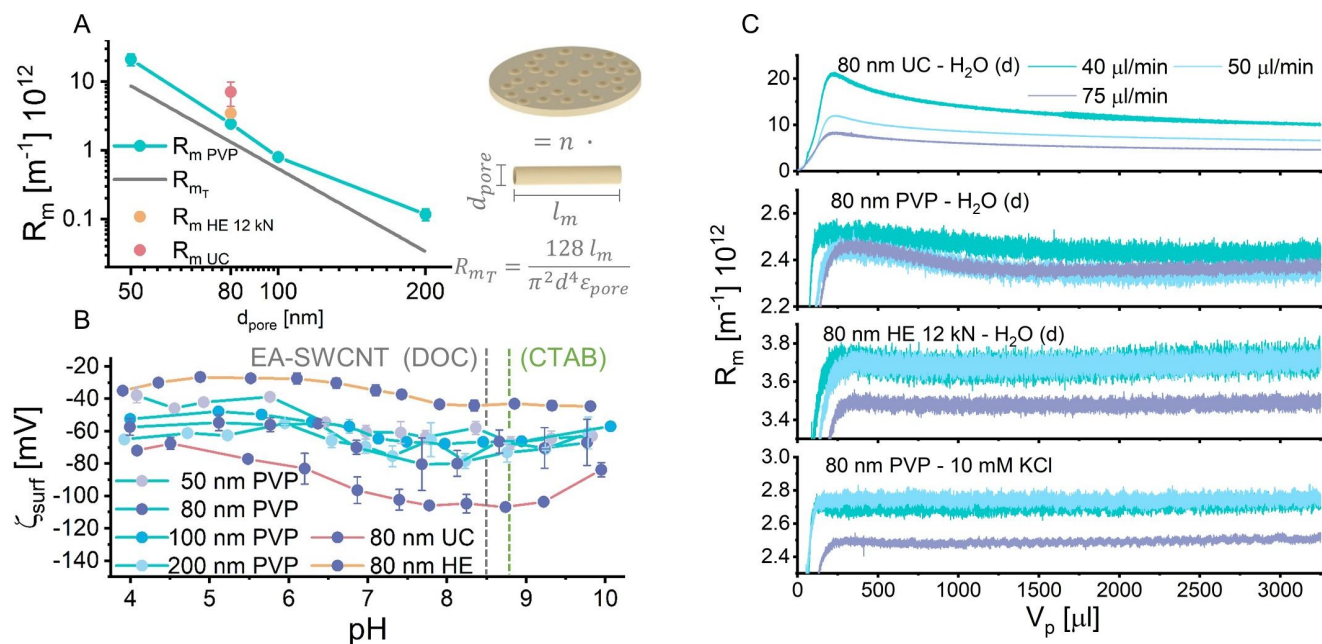


Figure 3.1.: (A) Experimental and theoretical values of the membrane resistance (R_m). (B) Surface zeta potential ζ_{surf} of PVP coated and uncoated (UC) membranes and PVP coated membranes after hot embossing (HE). (C) Volume evolution of R_m for various 80 nm membranes in either deionized water or 10 mM KCl. Reproduced from [1].

to the impermeable parts of the membrane as well as its zeta potential in the case of a real membrane.[213] Figure 3.1 (B) shows the zeta potential measured across the surface of the membranes, ζ_{surf} , for the pH range 4 – 10. In agreement with previous studies on polymer surfaces[214–216], hydrophobic membranes (the UC membranes) were found to have a lower zeta potential compared to hydrophilic membranes (PVP coated membranes) (≈ -95 mV vs. ≈ -60 mV-at pH = 6.93) and this resulted in a considerably higher R_m for the UC membranes. For example,

$R_m = 7.09 \times 10^{12} \text{ m}^{-1}$ vs. $2.43 \times 10^{12} \text{ m}^{-1}$ for an UC vs. PVP coated 80 nm membrane. As expected, due to ζ_{surf} being a surface sensitive parameter it was not found to be dependent on the pore size of the membrane. In contrast, the zeta potential measured through the pores, ζ_{pore} , varied with the pore diameter, Figure A.2. Figure 3.1 (C) shows the volume evolution of R_m for an 80 nm membrane with a total permeate volume (V_p) of 3.25 mL of either deionized water or 10 mmol KCl. For all membranes measured in deionized water, R_m reaches a maximum soon after filtration begins ($\approx 275 \mu\text{L}$) and then stabilizes to the value used in Figure 3.1 (A). The initial increase in resistance is likely due to a timing mismatch between the regulator sensor and the inline pressure sensor. As such, the resistance values are reliably only after $\approx 275 \mu\text{L}$. The membrane resistance R_m is often-reported to be a constant,[217] but certain effects can lead to a change in membrane resistance over time. Calvo *et al.* reported that polycarbonate track etched membranes tend to swell after the first contact with water, changing their morphology, opening up more pores and increasing in thickness, which could explain the decrease of resistance over time.[218] The in-line spectrometer was used to exclude the possibility that this decay in R_m was due to the removal of the PVP by deionized water. Only trace amounts of PVP were detected and indeed the largest initial peak and decay in R_m was observed for the UC membrane, Figure A.1. It can also be seen that the maximum resistance corresponds well to the absolute surface zeta potential, so one can assume, that the change in resistance might also be connected to the formation of an electric double layer. Previously, it has been reported that increasing the ionic strength by adding salt to an SWCNT dispersion hinders their alignment [41] due to a screening of the surface potential. Indeed for a 10 mM solution, this initial decay was not observed. On the contrary, adding DOC (0.04 - 0.35 wt%) did not suppress the peak and decay, Figure A.1 (B), albeit a higher R_m could be observed.

3.2. Zeta-Potential and Concentration of Dispersions made with Unsorted EA-SWCNTs

Zeta potential measurements were also performed on the unsorted EA-SWCNTs, Figures 3.2 (A) and (B). These had an average diameter of 1.4 nm and were dispersed in either DOC or CTAB. If only the surfactants are measured, the zeta potential increases linearly with surfactant concentration. This has been explained as an effect related to the formation of micelles at higher concentrations that shield the real zeta potential of a single surfactant molecule.[219, 220] In the presence of EA-SWCNTs, the absolute zeta potential, ζ_{CNT} , was found to decrease with increasing surfactant concentration. All proceeding experiments were performed with DOC dispersions at a concentration of 0.04 wt% and this corresponds to a $\zeta_{EA-SWCNT} = -14 \text{ mV}$. The zeta potential of a colloidal solution is often considered to indicate its stability and values between 15 mV are usually considered to be instable.[94] This is the case for DOC based dispersions below 0.1 wt% and corresponds to the concentration range that Walker *et al.* found best for alignment.[41] Alternatively, the zeta potential for CTAB dispersed EA-SWCNTs decreased from 90 mV at 0.25 wt% surfactant content to 72 mV at 0.125 wt%. This places all of the dispersions in a regime of stability, even at low surfactant concentration, Figure 3.2 (B). In light of the results presented later, it can be concluded that an

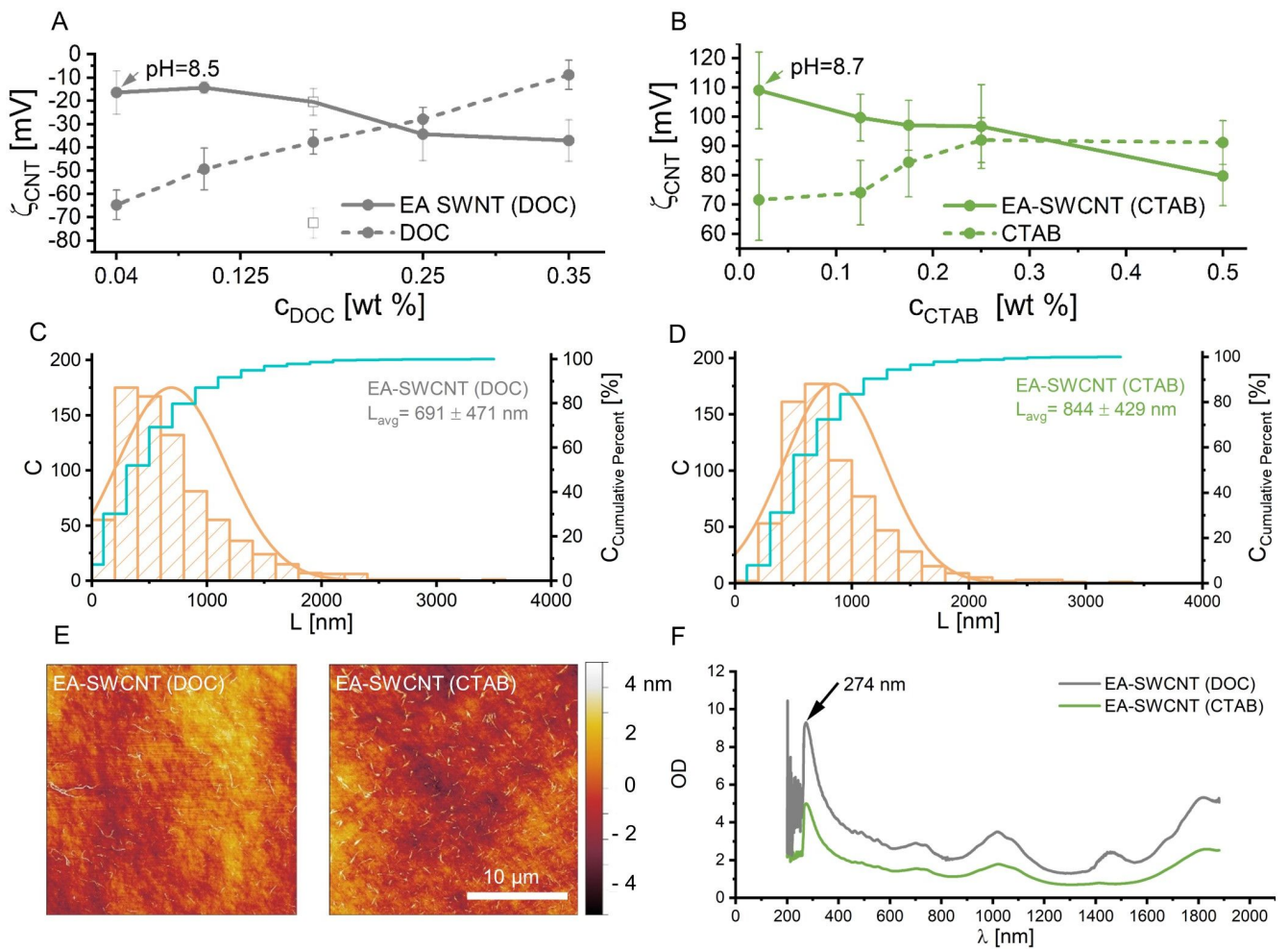


Figure 3.2.: Zeta potential with and without $8 \mu\text{g L}^{-1}$ of unsorted EA-SWCNTs in either DOC (A) or CTAB (B). Length distribution of unsorted EA-SWCNTs wrapped in DOC (C) and CTAB (D) obtained from statistical analysis of (E) nanotubes spin-coated on a silicon wafer and obtained from four $25 \times 25 \mu\text{m}^2$ topographies measured by AFM. (F) The π -plasmon peak (274 nm) was used to estimate the concentration of each sample. Figure reproduced from [1].

instable dispersion is not needed, but rather that the SWCNT walls should be depleted of surfactant. Complete zeta potential measurements, calibrating data of the instrument and the parameters of the unsorted EA-SWCNTs used for the PALS-system (eq. 1.49) can be found in Figure A.3. The average length was determined by means of measuring individual SWCNTs spin coated onto a Si-wafer via AFM, yielding 691 ± 471 nm for the EA-SWCNTs dispersed in DOC and 844 ± 471 nm (CTAB), respectively, as shown in Figures 3.2 (C), (D) and (E). AFM imaging also revealed that most CNTs were individualized and that the centrifugation step removed most of the bent or distorted tubes. A more detailed discussion of the impact of length and diameter will be given later in sections 3.10 to 3.15, but in order to establish an understanding of the process itself, all experiments shown in sections 3.3 to 3.9 are performed with the unsorted SWCNTs, which will be further only denoted as EA-SWCNTs. The absorption spectra used to calculate the concentration can be found in Figure 3.2 (F), as the optical density (OD) measured at the π -Plasmon peak can be

estimated to be equivalent to a concentration of $100 \mu\text{g mL}^{-1}$.

3.3. Optimization of the Slow Volume-Rate for unsorted EA-SWCNTs

Figure 3.3 (A) shows a series of slow filtration experiments using 4 mL of an $8 \mu\text{g mL}^{-1}$ dispersion of EA-SWCNTs with 0.04 wt% DOC at volume rates of $25 \mu\text{L min}^{-1}$ – $125 \mu\text{L min}^{-1}$ on an 80 nm membrane. $R_b + R_{cp}$ was calculated by subtracting R_m from R_{tot} . Immediately apparent is a resistance peak during the initial $\approx 500 \mu\text{L}$ of filtration that

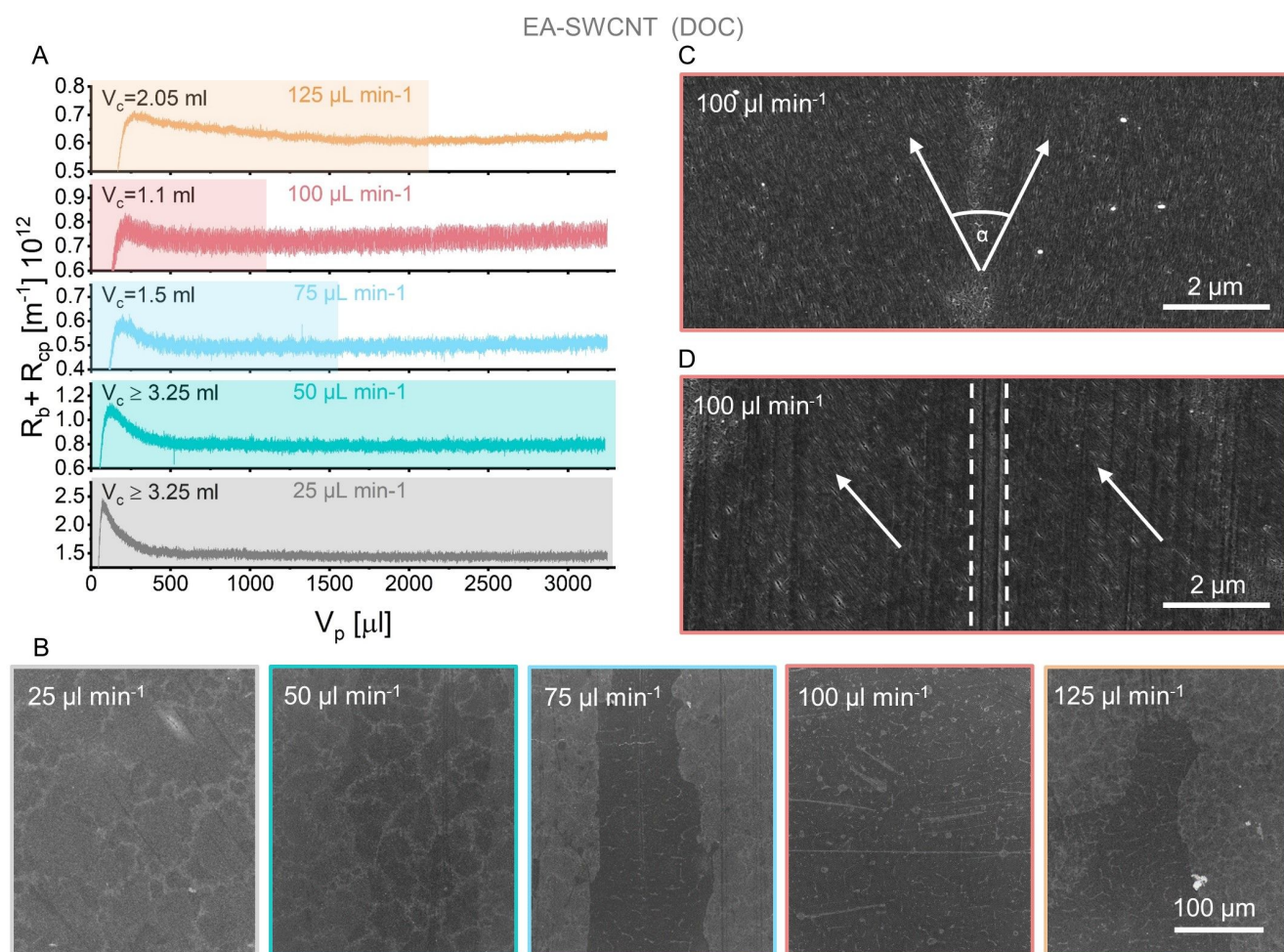


Figure 3.3.: (A) Resistance measured during slow filtration of 4 mL of an $8 \mu\text{g mL}^{-1}$ dispersion of unsorted EA-SWCNTs with 0.04 wt% DOC at volume rates of $25 \mu\text{L min}^{-1}$ – $125 \mu\text{L min}^{-1}$ on an 80 nm membrane. (B) SEM images of the SWCNT film (transferred to a silicon wafer) obtained at these volume rates with (C) an enlarged view of the $100 \mu\text{L min}^{-1}$ film showing mis-aligned SWCNT crystallites. (D) A SWCNT domain with an alignment direction (arrows) offset from that of a groove (dashed lines) in the membrane. Note: Finer grooves can also be seen in the image and these have not been highlighted. Reproduced from [1].

was largest for a flow rate of $25 \mu\text{L min}^{-1}$, reached a minimum at $100 \mu\text{L min}^{-1}$ and then increased for $125 \mu\text{L min}^{-1}$.

In agreement with the discussion of Figure 3.1 (C), the peak is attributed to the membrane itself rather than the SWCNTs and is therefore not considered in the following discussion. In Figure 3.3 (A), the concentration polarization regime has been shaded in color for each volume rate. This is the region prior to an observable increase in the resistance, i.e. before fouling occurs. At $25 \mu\text{L min}^{-1}$ and $50 \mu\text{L min}^{-1}$ no increase in $R_b + R_{cp}$ was observed and this

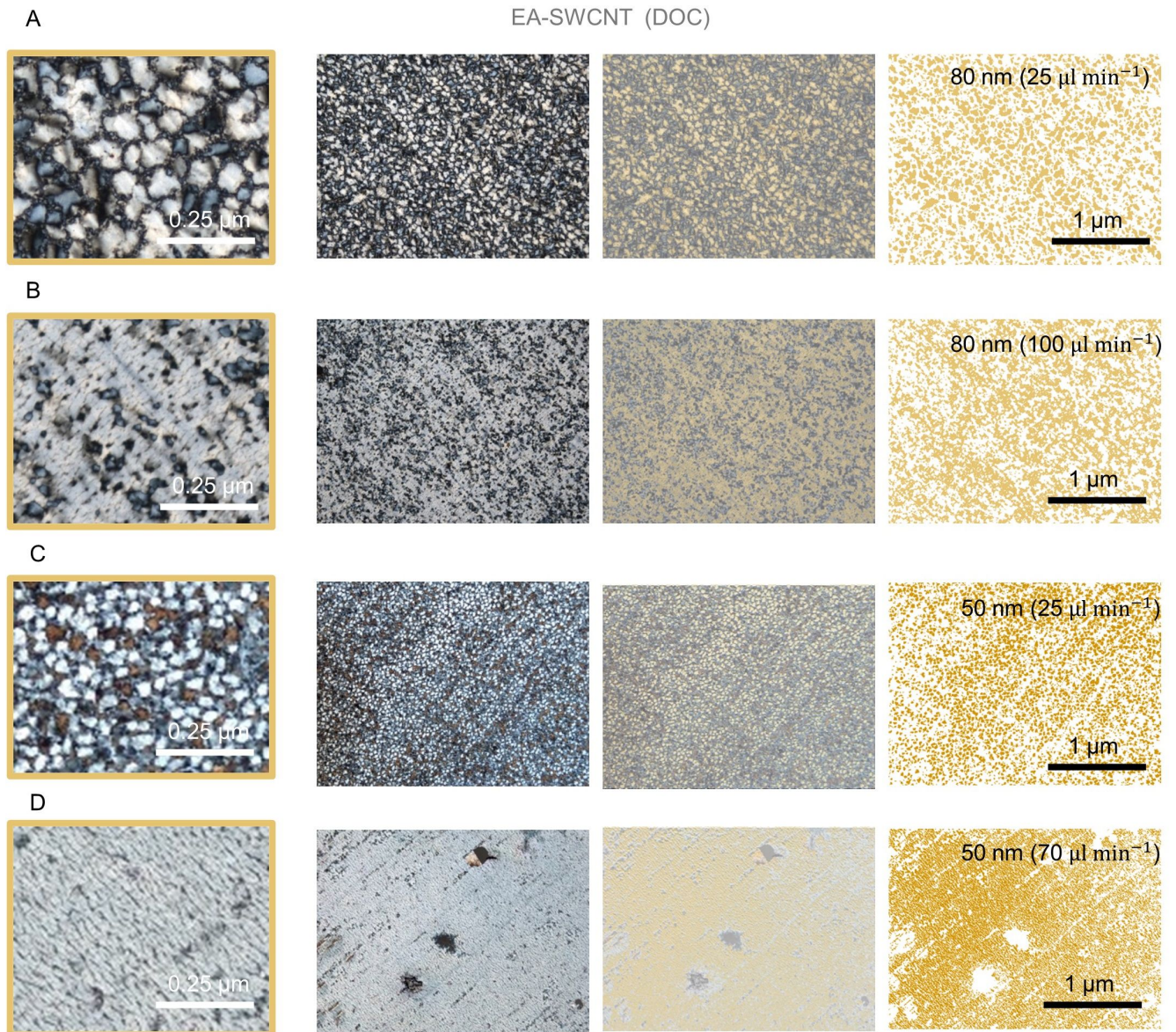


Figure 3.4.: Cross polarized microscopy images of 4 mL of an $8 \mu\text{g mL}^{-1}$ EA-SWCNT dispersed in 0.04 wt% DOC on an 80 nm membrane at (A) $25 \mu\text{L min}^{-1}$ and (B) $100 \mu\text{L min}^{-1}$ or 50 nm membrane at (C) $25 \mu\text{L min}^{-1}$ and (D) $70 \mu\text{L min}^{-1}$. The orange shade and fit show the grains detected (bright contrast) by machine vision and used later to evaluate their size. The samples were transferred onto a silicon substrate for imaging. Figure reproduced from [1].

implies that the critical volume V_c for fouling exceeds 3.25 mL at these volume rates. Here it is important to state that the observable retention of the membrane was measured to be 0.98, Figure A.4. Therefore, the possibility for

SWCNTs to simply pass through the membrane and thereby not increase the measured resistance can be excluded.

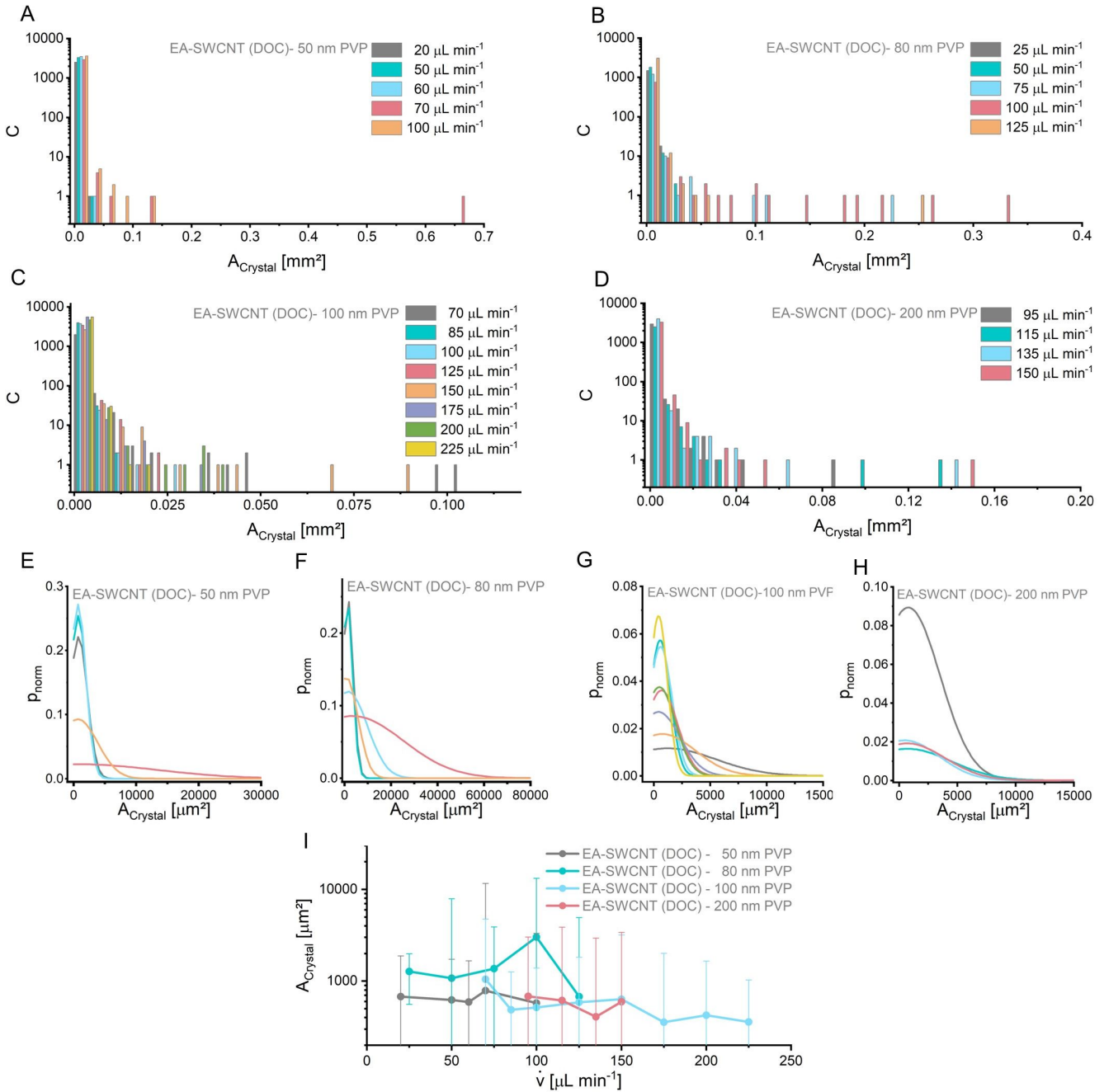


Figure 3.5.: Histogram plot of the grain size obtained from over 1000 counted grains with machine vision analysis of cross polarized microscopy images of films obtained at different volume rates on (A) 50 nm (B) 80 nm (C) 100 nm and (D) 200 nm membranes using 4 mL of an $8 \mu\text{g mL}^{-1}$ EA-SWCNT dispersed in 0.04 wt% DOC. (E-H) Corresponding normal distributions and (I) the logarithmic plot obtained from the average grains size where the error bars shown represent the standard deviation. Note: the abnormal grain-size at $100 \mu\text{L min}^{-1}$ on the 80 nm membrane, is an artefact of the machine vision algorithm not being able to accurately recognize single grains. Figure reproduced from [1].

In this regime, the SWCNTs reaching the surface gather in a dispersed state above the membrane.[164] Alternatively, for $75 \mu\text{L min}^{-1}$, $100 \mu\text{L min}^{-1}$ and $125 \mu\text{L min}^{-1}$, the resistance was found to increase after 1.5 mL, 1.1 mL and 2.05 mL, respectively. In all cases the resistance increase was found to be linear and this corresponds to the cake filtration mode of fouling, as shown in Figure 1.11.[164] Representative SEM images with constant imaging parameters of the film obtained for each volume rate are shown in 3.3 (B). In all cases, the films were transferred to silicon wafers such that the SWCNTs shown are those between the membrane and retentate (bottom layer). For reference, regions containing densely packed and aligned SWCNTs appear dark in contrast, whereas disoriented and less dense regions appear bright. Large SWCNT crystallites are visible at $25 \mu\text{L min}^{-1}$ and these were found to become more compact with increasing volume rate, until the entire membrane was covered with a dense film at $100 \mu\text{L min}^{-1}$. At $125 \mu\text{L min}^{-1}$, this trend is reversed and less dense areas comparable to $75 \mu\text{L min}^{-1}$ were observed. An increase in the critical volume was also found to occur at this volume rate. In all images, the thin regions of brighter contrast correspond to grain boundaries consisting of disordered SWCNTs, which divide crystallites at a small angle to each other and an example is shown for $100 \mu\text{L min}^{-1}$ in 3.3 (C). Similar results were obtained for the 50 nm, 100 nm and 200 nm pore size membranes and total resistance curves taken during filtration for these membranes can be found in Figure A.5. Although the crystallites are most often found to be orientated with the direction of the grooves, occasionally, they are also found to be mis-aligned, Figure 3.3 (D), which suggests that macro- and micro-grooves in the membrane do not function as a structural template for SWCNT alignment. Cross polarized microscopy and machine vision were used to evaluate the size and shape of these crystallites, Figure A.6 – A.9 and as an example Figure 3.4, shows the evaluation of the images taken from the (A) 80 nm and (B) 50 nm membrane. At slow volume rates ($\dot{v} = 25 \mu\text{L min}^{-1}$) the domains were round and large and as the volume rate was increased to the optimal value ($\dot{v} = 100 \mu\text{L min}^{-1}$ for the 80 nm membrane and $\dot{v} = 75 \mu\text{L min}^{-1}$), the grains decreased in size and elongated. The sizes of the grains (marked in yellow and individually counted) were then plotted as histograms (Figure 3.5 (A)- (D)) and corresponding normal distributions as shown in Figure 3.5 (E)-(H). Eventually, the average crystal areas $A_{crystal}$ was then plotted against the volume rate used for each pore size and it was found that the average size of the crystallites generally decreased with increasing volume rate for all membranes tested, Figure 3.5 (I). By comparing the shape of the grains found on the 80 nm membrane to the filtration curves plotted in 3.3 (A), it can be seen that this crossing point corresponds to filtrations with only concentration polarization and those with concentration polarization and cake formation. Thereby the shape of the crystallites also changed from round at $50 \mu\text{L min}^{-1}$ to a mixture of round and elongated domains at $75 \mu\text{L min}^{-1}$, to entirely elongated crystallites at $100 \mu\text{L min}^{-1}$, Figure A.7. For the 200 nm membrane, the slowest volume rate obtainable with the filtration setup already resulted in elongated domains, whilst for the 100 nm membranes, a mixture of round and elongated domains was always observed and this was independent of the volume rate used, Figures A.8 and A.9. For an 80 nm membrane with DOC dispersed SWCNTs, $100 \mu\text{L min}^{-1}$ is providing the best conditions for alignment, but at this stage, still with many misaligned crystallites. Apart from variations in the optimum volume rate (50 nm: $70 \mu\text{L min}^{-1}$, 100 nm: $150 \mu\text{L min}^{-1}$, 200 nm: $95 \mu\text{L min}^{-1}$), the best alignment was always obtained when the concentration polarization regime was the shortest, Figure A.6 – A.9. Previously, He et al. [40] have stated that the initial flow determines

whether or not the nanotubes form an aligned film, and this can now be interpreted to be the volume rate with the smallest critical volume, V_c . These experiments were repeated for 4 mL of an $8 \mu\text{g mL}^{-1}$ dispersion of EA-SWCNTs in 0.02 wt% CTAB, Figure 3.6. This is the first time that a positively charged surfactant has been investigated for

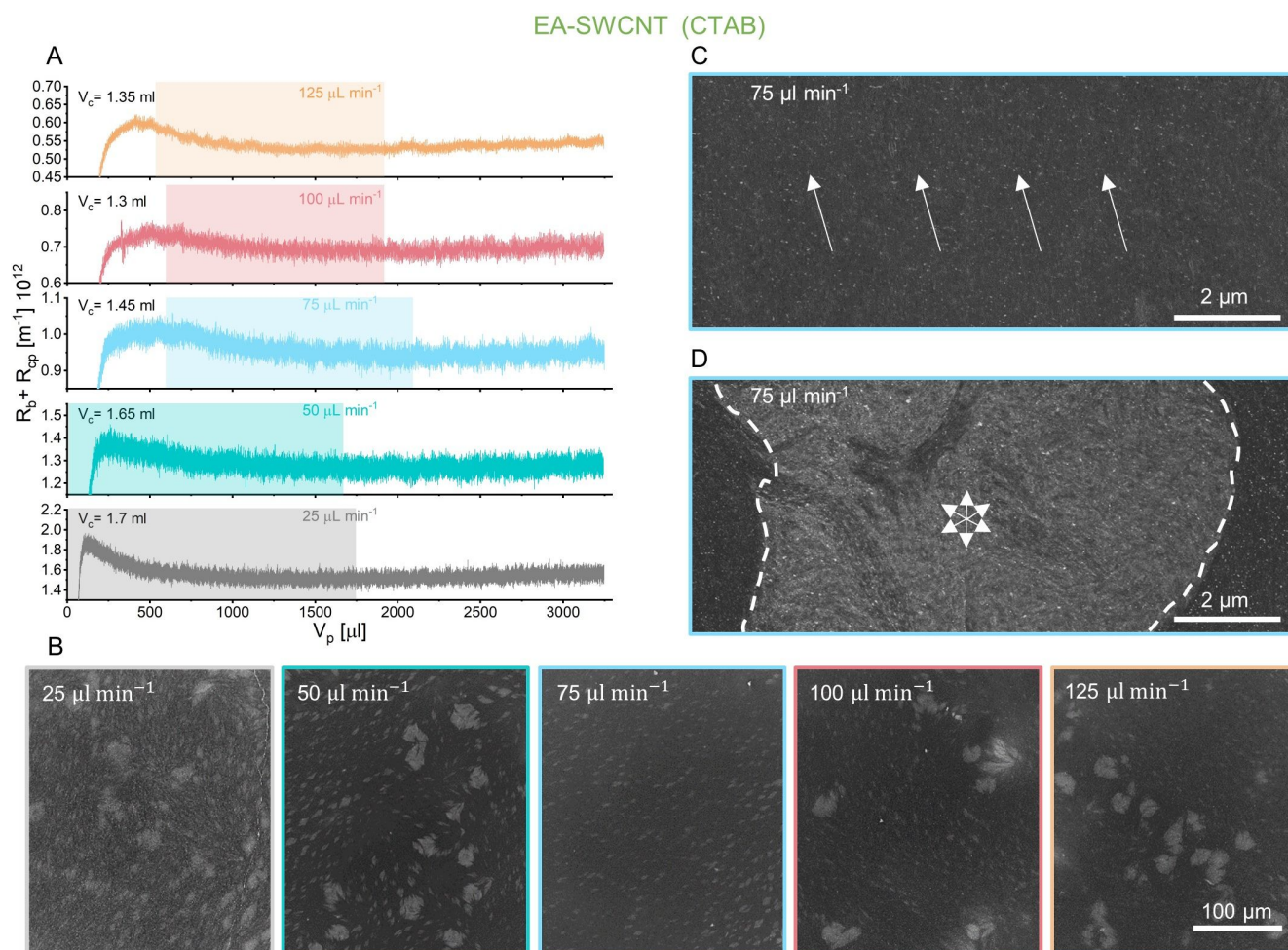


Figure 3.6.: (A) Resistance measured during filtration of 4 mL of an $8 \mu\text{g mL}^{-1}$ dispersion of unsorted EA-SWCNTs with 0.02 wt% CTAB at volume rates of $25 \mu\text{L min}^{-1}$ – $125 \mu\text{L min}^{-1}$ on an 80 nm membrane. Films were pushed down after 3.25 mL at $400 \mu\text{L min}^{-1}$. (B) SEM images of the SWCNT film (transferred to a silicon wafer) obtained at these volume rates with (C) an enlarged view of the $75 \mu\text{L min}^{-1}$ film showing large area un-directional SWCNT alignment. (D) A tear in the $75 \mu\text{L min}^{-1}$ film reveals that the first aligned layer is preceded by disordered SWCNTs. Figure reproduced from [1].

SWCNT alignment. Despite the lower critical volume, the measured resistance curves show a similar behavior to that of the DOC dispersed SWCNTs for volume rates up to $50 \mu\text{L min}^{-1}$. At higher volume rates, first an initial increase in resistance is observed, followed by a plateau and then the usual decrease in resistance leading up to fouling. Essentially, this implies that at first rapid fouling occurs; this is followed by concentration polarization and then a secondary fouling step. For all volume rates greater than $25 \mu\text{L min}^{-1}$ a compact film of SWCNTs was observed

and above $50 \mu\text{L min}^{-1}$ an unidirectionally aligned film without grains was obtained. Corresponding cross-polarized microscopy images are shown in Figure A.10. At first glance, this can easily be confused with a globally aligned SWCNT film. However, upon examination of tears in the film, it can be seen that this first aligned layer is followed by a disordered layer of SWCNTs, Figure 3.6 (D). Interestingly, cross-polarized microscopy images of the top side of the SWCNT film (still on the membrane) reveal that the SWCNTs start to align again at the top, forming a third layer, Figure A.11. For CTAB dispersed SWCNTs a disordered layer is sandwiched between two aligned films.

3.4. Optimization of the Fast Volume-Rate for Unsorted EA-SWCNTs

In an attempt to improve the alignment of the DOC dispersed SWCNTs, the volume rate of the fast filtration step was varied. This was performed with $750 \mu\text{L}$ of feed solution still in the filtration cell in order to homogeneously cover the membrane. Volume rates of $300 \mu\text{L min}^{-1}$ – $700 \mu\text{L min}^{-1}$ were tested. Figure A.12 (A) shows the resistance $R_b + R_{cp}$ measured for a 4 mL feed of an $8 \mu\text{g mL}^{-1}$ dispersion of EA-SWCNTs with $0.04 \text{ wt}\%$ DOC filtered onto an 80 nm membrane using a constant slow filtration step of $100 \mu\text{L min}^{-1}$. The sharp increase in resistance at $\approx 3.25 \text{ mL}$ is related to drying of the film and the linear increase after an initial rise at $\approx 2.75 \text{ mL}$ shows a caking behavior resulting from further compression of the film. Regardless of the push step applied, the absolute value of the resistance with respect to the volume rate did not follow any trend nor was it found to have an impact on the quality of alignment. This is demonstrated by almost indistinguishable cross polarized images in Figure A.12 (B) for push speeds of $700 \mu\text{L min}^{-1}$, $500 \mu\text{L min}^{-1}$ and $300 \mu\text{L min}^{-1}$. This was also true for experiments with CTAB, Figure A.13. Walker *et al.* previously reported that the meniscus formed during this last stage of the filtration can lead to the formation of spherulites and used a hydrophobic silane coating on their glass funnel to avoid them.[41] The custom filtration cell used here, facilitates hydrophobic PTFE and polycarbonate cylinders with contact angles of $\approx 115^\circ$ and $\approx 88^\circ$ [221, 222], respectively. One could argue, that a contact angle close to 90° degrees would afford an even liquid surface, but no benefit was found using polycarbonate, and thus PTFE was used instead, as it is easier to clean. As expected, the dispersions formed a slightly convex meniscus and thus no formation of spherulites could be observed. Instead, the formation of drying rings was observed, Figure 3.7 (A) and (B). The diameter of the drying rings was found to be dependent on the push step and increased with the volume rate for all membranes, regardless of their pore size, Figure 3.7 (C). A diameter of 22 mm corresponded to the area of filtration and was thus considered to be a SWCNT film without drying rings. Therefore, in all proceeding experiments, the push step was adjusted to be the lowest volume rate (i.e. $500 \mu\text{L min}^{-1}$ for an 80 nm membrane) resulting in a film free of drying rings. For the 50 nm membrane, the maximum output pressure of 2 bar was not sufficient to avoid the drying rings and instead a volume rate of $200 \mu\text{L min}^{-1}$ was used.

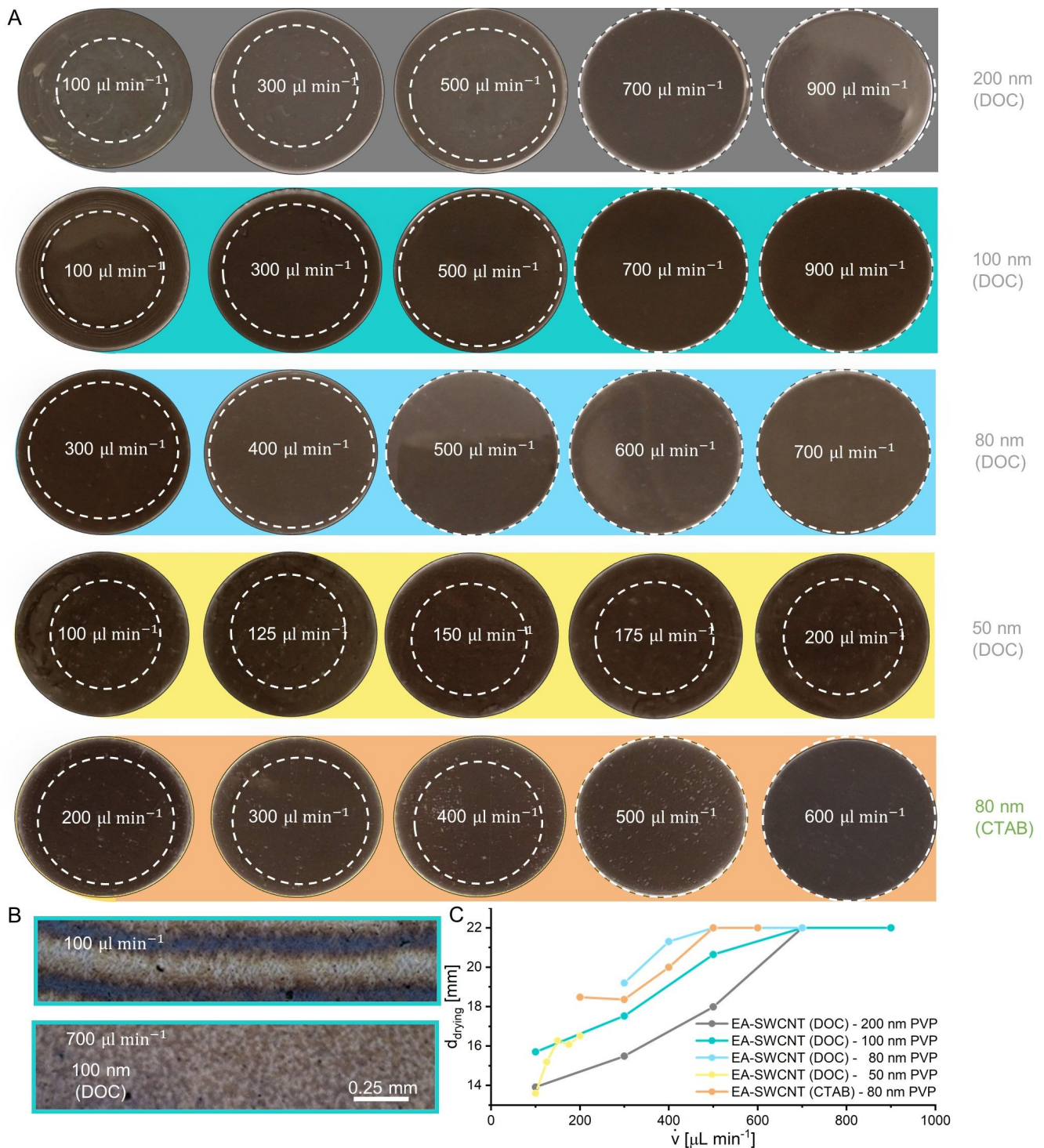


Figure 3.7.: (A) Size of the inner most drying ring obtained for SWCNT films pushed at different volume rates. (B) Light microscope image of the outer region of a SWCNT film pushed onto a 100 nm membrane at $700 \mu\text{L min}^{-1}$. (C) Dependence of the drying ring diameter on the volume rate in the fast filtration step. We considered the volume rate to be optimized when a drying ring was not visible ($d_{\text{drying}} = 22 \text{ mm}$). Figure reproduced from [1].

3.5. Influence of Deposited Mass on the Alignment of Unsorted EA-SWCNTs

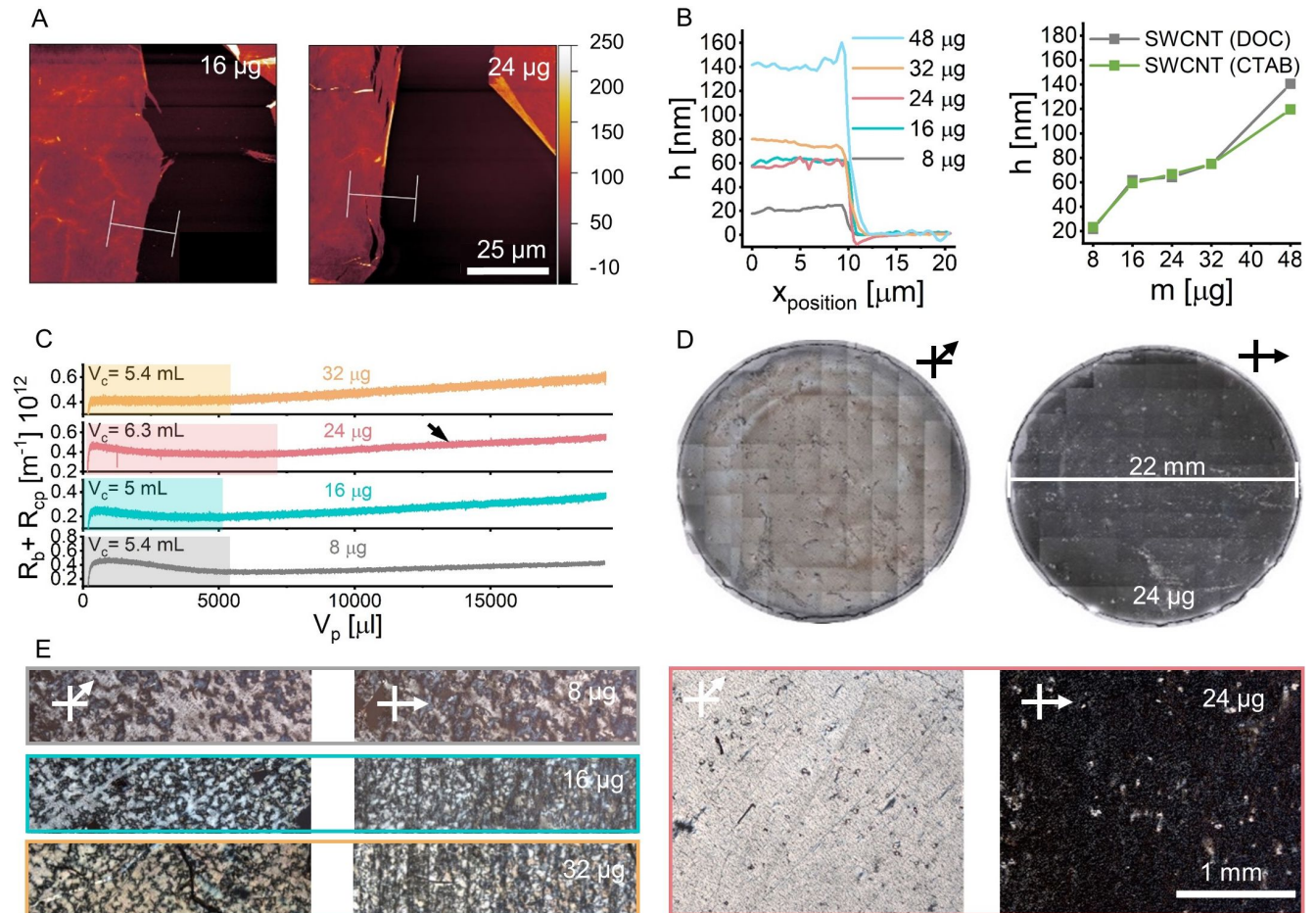


Figure 3.8.: (A) AFM topography images of SWCNT films transferred to silicon obtained from $100 \mu\text{L min}^{-1}$ filtration of 2 mL and 3 mL of an $8 \mu\text{g mL}^{-1}$ dispersion of EA-SWCNTs with 0.04 wt% DOC on an 80 nm membrane. (B) Height profile data for feed volumes of 1 mL – 6 mL. (C) Resistance measured during filtration of 20 mL of a $0.4 \mu\text{g mL}^{-1}$ – $1.6 \mu\text{g mL}^{-1}$ dispersion of unsorted EA-SWCNTs with 0.002 wt% – 0.0016 wt% DOC at volume rate of $100 \mu\text{L min}^{-1}$ and with push step of $500 \mu\text{L min}^{-1}$ on an 80 nm membrane. The total mass of SWCNTs filtered was $8 \mu\text{g}$ – $32 \mu\text{g}$ and the transition between intermediate blocking and cake filtration for the $24 \mu\text{g}$ case is indicated by an arrow. (D) Stitched cross polarized microscopy images of the film obtained from $24 \mu\text{g}$ of SWCNTs on the membrane (top surface). (E) Cross polarized microscopy of films after transfer to ITO-coated glass substrates (bottom surface) for SWCNT masses of $8 \mu\text{g}$ – $32 \mu\text{g}$. Reproduced from [1].

The role of filtered mass on the global alignment of SWCNTs was then investigated by varying the feed volume in 1 mL steps. All other parameters were held constant: $8 \mu\text{g mL}^{-1}$ dispersion of EA-SWCNTs with 0.04 wt% DOC on an 80 nm membrane with a $100 \mu\text{L min}^{-1}$ filtration step to a final volume of $750 \mu\text{L}$ followed by push step of $500 \mu\text{L min}^{-1}$. These films were transferred to a silicon wafer and their topography was measured by AFM, 3.8 (A) and Figure A.14. Intuitively, a linear increase in film thickness might be expected for increasing SWCNT mass. Instead, analysis of AFM

height profile data, revealed the existence of a plateau at ≈ 62 nm for masses of 16 – 24 μg , 3.8 (B). The same plateau was observed for experiments with CTAB dispersed SWCNTs, Figure 3.7. To further investigate this phenomenon, the masses used above were diluted in deionized water in order to fill the total capacity of the filter holder (20 mL). This effectively varied the concentration of the SWCNTs to be $0.4 \mu\text{g mL}^{-1}$ – $1.6 \mu\text{g mL}^{-1}$ and DOC to be 0.002 wt% – 0.016 wt%. The cake resistance measured for a $100 \mu\text{L min}^{-1}$ filtration step of these dispersions is shown in 3.8 (C). It can be seen, that the increase in resistance after concentration polarization became visually more apparent than what was seen previously in 3.3 (A). For the 24 μg sample, the initial increase in resistance was now best fit by an intermediate blocking mode of fouling after a critical volume of 6.3 mL and later ($V_p = 13.5$ mL, see black arrow) changed to cake filtration. This is in agreement with work by Nakamura *et al.* [156], who stated, that intermediate blocking is always followed by cake filtration once the membrane becomes fully coated. All other masses displayed only cake filtration and had a similar critical volume of ≈ 5.25 mL. Upon stitching 155 individual cross polarized micrographs taken with $5\times$ magnification, the 24 μg sample was found to afford a dense and globally aligned SWCNT film across the entire membrane, 3.8 (D). Cross polarized microscopy of the film after transfer to ITO coated glass, 3.8 (E) and SEM images in Figure A.15, showed that alignment was consistent on both sides of the film. Here it is important to note that the elongated SWCNT domains seen in Figure 3.4 were still present but that these now had a common alignment direction. In contrast, the other concentrations were found to result in the formation of either an incomplete layer (8 μg and 16 μg) or an overgrown layer (32 μg), 3.8 (E). A similar effect was observed for the non-diluted samples use for topography measurements discussed previously, Figure A.16. The dependence on mass can be understood in terms of the required mass to fill the membrane homogenously and furthers corroborates that the global alignment mechanism involves the formation of crystallites rather than individual SWCNTs.

3.6. Hot-Embossing of Membranes with Axial Patterns

Having identified precise conditions for global alignment on unmodified membranes in the previous section 3.3, at first, axial surface patterns are imprinted into the membranes using a repurposed tensile test machine for hot-embossing shown in Figure 3.9. [223, 224] Thereby a Teflon piece with the dimensions of the patterned field and a larger Kapton sheet were used to transmit and homogenize the force applied. The shim itself was held in place by a custom retaining device and the temperature could be monitored using Platinum-Thermocouples. At first, the membrane was

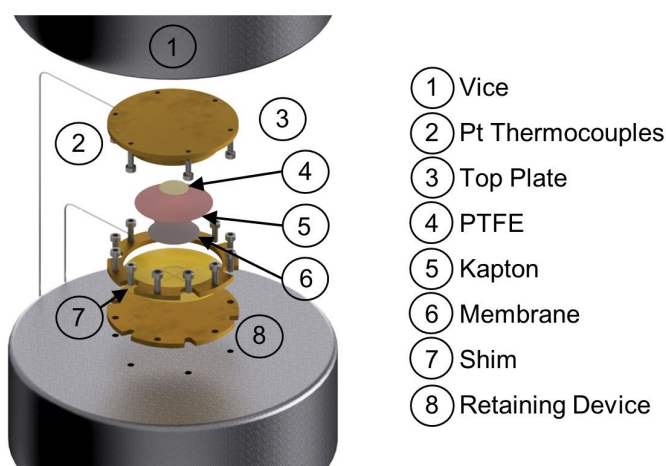


Figure 3.9.: Hot-Embossing setup used to imprint the PCTE membranes. The setup is based on a modified tensile test machine, which also allows for precise heating and cooling. Figure reproduced from [1].

heated up to the desired temperature, before various load of 8, 12, or 16 kN were applied, by closing the tensile test machine, Figure 3.10 (A). Hot-embossing was performed at a temperature of $\approx 120^\circ\text{C}$, which is slightly below the glass transition temperature of polycarbonate (147°C [139]) and allowed for plastic deformation of the membrane. The shim was in contact with the membrane for ≈ 10 min after heating up by $95^\circ\text{C min}^{-1}$, before the membrane was removed from the hot-embossing setup at 40°C using an average cooling rate of 4°C min^{-1} , as seen in Figure 3.10 (B).[1] A custom-made shim containing four different regions with parallel aligned groove spacings of $w = 150$ nm, 300 nm, 450 nm and 600 nm, resulted than in the replicated structures shown in Figure 3.10 (C), measured by an AFM. By analyzing the average heights of the pattern, Figure 3.10 (D), it can be seen that the smaller structures are imprinted with a lesser depth. As each pattern had an equivalent cumulative area of grooves and ridges, smaller lines required greater force for deformation and thus did not penetrate as deep as their wider counterparts. However, the widths were replicated well independent of the force applied as shown in Figure 3.10 (E) and as an example for 600 nm in Figure 3.10 (F). Additional AFM images of the stamped regions can be found in Figure A.17. An applied force of 8 kN was found to be insufficient for the smaller patterns, whereas 16 kN deformed the largest pattern. At 12 kN all structures were well replicated in the membrane, which can be seen by the height not changing anymore between 12 and 16 kN. Apart from applying a texture, hot embossing was also accompanied by several other key

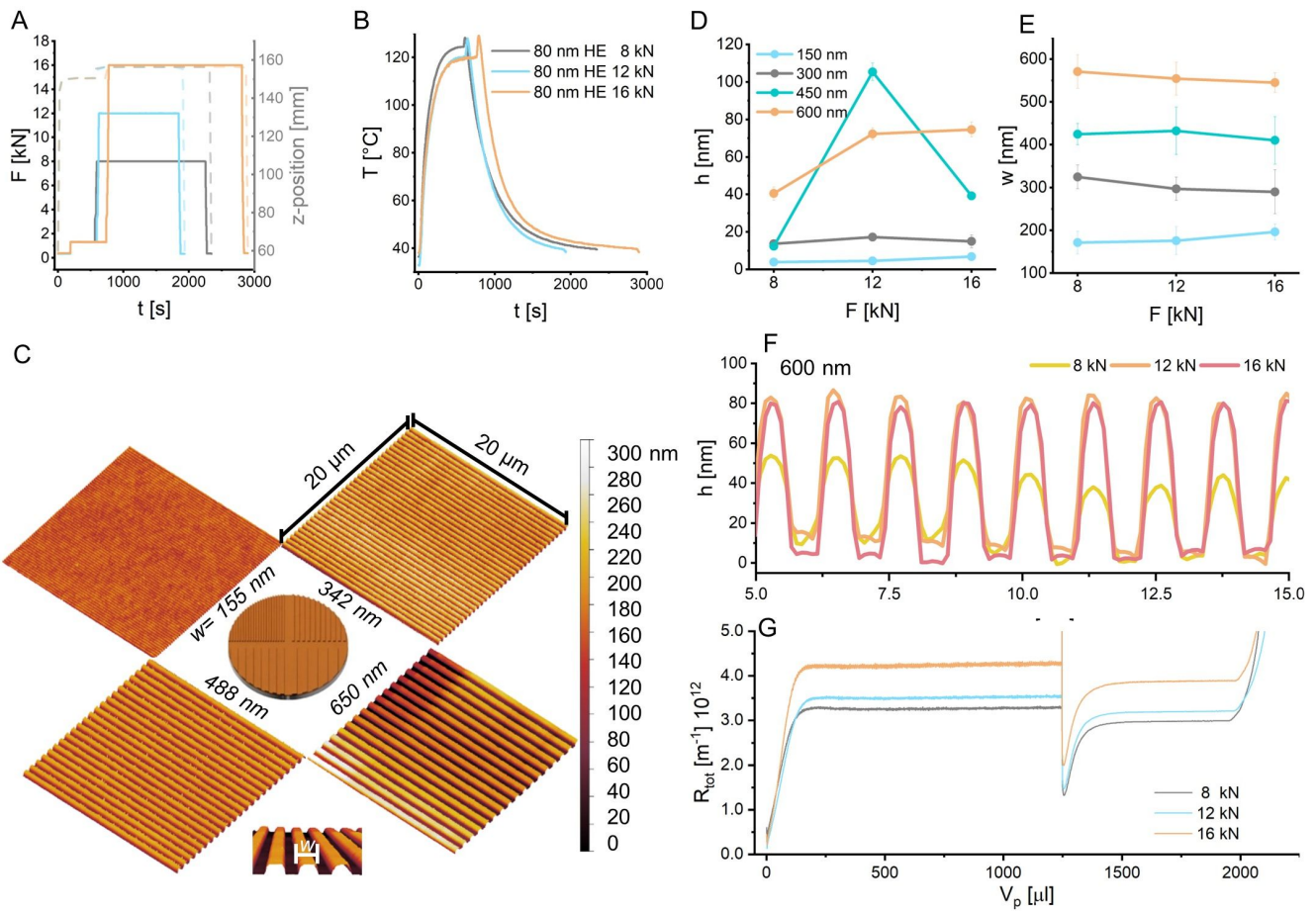


Figure 3.10.: (A) Force applied by the hot embossing setup as the shim is pressed into the membrane and (B) the corresponding temperature. (C) AFM topography images of an imprinted membrane with (D) the height and (E) the width of the pattern for various applied forces on an 80 nm membrane. (F) Topography lines averaged over 5 μm for a 600 nm pattern, where an increase in groove height is not seen for forces above 12 kN. (G) Filtration of 2 mL of an 8 μg mL⁻¹ EA-SWCNT dispersion in 0.04 wt% slowly at 100 μL min⁻¹ and pushed with 500 μL min⁻¹ on textured 80 nm membranes. The large increase in total resistance for the 16 kN imprinted membrane can be attributed to excessive deformation of the membrane. Figure reproduced from [1].

changes to the membrane. Firstly, greater deformation at the contact area with the shim (valleys) leads to a reduction of the pore size in this region. Figure A.18 provides a comparison of the pore size on the ridges and in the valleys for 12 kN of applied force on an 80 nm membrane. Due to membrane resistance being inversely proportional to the fourth power of the pore diameter this led to an increase in the overall membrane resistance (equation 1.20). This is also reflected in the total resistance measurements for the filtration of 2 mL of an 8 μg mL⁻¹ EA-SWCNT dispersion in 0.04 wt% DOC at 100 μL min⁻¹ and pushed with 500 μL min⁻¹ on an 80 nm membranes, Figure 3.10 (G), as the resistance is significantly higher for the membrane deformed with 16 kN. Furthermore, a reduction in the absolute zeta potential at the membrane surface from -60 mV for a PVP coated membrane at pH= 8.5 to -42 mV for the hot embossed membrane was observed, Figure 3.1 (C). Intuitively it might be expected that these changes to the

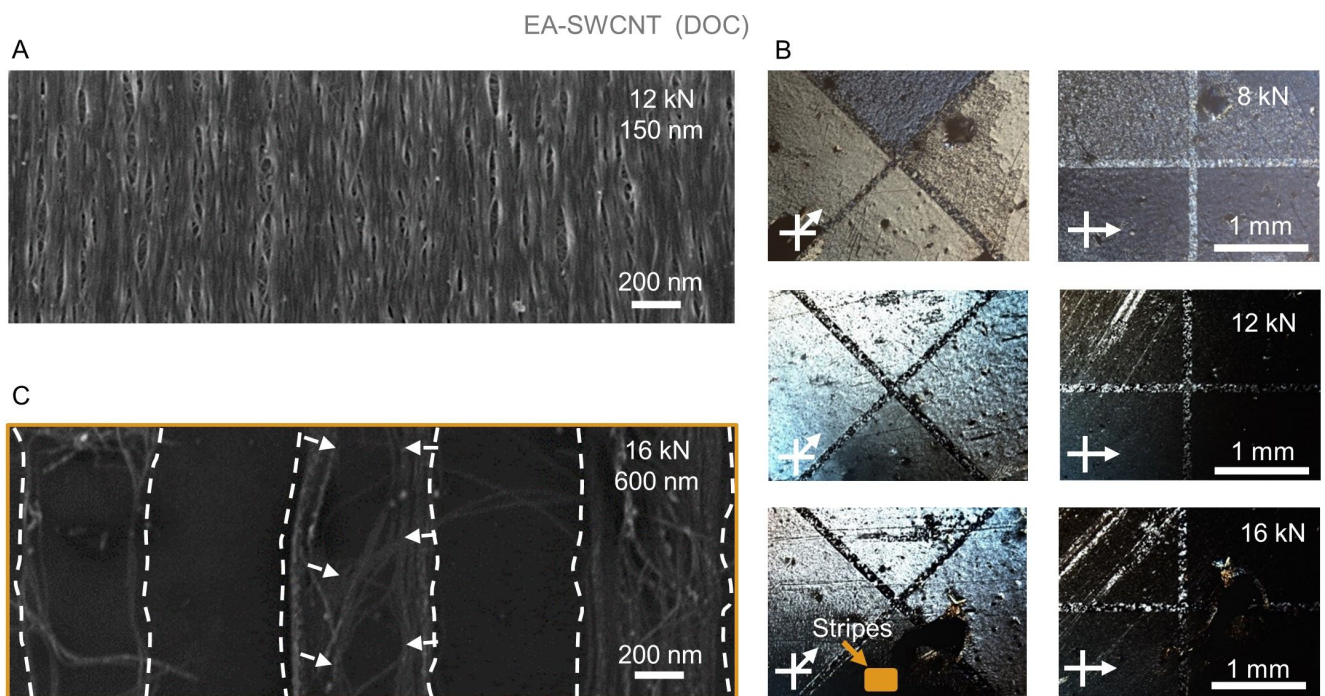


Figure 3.11.: (A) SEM image of the SWCNT film obtained by filtration of 2 mL of an $8 \mu\text{g mL}^{-1}$ EA-SWCNT dispersion in 0.04 wt% DOC at $100 \mu\text{L min}^{-1}$ with a push step of $500 \mu\text{L min}^{-1}$ on 150 nm grooves imprinted on an 80 nm at 12 kN. (B) Cross polarized microscopy images of transferred (silicon-substrate) SWCNT films prepared in the same way but on 80 nm membranes imprinted at 8 kN, 12 kN and 16 kN. (C) Evolution of SWCNT stripe alignment due to the uneven deformation of pores in valleys and ridges. Figure reproduced from [1].

membrane would lead to a significant variation in the conditions required for alignment, but in fact, SWCNTs on all imprinted membranes were aligned, regardless of the mass or volume rate used. An SEM image of the resulting SWCNT film for 600 nm grooves is shown in Figure 3.11 (A) with all groove spacings and applied forces shown in Figure A.19. The corresponding cross polarized microscopy images are shown in Figure 3.11 (B). Poor replication of the shim at applied forces of 8 kN and 16 kN can be seen in regions with less variation in the contrast between bright (45°) and dark (0°) positions. However, in areas with high deformation it was possible to find regions with incomplete coverage of SWCNTs, such as the 600 nm line spacing imprinted at 16 kN, Figure 3.11 (C). It can be seen that SWCNTs first align along the edge of a pattern and then those SWCNTs arriving later align to these until a ridge is fully covered. Contrary to an un-stamped membrane this alignment process now involves the assembly of individual SWCNTs.

3.7. Two-Dimensional Order Parameter of Axial Aligned EA-SWCNTs

The extent of alignment for each parallel aligned case, encompassing the films with and without an axial imprinted pattern, was evaluated by the S_{2D} order parameter using Raman spectroscopy and the approach of Zamora-Ledezma *et al.* [41, 110] This requires precise knowledge of the dichroic ratio Δ , which was obtained from absorption

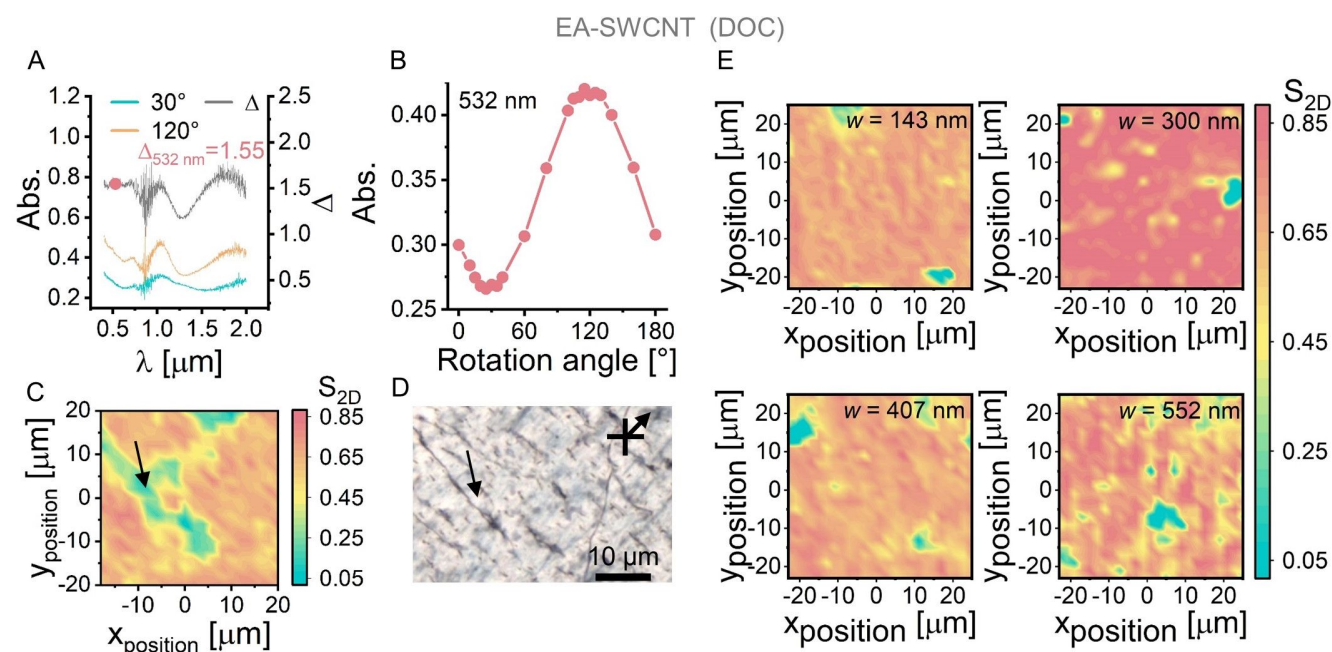


Figure 3.12.: (A) Measurement of the dichroic ratio of the sample shown in Figure 3.8 (D). (B) Angular dependence of the absorbance at 532 nm used to generate the Raman maps. (C) S_{2D} map of globally aligned film on an untextured membrane and (D) the corresponding cross-polarized light microscopy image in the bright position (45°) of a transferred film (silicon substrate). The black arrow indicates the position of a grain boundary. (E) S_{2D} maps of films on a 12 kN hot embossed membrane shown in Figure 3.11 (D) at various groove spacings. Figure reproduced from [1].

spectra (400 nm – 2400 nm) of the globally aligned film shown in Figure 3.8 (D) and (E). In order to measure it in transmission, part of the film was transferred to a glass substrate, which was then measured at intervals of 15° with linear polarized light, Figure 3.12 (A). Close to the absorption minima and maxima, finer intervals of 5° were used and the maximum was divided by the minimum to obtain the dichroic ratio, Figure 3.12 (B). As expected, the positions of the maximum and minimum were offset by 90° to each other. Since the Raman laser had a wavelength of 532 nm, a dichroic ratio of $\Delta_{UV532\text{ nm}} = 1.55$ has been chosen for further calculations of the order parameter. The dichroic ratio was additionally measured with an optical power meter and a polarizer in the Raman setup used and this afforded a value of $\Delta_{PM532\text{ nm}} = 1.52$. The additional Raman intensities (I_{HH} , I_{HV} , I_{VV} and I_{VH}) are shown in Figure A.20 and these allowed for 2D Raman maps ($1520\ \mu\text{m}^2$) of the S_{2D} parameter to be generated. For the un-textured surfaces, the disordered grain boundaries are clearly visible as regions of low S_{2D} , Figure 3.12 (C)

and the S_{2D} order parameter reached 0.78 inside the grains. For comparison, a cross polarized microscopy image of a grain boundary on the same film is shown in Figure 3.12 (D). For the textured surfaces a more uniform S_{2D} map was obtained, which did not show the presence of grains. The small misaligned regions are a result of poor shim replication as seen by AFM in Figure A.17. The highest alignment was measured ($S_{2D} = 0.85$) on a spacing of 300 nm. Interestingly the 150 nm grooves did not show a further increase in alignment. This might be due to the bundles of SWCNTs forming during filtration, getting too large for the grooves present in the membrane or the imprint depth of the smallest grooves not being deep enough (≈ 4.5 nm), as they could only fit less than four SWCNTs.

3.8. Radial Alignment of Unsorted EA-SWCNTs via Hot-Embossing

Similar to the axial shims, their radial counterparts followed the same procedure of electron beam lithography in conjunction with polymer masks and subsequent electroforming of the custom nickel shims. 3.14. Unlike the axial patterns, which have already been used in some shape or form by Fröhlich and Komatsu *et al.* [139, 225] for surface modifications of membranes, radial ones have not been used, yet. So they will be discussed in the following section in greater detail compared to their axial counterparts. A schematic of each and corresponding AFM topographies are shown in Figure 3.13. The three tested designs will hereafter be referred to as the (A) spoke (SP), (B) cake (CA) and (C) herringbone (HB) patterns, according to their basic building blocks. All shims had an unstructured circular region at their centre with a diameter of 2 mm and an outer perimeter of 22 mm. The outer perimeter was set to match the custom microfluidic setup and afforded a total embossed area of 3.81 cm². [1] As the name suggests the SP pattern consisted of 5236 spokes extending radially from the centre. These had a constant width and pitch of $w_{SP\ shim\ int.} = 600$ nm on the interior (int.) of the shim. Upon extension towards the exterior (ext.), the spoke width was held constant ($w_{SP\ shim\ ext.} = 560$ nm) and the pitch was linearly increased to ≈ 13 μ m. A variation in height of 10 nm was found between the interior ($h_{SP\ shim\ int.} = 170$ nm) and exterior ($h_{SP\ shim\ ext.} = 180$ nm) of the shim, due to inhomogeneities in the resist height during master fabrication via spin coating. The CA pattern was similar to the SP pattern except that now the width and pitch of the bars was increased linearly from the center to the outer perimeter of the shim. Once again, there were 5236 bars in total and the width and pitch of these was $w_{CA\ shim\ int.} = 560$ nm at the interior. On the exterior of the shim the pitch and width of the spokes was $w_{CA\ shim\ ext.} = 6.8$ μ m. No variation in height was found between the interior and exterior of the shim ($h_{CA\ shim\ int.} = h_{CA\ shim\ ext.} = 160$ nm). The HB pattern was obtained by exchanging the straight spokes of the SP pattern with herringbones consisting of bars orientated 45° to the radial direction and rotated by 90° every 1.45 μ m. The number of bars was consistent with the other shims and the width of these was held constant between the interior and exterior of the shim ($w_{HB\ shim\ int.} = 1.4$ μ m, $w_{HB\ shim\ ext.} = 1.35$ μ m). Like the SP pattern, a variation in height of 10 nm was found between the interior ($h_{HB\ shim\ int.} = 155$ nm) and exterior ($h_{HB\ shim\ ext.} = 165$ nm) of the shim. Despite a change in the applied loading used (20 kN), the hot-embossing procedure was identical to the procedure described in section 3.6, that was used to imprint the axial patterns. Forces $\gg 20$ kN resulted in the

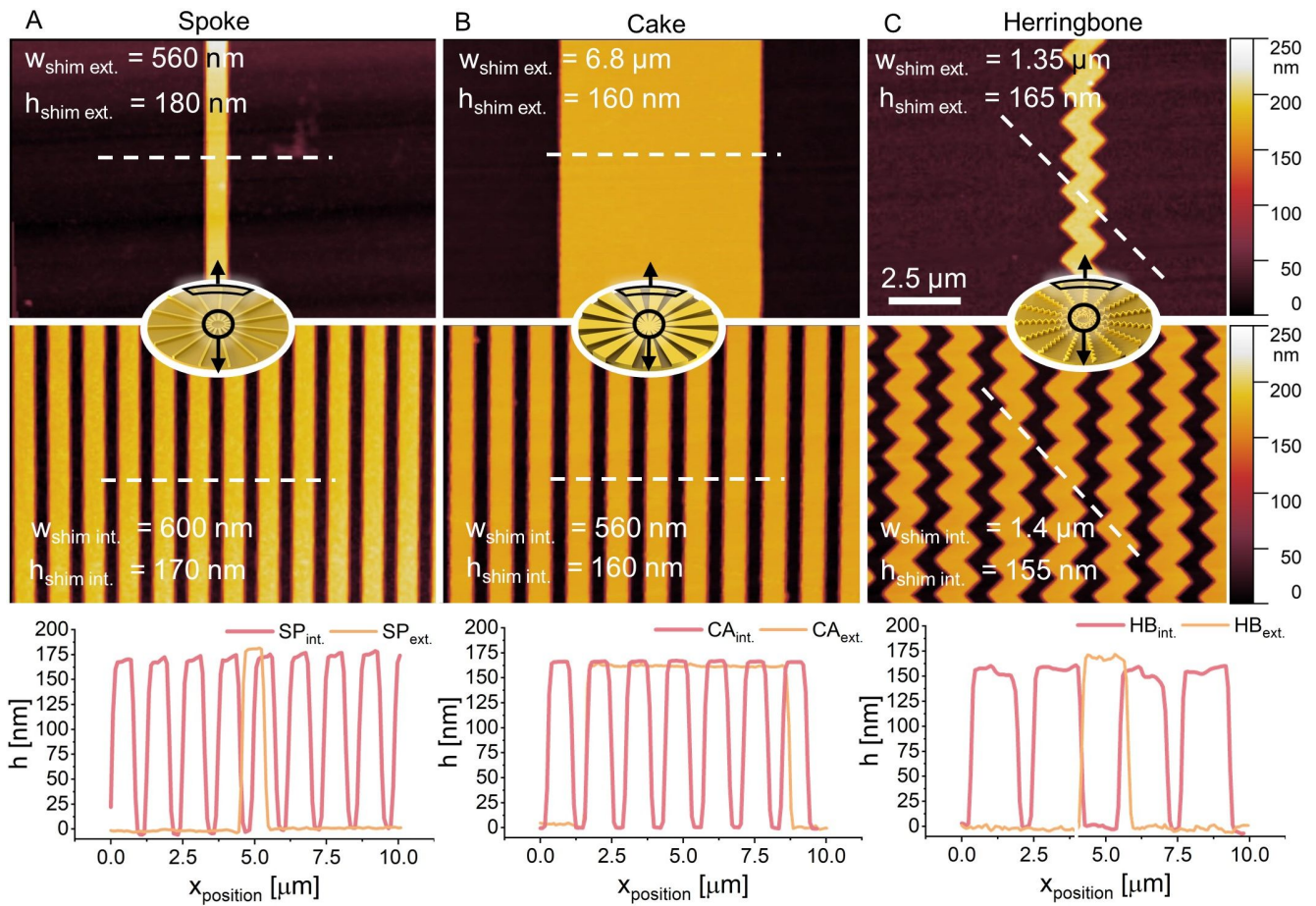


Figure 3.13.: Schematics and AFM topographies of the shim structures used for hot-embossing of the PCTE membranes. These had a (A) spoke (SP), (B) cake (CA) and (C) herringbone (HB) pattern, which are represented by images taken at the interior and exterior of the shim and corresponding line scans along the white dashed lines, used to determine the average width and height of those structures. Figure reproduced from [2].

membranes appearing transparent to the eye in some locations and were accompanied by a closure of the pores. Consequently, when SWCNTs were filtered through these membranes only the pores in the less deformed regions were open and a discontinuous SWCNT film was obtained. Lower loadings (16 kN) led to partial replication of the patterns in the membrane. AFM-Topographies membranes after hot-embossing are shown in Figure 3.14. In all cases it can be seen that the shims were reproduced laterally with an accuracy of ± 45 nm, which is in agreement with their axial counterparts (± 50 nm, cF. Figure 3.10(C)). The cake patterned shim was found to impart an even imprint on the membrane with a ≈ 10 nm difference between the height of the structures on the interior ($h_{CA HE int.} = 22$ nm) compared to the exterior ($h_{CA HE ext.} = 35$ nm) of the membrane. For the spoke and herringbone pattern the structures were found to be significantly taller on the exterior ($h_{SP HE ext.} = 145$ nm, $h_{HB HE ext.} = 145$ nm) of the membrane compared to the interior ($h_{SP HE int.} = 20$ nm, $h_{HB HE int.} = 70$ nm). This is due to the higher density of structures in the center compared to the outer circumference and thus lower deformation in the middle compared

to the circumference. On the contrary, for the cake pattern the spacing and width of the spokes are equal across the whole shim and this leads to a constant deformation. Comparing the height of the imprints to the shim height ($h_{SP\ shim\ avg} = 175\text{ nm}$, $h_{HB\ shim\ avg} = 160\text{ nm}$), also indicates how higher applied forces lead to the entire shim surface contacting the membrane and a closure of additional pores.

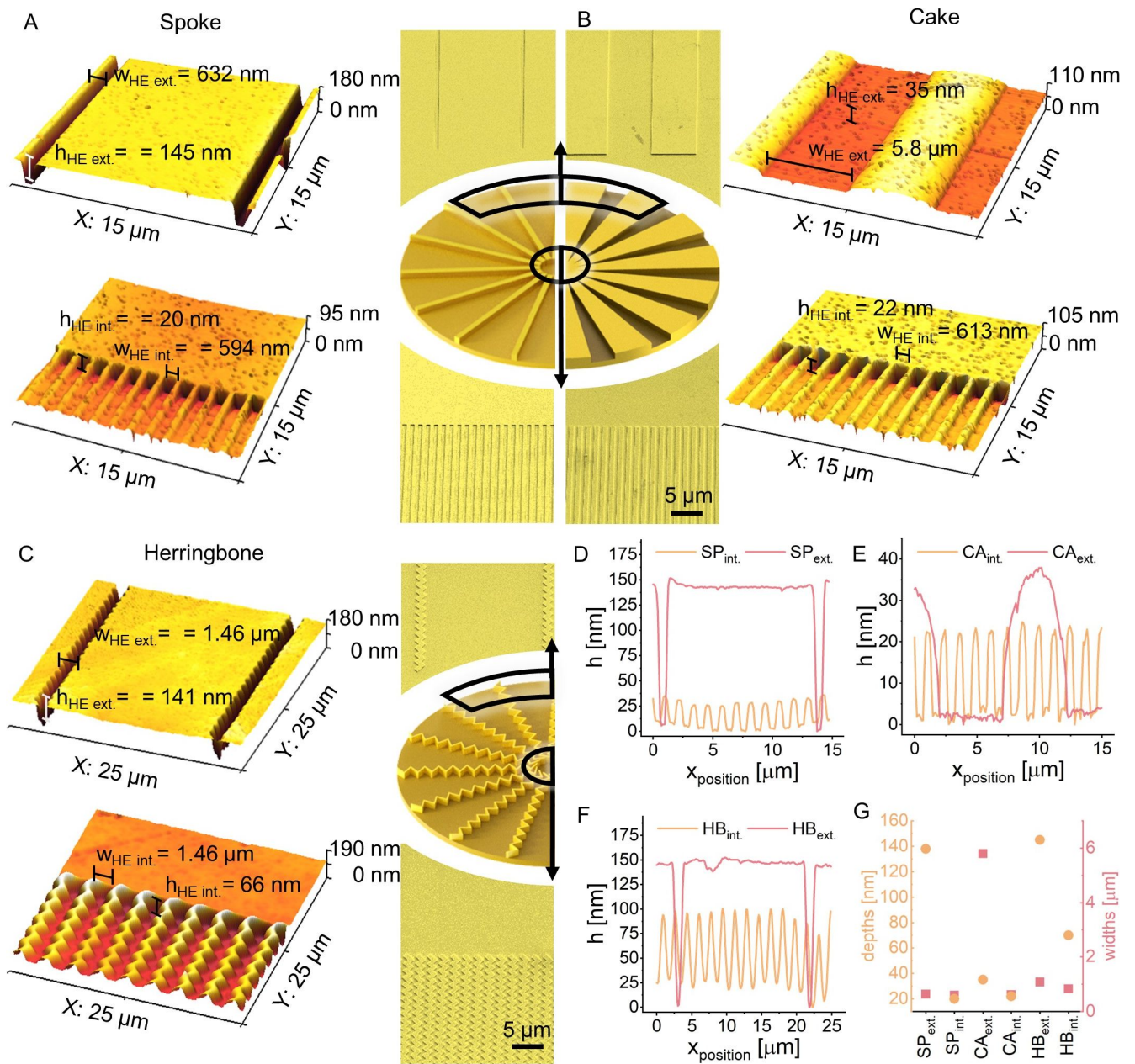


Figure 3.14.: Schematics of the shim structures used for hot-embossing. After embossing AFM and SEM were used to characterize the structure of the (A) spoke, (B) cake and (C) herringbone patterns in the PCTE membrane. The average width w and structure depth h depicted in the topographies and summed up in (G), were determined from the line scans shown in (D), (E) and (F). Figure reproduced from [2].

In order to warrant comparability with the experiments done with axial structures, the unsorted EA-SWCNTs were prepared by following the same protocols stated for the axial alignment, which meant that the dispersions used had a concentration of $8 \mu\text{g mL}^{-1}$ EA-SWCNTs dispersed in 0.04 wt% DOC. Furthermore the filtration parameters were consistent with those used previously for the uni-axially structured membranes; 1.25 mL of the diluted SWCNT dispersion was filtered at $100 \mu\text{L min}^{-1}$ followed by a pushing step of $500 \mu\text{L min}^{-1}$ for the last 0.75 mL.[1] The measured filtration resistance R_{cp+b} , showed an instantaneous linear increase over the volume filtered for all membranes except the ones imprinted with the HB pattern, Figure A.21. A linear increase in filtration resistance is consistent with cake filtration without an initial concentration polarization (CP) regime and can be interpreted as the SWCNTs not gathering above the membrane, but rather being directly adsorbed at the edges of the hot-embossed patterns, which could also be observed for the axial patterns (cf. Figure 3.10 (G)) For the HB pattern, an intermediate blocking could be observed, which was also found on the pristine 80 nm membranes forming a globally aligned film (cf. Figure 3.8 (C)). After filtration, the SWCNT films were transferred to either glass substrates or flexible printed circuit boards (fPCBs). The latter allowed for SEM imaging and electrical characterization of the film. The films were imaged close to the ground contact in the center ($r = 1.3 \text{ mm}$) and the cake shaped channel contacts in the outer perimeter being another 2 mm further outwards. It can be seen in Figure 3.15, that the SP and CA pattern were well replicated by the SWCNTs at the center and circumference of the film. Additional higher magnified images are available in the Appendix, Figure A.22. And in fact, for the SP and CA-pattern, the SWCNT alignment followed the templates,

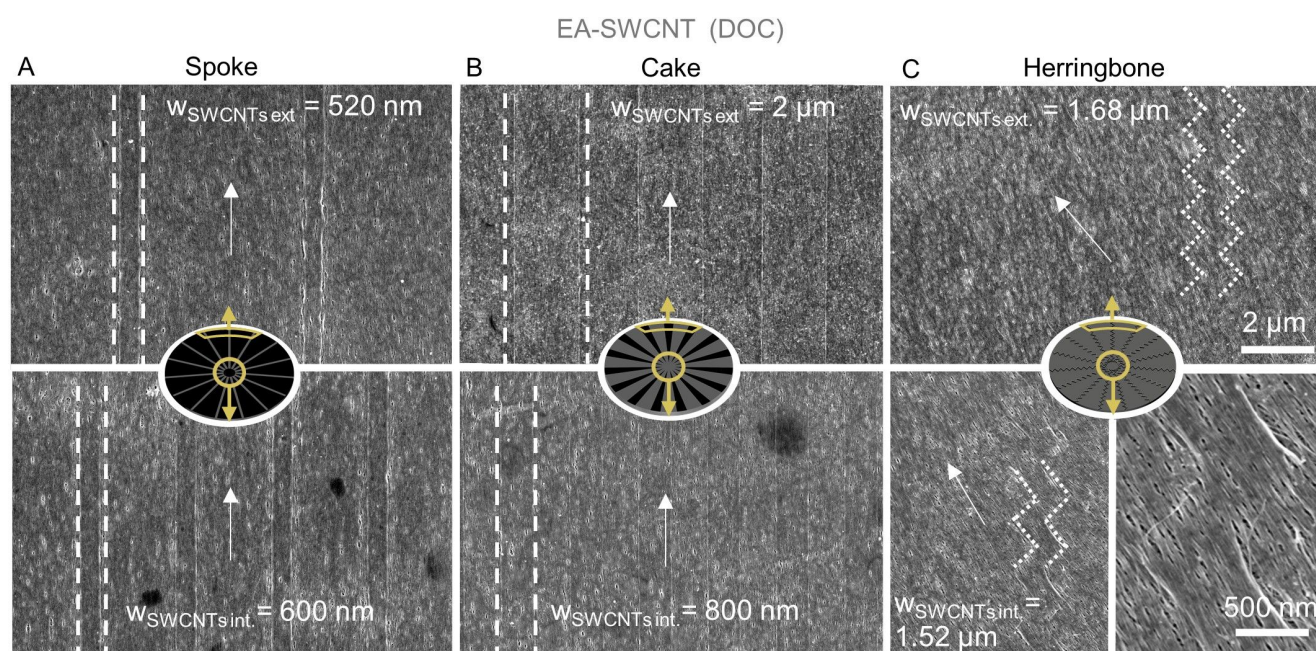


Figure 3.15.: Schematic representation and SEM images of unsorted EA-SWCNT (DOC) films transferred to a fPCB (Polyamide with gold contacts) made from membranes with (A) spoke (SP), (B) cake (CA) and (C) herringbone (HB) patterns. The alignment direction is indicated by an arrow to guide the eye. Figure reproduced from [2].

leading to a constant bar widths for the spokes pattern ($w_{SP \text{ SWCNTs } int.} = 600 \text{ nm}$, $w_{SP \text{ SWCNTs } ext.} = 520 \text{ nm}$)

and increasing bar widths for the cake pattern depending on the distance to the middle ($w_{CA\ SWCNTs\ int.} = 800\ \text{nm}$, $w_{CA\ SWCNTs\ ext.} = 2000\ \text{nm}$). For the HB pattern the SWCNTs did not mimic the pattern directly, but rather follow an average direction given by the alternating bars. Nevertheless, it was still possible to identify the original pattern due to a small height difference in the film. The HB pattern does thereby provide an insight into the limitations of the hot-embossing method for SWCNT alignment and the associated mechanism thereof as the SWCNTs ($l_{EA-SWCNTs\ unsorted} = 691 \pm 471\ \text{nm}$) are not able to mimic abrupt directional changes (90°) on a comparable length scale ($1.45\ \mu\text{m}$).

3.9. Characterization of Radial Aligned Films

To further characterize the radial alignment in the SP and CA films, scanning cross-polarized microscopy (SCPM) in reflectance was used to measure the films transferred to glass. Alternative to SEM, this enabled a macroscale characterization of the film by stitching multiple $5\times$ -magnified micrographs into a single image/map. Full maps were recorded under rotation of the SWCNT film in 10° intervals. Representative images for the CA film at 60° intervals are shown in Figure 3.16 (A). Two important observations can be made from the cross polarized images; (a) a flower-like light pattern of bright and dark regions is obtained and (b) this pattern remains invariant to sample rotation. The latter provides a confirmation of the homogeneity of the radial pattern and the former is a result of the changing SWCNT orientation relative to the polarization of the incident light. In order to analyze the observed light pattern, representative images of the cake and spoke films are evaluated by the accumulated intensity with respect to the film angle ϕ and the film radius r , displayed in Figure A.23. Thereby the film angle ϕ is starting at the 12 o'clock position and increases with a clockwise rotation, while the origin of the film radius r is placed at the center of the film and increases with the distance to the middle. The unaligned region in the middle of the film ($r < 1\ \text{mm}$) and the lesser aligned outer perimeter close to the filtration cylinder wall ($r > 7.5\ \text{mm}$) were excluded, resulting in the film angle ϕ resolved intensity plots shown in Figure 3.16 (B). The intensity distribution $I(\phi)$ can be compared to linear polarized light I_0 passing a linear polarizer grating at an angle ϕ and thus Malus law [197] can be used to derive $I = I_0 \cos^2 \phi \sin^2 \phi$ (derivation can be found in section 1.5.2, eq. 1.52 -1.54). The high intensities are thereby found at $\phi = 0 + n\frac{\pi}{2}$ and the low intensities at $\phi = \frac{\pi}{2} + n\frac{\pi}{2}$, for $n \in N$. To test this hypothesis, the intensity of the images is averaged over the radius for every film angle ϕ and the lowest value obtained is set to 0. The maximum value of the average intensity obtained over the radius is then set to 0.25, so it matches the maximum value of I that can be obtained for $I_0 = 1$, which would correspond to a perfect polarizer and the other values are then normalized accordingly. Fitting the formula to the averaged data yielded, $I_{0\ CA} = 0.82 \pm 0.02$ and $I_{0\ SP} = 0.76 \pm 0.02$, which could be considered as an indicator to assess large scale alignment of a film like the S_{2D} order parameter ranging from 0 to 1. Similar experiments were also performed in transmission with linearly polarized light. A schematic representation of the optical setup used to record those images can be found in Figure 2.4. A supercontinuum laser was used to produce an excitation wavelength of $650\ \text{nm}$, which was then guided through two convex, achromatic

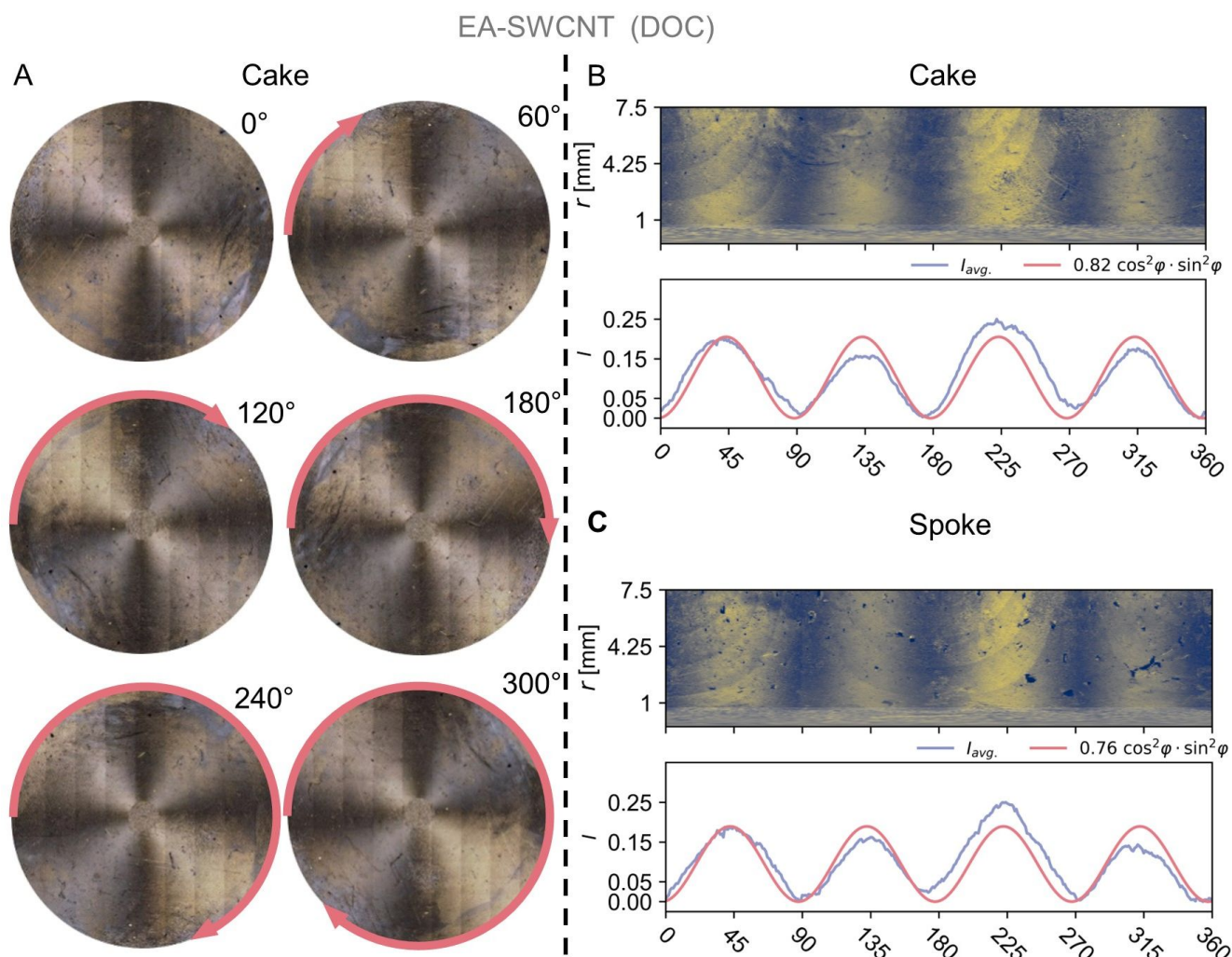


Figure 3.16.: (A) Scanning cross polarized microscopy of a unsorted EA-SWCNT (DOC) film created from the cake pattern at 60° intervals of sample rotation, showing the flower light pattern. (B) The accumulated intensity ignoring the unstructured center ($r < 1$ mm) as well as the lesser aligned outer region ($r > 7.5$ mm) for the (B) spoke and (C) cake patterns (cf. Figure A.23) could be fitted with $I = I_0 \cos^2 \phi \sin^2 \phi$ derived from Malu's law [197]. Figure reproduced from [2].

lenses to expand the beam to cover the area of the CNT film on a glass substrate. After transmission through the film, the light was then guided through two more achromatic lenses to shrink the beam so that it could be fully absorbed by a beam profiler. A cross-polarized measurement was performed by linearly polarizing the incident beam, transmitting it through the film, passing the transmitted beam through an analyzer that is polarized 90° to the incident beam, and finally recording the intensity. Once again, a flower pattern of bright and dark regions was obtained, Figure 3.17 (A). However, importantly, because this pattern also appears in transmission it indicates that there is a high level of SWCNT alignment within the film and not just on the upper-most surface as the film thickness is ≈ 60 nm given by the amount of SWCNTs used ($16 \mu\text{g}$). [1] The homogeneity of the SWCNT was further verified with the use of

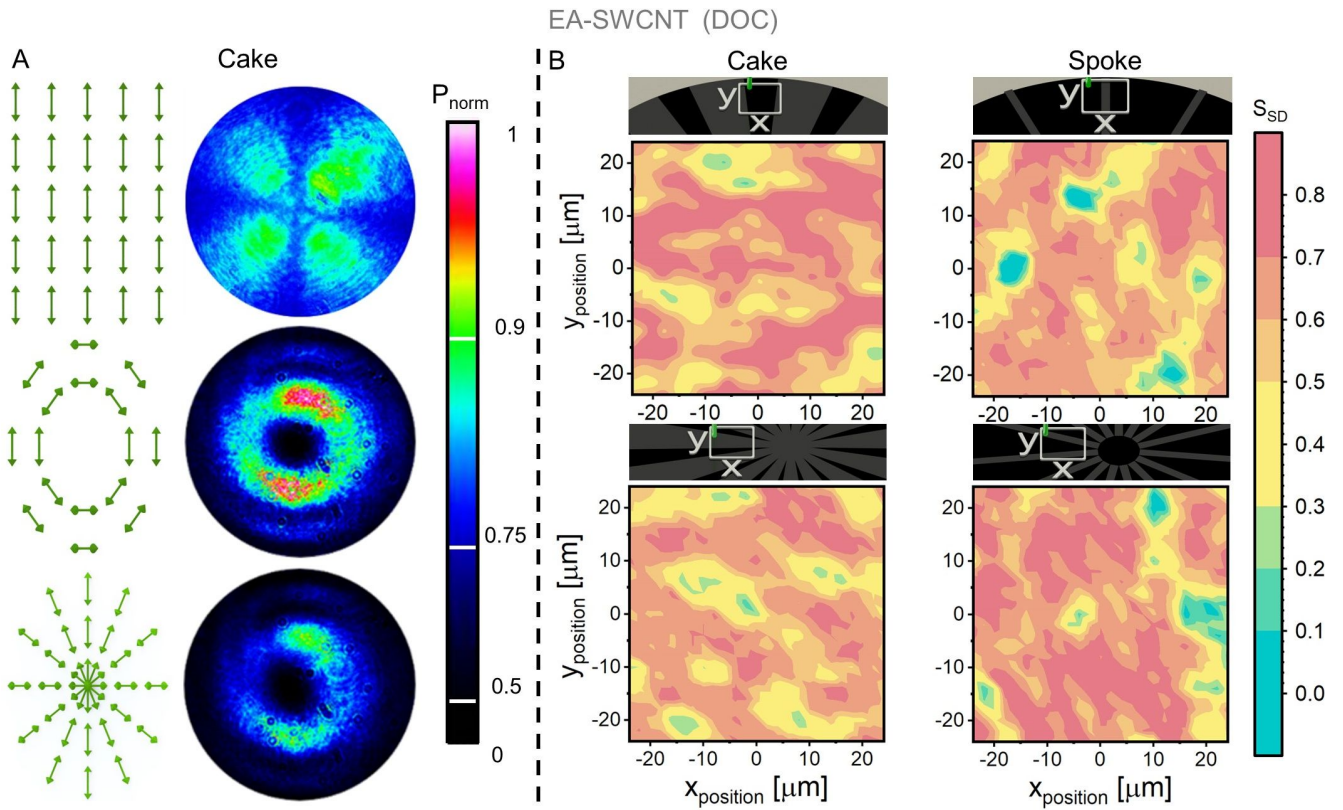


Figure 3.17.: (A) Laser transmittance measurements made with linear, azimuthal and radial polarized light and a CA patterned film. The linear polarization creates a flower like pattern similar to the CPM images shown above. On the contrary, for the latter polarizations the beam profiles do not change, but an increase in absorption can be observed for the radial polarization coinciding with the alignment of the unsorted EA-SWCNTs (DOC). (B) Raman mapping showing the order parameter S_{2D} measured with a 532 nm laser on the films interior (bottom) and exterior (top). Figure reproduced from [2].

azimuthal and radially polarized light fields and is depicted in Figure 3.17 (B) for a CA film and in Figure A.24 for a SP film. These measurements rely upon the difference in absorption cross section parallel (larger) and perpendicular (smaller) to the SWCNTs axis.[194] For azimuthal polarized light the electric field is perpendicular to the axis of the SWCNTs and for radially polarized light it is parallel. This leads to a difference in the transmitted intensity for the two different light fields for a laser power measured right before the films of 9.1 μW (Spoke pattern: 5.55 μW (azimuthal) vs 4.48 μW (radial); Cake pattern: 6.31 μW (azimuthal) vs. 5.41 μW (radial)). Once again, resonant Raman maps measured with a 532 nm laser excitation over an area of 576 μm^2 in the center and circumference of the film were used to evaluate the two dimensional alignment parameter S_{2D} , following the method of Zamora-Ledezma *et al.* [110], Figure 3.17 (C). The intensities of the G^+ mode ($\approx 1590 \pm 3 \text{ cm}^{-1}$) in the different polarization configurations (I_{HH} , I_{VV} and I_{VH}) can be found in Figure A.25 and Figure A.26. For the calculation of S_{2D} , the dichroic ratio of the unsorted EA-SWCNT $\Delta_{EA-SWCNT 532nm} = 1.55$ was used, that can be found in Figure 3.12. The S_{2D} value measured in the middle and perimeter of the films were 0.82 and 0.78 for the spoke pattern and 0.82 and 0.85

for the cake pattern, respectively. These values are comparable to those measured for the axial alignment with

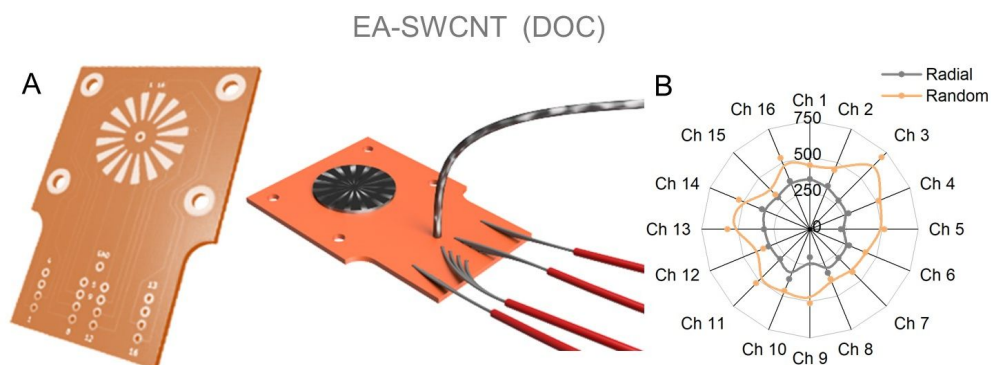


Figure 3.18.: (A) Schematic representation of the fPCB used to measure the resistance of the unsorted EA-SWCNTs (DOC). The distance between the ground pin located in the middle and the outer contact was 2.7 mm. (B) Resistances measured at each channel for a radially aligned and random SWCNT film. Figure reproduced from [2].

($S_{2D\ HE} = 0.85$) and without ($S_{2D} = 0.78$) the usage of hot-embossed membrane (cF. Figure 3.12), as well as order parameters reported in the literature ($S_{3D\ He\ et\ al.} = 0.96$ [40]), $S_{2D\ Walker\ et\ al.} = 0.9$) These measurements also reveal that the quality of alignment is similar for both films and that there is little variation between the centre and perimeter of the film. Towards the use of radially aligned SWCNT films in electronic devices as discussed in section 1.3.1, two terminal electrical resistance measurements of a cake patterned film were compared to an unaligned, random film. These measurements were made at sixteen equally spaced channels around the circumference of the film on a fPCB, Figure 3.18 (A). A common ground pin was the middle of the fPCB and slices were made with a sharp ceramic needle to separate the different elements, which were at an angle of 22.5° to their neighbours. The serial resistances stemming from a custom measurement setup comprising of an Arduino UNO, a multiplexer board and a multimeter were determined via a $100\ \Omega$ reference resistance to be $\approx 60\ \Omega$ and was thus subtracted from the measured values. The random film was produced with identical mass, concentration and filtration parameters as its aligned counterparts, but with an unmodified membrane. As expected, it can be seen that the average resistance of the radially aligned film is lower compared to its disordered counterpart $304 \pm 49\ \Omega$ vs. $478 \pm 93\ \Omega$. Furthermore the radial aligned film also had a lower standard deviation indicating an improvement in consistency in resistance and thus leading to a more circular shape of resistances found at various angles of the film.

3.10. Length Sorting of EA- and CoMoCat-SWCNTs

After investigating the influence of membrane modifications on the alignment, this sections focuses on the constitution of the SWCNTs and thereby on the length and diameter in particular. A total of 12 fractions of sufficient concentration were obtained from the SEC column and alternate fractions were used in filtration experiments to minimize the length overlap. These were labelled A2, A4, A6 and A10 for the EA-SWCNTs. The average length of each was determined

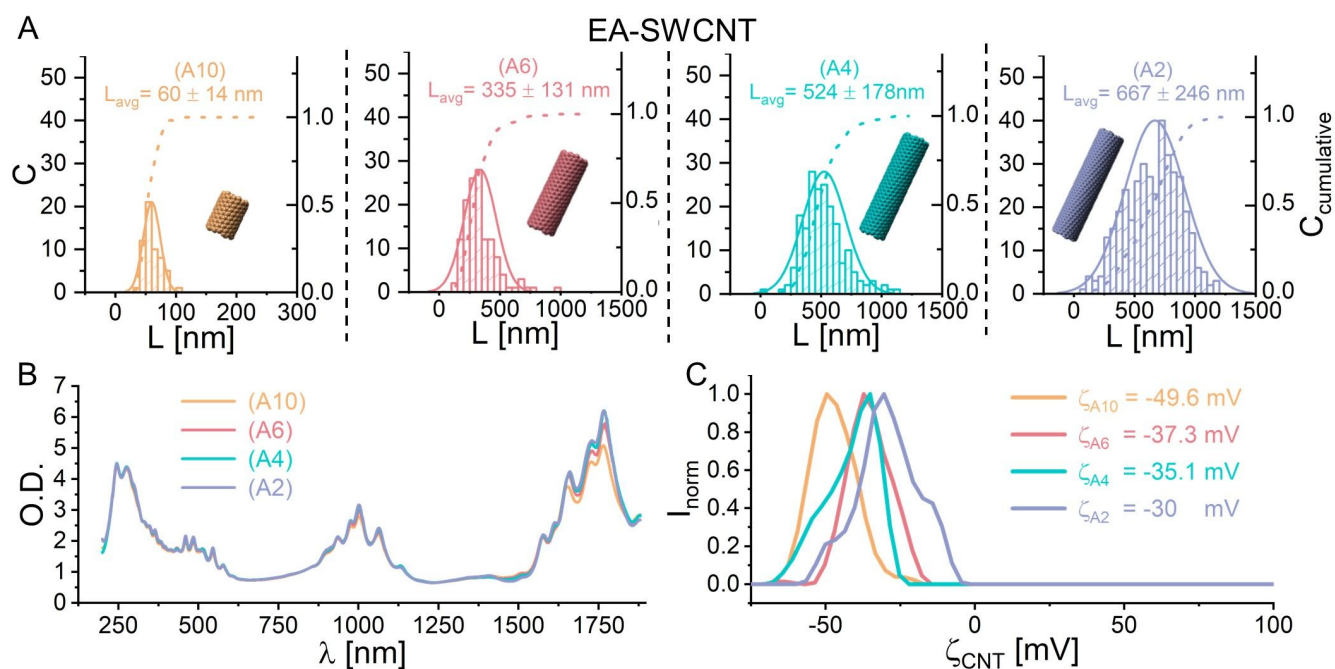


Figure 3.19.: (A) Length determination of the EA-SWCNT fractions by AFM analysis of individualized SWCNTs on a silicon wafer. (B) Absorption spectra of the EA-SWCNT fractions. (C) Zeta potential ζ_{SWCNT} measurements at a concentration of $8 \mu\text{g mL}^{-1}$ SWCNTs and 0.04 wt% DOC. Figure reproduced from [3].

by AFM, Figure 3.19 (A). As expected for the used sorting method (SEC), the average SWCNT length L_{avg} increased with decreasing fraction number. The average lengths of the EA-SWCNT fractions were A2: 667 ± 246 nm, A4: 524 ± 178 nm, A6: 335 ± 131 nm and A10: 60 ± 14 nm and there were no significant differences in the optical spectrum between each fraction as shown in Figure 3.19 (B). These length distributions are significantly narrower than any used in previous aligned filtration studies, [40, 41] which is also true for the unsorted EA-SWCNTs used before (cF. Figure 3.2, $L_{EA-SWCNT} = 691 \pm 471$ nm). The high degree of semiconducting species purity and lack of impurities in the fractions used are also reflected in the clearly distinguishable SWCNT optical transitions and the very low background absorption of the absorbance spectra. The concentration of each fraction was evaluated as described previously [1] using the absorbance of the π -plasmon peak after dilution by a factor of 10 with deionized water (Figure A.27). Again, each fraction was adjusted to a SWCNT concentration of $8 \mu\text{g mL}^{-1}$, dispersed in 0.04 wt% DOC and the zeta potential measured, Figure 3.19 (C). The shorter SWCNTs were reported by the instrument to be slightly more charged than the longer SWCNTs (A10: -49.6 mV vs. A2: -30 mV). This could be interpreted as a tendency of the surfactant to more densely cover shorter SWCNTs, however, the observed variation may also be due to deviations of the SWCNT sample from the geometric considerations embedded in the instrument's implementation of the Smoluchowski equation. Both the embedded consideration of the rod-shaped SWCNTs as spheres and the relative scale of the Debye length, ≈ 10 nm for a 1 mmol L^{-1} symmetric electrolyte, [166] to the diameter of the SWCNT plus its surfactant shell could affect the measurement accuracy. An increase in SWCNT length will make the geometrical deviation from a sphere

larger and the values reported for the earlier fractions less plausible. Nevertheless it is interesting to compare the zeta potential measured for the raw, unsorted EA-SWCNTs used before (cF. Figure 3.2, -15.8 mV) to any of the fractions after ATPE/SEC separation. This suggests that the final zeta potential of the SWCNTs is in fact dependent on the processing steps applied. The same procedure was repeated using CoMoCAT-SWCNTs, which were labeled

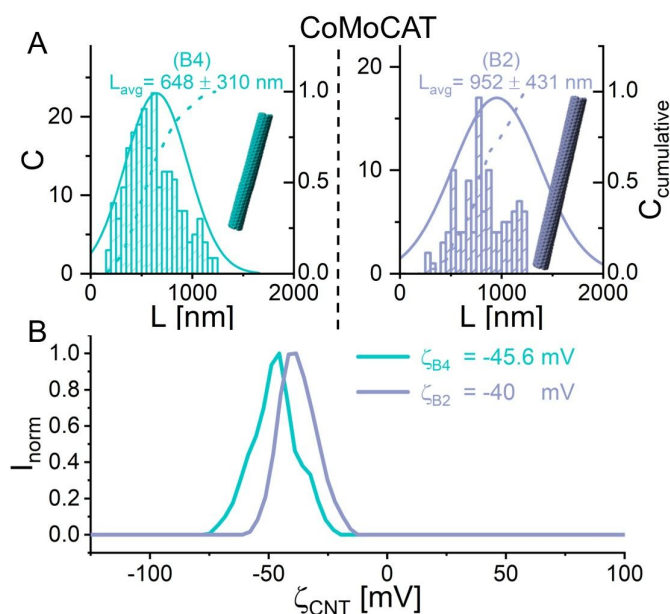


Figure 3.20.: Average length of the CoMoCAT fractions determined from (A) atomic force microscopy (AFM) topographies and (B) Zeta potential of the fractions dispersed in 0.04 wt% DOC and at a SWCNT concentration of $8 \mu\text{g mL}^{-1}$. Figure reproduced from [3].

B2 (952 ± 431 nm) and B4 (648 ± 310 nm). AFM and Zeta-Potential measurements are shown in Figure 3.20 The measured zeta potentials are more comparable to the shorter SWCNTs, which could be attributed to a lower surface coverage of the surfactants, due to the higher surface curvature, as the SWCNTs only have a diameter of $d_t \approx 0.78$ nm. However, in the experiments shown in the next sections the EA-SWCNTs will be discussed first.

3.11. Filtration of Length-Sorted EA-SWCNTs

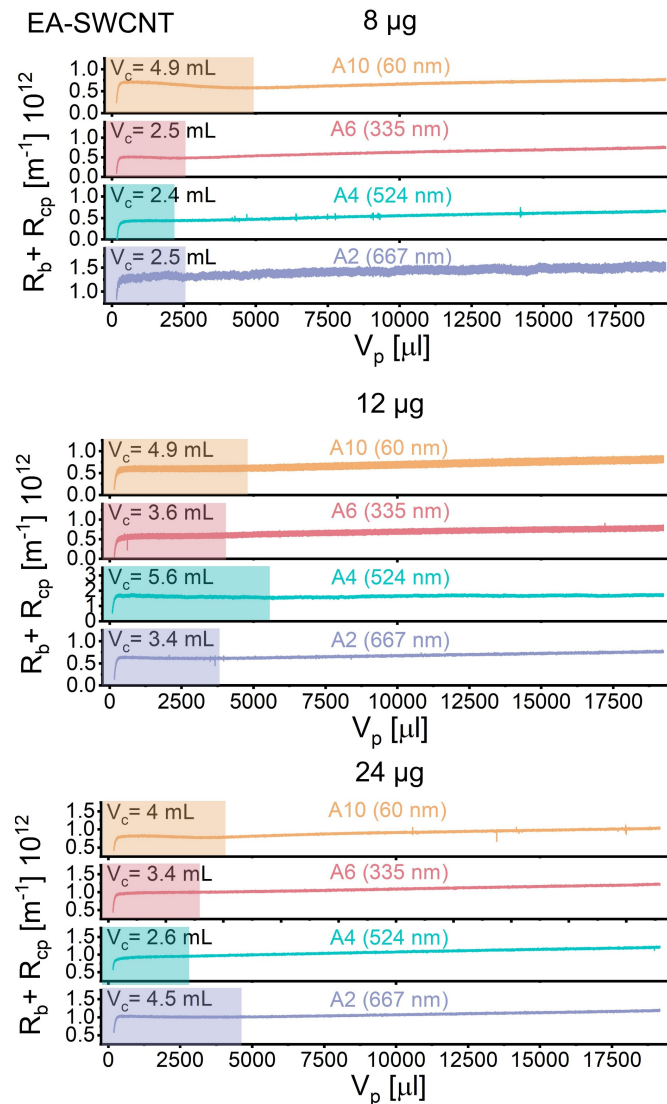


Figure 3.21.: Evolution of the filtration resistance, which is the sum of the blocking resistance (R_b) (the accumulation of mass on the membrane) and resistance from concentration polarization (R_{cp}), obtained by subtracting the membrane resistance $R_m = 2.43 \times 10^{12} \text{ m}^{-1}$ [1] from the total resistance (R_{tot}) as measured during the slow filtration step ($\dot{v} = 100 \mu\text{L min}^{-1}$) for total SWCNT masses of 8 μg , 12 μg and 24 μg . Each mass was dispersed in 20 mL of H_2O . Figure reproduced from [3].

SWCNT films from each fraction were prepared with the custom-made microfluidic dead-end filtration setup described in detail in the method section (cF. Figure 2.1). For the unsorted EA-SWCNTs the total mass of SWCNTs filtered was shown to be an important parameter to achieve global alignment (section 3.5) and so films containing 8 μg , 12 μg and 24 μg SWCNTs deposited onto a membrane 80 nm were made for each length fraction.

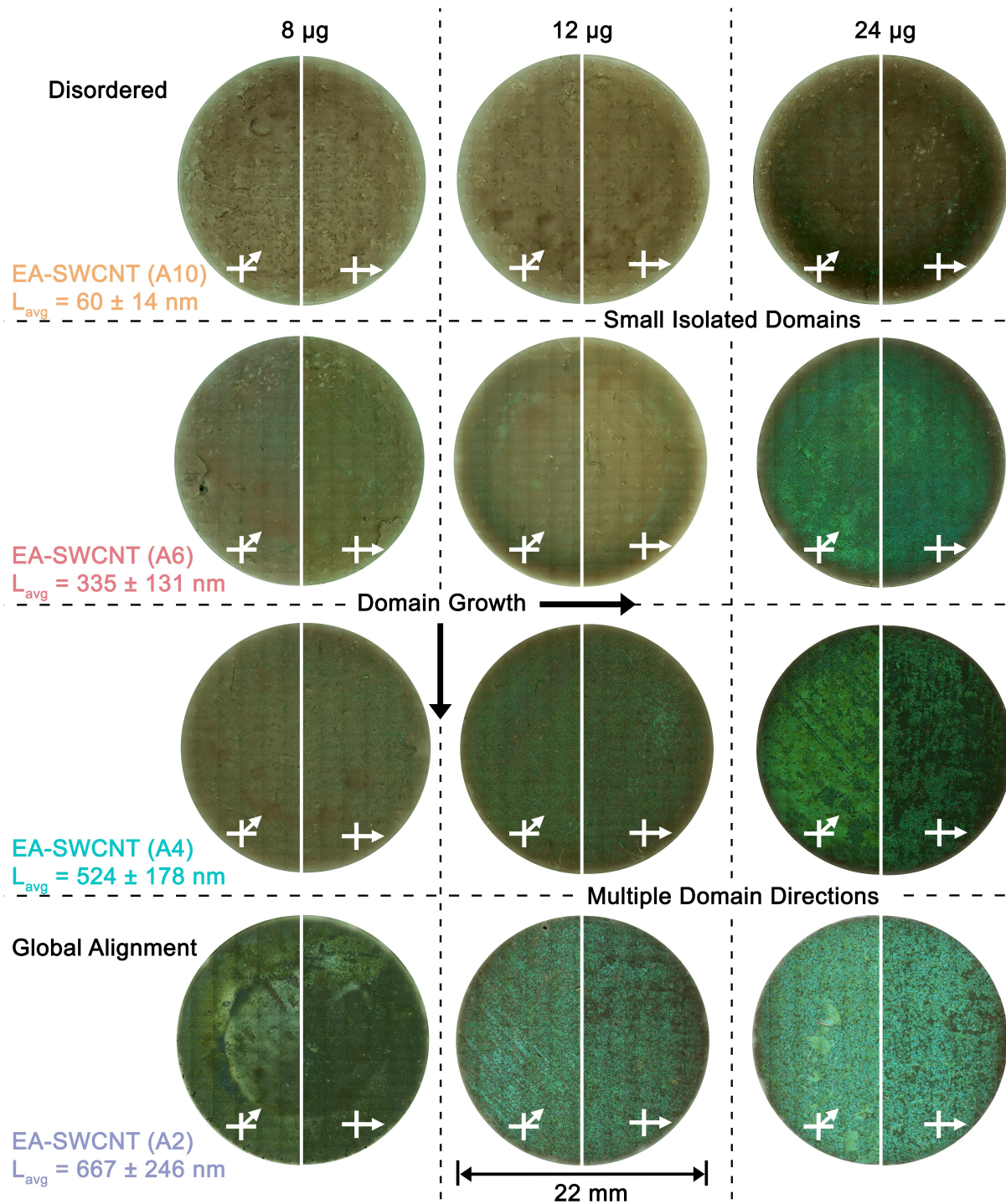


Figure 3.22.: Cross polarized microscopy of one half of an EA-SWCNT film from the length fractions A10 – A2 in the bright (45°) and dark (0°) orientation. Images were recorded with the SWCNT film on the PCTE membrane. Figure reproduced from [3].

Similar to the unsorted EA-SWCNTs, for each fraction a highly concentrated stock solution was diluted to an intermediate solution with $8 \mu\text{g mL}^{-1}$ SWCNTs (0.04 wt% DOC), and 1 mL, 1.5 mL or 3 mL of that intermediate solution were diluted once more to a final volume of 20 mL with deionized water, leading to the SWCNT/DOC concentrations found in the Appendix, Figure A.27. The filtration consisted of a slow flow ($100 \mu\text{L min}^{-1}$) step for a majority (19.25 mL) of the volume followed by a fast filtration ($500 \mu\text{L min}^{-1}$) step during the final 750 μL , which is similar to the optimal conditions found for the unsorted EA-SWCNTs in Figure 3.8. The filtration resistance ($R_b + R_{cp} = R_{tot} - R_m$ with $R_m = 2.43 \times 10^{12} \text{ m}^{-1}$, see section 3.1), is plotted in Figure 3.21 for 8, 12 and 24 μg . In the previous section 3.3 it was shown that the optimal slow volume rate could be identified by a minimal CP regime, which corresponds to the initial volume during which the carbon nanotubes are floating above the membrane and have not yet caused an increase in the filtration resistance. Despite a variation of both SWCNT mass and length, no obvious impact on the concentration polarization regime could be observed. This observation is potentially due to the use of highly dilute SWCNT solutions, or because the effect is greatest for a changes in the volume rate, which was consistent for all filtrations done with length sorted material ($100 \mu\text{L min}^{-1}$). The resulting SWCNT films were imaged by scanning cross-polarized microscopy, with automatic stitching multiple cross-polarized images ($5\times$ magnification) such that the complete 22 mm diameter circle of each SWCNT film is mapped. Bright (SWCNT alignment direction at 45° to the analyzer polarization) and dark (0° or 90° to the analyzer polarization) positions are shown. The alignment vectors were manually identified by rotating the sample and visually maximizing the intensity at the brightest position close to the center for each film, and then rotating the film by 45° from that position for the dark image. If no clear contrast difference could be found (due to a lack of SWCNT alignment), then an arbitrary bright position was chosen and the dark position was defined to be 45° offset from that. One half of the SWCNT film is shown for each orientation in Figure 3.22 and full film images can be found in Figure A.28. Additionally, representative $5\times$ magnification images of all films are shown in Figures A.29 – A.31. A portion of each film was also transferred to a silicon substrate [41] such that the side of the film facing the membrane during filtration could be imaged, Figures A.32 – A.34. A comparison of both sides of the film (removing the membrane)[41] suggests that the morphology of the SWCNT film is consistent throughout its entire thickness. Machine vision was used to quantify the SWCNT domain size in each of the films.[1] Examples of the detected domains are reported in Figure 3.23 (A). Depending on the sample, one of two modes of detection were used, if the domain size was significantly smaller than the image size and full-sized domains could be identified in the image, then the domains were measured directly (i.e., 12 μg film of A2, $A_{avg A2 12 \mu\text{g}} = 2009 \mu\text{m}^2 \pm 12\ 344 \mu\text{m}^2$). If the image contained large domains that exceeded the image-area (i.e., 8 μg film of A2) then the software would detect the grain-boundaries and subtract this area from the total image area ($A_{A2 8 \mu\text{g}} = 2.329 \text{ mm}^2$). The cross-polarized images and the detected domains or grain boundaries are shown in Figures A.35 – A.37. Figure 3.23 (B) plots the grain size distribution as a histogram along with the corresponding normal distribution, from which the average domain size and respective standard deviation were calculated in Figure 3.23 (C). For the A10 ($L_{avg} = 60 \text{ nm} \pm 14 \text{ nm}$) fraction, small isolated SWCNT domains (bright spots in cross-polarized microscopy) can clearly be seen for the 24 μg ($A_{avg A10 24 \mu\text{g}} = 229 \mu\text{m}^2 \pm 643 \mu\text{m}^2$) film, whereas for 8 μg ($A_{avg A10 8 \mu\text{g}} = 184 \mu\text{m}^2 \pm 249 \mu\text{m}^2$) film and 12 μg ($A_{avg A10 12 \mu\text{g}} = 194 \mu\text{m}^2 \pm 320 \mu\text{m}^2$)

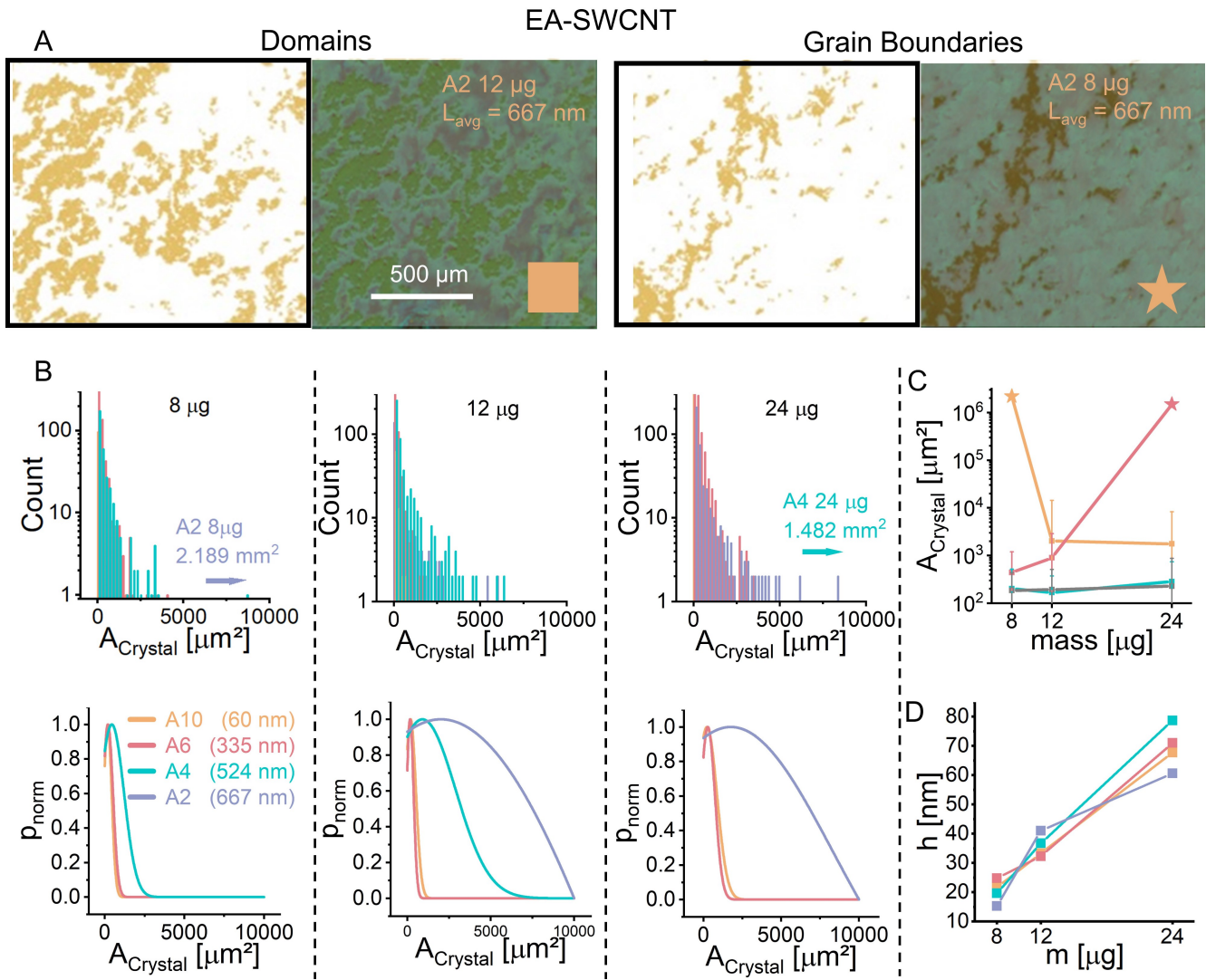


Figure 3.23.: (A) The two machine vision techniques used to characterize the domain size. Small domains were measured directly (A2, 12 μg , box) or indirectly by subtracting the grain boundary from the entire pixels in the image (A2, 8 μg , star). (B) Histograms and a normal distribution of the domain-sizes which are summarized in (C). (D) Film height measured by AFM. Figure reproduced from [3].

they were most often much smaller and barely visible. These bright spots correspond to small locally aligned domains of SWCNTs, however, because they can be seen in both the “bright” and “dark” cross-polarized microscopy images they do not have a common alignment direction. For the A6 ($L_{\text{avg}} = 335 \text{ nm} \pm 131 \text{ nm}$) film, these small SWCNT domains are now visible for all masses and in the case of the 24 μg film it is particularly evident that the domain size ($A_{\text{avg A6 24}\mu\text{g}} = 284 \mu\text{m}^2 \pm 456 \mu\text{m}^2$) has increased relative to A10. A slight increase in domain size ($A_{\text{avg A6 12}\mu\text{g}} = 168 \mu\text{m}^2 \pm 205 \mu\text{m}^2$, $A_{\text{avg A6 24}\mu\text{g}} = 284 \mu\text{m}^2 \pm 456 \mu\text{m}^2$) is also observed between the 12 μg and 24 μg films of A6. The A4 ($L_{\text{avg}} = 524 \text{ nm} \pm 178 \text{ nm}$) film follows the same trend ($A_{\text{avg A4 8}\mu\text{g}} = 441 \mu\text{m}^2 \pm 763 \mu\text{m}^2$, $A_{\text{avg A4 12}\mu\text{g}} = 904 \mu\text{m}^2 \pm 1992 \mu\text{m}^2$) and has domains that are again larger than A6 but in the case of 24 μg film

these become connected and have a common alignment direction. This is evidenced by a clear contrast difference between the bright and dark cross-polarized light images shown in Figure A.31. However, despite the area of the connected domains being large ($A_{avg\ A4\ 24\ \mu g} = 1.482\ \text{mm}^2$) it can be seen in Figure 3.22 and Figure A.28, that multiple alignment directions still exist across the entire film. As the hot-embossing experiments (section 3.6 and 3.8) show, it can be argued, that the constitution of the membranes (groove density and directional charges) play an important role for a successful global alignment, which has also been stated by other researchers.[41, 134, 226] Global alignment might be possible using this fraction and film mass loading, but unfortunately the sample mass needed to test this hypothesis was not available. Even larger connected areas can be seen for the A2 ($L_{avg} = 667\ \text{nm} \pm 246\ \text{nm}$) dispersion for the $8\ \mu\text{g}$ film, but in this case these areas now encompass most of the membrane, and the sample was considered globally aligned. An increase in the deposited mass of A2 led to a more disordered film. While the domain size ($A_{avg\ A2\ 12\ \mu g} = 2009\ \mu\text{m}^2 \pm 12\ 344\ \mu\text{m}^2$, $A_{avg\ A2\ 24\ \mu g} = 1758\ \mu\text{m}^2 \pm 456\ \mu\text{m}^2$) remained almost constant, and even slightly decreased, one can suspect that the amount of domains increased to a point where the combined domain area surpassed the area of the membrane, eventually disturbing the global order. The same phenomenon has been observed above with unsorted EA-SWCNT (cf. Figure 3.8) and increases in mass from $24\ \mu\text{g}$ to $32\ \mu\text{g}$. [1] As a next step of characterization, film thicknesses measured using AFM topographies (Figure A.38) were determined after film transfer to Si wafers and are shown in Figure 3.23 (D). The values were evaluated again by the step height between the film and substrate, Figure A.39. The smaller length sorted fractions (A10, A6 and A4) show a linear relationship between film height and mass, while A2 appears to become compacted with an increase in mass around $8\ \mu\text{g}$ total deposited mass. This is consistent to the unsorted EA-SWCNTs dispersed in DOC and CTAB shown in Figure 3.8 (B), which also compacted at their optimal mass ($24\ \mu\text{g}$). Thus it can be speculated, that larger masses would be needed for A4 to show the plateau, as a $24\ \mu\text{g}$ film might be sufficient for global alignment. Scanning electron microscopy (SEM) images of the films transferred to Si wafers on small scales ($2 \times 2\ \mu\text{m}^2$) corroborate that A10 and A6 predominately form smaller domains or that they are even completely disordered, Figure A.40. Images taken from films of A4 and A2 are considerably more difficult to interpret. On the length scale measured by an SEM, each of these films appear to be highly aligned. Indeed, this highlights how misleading SEM can be when trying to verify global aligned and thus every global alignment discussed in this dissertation is also supported by cross-polarized microscopy and S_{2D} Raman-mapping.

3.12. Alignment of Length-Sorted CoMoCAT-SWCNTs

As length appears to be an important factor for global alignment of the large diameter EA-SWCNTs ($d_t \approx 1.4\ \text{nm}$), this section explores, if this also translates to the small diameter CoMoCAT-SWCNTs ($d_t \approx 0.78\ \text{nm}$). These SWCNTs are considerably more difficult to deposit in an aligned fashion than the EA-SWCNTs and this is the reason, why only a few reports exist on their use.[40, 148, 227] Akin to the unsorted EA-SWCNTs, one could suggest that a variation in the initial volume rate, the control mode (constant flux, constant transmembrane pressure, constant pressure)

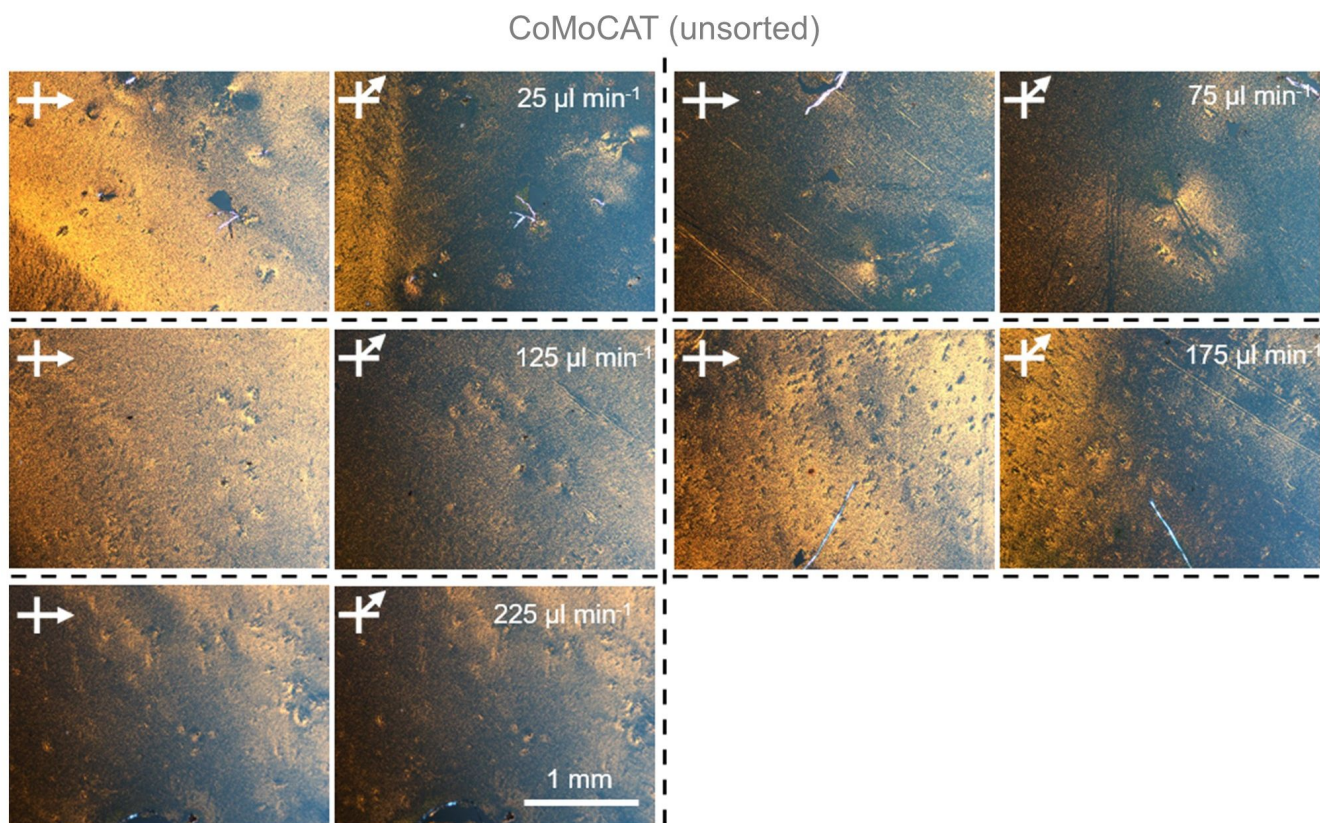


Figure 3.24.: Optimization of the slow volume-rate for unsorted CoMoCAT-SWCNTs filtered onto an 80 nm membrane with a final push step of $500 \mu\text{L min}^{-1}$. Cross polarized microscopy mages were recorded after transfer of the SWCNT film to a silicon wafer. The film filtered at $125 \mu\text{L min}^{-1}$ shows a slight tendency towards global alignment (greater contrast between bright and dark positions) but a closer inspection in Figure 3.25 reveals $10 \times 10 \mu\text{m}^2$ domains separated by large grain boundaries with a size similar to the domains. Reproduced from [3].

fast filtration volume rate or pore-size of the membrane (50 nm, 80 nm, 100 nm and 200 nm) will allow them to be aligned and that it is only a matter of process optimization. Indeed, upon comparison of the average length of DOC dispersed CoMoCAT SWCNTs ($L_{avg} = 798 \text{ nm} \pm 545 \text{ nm}$) and their zeta potential ($\zeta_{CoMoCAT} = -29.5 \text{ mV}$) to the longest A2 EA-SWCNTs fraction ($L_{avg} = 667 \text{ nm} \pm 246 \text{ nm}$, $\zeta_{A2} = -30 \text{ mV}$), their global alignment appears to be only a matter of optimization. However, several attempts in finding optimal parameters ended up in not showing any reliable trend. As an example, Figure 3.24 shows cross-polarized microscopy images of CoMoCAT SWCNTs filtered onto an 80 nm pore-sized membrane at varying volume-rates during the slow flow step. It might appear that some of the regions are aligned, and upon closer inspection with an SEM, Figure 3.25, aligned domains with sizes up to $10 \times 10 \mu\text{m}^2$ can be found. These domains are large enough to provide a high S_{2D} value when measured by single point Raman spectroscopy, and if these are then imaged by an SEM with the appropriate magnification, it is not possible to distinguish them from the globally aligned EA-SWCNTs films shown in Figure A.40. Thus it can be speculated, that this might be source of data in previous reports on small diameter SWCNTs, in which the small spot measured leads the S_{2D} values to significantly exceed values measured by larger area sampling methods; and that

CoMoCAT (unsorted)

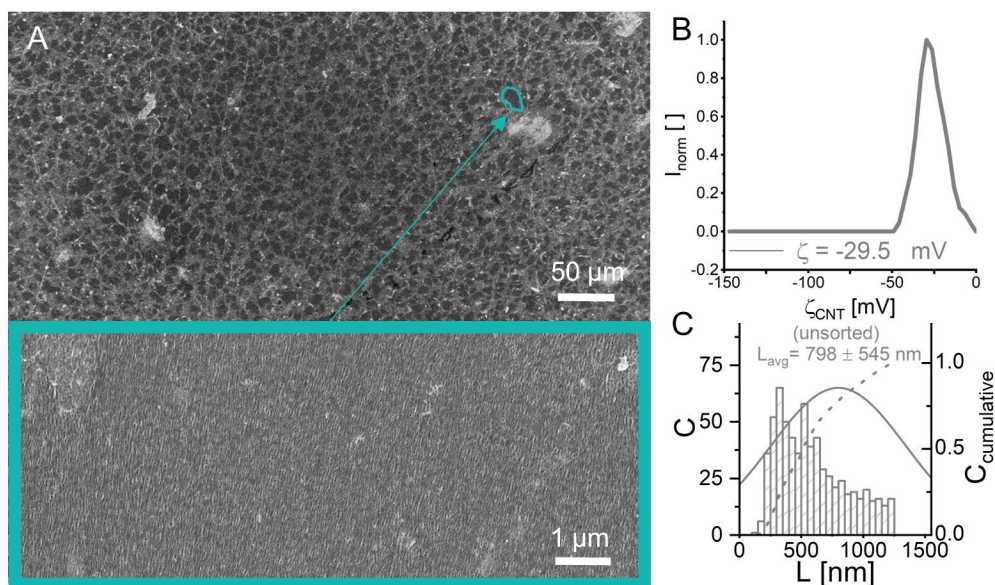


Figure 3.25.: (A) SEM images of the CoMoCAT film filtered at $125 \mu\text{L min}^{-1}$ and shown in Figure 3.24. The film mainly consisted of small-sized domains with equally-sized grain boundaries. (B) Zeta potential of the CoMoCAT dispersion ($8 \mu\text{g mL}^{-1}$) in 0.04 wt% DOC. (C) The average length of the SWCNTs as determined from AFM topographies. Reproduced from [3].

global alignment may not have actually been achieved. [40, 148] Using identical filtration parameters to the un- and sorted EA-SWCNTs (mass diluted to 20 mL with H_2O , $100 \mu\text{L min}^{-1}$ slow filtration, $500 \mu\text{L min}^{-1}$ fast filtration for the last $750 \mu\text{L}$, and 80 nm pore size) SWCNT films from the length sorted CoMoCAT fractions B2 ($952 \text{ nm} \pm 431 \text{ nm}$) and B4 ($648 \text{ nm} \pm 310 \text{ nm}$) were prepared. Total masses of $8 \mu\text{g}$ and $12 \mu\text{g}$ were used and the concentration of each fraction was again determined by evaluating the π -plasmon peak, Figure A.27. Cross polarized microscopy images of one half of the SWCNT film are shown in Figure 3.26 and full film images can be found in Figure A.41 and A.42. Representative $5\times$ magnification images on the membrane and after transfer to a silicon substrate are shown in Figures A.43 – A.45 and machine vision was again used to evaluate the SWCNT domain size, Figure A.46 and A.47. Compared to the non-length sorted CoMoCAT films, Figure 3.24 and 3.25, the domain size of the B4 films was slightly smaller ($8 \mu\text{g}$: $234 \mu\text{m}^2 \pm 383 \mu\text{m}^2$, $12 \mu\text{g}$: $158 \mu\text{m}^2 \pm 195 \mu\text{m}^2$) and this is consistent with their shorter length ($648 \text{ nm} \pm 310 \text{ nm}$ vs. $798 \text{ nm} \pm 545 \text{ nm}$). Essentially, B4 behaved like the unsorted fraction and had all its associated problems in achieving global alignment. On the contrary, films made from $8 \mu\text{g}$ of B2 ($L_{\text{avg}} = 952 \text{ nm} \pm 431 \text{ nm}$) had significantly larger domain sizes ($1467 \mu\text{m}^2 \pm 2542 \mu\text{m}^2$) and these became even larger (2.329 mm^2) for the $12 \mu\text{g}$ sample. Once again, the morphology of the film was the same on the front and back of the film, but despite the dramatic improvement in the domain size, the individual domains still did not have a common alignment direction. In section 3.6, it was shown, that hot-embossing had a profound impact on the achievable alignment, which was also reflected in the higher S_{2D} compared to the alignment achieved without membrane modification, Figure 3.12.

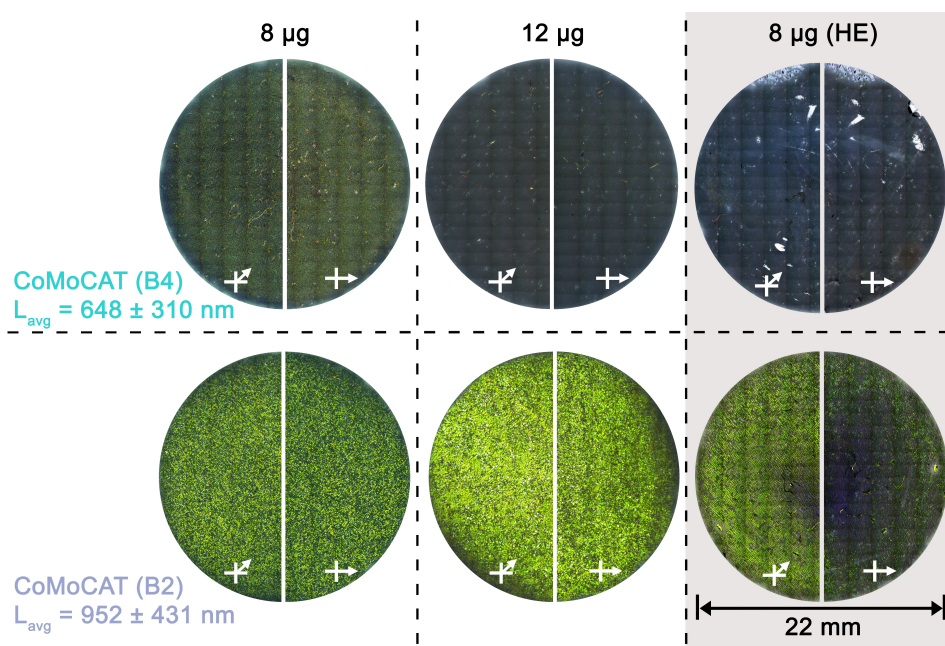


Figure 3.26.: Cross polarized microscopy of one half of a CoMoCAT film from the length fractions B4 and B2 in the bright (45°) and dark (0°) orientation and on pristine and hot-embossed (HE) membranes. Figure reproduced from [3].

By using the axial shim containing a stripe pattern with line widths of 150 nm, 300 nm, 450 nm and 600 nm in each of the four quadrants into the membrane, and repeating the filtration of $8 \mu\text{g}$ of B2 and B4, Figure 3.26. Although the B4 SWCNTs did not appear to benefit from the template and the film remained disordered, the B2 film now showed large range order in the direction of the template, Figure A.45. The domain-size also slightly increased to $(2176 \pm 5504 \mu\text{m}^2)$ but showed no correlation to the width of the striped patterns. SEM images can be found in Figure A.48. Considering that the size of the single SWCNT domains on both pristine and hot embossed membranes is similar, it can be argued that the growth of the domains in highly dilute systems ($0.53 \mu\text{g mL}^{-1}$) depends on the attractive and repulsive forces between the SWCNTs as well as the SWCNTs and the membrane, and that the alignment director can be given by the grooves of the membrane. Compared to the initial experiments discussed in section 3.6, which have been done with much higher concentration of unsorted EA-SWCNTs ($8 \mu\text{g mL}^{-1}$), this alignment still relies on the formation of crystalites, contrary to the deposition of individual SWCNTs observed before, Figure 3.11 (C).

3.13. Evaluation of the Two-Dimensional Order Parameter for Length-Sorted EA- and CoMoCAT-SWCNTs

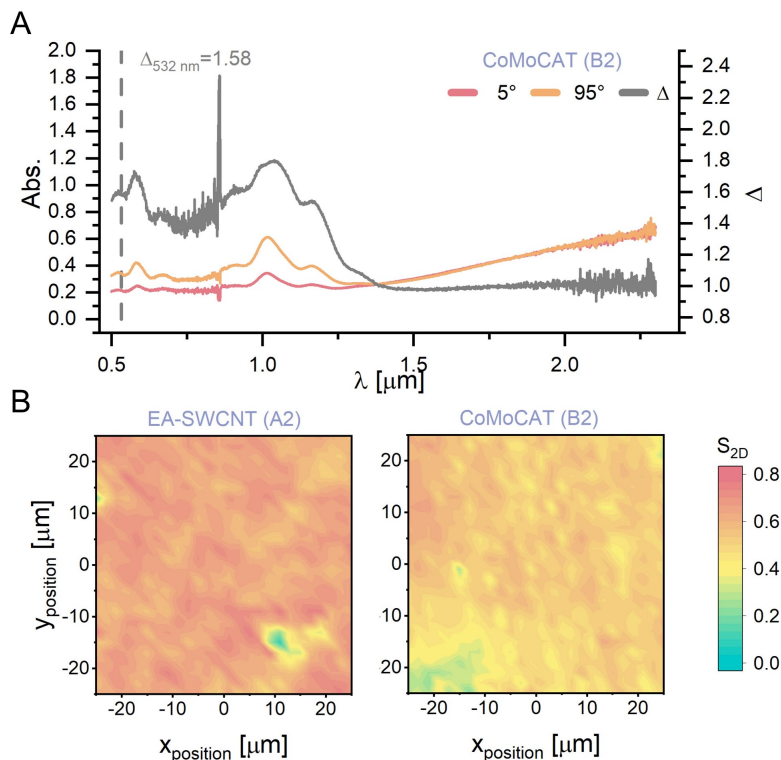


Figure 3.27.: (A) Dichroic ratio of a globally aligned CoMoCAT (B2) film made with an HE membrane and transferred to an ITO glass substrate. For the calculation of the S_{2D} maps in (B), a dichroic ratios of $\Delta_{EA-SWCNT} = 1.55$ [1] and $\Delta_{CoMoCAT} = 1.58$ for a laser excitation at 532 nm were used. The S_{2Dmax} values reach ≈ 0.76 for the EA-SWCNT (A2) and ≈ 0.6 for the CoMoCAT (B2) films. Reproduced from [3].

In order to quantify the angular dependence of the absorption, a similar film made with an HE membrane and CoMoCAT (B2) SWCNTs was transferred to an ITO-coated glass substrate and measured in transmittance using a spectrometer and a Glan-Thompson polarizing prism, Figure A.49. The highest and lowest absorption measured with the SWCNTs being parallel and perpendicular to the incident light source were determined to be at 5° and 95° , respectively and were thus used to determine the dichroic ratio $\Delta(\lambda)$, Figure 3.27 in a similar fashion shown earlier for the unsorted EA-SWCNTs (cf. 3.12 (B)). Using the dichroic ratio at the wavelength of the Raman laser for the SWCNTs used ($\Delta_{CoMoCAT}(532nm) = 1.58$ and the previously determined $\Delta_{EA-SWCNT}(532nm) = 1.55$), allows for a map of the order parameter S_{2D} via Raman spectroscopy following the approach of Zamora-Ledezma et al. [110] over $625 \mu m^2$, yielding $S_{2Dmax} \approx 0.76$ for the EA-SWCNT (A2) and ≈ 0.6 for the CoMoCAT (B2) films. The measured intensities of the different optical configurations (I_{HH} , I_{HV} , I_{VV} and I_{VH}) are shown in the appendix, Figure A.50. Compared to the values obtained for the global aligned film using EA-SWCNT and similar filtration

parameters ($S_{2Dmax} \approx 0.83$, cF. Figure 3.12), the films shown here are slightly less aligned. For CoMoCAT SWCNTs with comparable length, He *et al.* stated a spot measurement with $S_{3D} \approx 0.73$ [40], which cannot be compared to S_{2D} directly.

3.14. Derjaguin, Landau, Verwey, Overbeek for Unsorted EA-SWCNTs Dispersed in DOC and CTAB

Revisiting the mass balance given in section 1.4 and especially eq. 1.13, shows that the mass transport N is influenced by, the convective transport (Jc), the concentration gradient ($\frac{\partial c}{\partial z}$) building up at the membrane surface establishing a diffusive transport and the interaction potential (Φ_{TOT}) between the surface of the membrane and the filtered species. If the convective transport towards the membrane is counteracted by diffusion and the interaction potential, the particle will remain in a dispersed state, otherwise it will deposit onto the membrane surface. In general, the filtration technique relies on very dilute dispersions of SWCNTs ($8 \mu\text{g mL}^{-1}$) and it was found that alignment was enhanced by diluting the feed solution even further ($0.53 \mu\text{g mL}^{-1}$, cF. Figure 3.8), which implies that there is a close to homogenous distribution of SWCNTs and a negligible concentration gradient. Therefore, at room temperature the filtration of SWCNTs depends primarily upon the flux, J , and the interaction potential, Φ_{TOT} . Given that the zeta potential of the membrane and the SWCNTs have been measured, DLVO theory can be used to describe the interaction potential for an isolated SWCNT at the membrane surface using the Parameters listed in the Appendix A.7.[180] In this section the total interaction potential will be discussed first for the unsorted EA-SWCNTs dispersed in a negative (DOC) and positive (CTAB) surfactant and filtered onto various membranes.

The pH of the unsorted EA-SWCNT dispersions used in sections 3.2 - 3.9 was 8.5 for DOC and 8.7 for CTAB, Figure 3.1 (B), and this implies that during filtration ζ_{surf} equals $\approx -42 \text{ mV}$ for the hot embossed (HE) membranes, -60 mV for the PVP-coated (PVP) membranes and -110 mV for the uncoated (UC) membranes. Φ_{TOT} was calculated as the sum of the electrical double layer (Φ_{EDL}) and van der Waals (Φ_{VDW}) interactions at a distance z , above the membrane surface. Ideally, Φ_{EDL} requires knowledge of the surface potential (γ) of the SWCNTs and the membrane, but these were approximated from their zeta potentials using the approach of Wu *et al.* [180] In the case of unsorted EA-SWCNTs dispersed in DOC, the membrane and the SWCNTs have a zeta potential of equal sign and this leads to an Φ_{EDL} that is repulsive whilst for CTAB dispersed SWCNTs they have an opposite sign and Φ_{EDL} is attractive. In both cases Φ_{VDW} is always attractive. These two cases are shown in Figure A.51. For DOC dispersed SWCNTs, Φ_{TOT} has a shallow secondary minimum located 23.7 nm (HE), 25 nm (PVP) or 26.4 nm (UC) above the membrane surface, while the primary minimum is found on the surface itself. Figure 3.28 (A) displays Φ_{TOT} for membrane potentials ranging from -120 mV to -10 mV , where it can be seen that the location of the minimum approaches the surface for less negative zeta potentials. Due to the absence of a repulsive component in the case of CTAB, there is no secondary minimum and the SWCNTs are attracted directly to the surface, Figure 3.28 (B). As an outcome

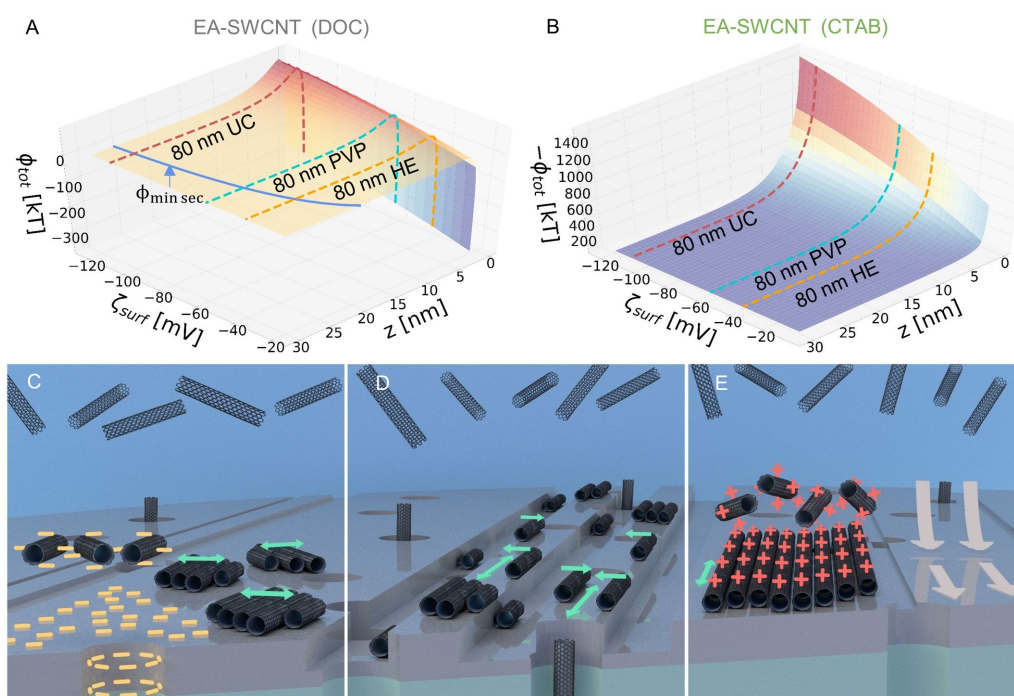


Figure 3.28.: Calculation of the total potential $\Phi_{TOT}(z)$ of a DOC (A) and CTAB (B) dispersed SWCNT with respect to the zeta potential of the membrane surface ζ_{surf} utilizing DLVO theory.[180] The potential corresponding to an uncoated (UC), PVP coated and hot embossed (HE) 80 nm membrane are marked with a dashed line, as well as the shallow secondary minimum (≈ -0.15 kT). Illustration of the alignment of (C) DOC dispersed SWCNTs on a pristine PVP coated membrane, (D) a hot embossed membrane and (E) CTAB dispersed SWCNTs on an untextured membrane. The beige arrows indicate shear flow parallel to the membrane which acts as an alignment director for the SWCNTs. Figure reproduced from [1].

of the optimization of the slow volume-rate \dot{v} shown in section 3.3, concentration polarization was found to be an essential part of the alignment. This indicates that the SWCNTs must accumulate close to the membrane as stated by others.[40, 41, 138, 139, 228] For unsorted DOC dispersed EA-SWCNTs, this requires the volume rate to be carefully adjusted in order to gather the SWCNTs close to the membrane ($100 \mu\text{L min}^{-1}$), which would identify the secondary minimum as a favorable position. This could also explain, why many researchers report the initial volume rate during the slow-filtration regime to be crucial for global alignment.[1, 40, 41] On the contrary, as the secondary minimum is not deep enough (cF. Figure A.51) to accumulate the SWCNTs on its own at room temperature, lower volume rates will increase the concentration polarization volume, as the SWCNTs will be distributed over a longer distance to the membrane and do not form crystallites ($25 \mu\text{L min}^{-1} - 75 \mu\text{L min}^{-1}$). At higher volume rates ($125 \mu\text{L min}^{-1}$), turbulence might disturb the orientation of the crystallites formed in the secondary minimum as it is very close to the membrane (< 30 nm) and once again a film with multiple alignment orientations is obtained.

In the case that the membrane is textured (Figure 3.28 (D)), a lower surface zeta potential (-49 mV) results in the secondary minimum being slightly closer to the surface (23.7 nm) but more importantly, at a distance that is shorter

than the depth of the grooves (80 nm). This means that a CNT approaching the surface can circumvent the potential barrier at the edge of a groove because of a discontinuity in its position from the surface at this edge, Figure A.52. This leads to the observation of almost no concentration polarization regime in Figure 3.10 (G) and allows for the SWCNTs to assemble immediately on the membrane surface. Due to the fact that these initial CNTs are all orientated in the same direction no grain boundaries and thus crystallites are observed. For CTAB, the SWCNTs also accumulate directly on the surface regardless of the volume rate applied, Figure 3.28 (E). However, unlike in the case of DOC, the concentration of SWCNTs within this initial fouling step (500 μL) is not sufficient to form crystallites and the high surface charge on the CTAB dispersed SWCNTs ($\zeta_{CTAB} = 72 \text{ mV}$ vs. $\zeta_{DOC} = -14 \text{ mV}$) results in the first layer of SWCNTs establishing a new potential barrier and a secondary minimum to the surface. This is evidenced by the secondary concentration polarization regime seen in Figure 3.6.

For textured surfaces the driving force for global alignment can easily be understood. A pore size difference between the ridges and valleys provides a directional flow through the ridges and this is combined with a negligible potential barrier at the edges. This drives the SWCNTs to first assemble at the edges and follow the embossed pattern, Figure 3.11 (E). However, the driving force for alignment on un-textured membranes appears to be more complex. Both positive and negatively charged SWCNTs were found to align and pre-existing grooves in the membrane appeared to be less important, Figure 3.3 (D). Clearly there must be an additional interaction between the membrane and SWCNTs in order to drive global alignment. Due to the proven close proximity of the SWCNTs to the membrane surface and the elongation of the crystallites with increasing volume rate it can be speculated that shear flow across the membrane surface is responsible for alignment. Due to the 1D structure of the CNTs, this flow needs to be either uni- or bi-directional and it is intuitively difficult to understand where such a shear flow should originate for a dead-end filtration setup on a symmetric and circular membrane. Perhaps, the average direction of grooves present in the membrane from manufacture provide a directionality to the flow of liquid across the surface and that these drive the alignment of CNTs. In this way, it is possible for certain isolated grooves to be misaligned with the overall direction of all others and hence the liquid flow across the surface. This will lead to the observation that occasionally, and in localized regions, that CNTs and grooves can be misaligned.

3.15. Derivation of the Relationship between SWCNT Length and Diameter using DLVO-Theory

In the past, it has been suggested to describe the formation of domains with the classical Onsager argument involving a crystal phase formation which is valid for high concentrations of rigid rods.[229, 230] By estimating the typical SWCNT density of an enriched phase to be 1.5 g mL^{-1} [231], Lagerwall *et al.* suggested that a ratio of $d_t/L = 0.001$ should facilitate the formation of a nematic phase and thus the formation of domains.[137] The concentrations of the SWCNT dispersions used in this study ranged from $0.53 \mu\text{g mL}^{-1}$ to $1.6 \mu\text{g mL}^{-1}$. In the bulk this is six orders of

magnitude different from the concentration used by Lagerwall *et al.*, but the actual concentration in the enriched 2D plane is unknown but certainly significantly higher than the bulk. According to Onsager's model, a lower ratio has a higher tendency to grow crystals and this would predict that in-fact only the unsorted and B2 CoMoCAT sample would be able to form and grow domains, Figure 3.29. However, this clearly contradicts the observations made in

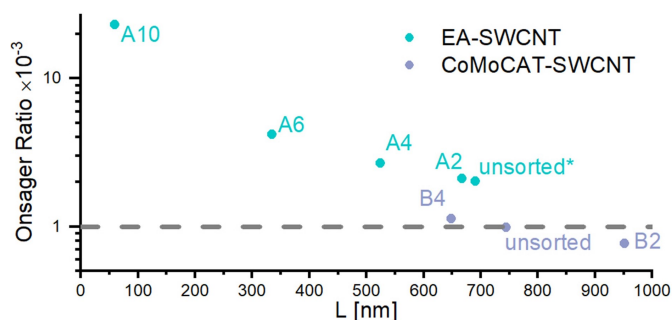


Figure 3.29.: Logarithmic plot of the Onsager ratio $d_t L^{-1}$ with respect to length for the SWCNTs. The threshold for alignment given by the considerations of Lagerwall *et al.* is plotted as a dotted line at $d_t L^{-1} = 1 \times 10^{-3}$. [137]. Figure reproduced from [3].

sections 3.11 and 3.12 and that of others. [1, 40, 41] This is likely due to the membrane not being represented, which provides a driving force for alignment by morphology, i.e., grooves [139], directional charges, [40, 41] or directional flow patterns [1]. In either case, however, the SWCNTs must be reorienting as they approach the surface for any aligned film. Once again, the tailored formulas from Wu *et al.* (eq. 1.44 and 1.45, [180]) are used to calculate the total interaction potential $\Phi_{TOT} = \Phi_{VDW} + \Phi_{EDL}$ for a SWCNT approaching a 80 nm membrane, but this time, the focus is on the length sorted EA- and CoMoCAT species dispersed in DOC.

In order to perform these calculations, knowledge of the ionic strength at the membrane surface is required. A DOC concentration of 0.04 wt% in the bulk corresponds to an ionic strength of 1 mmol L^{-1} , which is unlikely to increase at the membrane, as the molecule (MW 0.414 kDA) is not large enough to get retained. For this reason, an ionic strength of 1 mmol L^{-1} is chosen for the curves shown in Figure 3.30. For the case, that the DOC concentration might increase at the membrane, due to absorption or retention of the micelles formed, calculations for 1 mmol L^{-1} , 10 mmol L^{-1} and 100 mmol L^{-1} can be found in Figure A.53. More details on the parameters can be found in the appendix A.8. In Figure 3.30 (A) Φ_{TOT} is plotted for all fractions and diameters used in this dissertation up to a distance of $z = 40 \text{ nm}$ from the membrane. The secondary minimum located at $z \approx 27 \text{ nm}$ is too small compared to the primary energy barrier to the surface ($\Phi_{TOTmax} \approx 25 \text{ kT}$ to 150 kT) to be visible in Figure 3.30 (A) and an enlarged view is shown Figure 3.30 (B) for every SWCNT, respectively. By comparing the depth of secondary minima with the experimental achieved alignment shown in sections 3.11 and 3.12, it can be concluded that fractions with a secondary minimum equal to- or deeper than -0.075 kT form domains and that these increase in size with increasing SWCNT mass. This threshold value changes with the ionic strength used and for reference, an ionic strength of 100 mmol L^{-1} or 1 mmol L^{-1} corresponds to a secondary minimum with a depth of -1.102 kT and -0.058 kT , respectively. For

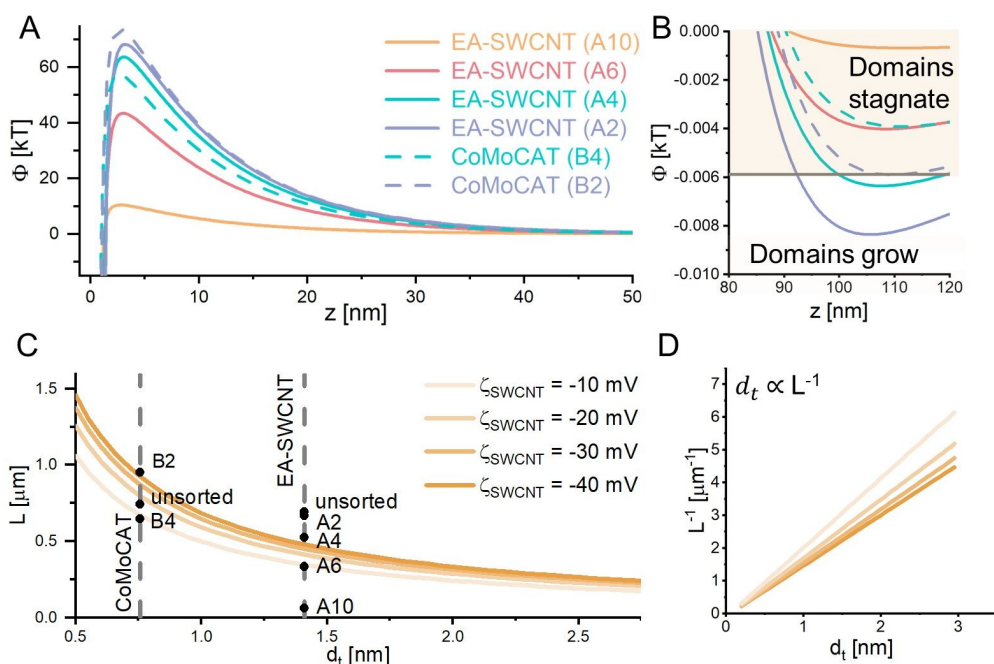


Figure 3.30.: (A) DLVO calculations for all SWCNT fractions used in this work, showing the Φ_{TOT} to a distance, $z = 50$ nm from the membrane surface. (B) An enlarged view of the secondary minimum of Φ_{TOT} at $z \approx 28$ nm. (C) All combinations of length L , diameter d_t and zeta potential of the SWCNT ζ_{SWCNT} with a sufficient depth of the potential secondary minima for global alignment. (D) The curves show in (C) follows a $d_t \propto L^{-1}$ relationship (D). Figure reproduced from [3].

the large diameter EA-SWCNTs ($d_t \approx 1.4$ nm) this was true for the fractions A4 ($L_{avg} = 524$ nm \pm 178 nm) and A2 ($L_{avg} = 667$ nm \pm 246 nm), while only the longest small diameter CoMoCAT SWCNTs (B2) ($d_t \approx 0.78$ nm, $L_{avg} = 952$ nm \pm 431 nm) showed the capacity to grow domains with increasing mass. On the contrary, when the secondary minimum is shallower than the threshold value, the domains stagnate and do not increase in size with increasing mass, as it could be observed for all other fractions. However, similar to the unsorted EA-SWCNTs dispersed in DOC, all three threshold values are small relative to the thermal energy available at room temperature as DLVO calculations do not account for the volume rate used during filtration, or the interaction between neighboring carbon nanotubes during enrichment. Under the assumption that a secondary minimum with a depth of at least -0.058 kT is required, the smallest required length L of a hypothetical SWCNT with a given diameter d_t and zeta potential ζ_{SWCNT} is shown in Figure 3.30 (C). The zeta potential was varied between -40 mV and -10 mV with the hope that the zeta potential measured by other researchers for their SWCNTs will most likely fall within this range. Figure 3.30 (C) can be understood as follows: A SWCNT will form domains of sufficient size for global alignment only if it is long enough, and this is the case when it coincides with or is above the respective boundary curve for a given zeta potential. Every combination of d_t and L below the boundary curve does not have a sufficient secondary minimum for domain growth. This rule can be further corroborated by including all fractions and all unsorted SWCNTs used before. It can now also be seen why small diameter SWCNTs are more difficult to align: The influence of the ζ_{SWCNT}

decreases with the length of the SWCNTs and thus it might not be advisable to tailor the zeta-potential of large diameter tubes in order to improve alignment. For reference a SWCNT dispersion prepared by sonication, which is the most common method, usually has a number average length of less (or much less) than 600 nm – 800 nm and very rarely > 1000 nm. For EA-SWCNTs this does not pose a problem, but for the small diameter SWCNTs their length is simply too short, or the required zeta potential unattainable, for global alignment. Importantly, as seen in Figure A.50 the relationship between the required length for alignment and the SWCNT's diameter was not found to vary significantly for the ionic strengths discussed above. The largest impact on the calculated length was found for a CoMoCAT SWCNT and amounted to ≈ 50 nm. It is worth mentioning that He *et al.*, have claimed global alignment of CoMoCAT raw material with $L = 420$ nm[40] and Katsutani *et al.* with $L = 200$ nm.[148] In the filtration regime explored in this dissertation, such films would only form small aligned domains with limited registration to each other, not achieving universal and strong global alignment along the same vector. Plotting the curves in Figure 3.30 (C) with respect to an inverse length L^{-1} , yields an inverse proportional relationship $d_t \propto L^{-1}$, Figure 3.30 (D), which allows for a linear fit $L^{-1} = m_{\zeta \text{ SWCNT}} d_t + b_{\zeta \text{ SWCNT}}$, with $m_{\zeta \text{ SWCNT}}$ and $b_{\zeta \text{ SWCNT}}$ being the slope and intercept. The fitting parameters of the corresponding curves can be found again in the appendix A.8 and are more accurate for higher charged SWCNTs, due to the curves being slightly more linear.

- This page is left blank intentionally. -

4. Discussion and Outlook

Global uni-axial and radial alignment of carbon nanotubes using dead-end filtration was achieved on textured and un-textured membranes using small CoMoCAT- ($d_t = 0.78$ nm) and large diameter EA-SWCNTs ($d_t = 1.4$ nm), with the latter also involving negatively (DOC) and positively (CTAB) charged surfactants. In order to investigate the underlying mechanisms, the membranes used have been evaluated at first in terms of their resistance R_m and zeta-potential. While the membrane resistance could be approximated by describing them as a stack of pores, one could conclude, that this model could be improved by including the charges on the membrane surface, which was especially true by comparing coated and uncoated membranes with the same pore size having different R_m . It could also be shown, that the zeta potential might be a key factor in the beginning of the filtration, as an observable peak in R_m was scaling with ζ_{surf} and even vanished at higher ionic strength (KCl), while the latter was deemed by Walker *et al.* as being detrimental to global alignment.[41] Surprisingly, increasing concentrations of DOC, did not have the same effect. However, over a course of many performed experiments, differences in the constitution of the membranes (batches), had also an effect on alignment, which one could suspect to be due to additional grooves or variations in porosity or thickness. By using the custom-built and programmed microfluidic filtration rig, it was possible to initially improve the alignment achieved for each membrane by optimizing the slow filtration step by using flow intervals of $25 \mu\text{L min}^{-1}$ for unsorted EA-SWCNTs dispersed in DOC. The improvement in alignment thereby manifested as an elongation and decrease of the size of the single domains with an increasing volume rate, but more importantly the shared direction was found to be dependent on specific volume rates with respect to the pore size. For all pore sizes tested using pristine membranes (50, 80, 100 and 200 nm), the optimal volume rate, was also always accompanied by a minimal CP-regime. From those experiments, the 80 nm pore sized membranes were also found to be most promising, which is in accordance to results published by others [40, 41, 139]. An optimal volume-rate was also determined for the positively charged unsorted EA-SWCNTs (CTAB), which afforded alignment without any grain-boundaries present, but came with a disordered film being sandwiched in between aligned films found on the top and bottom. This might be due to the comparably high absolute charge of the surfactant ($\zeta_{EA-SWCNT CTAB} = 72$ mV, $\zeta_{EA-SWCNT DOC} = -14$ mV), repelling SWCNTs depositing after the first layer. This opens the possibility, that an additional increase in volume-rate after the first layer deposited might facilitate a more homogeneous alignment throughout the film. As the morphology is different to films obtained with SWCNTs repelled by the membrane, it can be argued, that also the alignment mechanism must be different, since other groups stated, that a 2D-plane of floating SWCNTs should be imperative for this method.[40, 41, 144] However, in all cases (pore-size and charge of SWCNTs), the final pushing and drying steps were found to have little effect on the overall alignment. In order to turn the aligned regions achieved by the flow-rate optimization into a global aligned film, the appropriate mass was identified by measuring the height of several films, which revealed a compaction zone, where the film height would not increase with mass. This also seemed to be important for the length-sorted SWCNTs used later and once more indicates, that the alignment on pristine membranes might be connected to a crystallization

Author, Date	SWCNTs	Membrane Modification	Area	Order Parameter
He et al., 2016 [40]	EA-SWCNTs	Pristine	1.76 cm ²	$S_{3D} = 0.96$
He et al., 2016 [40]	CoMoCAT-SWCNTs	Pristine	1.76 cm ²	$S_{3D} = 0.75$
Walker et al., 2019 [41]	EA-SWCNTs	Pristine	1.76 cm ²	$S_{2D} = 0.90$
Walker et al., 2022 [144]	EA-SWCNTs	Pristine	1.76 cm ²	$S_{2D} = 0.71$
Rust et al., 2022 [1]	EA-SWCNTs	Pristine	3.81 cm ²	$S_{2D} = 0.78$
Rust et al., 2022 [1]	EA-SWCNTs	HE, uni-axial	3.81 cm ²	$S_{2D} = 0.83$
Rust et al., 2023 [2]	EA-SWCNTs	HE, radial	3.81 cm ²	$S_{2D} = 0.85$
Rust et al., 2022 [3]	EA-SWCNTs (A2)	Pristine	3.81 cm ²	$S_{2D} = 0.76$
Rust et al., 2023 [3]	CoMoCAT-SWCNTs (B2)	HE, uni-axial	3.81 cm ²	$S_{2D} = 0.60$

Table 4.1.: Order parameters of various globally aligned films via the dead-end filtration method published in literature compared to own work shown in this dissertation.

process. Actual global alignment was then achieved for the unsorted EA-SWCNTs (DOC) using 24 μg on a membrane area of 3.8 cm² by further diluting the concentration to 1.6 $\mu\text{g mL}^{-1}$, but keeping the optimized flow-rates, which was rationalized by the increase of total time by keeping the SWCNTs in the secondary minimum. Additionally, modifications of the membrane with uni-axial and radial patterns provided ample improvement of the alignment, as discussed later in terms of increased two dimensional order-parameters S_{2D} . After the optimal force was identified for each shim used (hence, imprinting the shim without excessively closing the pores), all of the patterns deployed could be reproduced, with the exception being the herringbone pattern. It was also found that for all of those patterns, the filtration curves indicated an instantaneous fouling mode without any CP regime, not needing flow-rate optimization nor tailoring the mass needed, with the exception being the aforementioned HB pattern, which showed a curve previously observed for unmodified membranes. This again, indicates, that there might be a different mechanism at work. After modifying the membranes, the next chapters focused on the importance of the length and diameter of the used SWCNTs, revealing that it was beneficial for the alignment, when the absolute van-der-Waals forces increase, namely by increasing the length or diameter. However, since the flow-profiles used, were similar to previous optimized parameters (slow filtration 100 $\mu\text{L min}^{-1}$ for 19.25 mL, fast filtration 500 $\mu\text{L min}^{-1}$ for 0.75 mL on 80 nm membranes), no change in CP regimes could be observed. In order to compare the champion films obtained in this work to other research groups, a table shown below lists several results, by area, S_{2D} and membrane modification, table 4.1.

Eventually, all experimental results were complemented by DLVO-analysis tailored to an individual SWCNT [180] in order to identify possible mechanisms. Thereby it was shown, that for unsorted EA-SWCNTs dispersed in DOC, only a minor secondary minimum close to the membrane ($\phi_{tot\ min} \approx -0.105kT$, $z \approx 30\ \text{nm}$) exists: which led to the following conclusions for a pristine membrane: If the flow-rate is optimized, the SWCNTs will gather in the shallow, secondary minimum, where they enrich and form domains as previously stated by others. [40, 41, 144] Since the secondary minimum is very shallow, it is not able to draw in SWCNTs at lower flow-rates, which leads to the domains possibly growing with time, but being disordered as they are further away from the membrane, which might provide directionality by grooves and/or a subsequent shear-flow or directional charges. Flow-rates being too

high, will lead to turbulence and thus disturbing the directions of the SWCNTs being really close to the membrane. This problem can be circumvented by using positively charged SWCNTs, but as discussed above, this might also come with a change in alignment mechanism. Hot-embossed membranes were also found to be able to deposit individual SWCNTs preferably on the edges of the imprinted grooves instead of forming complete domains, which could be due to the grooves being deeper than the secondary minimum and only a small mass being deposited, due to the excessive closing of the pores in the hot-embossed region. Finally the model was also used for the length-sorted small and large diameter SWCNTs and by linking the experimental findings to the secondary minimum achieved, a proportionality between $d_t \propto L^{-1}$ could be found, that might serve as a tool in the future to identify suitable SWCNTs for alignment.

In the future, several improvements might be possible by converting the dead-end filtration setup to a cross-flow setup, which would offer a shear flow across the membrane by design. Additionally, director fields, like electric fields or acoustic waves, might also for improving the alignment or tailoring the morphology even further. For hot-embossing, new designs like the one proposed from Mehta et al. [232] could allow for converting polarization elements, turning linear polarized into radial and azimuthal light based on their orientation to the incident light source, and thus making them even more interesting for terahertz applications. Additionally, the combination of flexible printed circuit boards and aligned films might offer the possibility of various sensing applications. With the guidance of the proposed proportionality ($d_t \propto L^{-1}$), it is now also feasible to introduce single-chirality SWCNTs, as those do not allow for copious optimization runs, due to limited availability. Lastly the constitution of the membrane (coating, porosity, thickness, pore-size and grooves) has shown to be of major importance. Tailoring those membranes to this very method, might increase reproducibility and even remove some of the need of sophisticated microfluidic equipment as shown in this work.

- This page is left blank intentionally. -

A. Appendix

A.1. Resistance and Zeta-Potential of Membranes

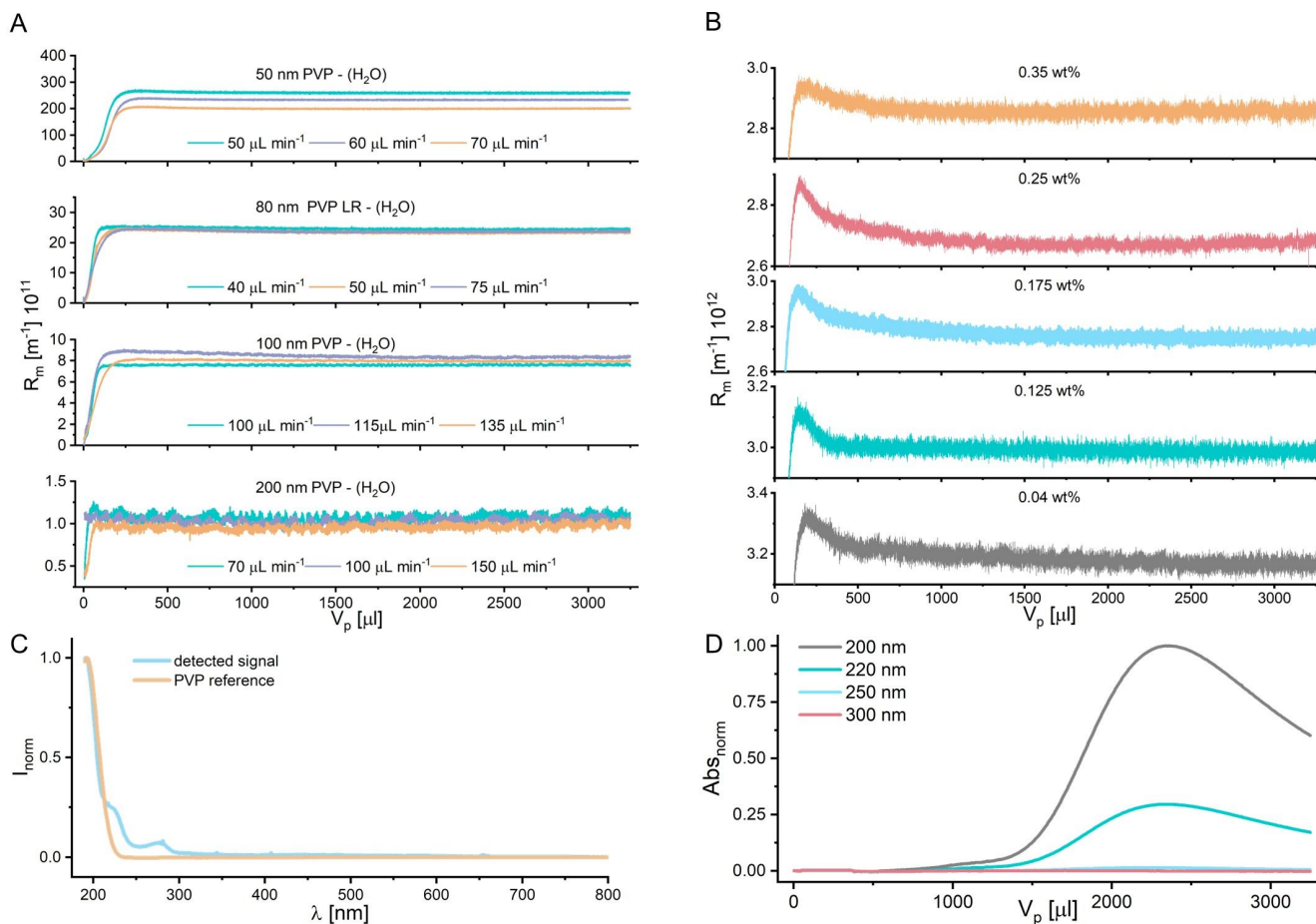


Figure A.1.: (A) Measurement of R_m for unmodified membranes with deionized water at different volume rates. (B) R_m measurement of an 80 nm membrane at 100 µL min⁻¹ for DOC concentrations of 0.04 – 0.35 wt%. Unlike in the case of KCl addition, no change in the initial peak was observed. (E) and (F) show spectra and recorded traces measured at a fixed wavelength for a 3.25 mL permeated volume on the 80 nm membrane. The measured spectra were compared to a PVP reference (Sigma Aldrich, PVP40, Batch 064K0006). Figure reproduced from [1].

Every measurement was performed with 200 mL of 0.01 mol KCl (aq.) and a pressure difference, P , of 600 mbar. For the measurements of the pores this pressure difference is comparable to the transmembrane pressure p_{TMP} , while for the surface measurements it is defined by the pressure difference, P , of the inlet at outlet of the channel. For surface measurements, two equivalent membranes separated by a gap were used to confine the flow. In both cases, the zeta potential was calculated using the Helmholtz-Smoluchowski for a constant potential gradient:

$$\zeta = \frac{\partial U}{\partial P} \frac{\mu}{\epsilon \epsilon_0} \kappa \quad (\text{A.1})$$

The determination of the gradient $\partial U/\partial P$ is depicted in Figure A.2 (C) for an 80 nm membrane at pH 4 in both configurations. For every pH value this process is repeated three times and averaged to a single value as it is shown in Figure A.2 (D). The viscosity, μ (Figure A.2 (E)) and conductivity κ (Figure A.2 (F)) are likewise measured thrice and averaged. The permittivity $\epsilon \epsilon_0$ is being taken to be constant for water at 25 °C. During measurement the adhesive used to fix the membrane on the mounting pieces swells and this leads to a reduction in the channel gap, h_{gap} , Figure A.2 (G). Additionally, due to the blocked exits of the pores, only the surface is measured. This does not affect the measurement when equation A.1 is used for the evaluation of zeta potential. However, it is important to consider the gap height when the zeta potential is determined from constant current gradient $\partial I/\partial P_{TMP}$, as the channel area A is then getting smaller over time:

$$\zeta = \frac{\partial I}{\partial P} \frac{\mu}{\epsilon \epsilon_0} \frac{L}{A} \quad (\text{A.2})$$

In addition to the surface zeta potential ζ_{surf} shown in Figure 3.1 (B), the complementary zeta potential in the direction of the pores ζ_{pore} is plotted against pH in Figure A.2 (H). The pore zeta potential was observed to be rather independent of the surface potential and both coated and uncoated 80 nm membranes were found to have almost the same zeta potential (i.e. $\zeta_{poreUC} = -11$ mV, $\zeta_{porePVP} = -16$ mV at pH = 8.7, which is the pH value of EA-SWCNT (DOC)). Despite the electrolyte also being in contact with the surface of the membrane, we thus conclude that this measurement method mostly probes the pores. For pH values smaller than 4.5, the zeta potential of the PVP coated membranes increases with pore size, which seems to contradict equation (2), which shows a reciprocal dependence on the channel area A consisting of the total pore area. But because $\partial I/\partial P$ is the gradient of the current resulting from charged particles passing the membrane, the larger pore sizes (and thus less resistance) will also result in larger currents. This can also be understood by using the ohmic law $U/R = I$ with the membrane resistance R , while we observed $\partial U/\partial P$ to be rather equal for all measured pore sizes. Contrary to the surface zeta potentials, ζ_{surf} , all pore potentials were found to be stable over all pH values measured. The 200 nm membrane was the only membrane showing a dependence on pH and had a decrease in the absolute potential above pH 4.5

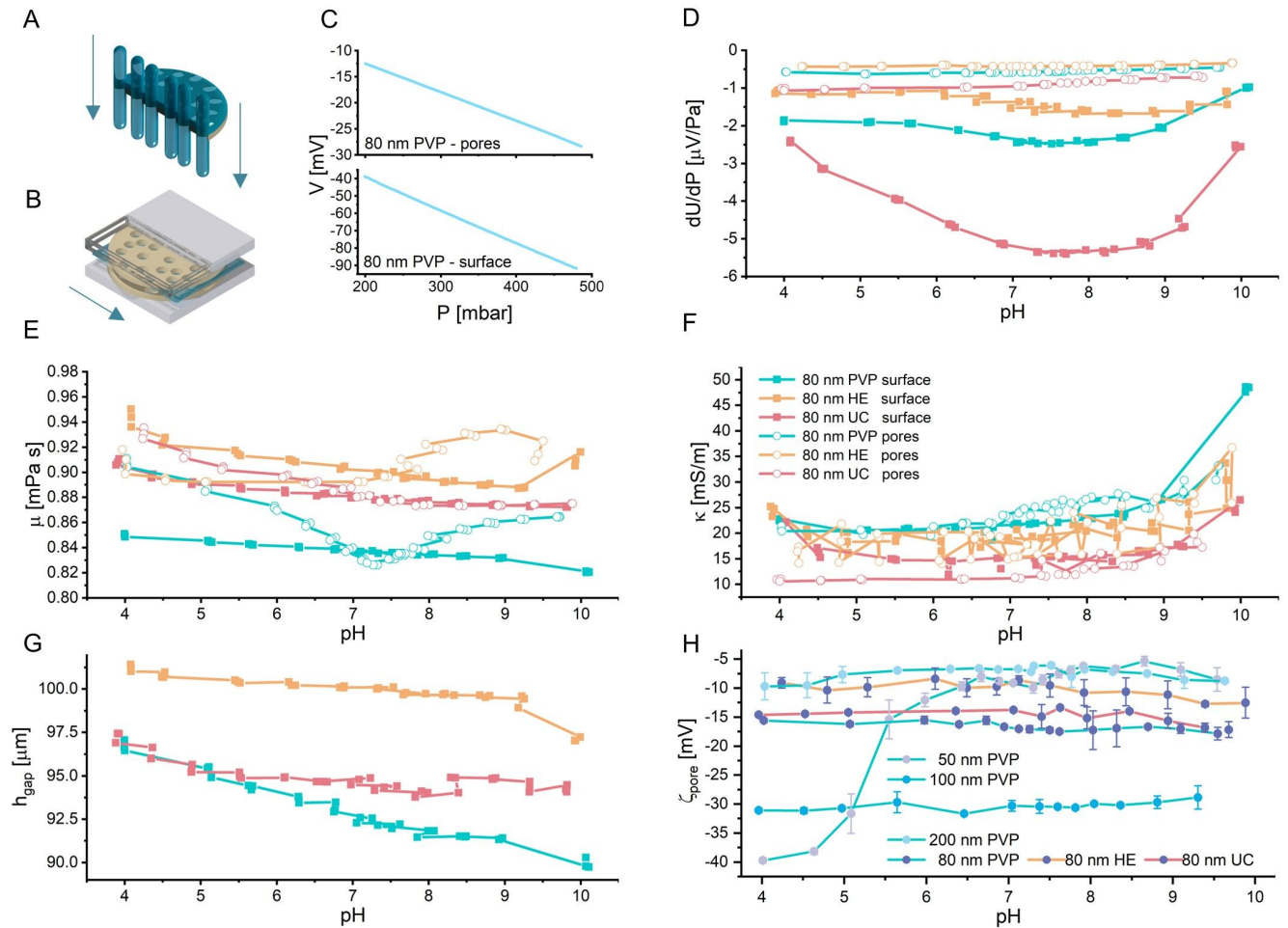


Figure A.2.: Measurement of the zeta potential in (A) the direction of the pores and (B) across the surface of the membrane. (C) Plot of the linear slope of $\frac{\partial U}{\partial P}$ at pH 4 in the pore and across surface for a single measurement. (D) Evaluation of $\frac{\partial U}{\partial P}$ using a linear fit for the different membranes at pH 4 – 10. (E) viscosity (F) conductivity, recorded for differently treated 80 nm membranes and used to calculate the zeta potential with the Helmholtz-Smoluchowski equation for constant potential. (G) Reduction of the gap height with time for the surface measurements which can be attribute to swelling of the adhesive used to hold the two membranes in place. (H) Pore zeta potential for the set of membranes shown in Figure 3.1 (B). Figure reproduced from [1].

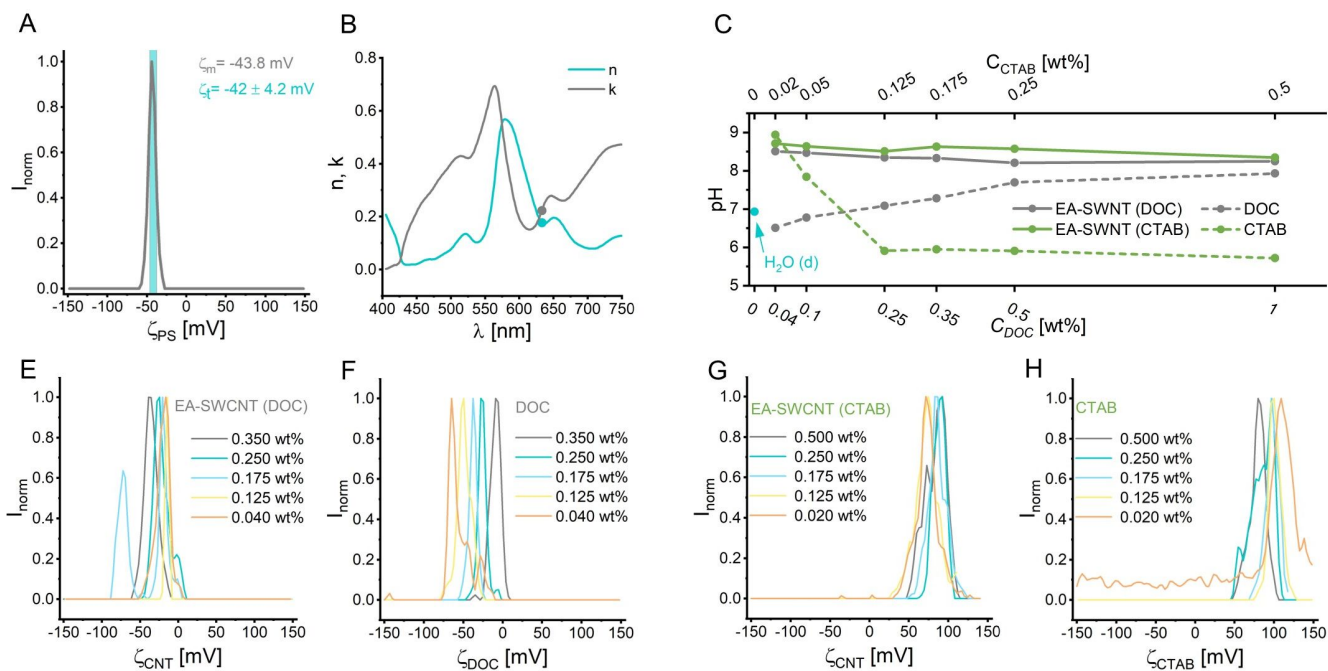


Figure A.3.: (A) Measurement of a polystyrene standard (DTS 1235) with known zeta potential $\zeta_S = -42 \text{ mV} \pm 4.2 \text{ mV}$ to validate the accuracy of the Zetasizer. (B) The n and k values used for the determination of zeta potential at a laser wavelength of 632 nm. (C) The pH values of all dispersions used throughout this work. Individual zeta potential measurements for $8 \mu\text{g mL}^{-1}$ EA-SWCNT dispersed in (E) DOC and (G) CTAB and the surfactants alone (F,H). Figure reproduced from [1].

A.2. Determination of Suitable Slow Volume-Rate for EA-SWCNTs

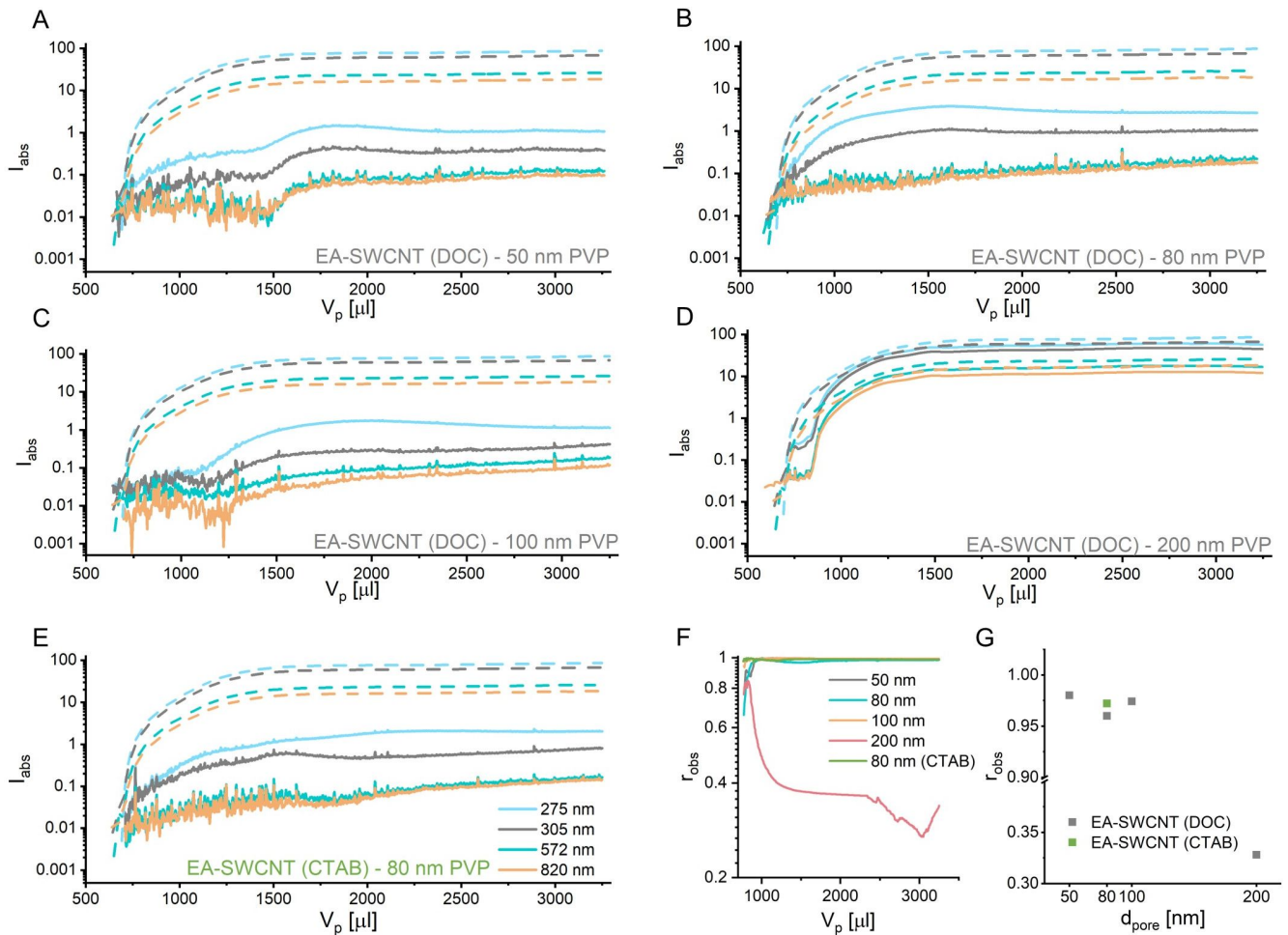


Figure A.4.: (A) Measurement of membrane retention by tracking the absorption intensity of the permeate at 275 nm, 305 nm, 572 nm and 820 nm using the in-line UV-Vis array during filtration. 3.25 mL of an $8 \mu\text{g mL}^{-1}$ unsorted EA-SWCNTs dispersion in 0.04 wt% DOC was passed through (A) 50 nm, (B) 80 nm, (C) 100 nm and (D) 200 nm pore sizes. (E) An 80 nm pore size membrane with 3.25 mL of an $8 \mu\text{g mL}^{-1}$ EA-SWCNT dispersion in 0.02 wt% CTAB. All experiments were performed at $100 \mu\text{L min}^{-1}$ and shown for $V_p > 700 \mu\text{L}$, due to the dead volume between the filtration cell and detector. Dashed lines represent the calibration without the membrane. (F) The retention for all membranes was calculated as the ratio of SWCNTs in the feed solution and those passing the membrane in place, assuming that the concentration was proportional to the absorption measured in the π -plasmon peak (275 nm), similar to the method described in Figure 3.2 (D) (G) Average values of the retention plotted against the membrane pore diameter. Figure reproduced from [1].

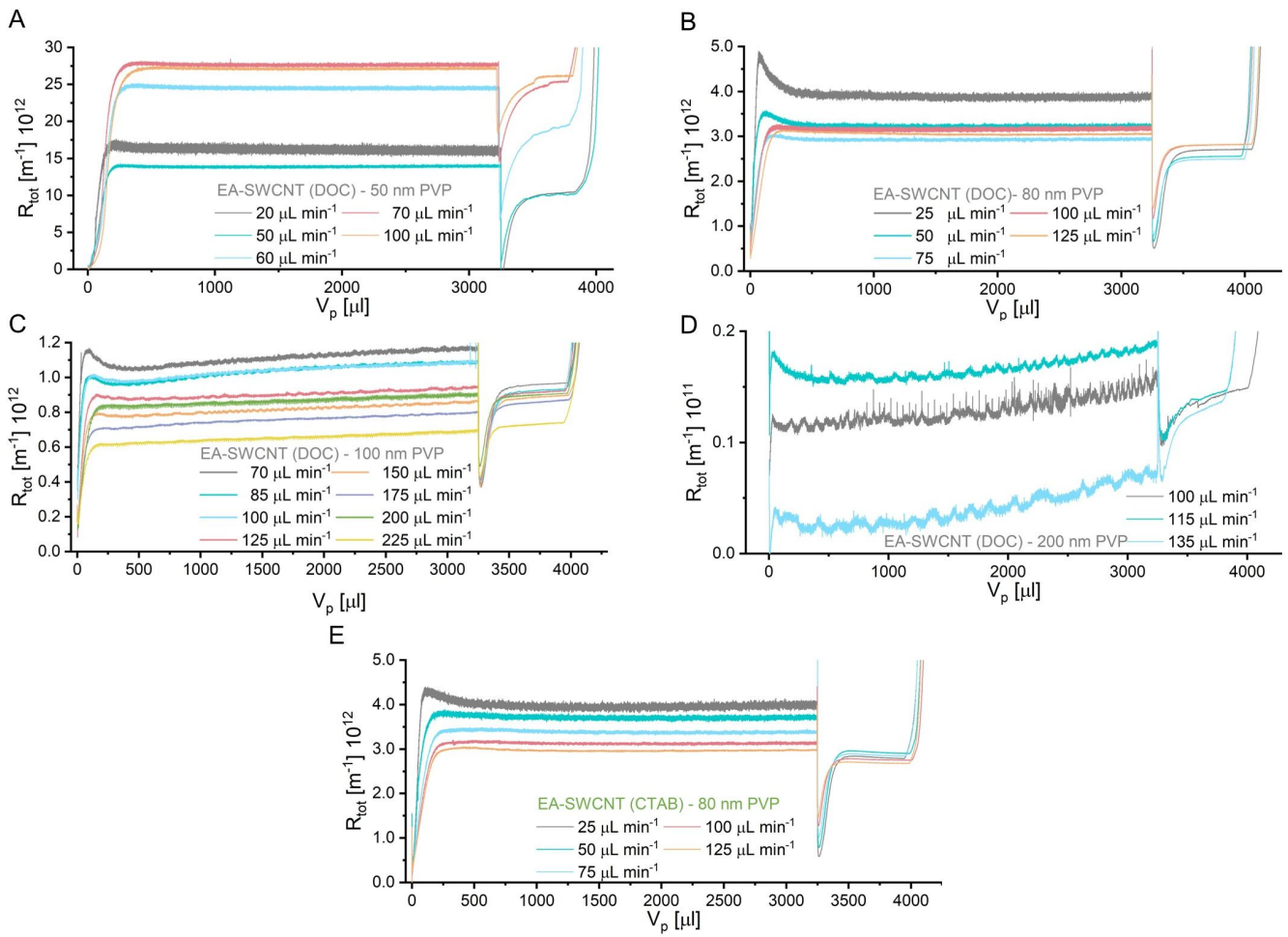


Figure A.5.: Total resistance curves for 4 mL of an $8 \mu\text{g mL}^{-1}$ unsorted EA-SWCNT dispersion in 0.04 wt% DOC on a (A) 50 nm, (B) 80 nm, (C) 100 nm (D) 200 nm (E) Total resistance curves for 4 mL of an $8 \mu\text{g mL}^{-1}$ EA-SWCNT dispersion in 0.02 wt% CTAB on an 80 nm (low resistance) membrane. In all cases the fast filtration step optimized for each membrane is shown. Figure reproduced from [1].

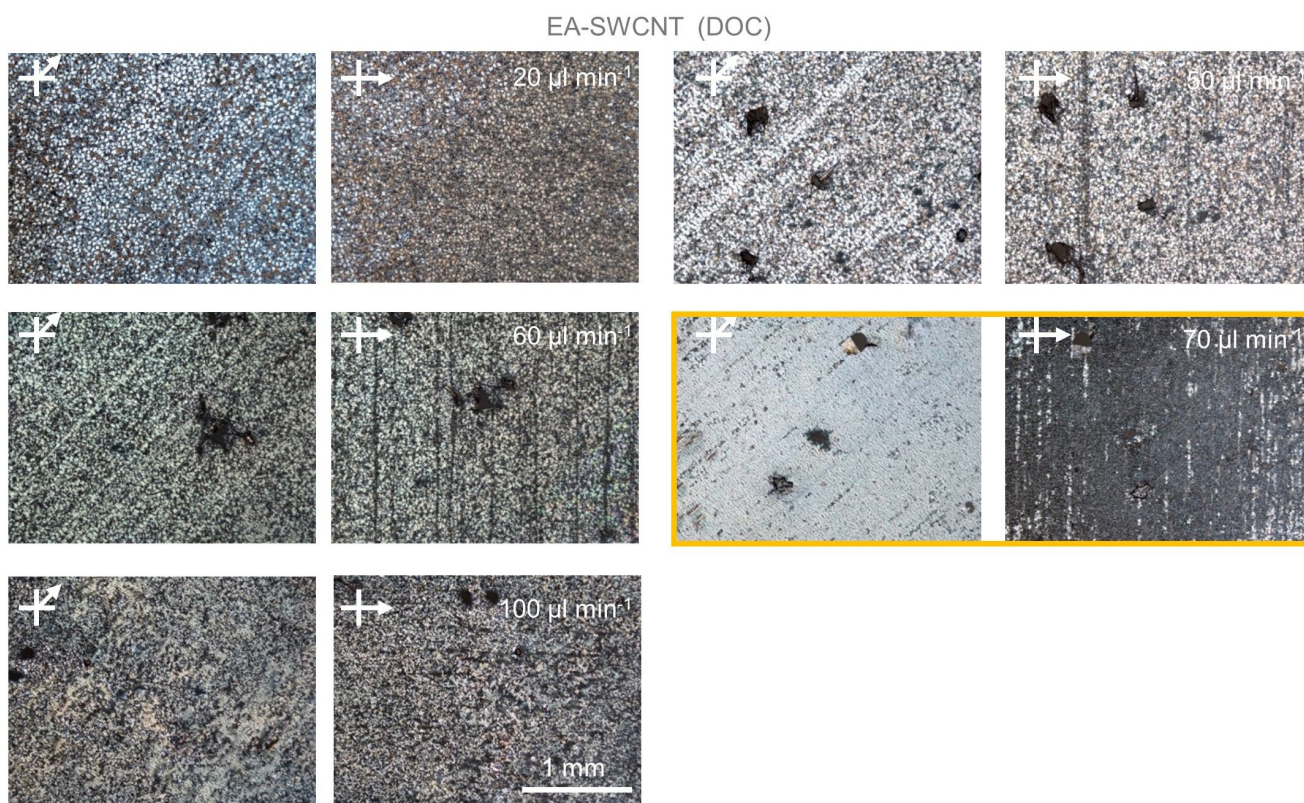


Figure A.6.: Cross polarized microscopy images corresponding to the slow flow series shown in Figure A.5 (A) for 4 mL of an $8 \mu\text{g mL}^{-1}$ unsorted EA-SWCNT dispersion in 0.04 wt% DOC with a push step of $200 \mu\text{L min}^{-1}$ on a 50 nm membrane. The optimum volume rate is marked with an orange box and corresponds to the lowest concentration polarization volume. The samples were transferred onto a silicon substrate for imaging. Figure reproduced from [1].



EA-SWCNT (DOC)

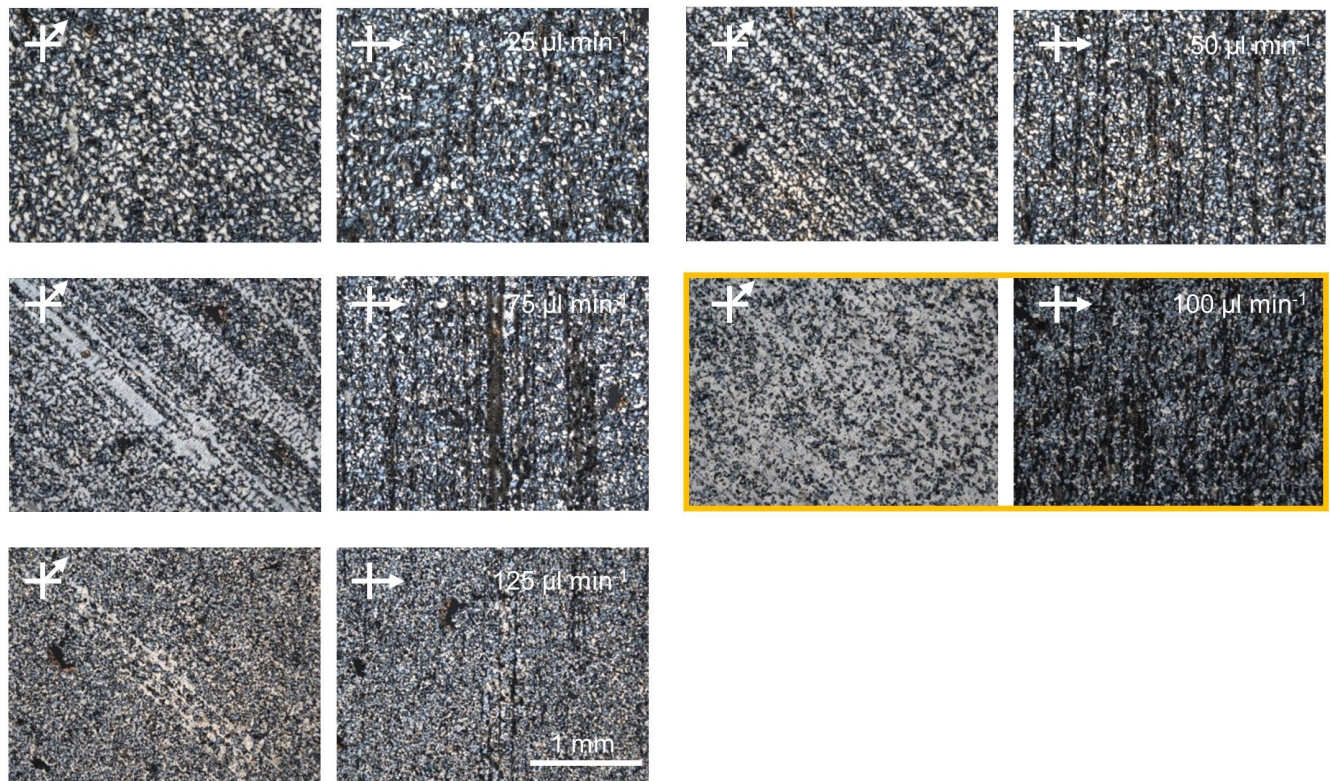


Figure A.7.: Cross polarized microscopy images corresponding to the slow flow series shown in Figure A.5 (B) for 4 mL of an $8 \mu\text{g mL}^{-1}$ unsorted EA-SWCNT dispersion in 0.04 wt% DOC with a push step of $500 \mu\text{L min}^{-1}$ on an 80 nm (low resistance) membrane. The optimum volume rate is marked with an orange box and corresponds to the lowest concentration polarization volume. The samples were transferred onto a silicon substrate for imaging. Figure reproduced from [1].

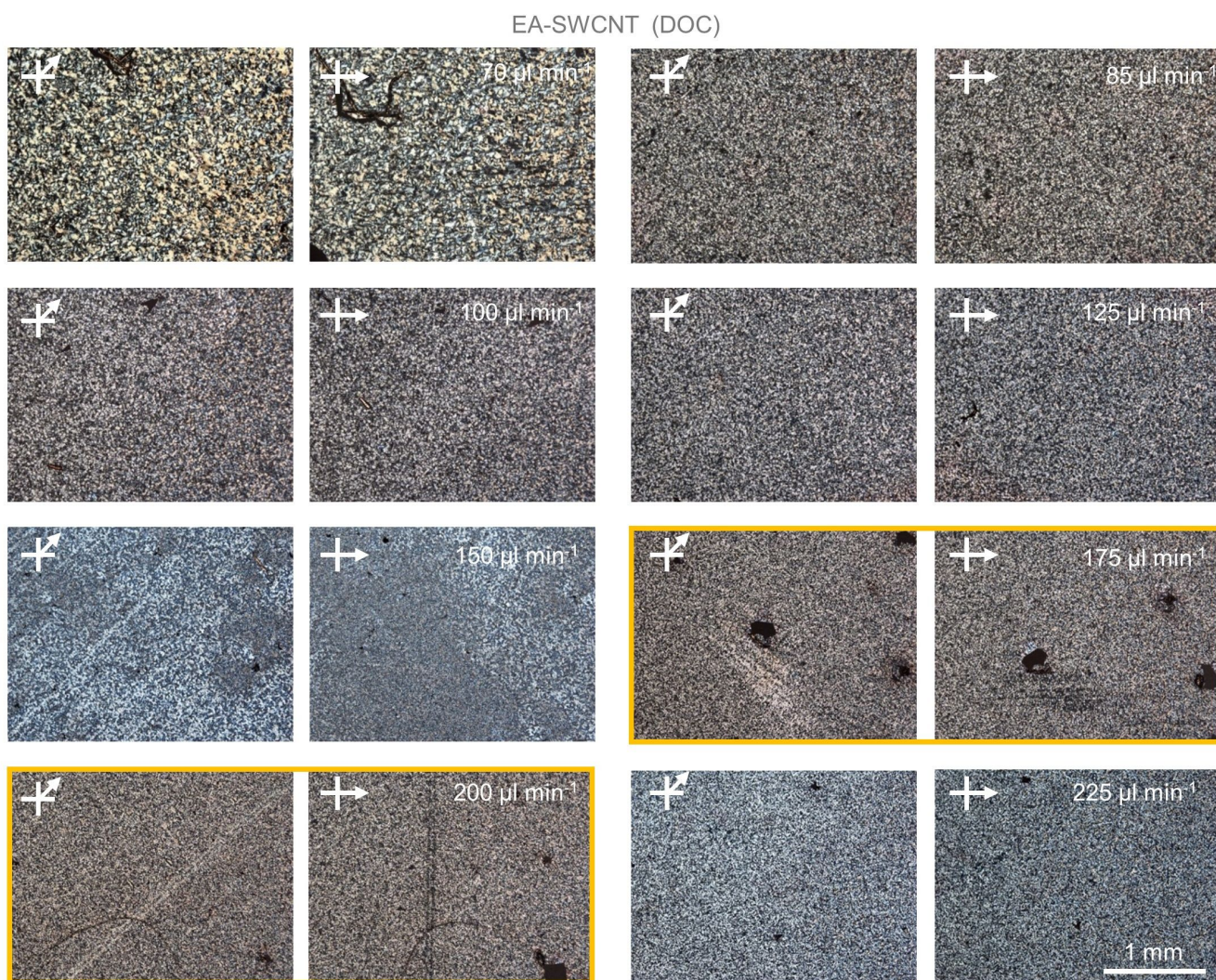


Figure A.8.: Cross polarized microscopy images corresponding to the slow flow series shown in Figure A.5 (C) for 4 mL of an $8 \mu\text{g mL}^{-1}$ unsorted EA-SWCNT dispersion in 0.04 wt% DOC with a push step of $700 \mu\text{L min}^{-1}$ on a 100 nm membrane. The optimum volume rate is marked with an orange box and corresponds to the lowest concentration polarization volume. The result obtained at $175 \mu\text{L min}^{-1}$ and $200 \mu\text{L min}^{-1}$ were indistinguishable from each other. The samples were transferred onto a silicon substrate for imaging. Figure reproduced from [1].

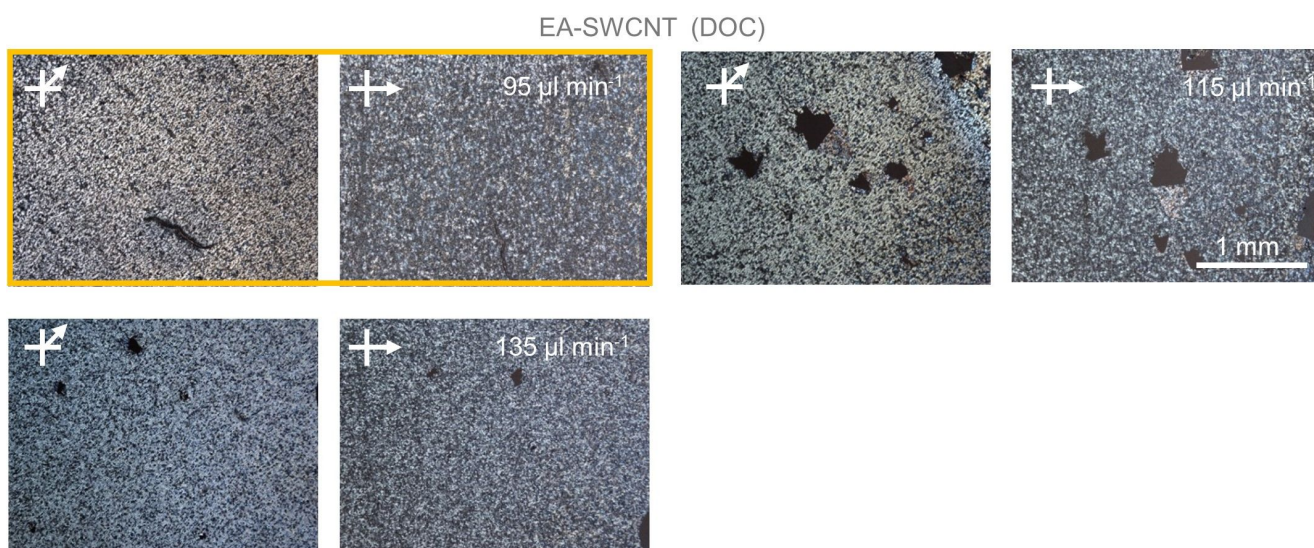


Figure A.9.: Cross polarized microscopy images corresponding to the slow flow series shown in Figure A.5 (D) for 4 mL of an $8 \mu\text{g mL}^{-1}$ unsorted EA-SWCNT dispersion in 0.04 wt% DOC with a push step of $700 \mu\text{L min}^{-1}$ on a 200 nm membrane. The optimum volume rate is marked with an orange box and corresponds to the lowest concentration polarization volume. The samples were transferred onto a silicon substrate for imaging. Figure reproduced from [1].

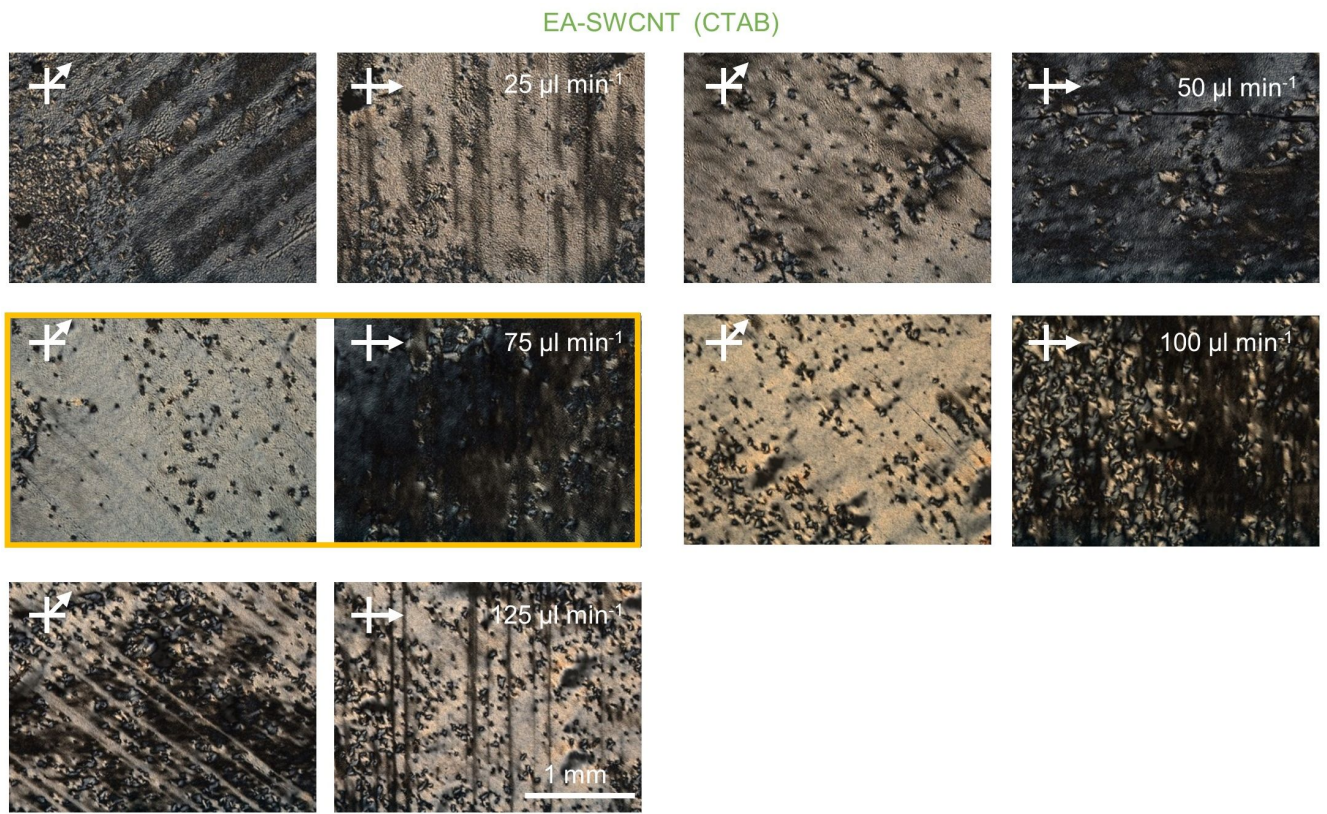


Figure A.10.: Cross polarized microscopy images corresponding to the slow flow series shown in Figure 3.6 (A) for 4 mL of an $8 \mu\text{g mL}^{-1}$ unsorted EA-SWCNT dispersion in 0.02 wt% CTAB with a push step of $400 \mu\text{L min}^{-1}$ on an 80 nm membrane. The samples were transferred onto a silicon substrate for imaging. Figure reproduced from [1].

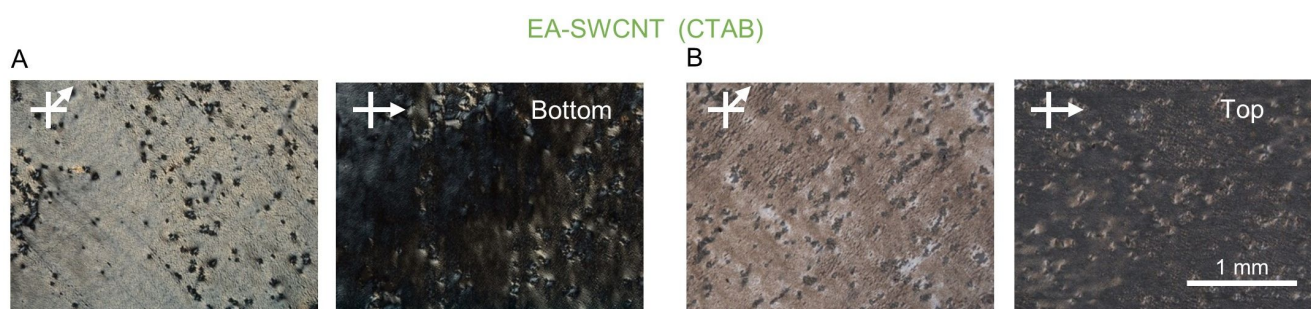


Figure A.11.: Cross polarized microscopy images of the (A) bottom (membrane side, transferred to a silicon substrate) and (B) top of the SWCNT film (on the membrane) obtained for 4 mL of an $8 \mu\text{g mL}^{-1}$ unsorted EA-SWCNT dispersion in 0.02 wt% CTAB filtered at $75 \mu\text{L min}^{-1}$ with a push step of $400 \mu\text{L min}^{-1}$ on an 80 nm membrane (low resistance). Figure reproduced from [1].

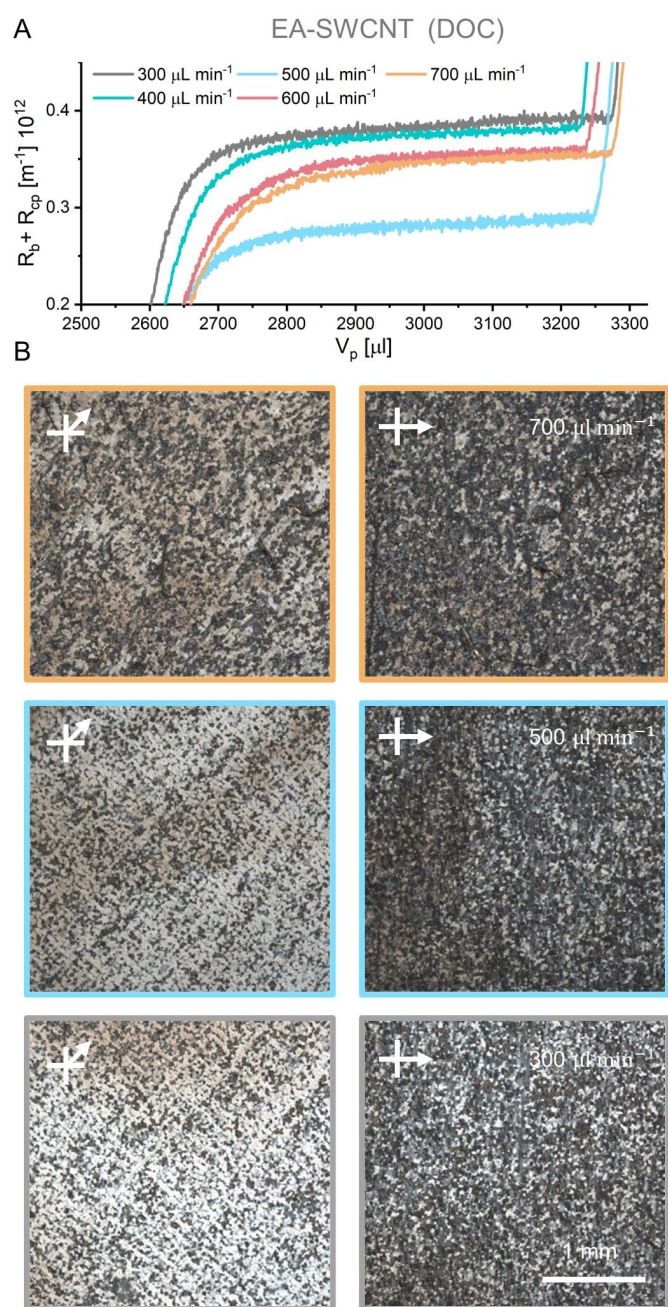


Figure A.12.: (A) Resistance measured after 2.5 mL of an $8 \mu\text{g mL}^{-1}$ dispersion of unsorted EA-SWCNTs with 0.04 wt% DOC filtered at $100 \mu\text{L min}^{-1}$ on an 80 nm membrane with push steps of $300 \mu\text{L min}^{-1}$ – $700 \mu\text{L min}^{-1}$. (B) Cross polarized micrography images of SWCNT films (transferred to silicon wafers) pushed at $200 \mu\text{L min}^{-1}$, $400 \mu\text{L min}^{-1}$ and $600 \mu\text{L min}^{-1}$. All films have been transferred to a silicon substrate. Figure reproduced from [1].

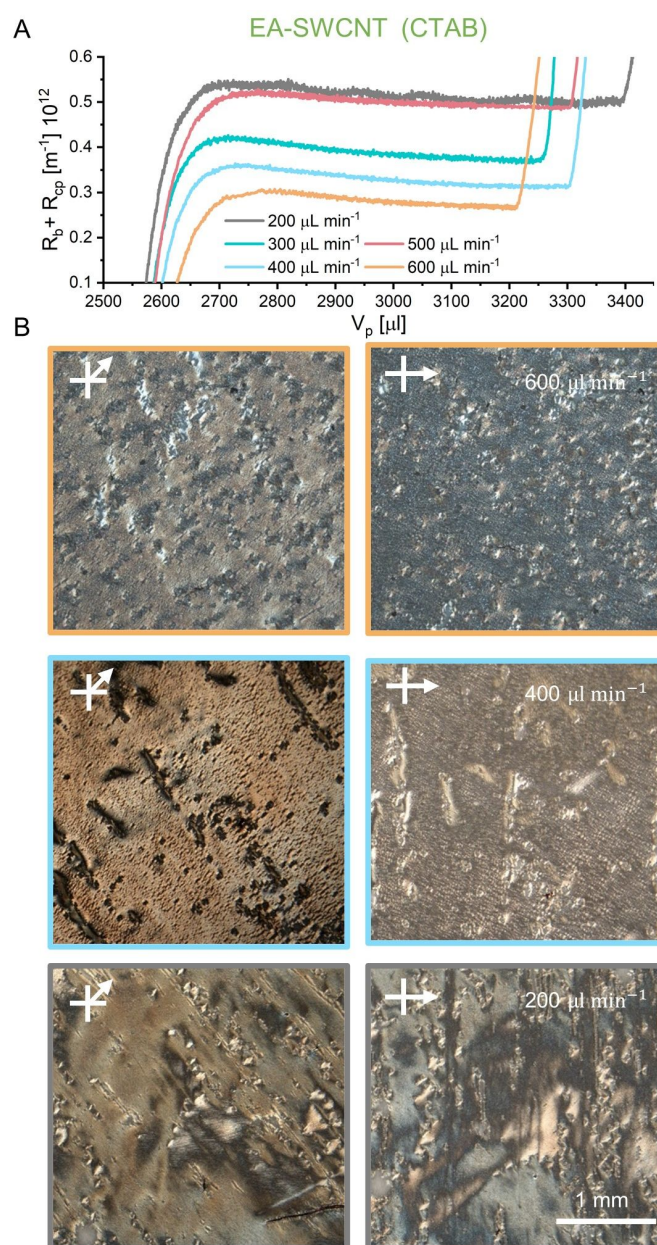


Figure A.13.: (A) Resistance measured after 2.5 mL of an $8 \mu\text{g mL}^{-1}$ dispersion of unsorted EA-SWCNTs with 0.02 wt% CTAB filtered at $100 \mu\text{L min}^{-1}$ on an 80 nm membrane with push steps of $200 \mu\text{L min}^{-1}$ – $600 \mu\text{L min}^{-1}$. (B) Cross polarized micrography images of SWCNT films (transferred to silicon wafers) pushed at $200 \mu\text{L min}^{-1}$, $400 \mu\text{L min}^{-1}$ and $600 \mu\text{L min}^{-1}$. All films have been transferred to a silicon substrate. Figure reproduced from [1].

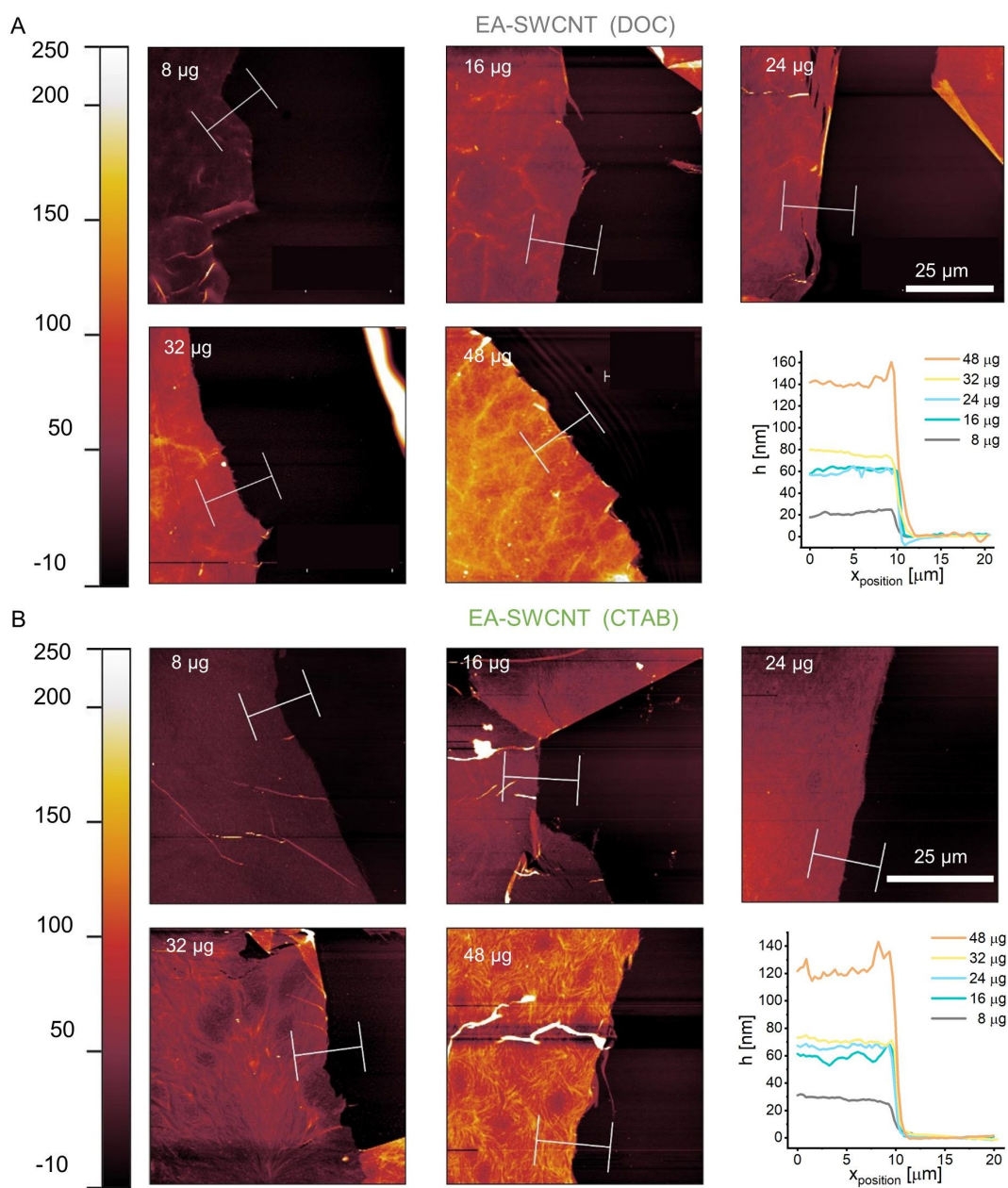


Figure A.14.: AFM topographies for (A) 1 mL – 6 mL of an $8 \mu\text{g mL}^{-1}$ dispersion of unsorted EA-SWCNTs with 0.04 wt% DOC on an 80 nm membrane with a $100 \mu\text{L min}^{-1}$ filtration step and push volume rate of $500 \mu\text{L min}^{-1}$ and (B) 1 mL – 6 mL of an $8 \mu\text{g mL}^{-1}$ dispersion of unsorted EA-SWCNTs with 0.02 wt% CTAB on an 80 nm membrane with a $75 \mu\text{L min}^{-1}$ filtration step and push volume rate of $400 \mu\text{L min}^{-1}$. In all images the averaged area ($10 \times 20 \mu\text{m}^2$) used to generate the height profiles is shown. Figure reproduced from [1].

EA-SWCNT (DOC)

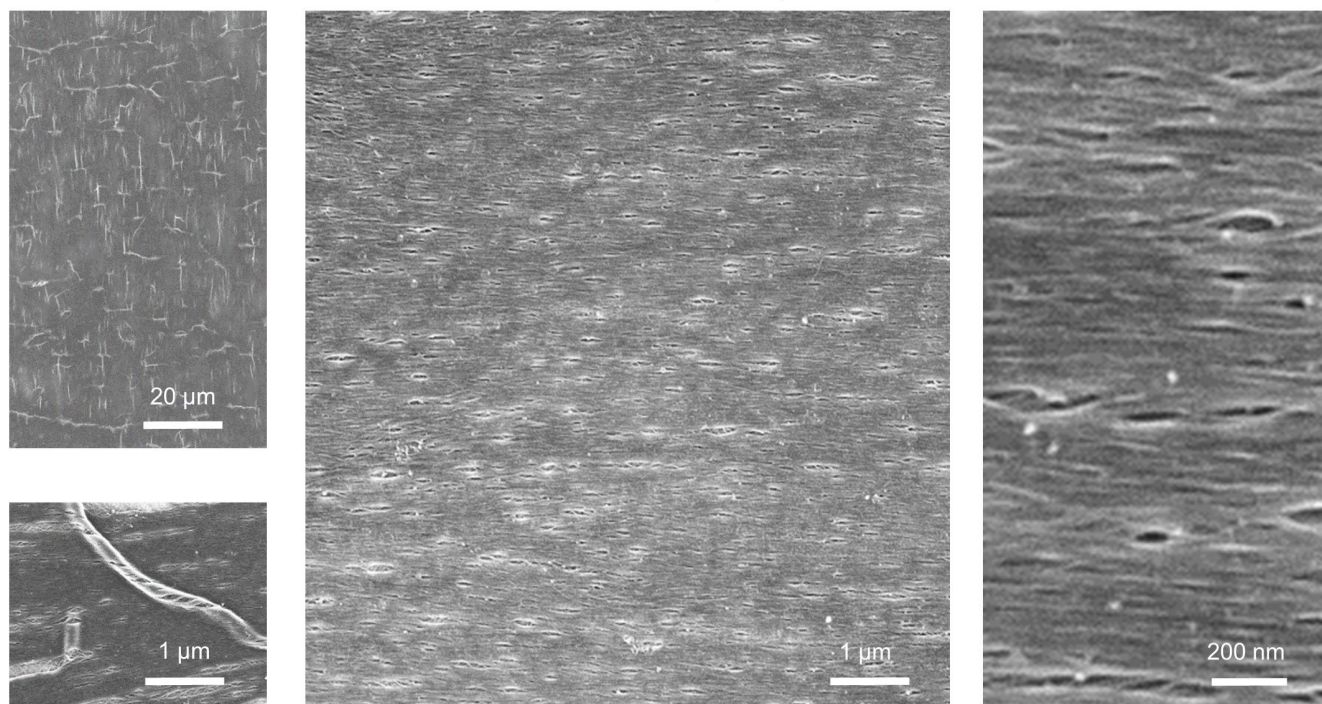


Figure A.15.: SEM images of the SWCNT film obtained from filtration of 20 mL of a $1.2 \mu\text{g mL}^{-1}$ dispersion of unsorted EA-SWCNTs with 0.06 wt% DOC at a volume rate of $100 \mu\text{L min}^{-1}$ and with a push step of $500 \mu\text{L min}^{-1}$ on an 80 nm membrane. The total mass of SWCNTs filtered was 24 μg and the film was transferred to ITO. Figure reproduced from [1].

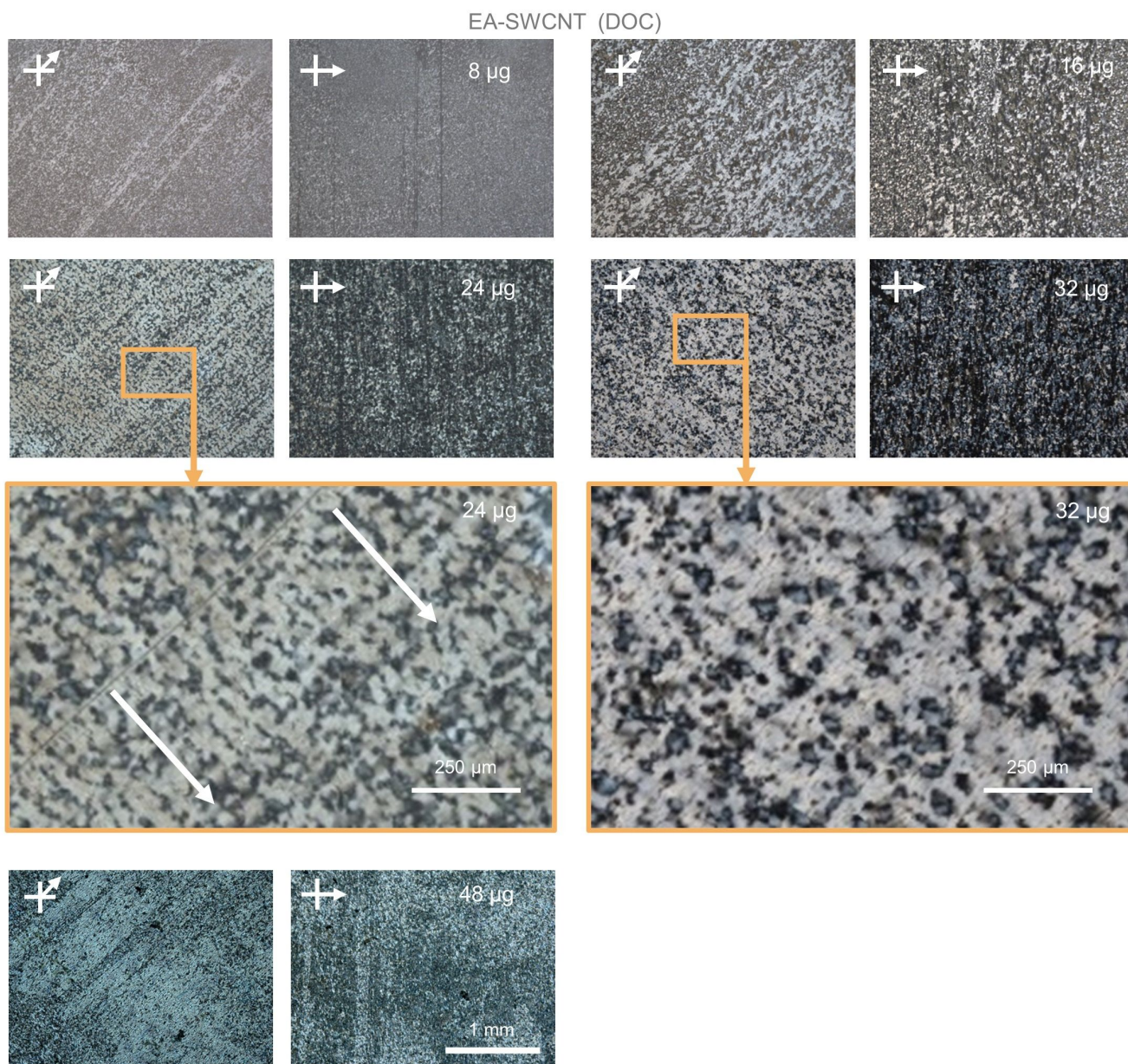


Figure A.16.: Cross polarized microscopy images of films made from 1 mL – 6 mL of an $8 \mu\text{g mL}^{-1}$ dispersion of EA-SWCNTs with 0.04 wt% DOC on an 80 nm membrane with a $100 \mu\text{L min}^{-1}$ slow filtration step and a push volume rate of $500 \mu\text{L min}^{-1}$. For 24 μg and 32 μg the mass is insufficient to completely fill the membrane and many holes (dark spots in the bright image) are visible. At 24 μg the membrane is fully covered while the single domains start to form overlayers (32 μg), which eventually cover the whole surface (48 μg). All films have been transferred to a silicon substrate. Figure reproduced from [1].

A.3. Hot-Embossing of Membranes with Axial Patterns

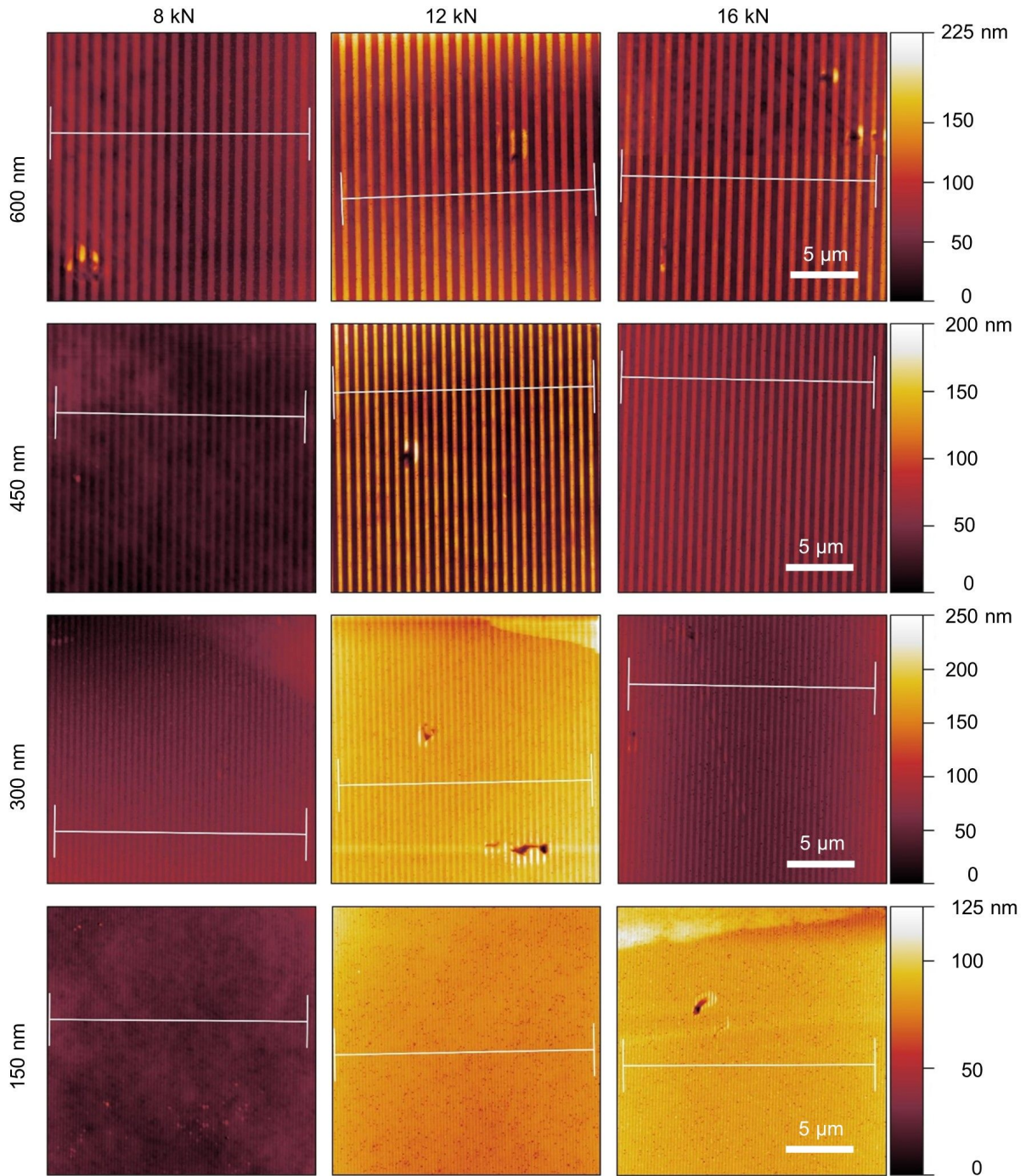


Figure A.17.: AFM topographies of an 80 nm membrane hot embossed with an applied force of 8 kN – 16 kN at $\approx 120^\circ\text{C}$. Figure reproduced from [1].

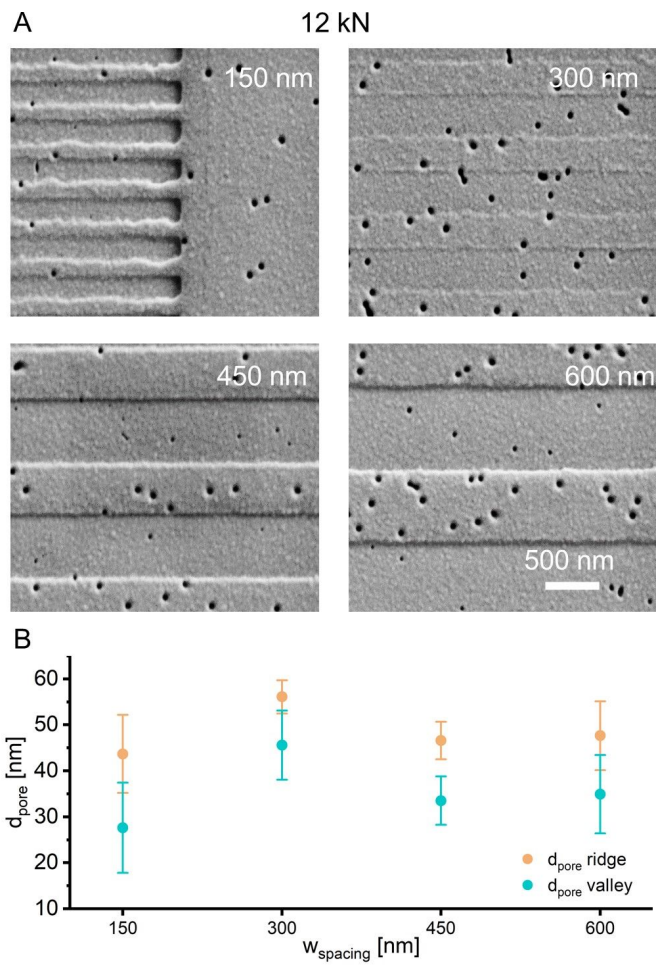


Figure A.18.: (A) SEM images used to evaluate the pore sizes after hot embossing of an 80 nm membrane at 12 kN. The pores located on the ridges are larger compared to those in the valleys due to an inhomogeneous distribution of force during embossing, which is plotted in the graph shown in (B). Figure reproduced from [1].

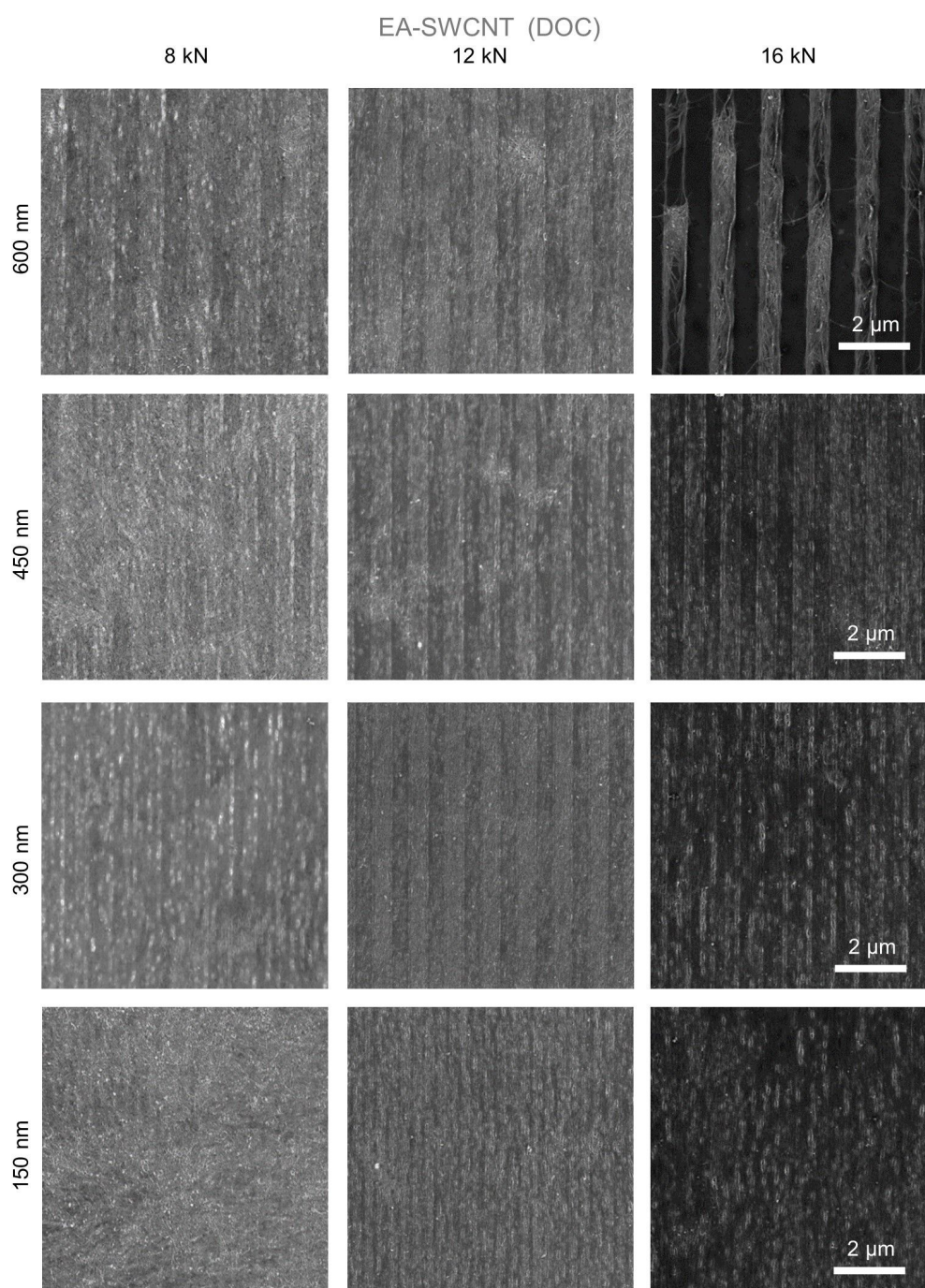


Figure A.19.: SEM images of the SWCNT film obtained by filtration of 2 mL of an $8 \mu\text{g mL}^{-1}$ unsorted EA-SWCNT dispersion in 0.04 wt% DOC at $100 \mu\text{L min}^{-1}$ with a push step of $500 \mu\text{L min}^{-1}$ on 150 – 600 nm grooves imprinted on an 80 nm at 8 kN – 16 kN. Note: At 8 kN, the pattern was poorly reproduced for 150 nm and this resulted in weak alignment for this pattern. At 16 kN, the formation of stripes can be observed for the 600 nm pattern due to excessive deformation of the membrane. Figure reproduced from [1].

A.4. Raman Analysis of Aligned EA-SWCNT-films

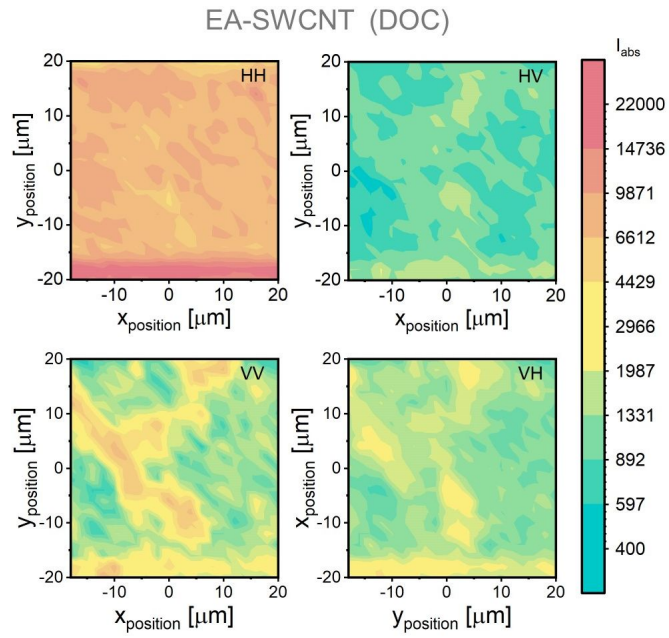


Figure A.20.: Raman intensities I_{HH} , I_{HV} , I_{VV} and I_{VH} used for the calculation of S_{2D} in combination with the dichroic ratio ($\Delta_{532nm} = 1.55$) determined in 3.11 (A). The grain boundary is most visible in I_{VV} . Figure reproduced from [1].

A.5. Hot-Embossing of Membranes with Radial Patterns

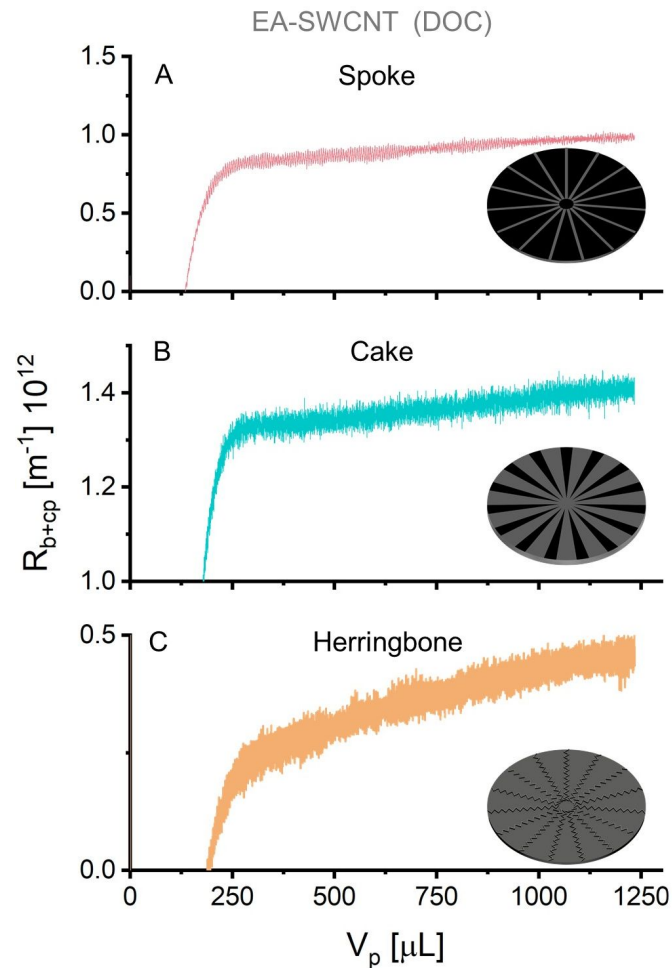


Figure A.21.: Evolution of the filtration resistance for 1.25 mL of $8 \mu\text{g mL}^{-1}$ unsorted EA-SWCNTs (0.04 wt% DOC) at $100 \mu\text{L min}^{-1}$ for (A) spoke, (B) cake and (C) herringbone patterned membranes. In order to calculate R_{b+cp} , the membrane resistance $R_m = 2.43 \times 10^{12} \text{ m}^{-1}$ has been taken from Figure 3.1. The final 0.75 mL were filtered at $500 \mu\text{L min}^{-1}$ and are not shown here. All filtration curves show direct cake-filtration behavior without any concentration polarization regime indicated by an immediate linear increase in resistance, except the filtration using the HB-patterned membrane, showing an intermediate blocking behavior (logarithmic increase of resistance). Figure reproduced from [2].

EA-SWCNT (DOC)

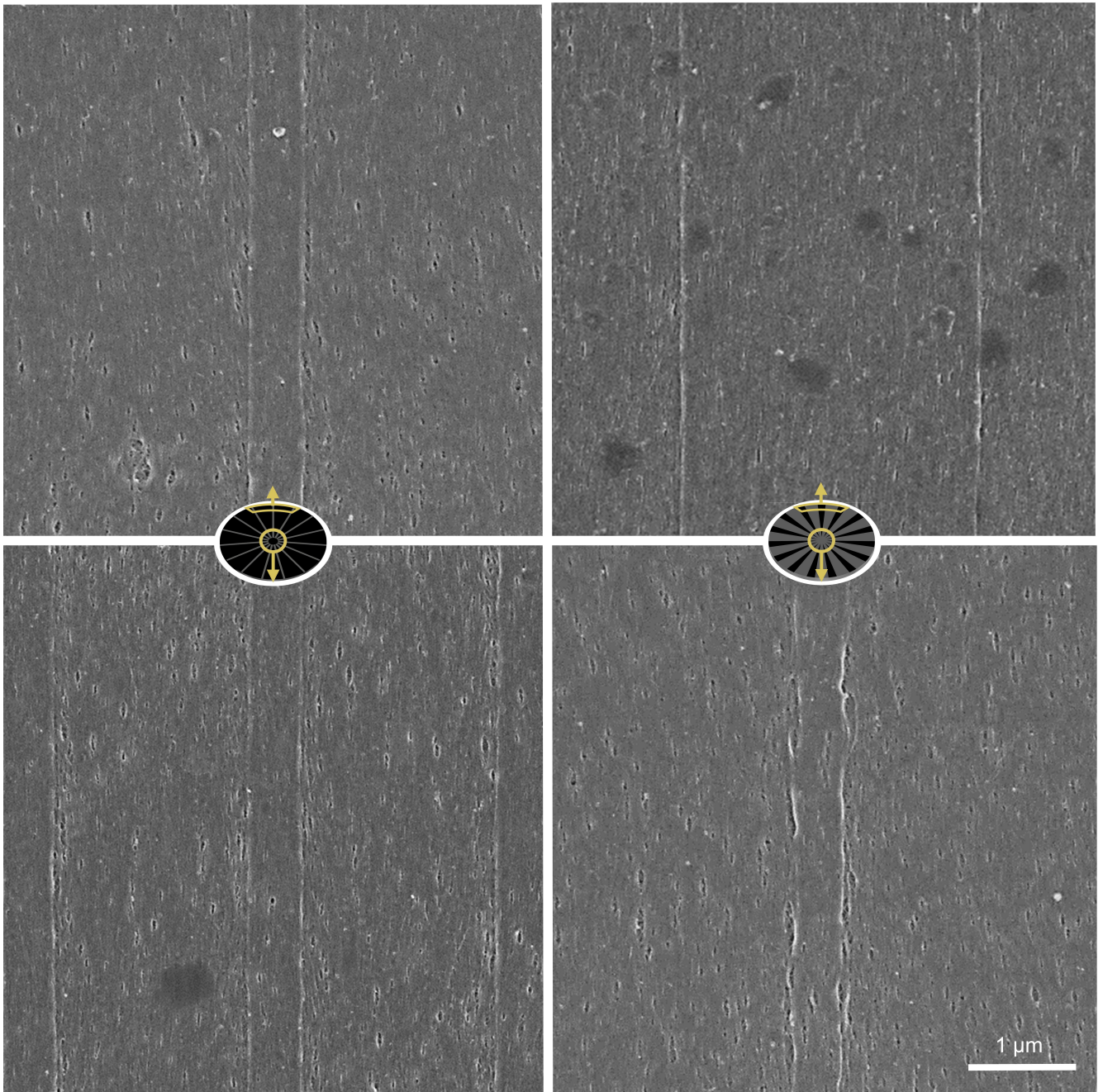


Figure A.22.: Higher magnified SEM images of the CA and SP pattern, showing a homogeneous coverage by the unsorted EA-SWCNTs. Figure reproduced from [2].

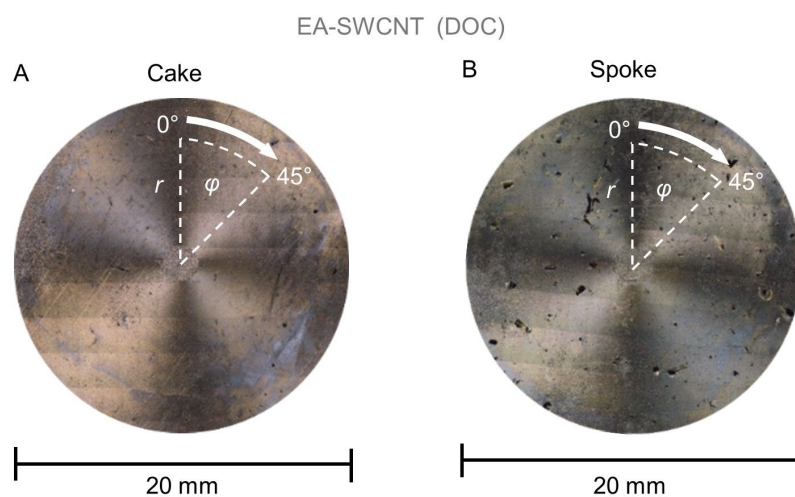


Figure A.23.: Placement of the radius r and film angle ϕ on the CA (A) and SP (B) films for the calculation of the accumulated intensity shown in Figure 3 (B). Therefore, the radius r is extending by 7.5 mm and does not include the unpatterned region ($r < 1$ mm) in the middle. The film angle ϕ is increasing in the clockwise direction starting from the 12 'o clock position. Figure reproduced from [2].

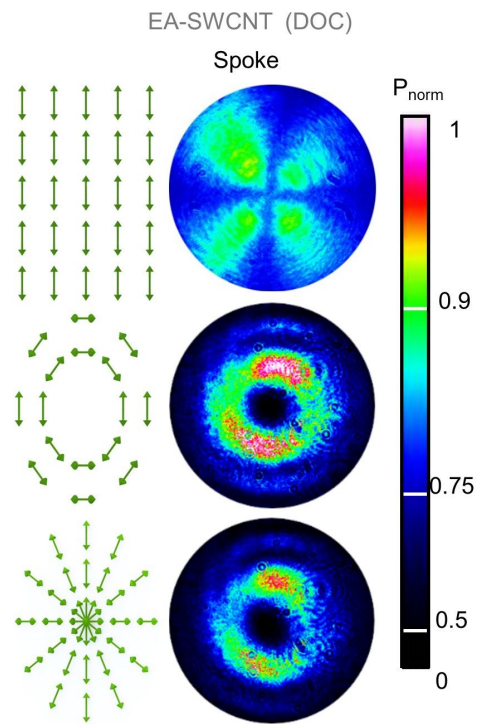


Figure A.24.: Laser transmittance measurements made with linear, azimuthal and radial polarized light fields with the SP film. The total power of the light reaching the beam profiler using the azimuthal light field was $5.55 \mu\text{W}$ and for the radial field $4.48 \mu\text{W}$. Figure reproduced from [2].

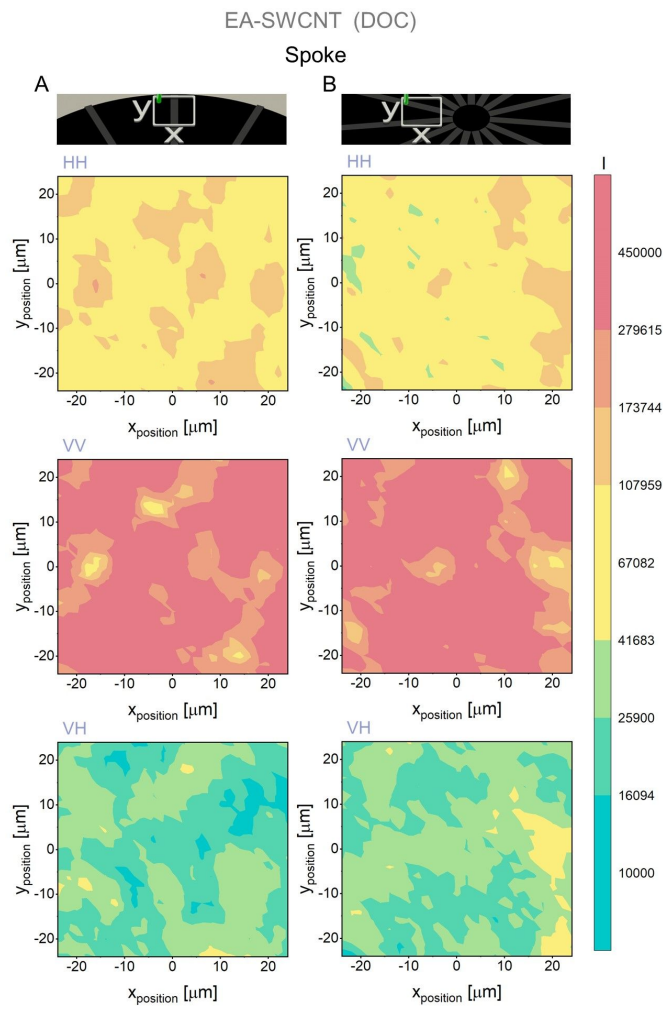


Figure A.25.: Intensity components I_{HH} , I_{VV} and I_{VH} used to evaluate the order parameter S_{2D} at (A) the perimeter and (B) the centre of a spoke patterned SWCNT. Figure reproduced from [2].

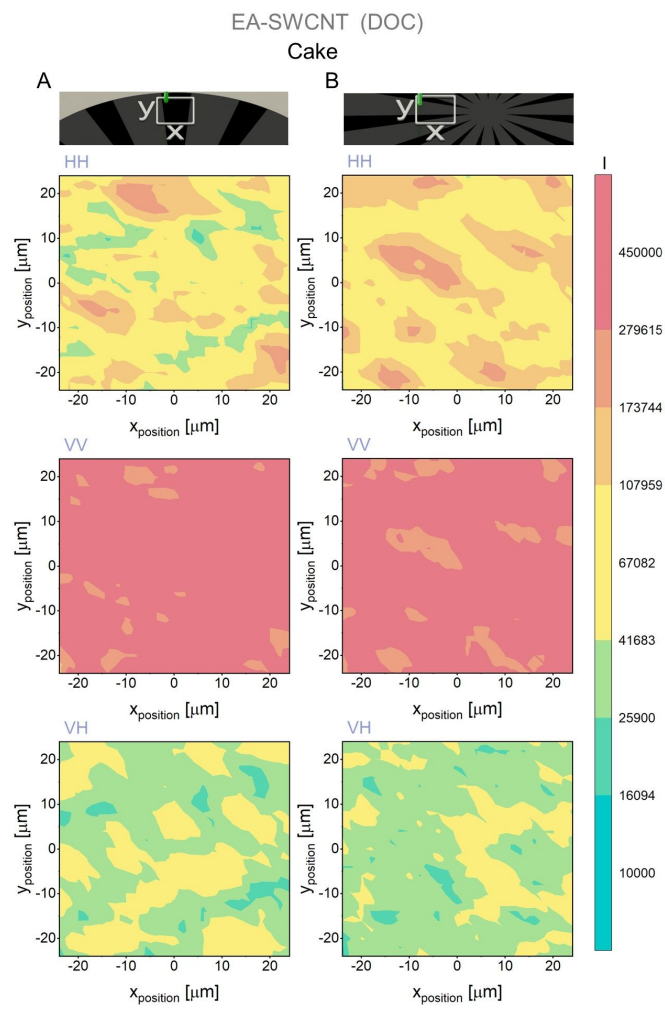


Figure A.26.: Intensity components I_{HH} , I_{VV} and I_{VH} used to evaluate the order parameter S_{2D} at (A) the perimeter and (B) the centre of a cake patterned SWCNT. Figure reproduced from [2].

A.6. Length-Sorting of EA- and CoMoCAT-SWCNTs

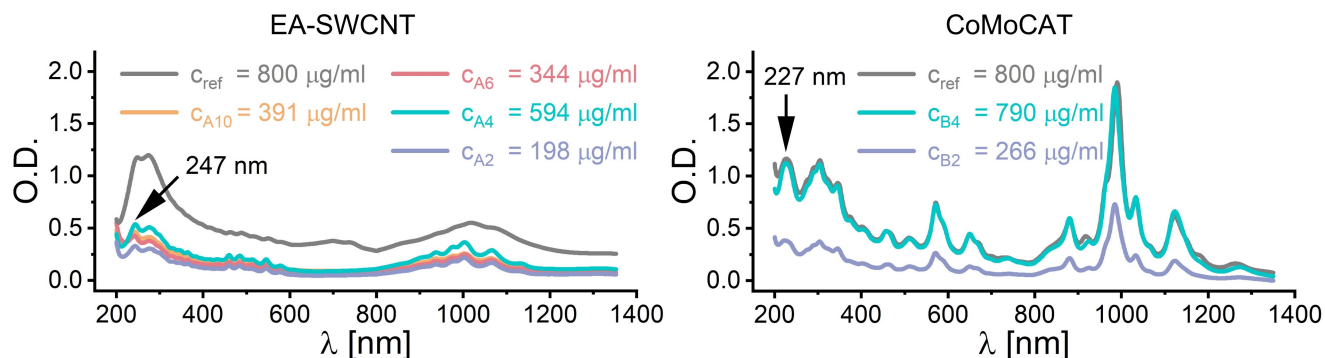


Figure A.27.: Absolute absorbance spectra of the SWCNT samples after dilution plotted as optical density (O.D.) as a function of wavelength λ . The concentration of each fraction was estimated using the π -plasmon peak (274 nm for EA-SWCNTs and 227 nm for CoMoCAT SWCNTs). Enrichment of the dispersions was performed by repeatedly filtering the dispersions onto a microfiltration membrane (300 kDa) similar to the unsorted EA-SWCNTs. The DOC-surfactant concentration of the enriched samples was 1 wt%. This allowed for concentration adjustment of all intermediate stock solutions to $8 \mu\text{g mL}^{-1}$ SWCNTs and 0.04 wt% DOC. For filtration, 1 mL, 1.5 mL or 3 mL of this intermediate solution was diluted to 20 mL with H_2O (d), leading to $8 \mu\text{g}$ ($0.4 \mu\text{g mL}^{-1}$ SWCNTs, 0.02 wt% DOC), $12 \mu\text{g}$ ($0.6 \mu\text{g mL}^{-1}$ SWCNTs, 0.03 wt% DOC), or $24 \mu\text{g}$ ($1.2 \mu\text{g mL}^{-1}$ SWCNTs, 0.06 wt% DOC) being deposited onto the membrane, respectively. Figure reproduced from [3].

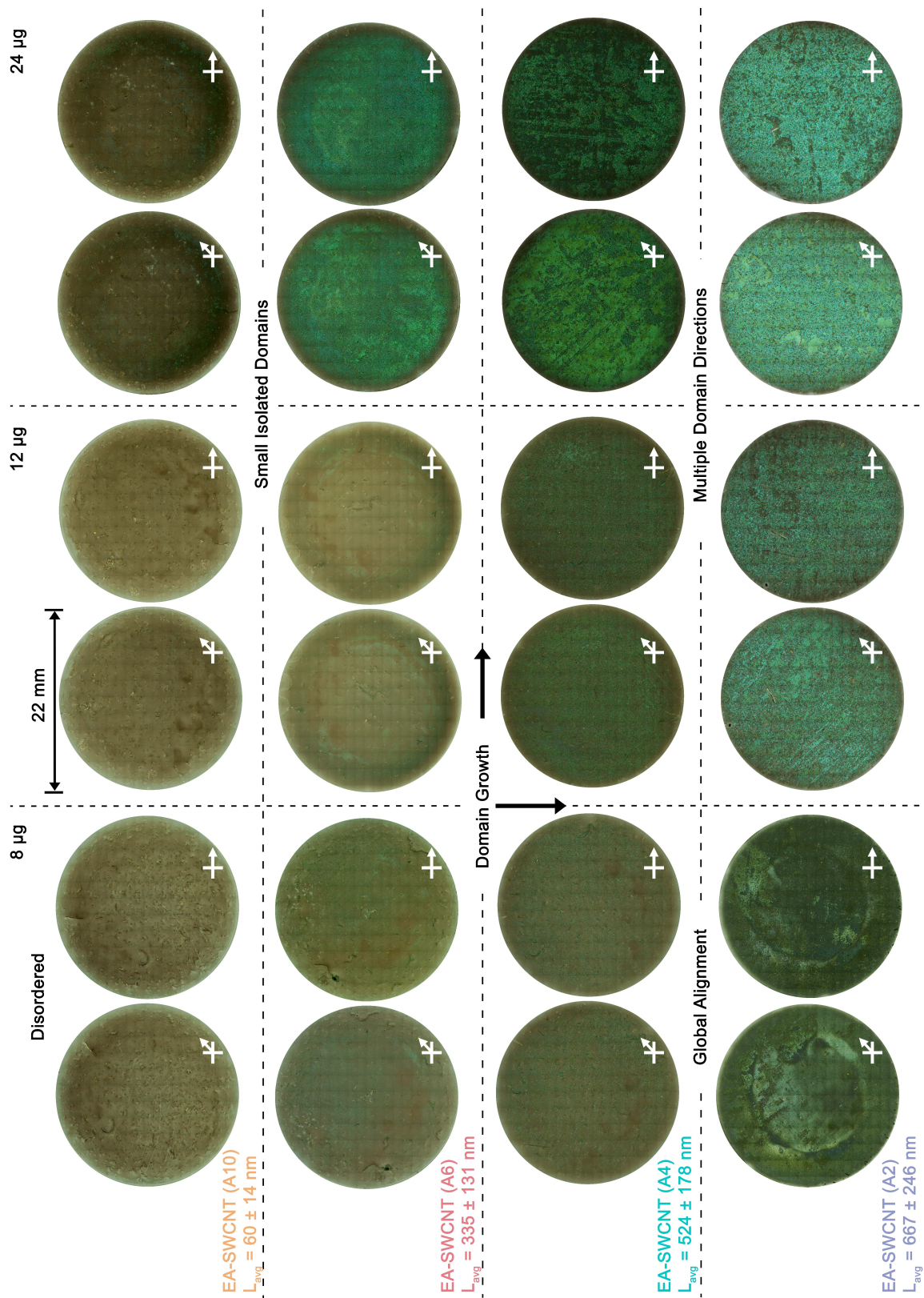


Figure A.28.: Cross polarized microscopy of EA-SWCNT films from length fractions A10 – A2 in the bright (45°) and dark (0°) orientation. Images were recorded with the SWCNT film on the polycarbonate track-etched (PCTE) membrane. Figure reproduced from [3].

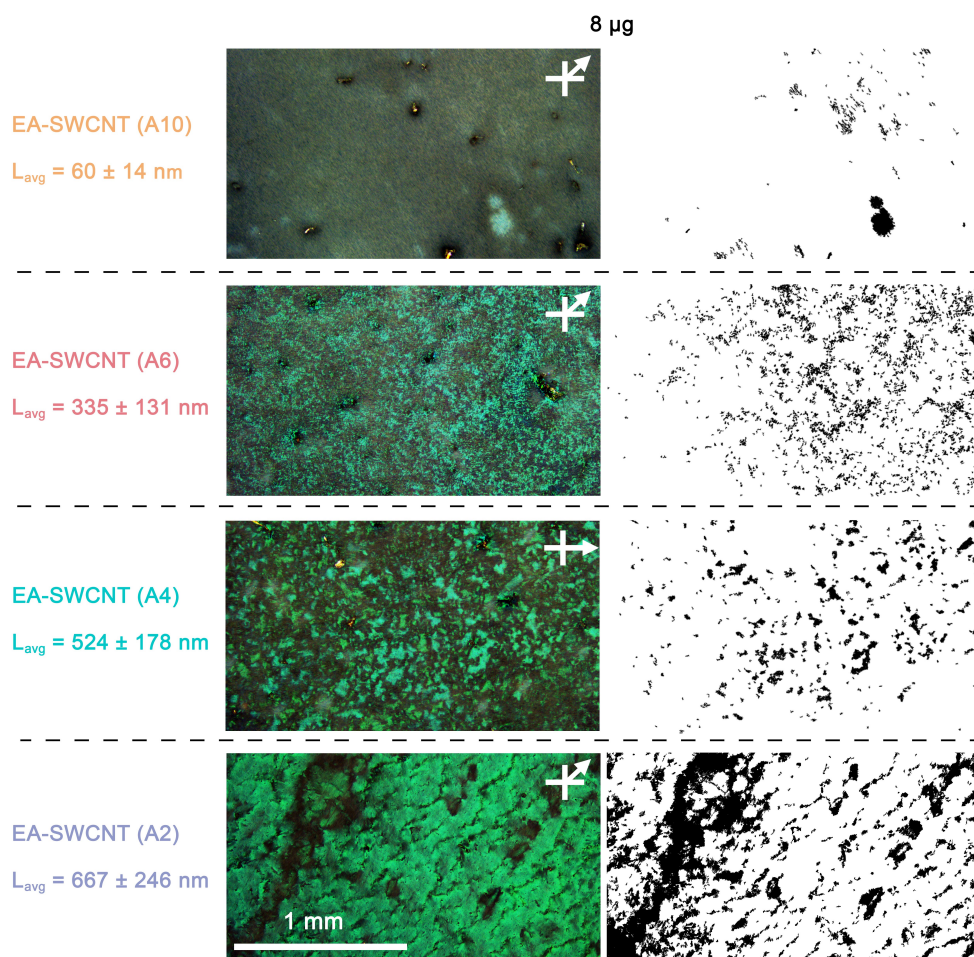


Figure A.29.: Cross polarized microscopy of EA-SWCNT films from 8 μg of the length sorted fractions A10 through A2 in the bright (45°) and dark (0°) orientation. Images were recorded with the SWCNT film on the PCTE membrane. Figure reproduced from [3].

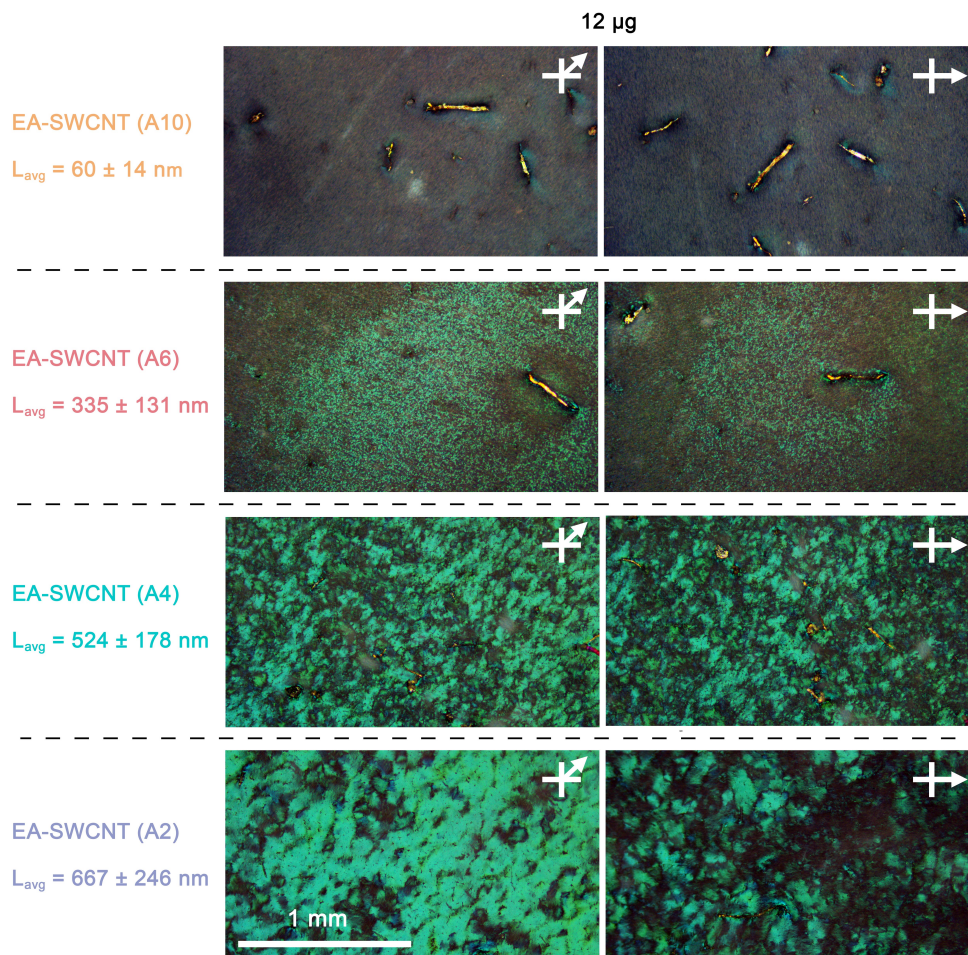


Figure A.30.: Cross polarized microscopy of EA-SWCNT films from 12 μg of the length sorted fractions A10 through A2 in the bright (45°) and dark (0°) orientation. Images were recorded with the SWCNT film on the PCTE membrane. Figure reproduced from [3].

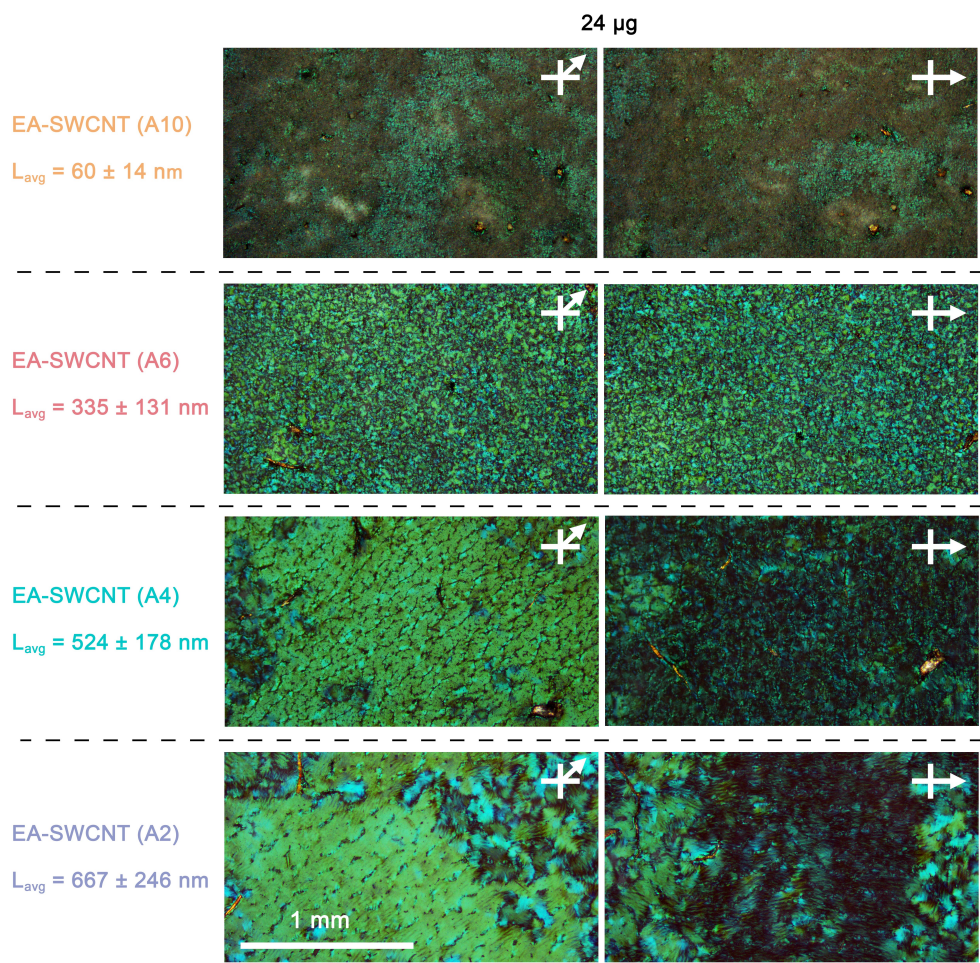


Figure A.31.: Cross polarized microscopy of EA-SWCNT films from 24 μg of the length sorted fractions A10 through A2 in the bright (45°) and dark (0°) orientation. Images were recorded with the SWCNT film on the PCTE membrane. Figure reproduced from [3].

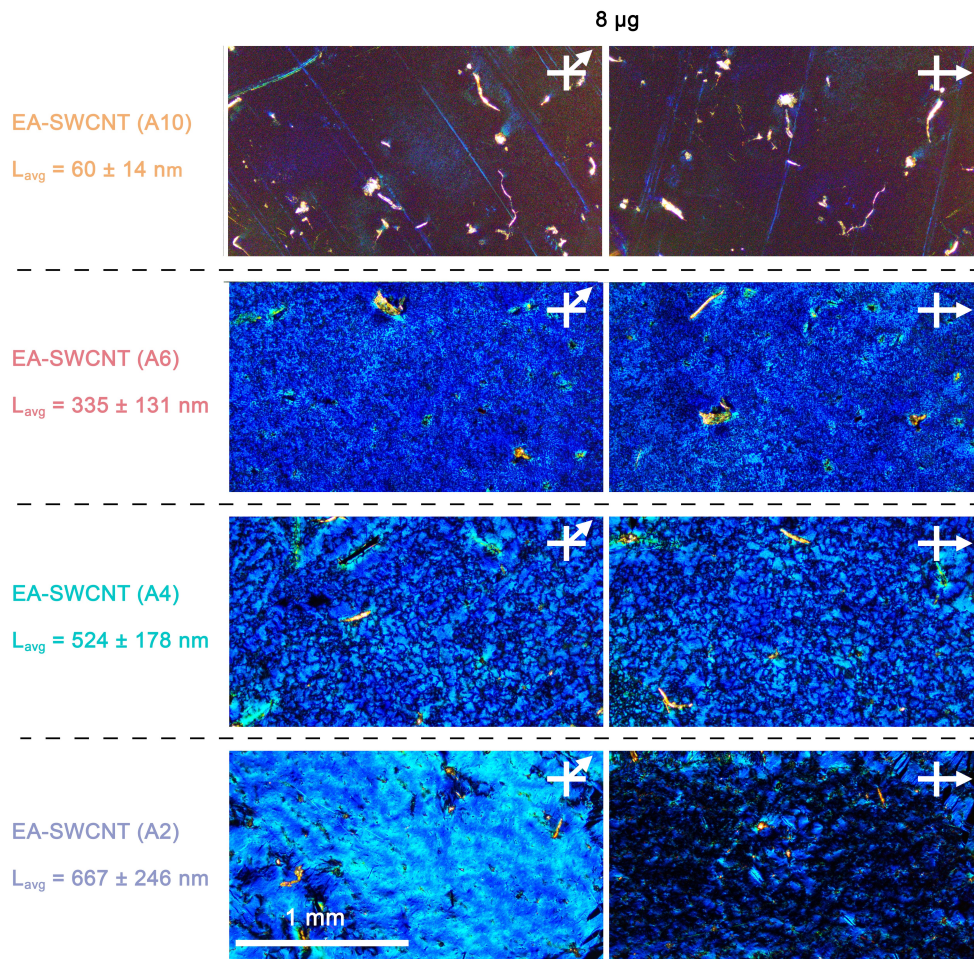


Figure A.32.: Cross polarized microscopy of the back side (membrane contact side) of the EA-SWCNT films from 8 μg of the length sorted fractions A10 through A2 in the bright (45°) and dark (0°) orientation. Images were recorded after transfer of the SWCNT film to a silicon wafer. Figure reproduced from [3].

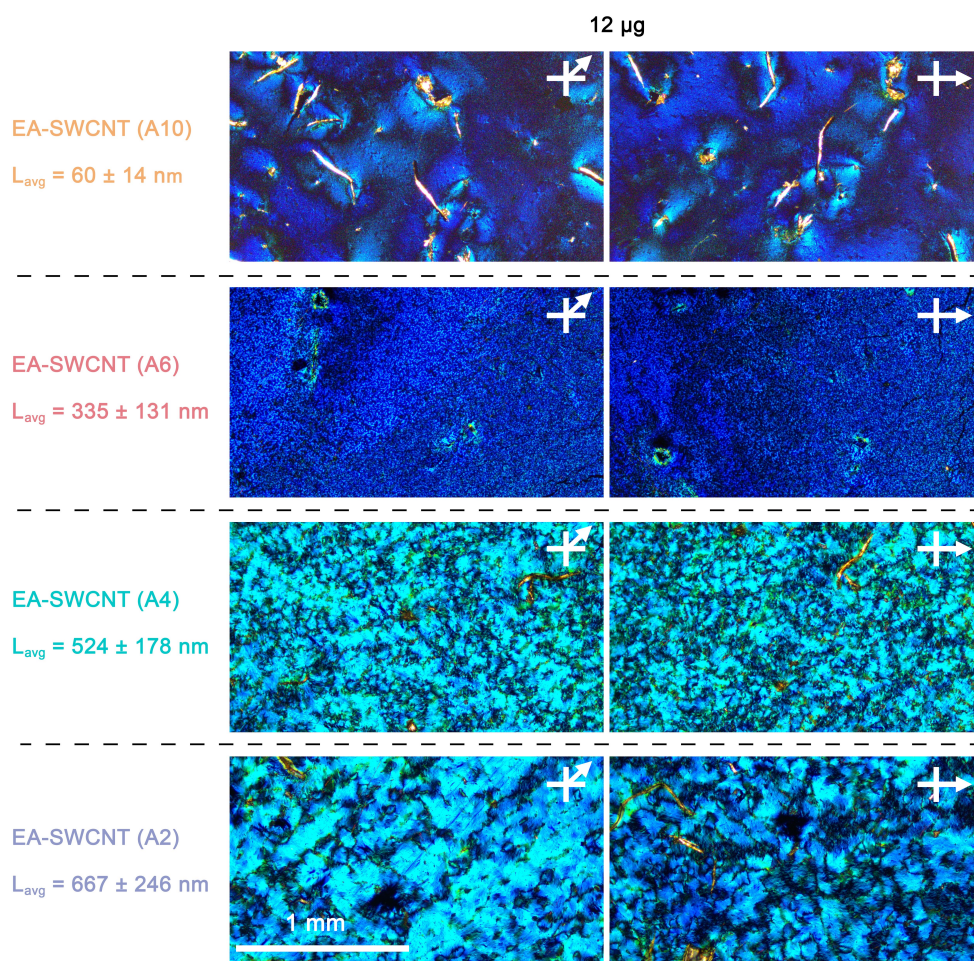


Figure A.33.: Cross polarized microscopy of the back side (membrane contact side) of the EA-SWCNT films from 12 μg of the length sorted fractions A10 through A2 in the bright (45°) and dark (0°) orientation. Images were recorded after transfer of the SWCNT film to silicon. Figure reproduced from [3].

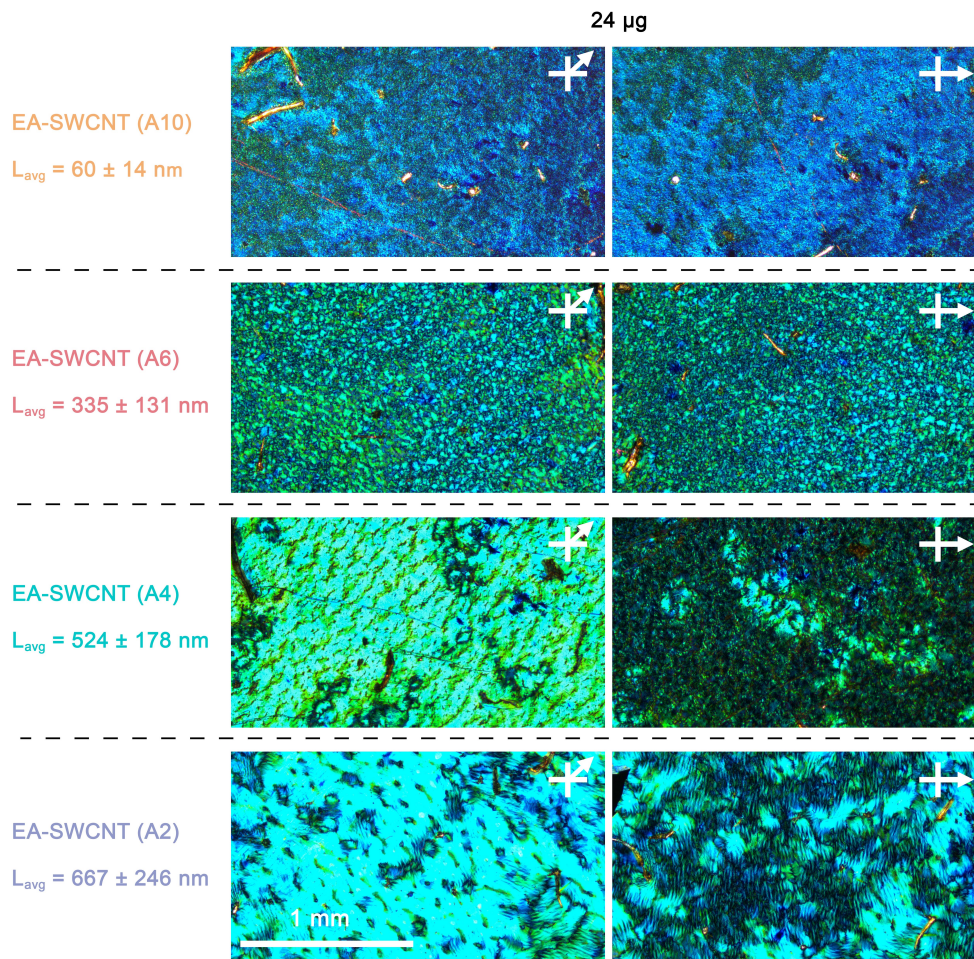


Figure A.34.: Cross polarized microscopy of the back side (membrane contact side) of the EA-SWCNT films from 12 μg of the length sorted fractions A10 through A2 in the bright (45°) and dark (0°) orientation. Images were recorded after transfer of the SWCNT film to silicon. Figure reproduced from [3].

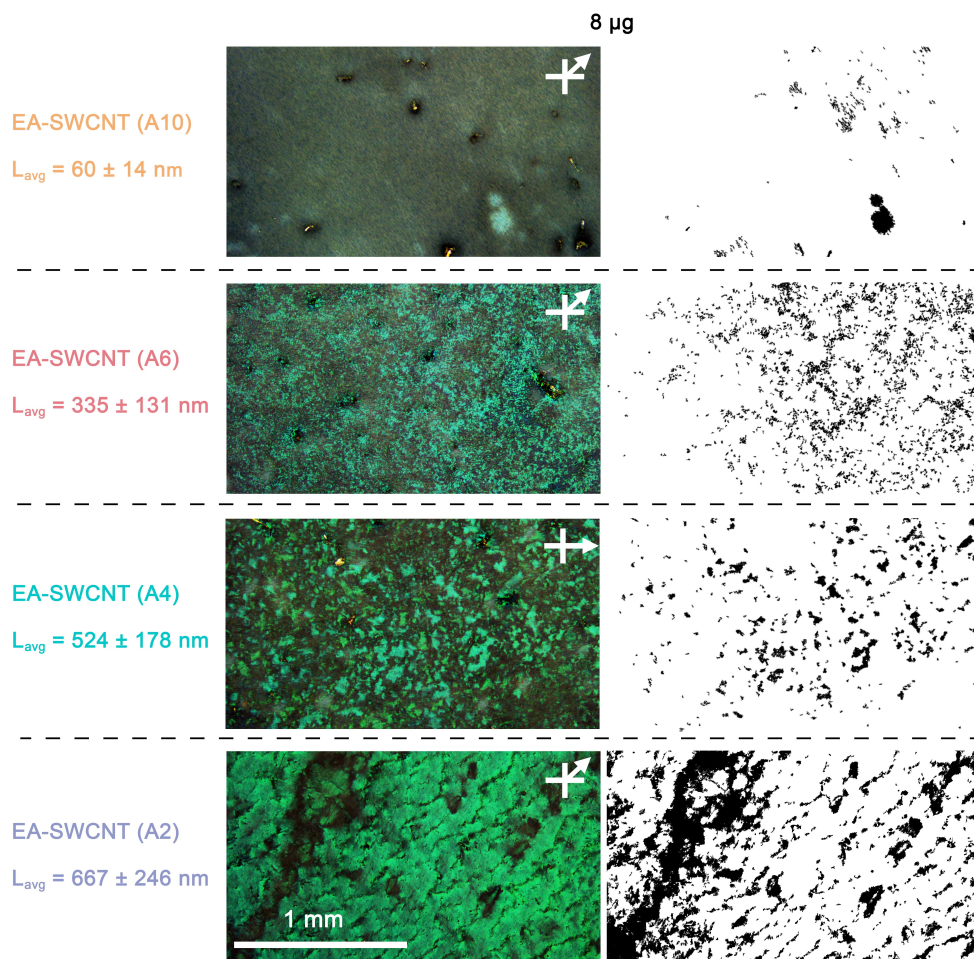


Figure A.35.: Cross polarized microscopy of EA-SWCNT films from 8 μg of the length sorted fractions A10 through A2 in the bright (45°) or dark (0°) orientation and maps of the detected grains (A10 through A4) or grain boundaries (A2) using machine vision. Figure reproduced from [3].

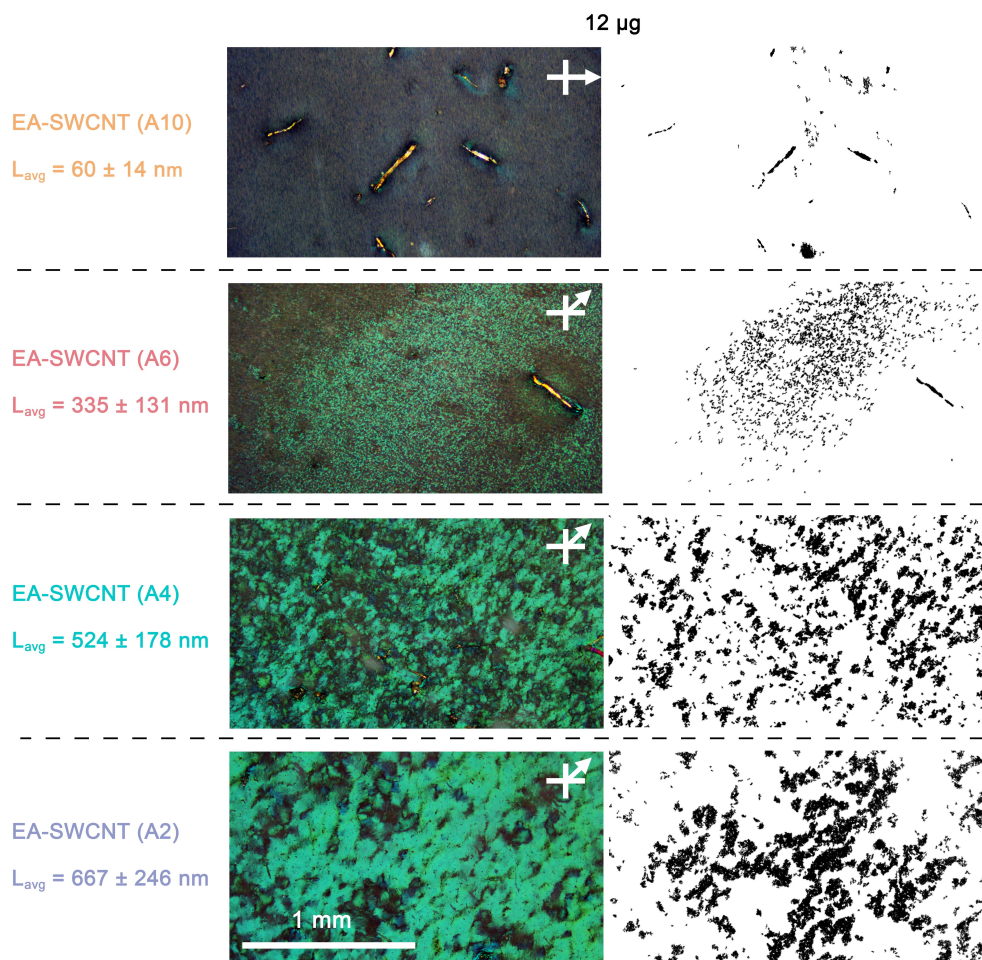


Figure A.36.: Cross polarized microscopy of EA-SWCNT films from 12 μ g of the length sorted fractions A10 – A2 in the bright (45°) or dark (0°) orientation and maps of the detected grains using machine vision. The elongated elements seen in A10 and A6 have been neglected from the evaluation and are attributed to sample contamination. Figure reproduced from [3].

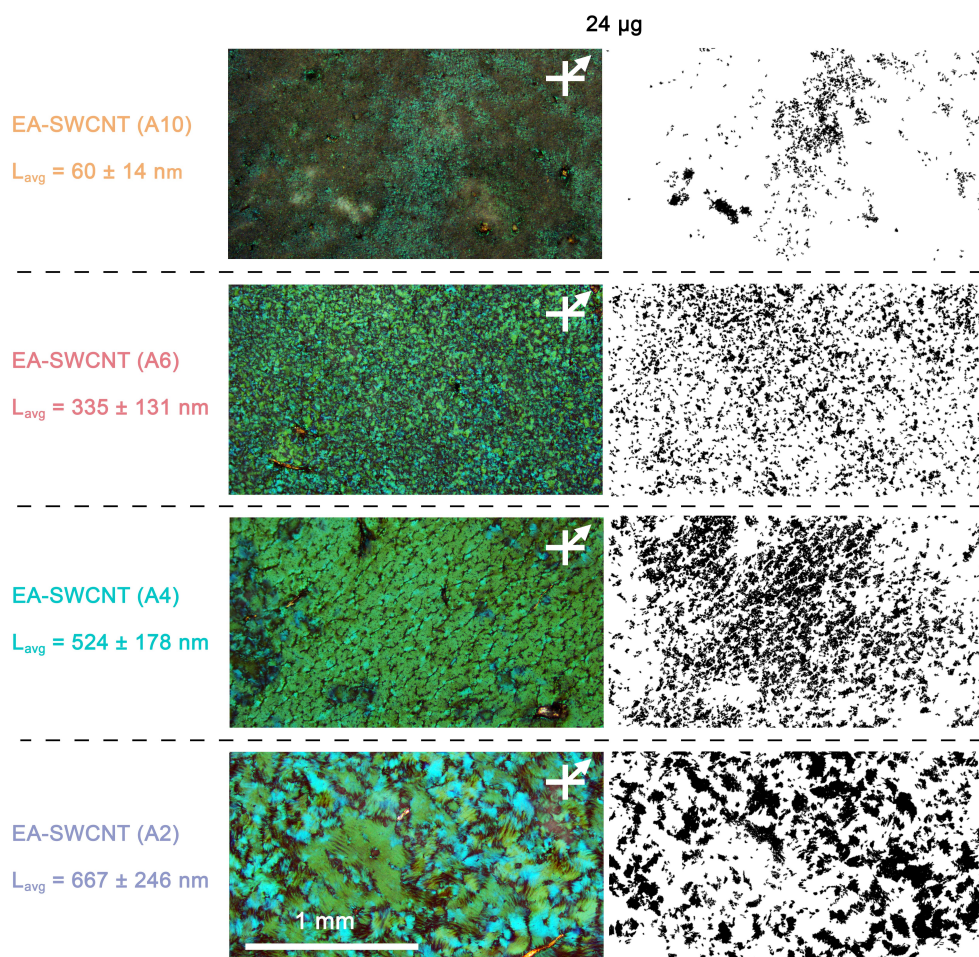


Figure A.37.: Cross polarized microscopy of EA-SWCNT films from 24 μ g of the length sorted fractions A10 – A2 in the bright (45°) or dark (0°) orientation and maps of the detected grains (A10 – A4) or grain boundaries (A2) using machine vision. Figure reproduced from [3].

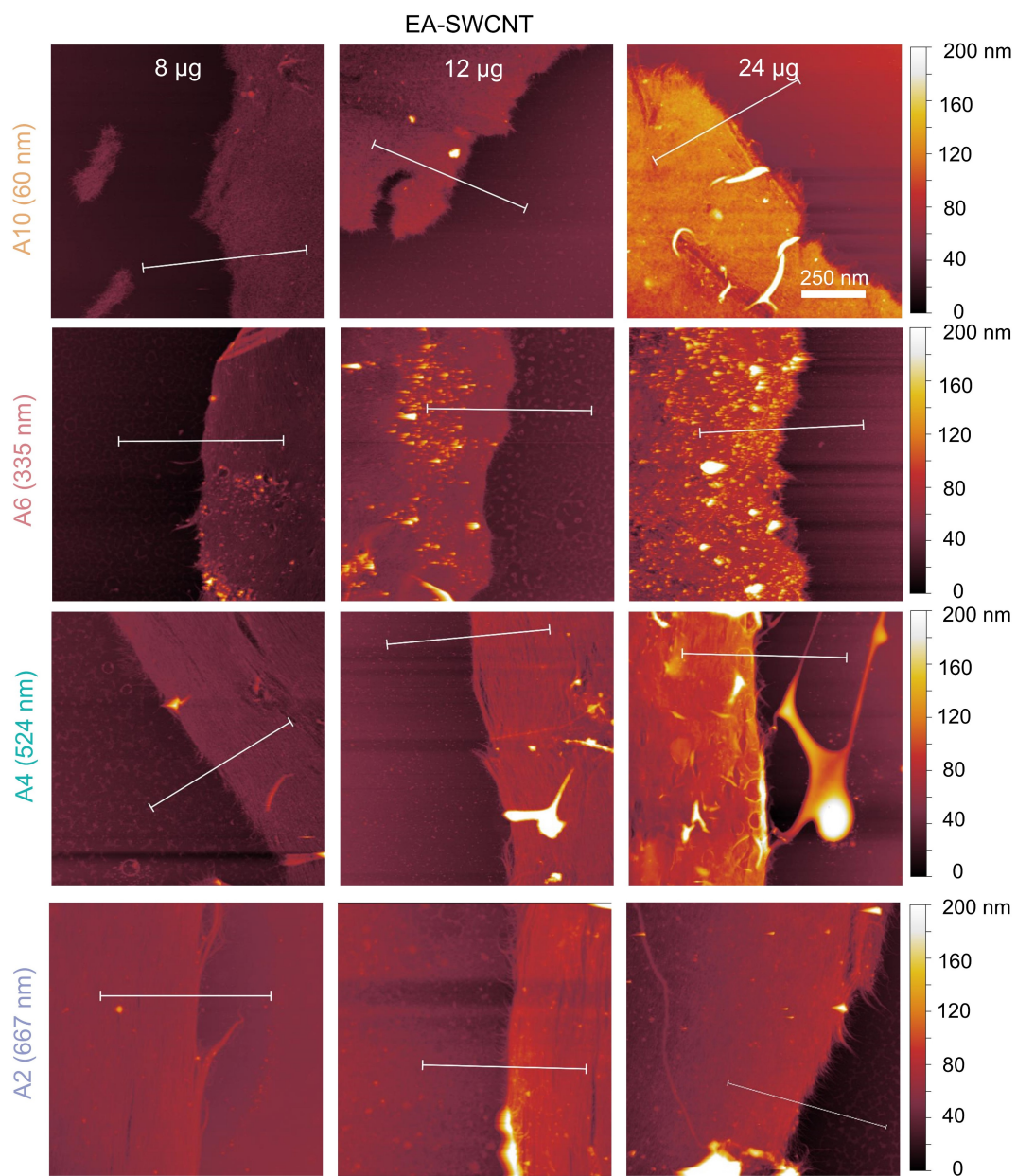


Figure A.38.: AFM Topographies measured in tapping mode of EA-SWCNT films made from the length sorted fractions A10 – A2 at masses of 8 μg , 12 μg and 24 μg . Images were recorded after transfer of the SWCNT film to a silicon substrate and the thickness measurement in Figure A.39 is indicated by the white bar. Figure reproduced from [3].

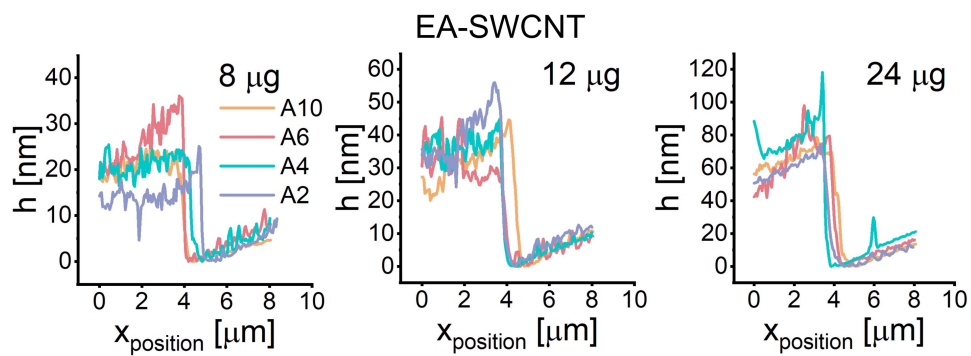


Figure A.39.: Evaluation of the film thickness from height h measurements shown in Figure A.38. The average film height was determined by the step height between the substrate and the film and is plotted in Figure 3.23 (D). Figure reproduced from [3].

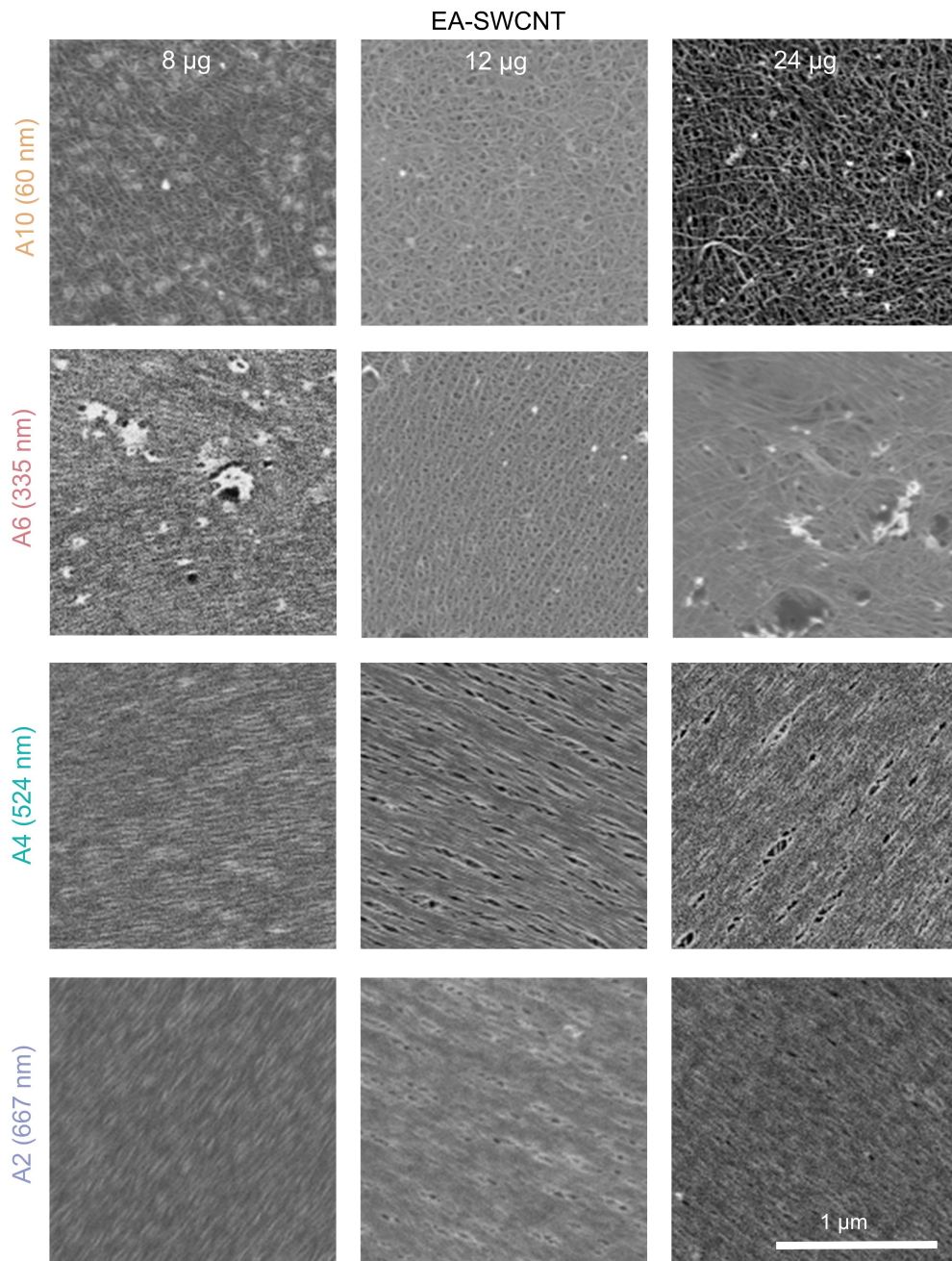


Figure A.40.: SEM images of EA-SWCNT films transferred to silicon. The films made from short SWCNTs (A10) mainly consist of disordered regions, A6 shows nematic regions and smaller domains and A4 and A2 consist of aligned domains, and are indistinguishable from each on this length scale. Figure reproduced from [3].

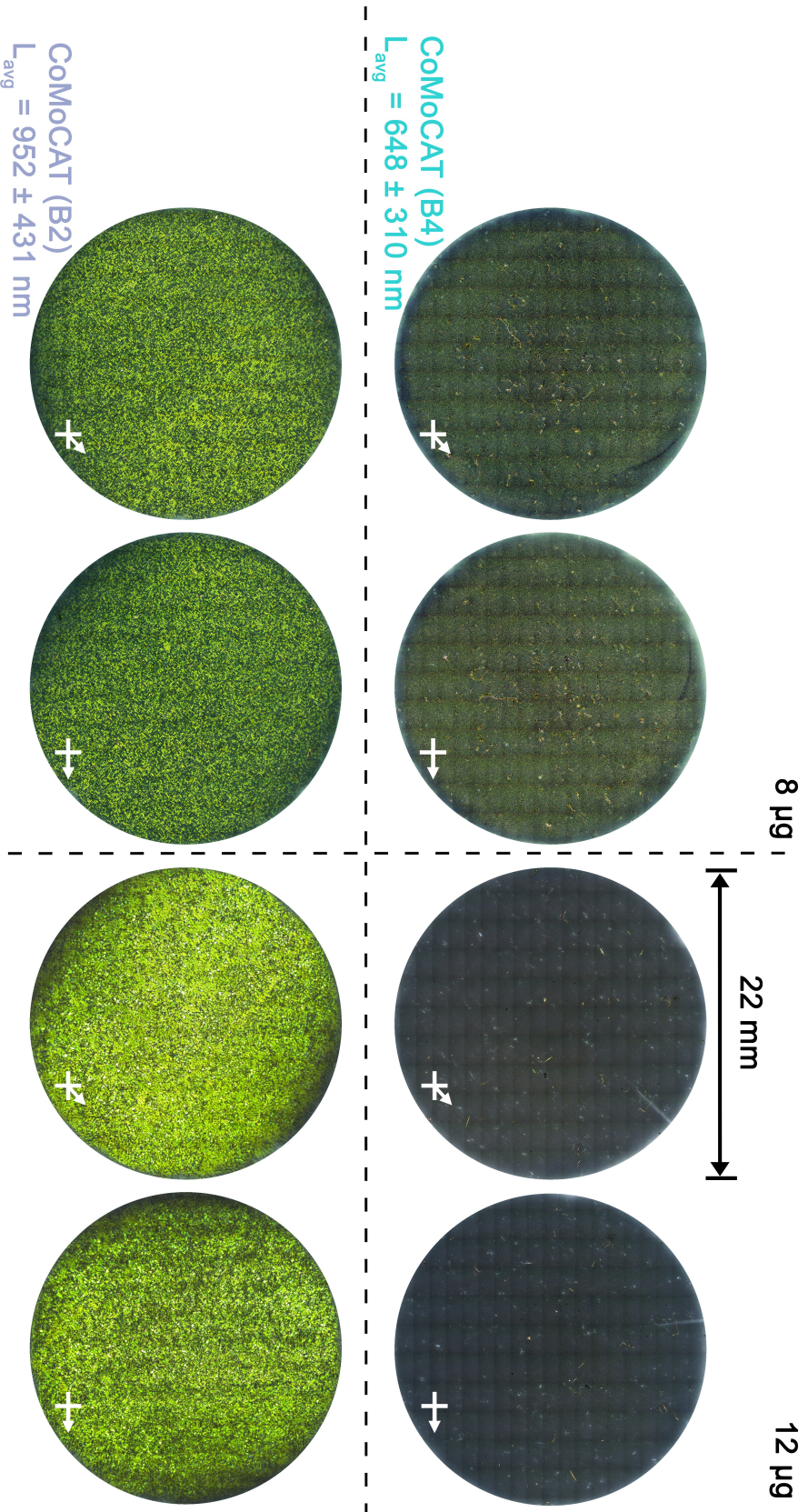


Figure A.41: Cross polarized microscopy of CoMoCAT films from length fractions B2 and B4 in the bright (45°) and dark (0°) orientation and on pristine membranes. Figure reproduced from [3].

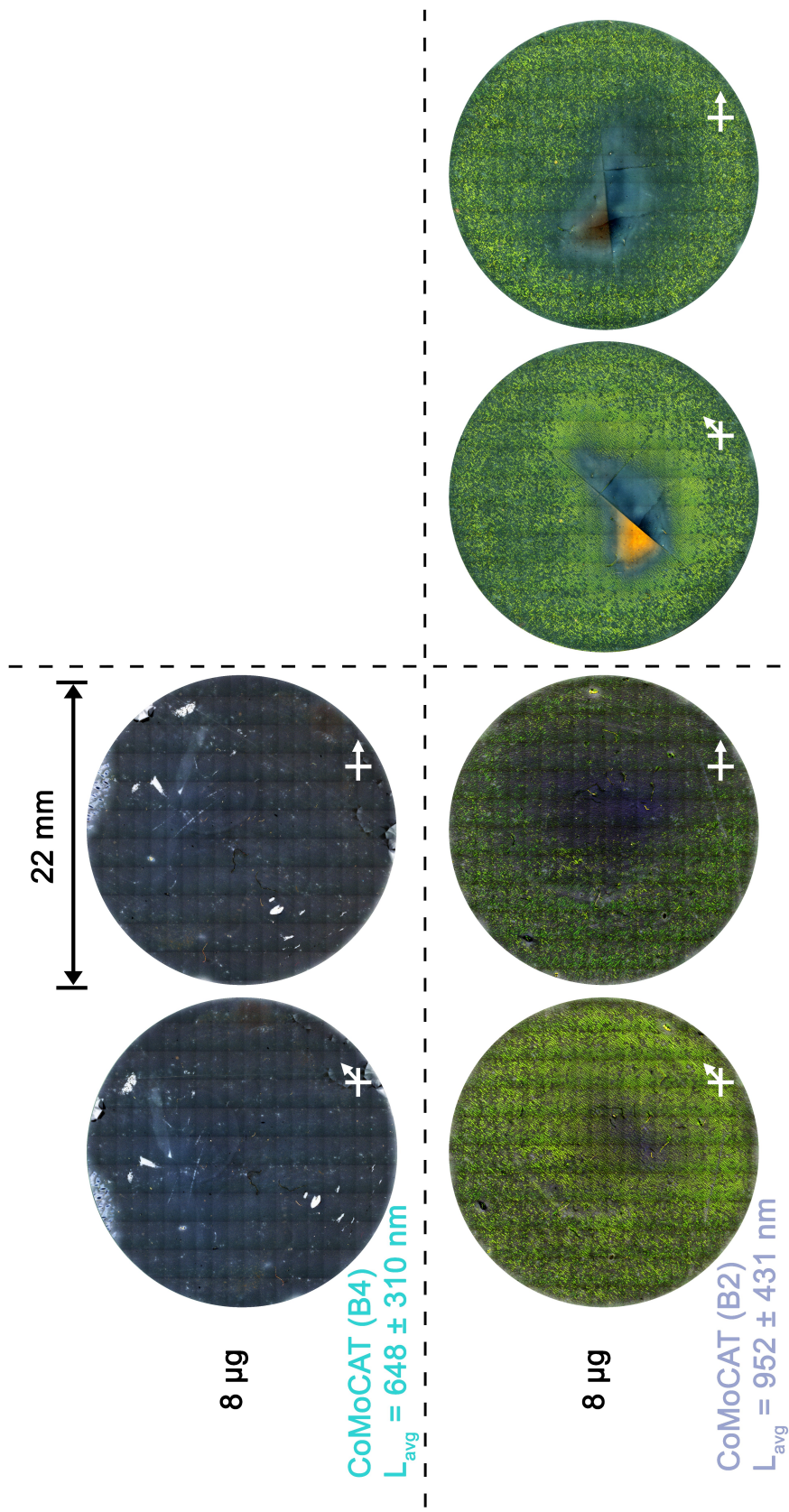


Figure A.42.: Cross polarized microscopy of CoMoCAT films from length fractions B2 and B4 in the bright (45°) and dark (0°) orientation and on pristine membranes. Figure reproduced from [3].

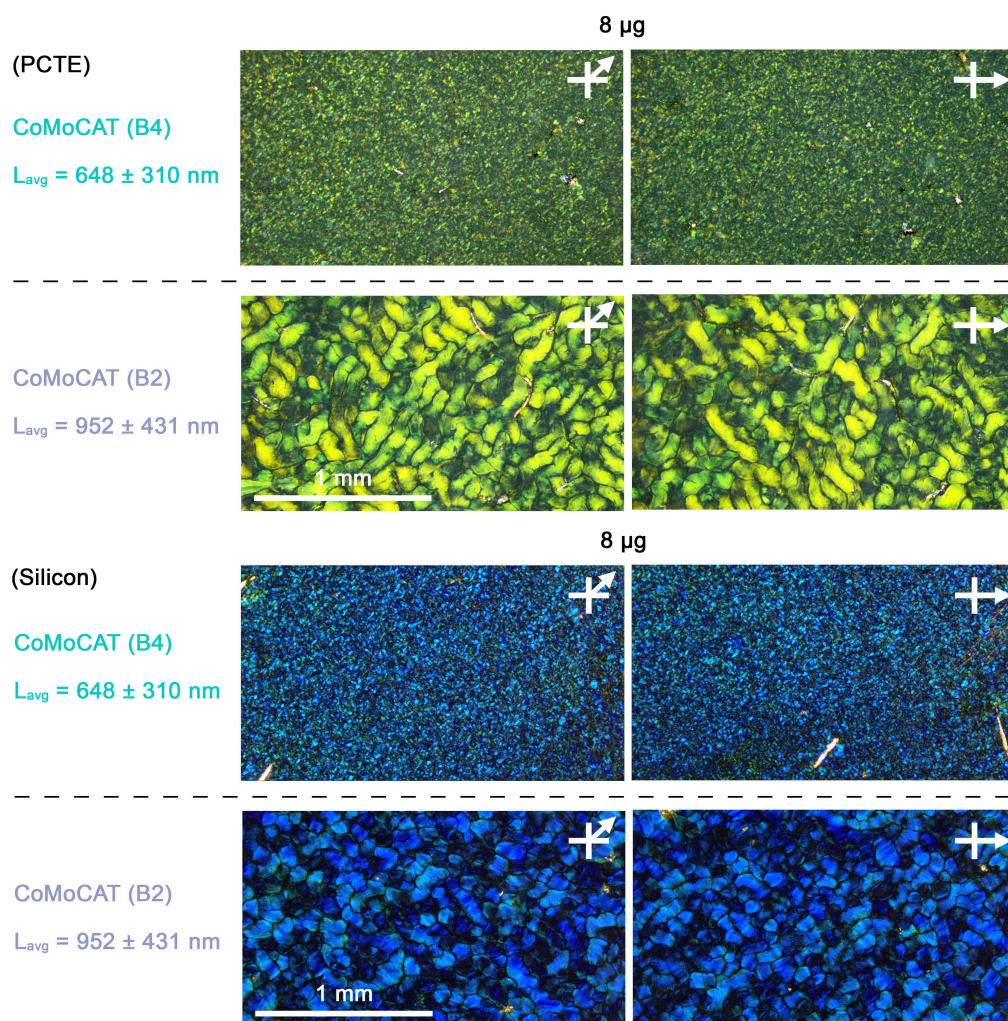


Figure A.43.: Cross-polarized light microscopy images of CoMoCAT films from 8 μg of the length-sorted fractions B4 and B2 in the bright (45°) and dark (0°) orientation. Images were recorded both on the membrane (top) and after transfer (bottom) of the SWCNT film to silicon. Figure reproduced from [3].

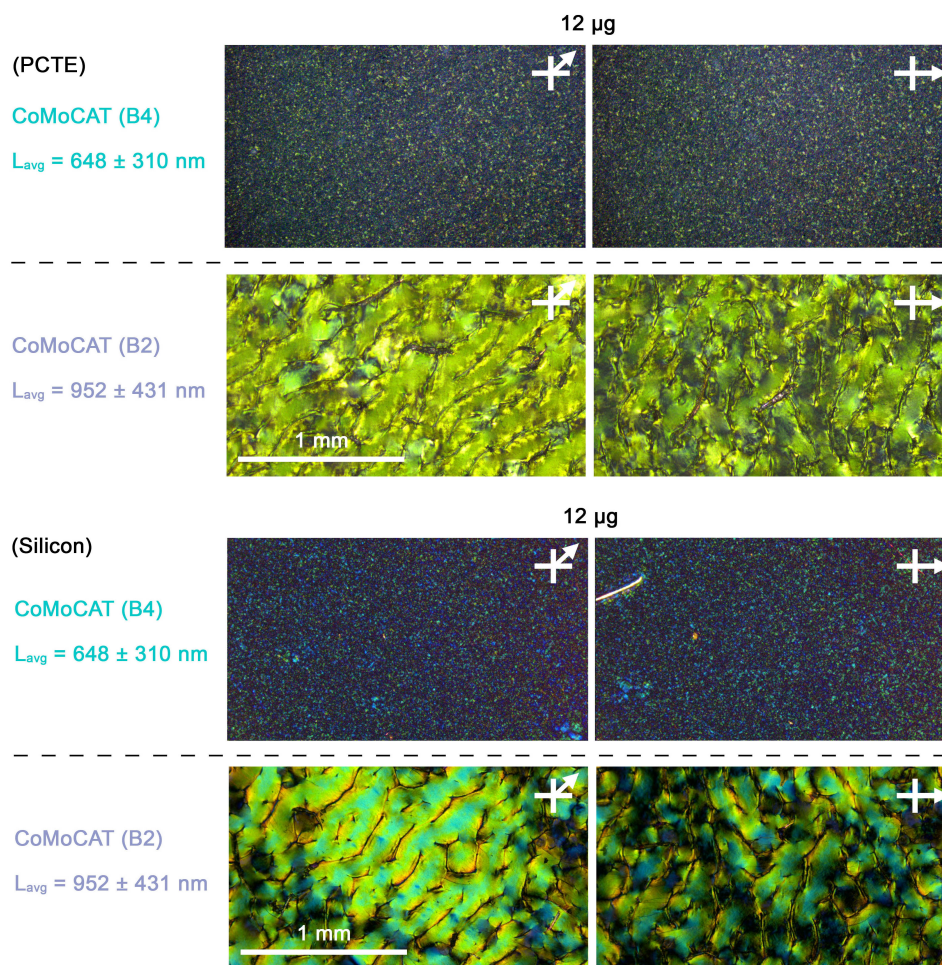


Figure A.44.: Cross-polarized light microscopy images of CoMoCAT films from 12 μg of the length-sorted fractions B4 and B2 in the bright (45°) and dark (0°) orientation. Images were recorded both on the membrane (top) and after transfer (bottom) of the SWCNT film to silicon. Figure reproduced from [3].

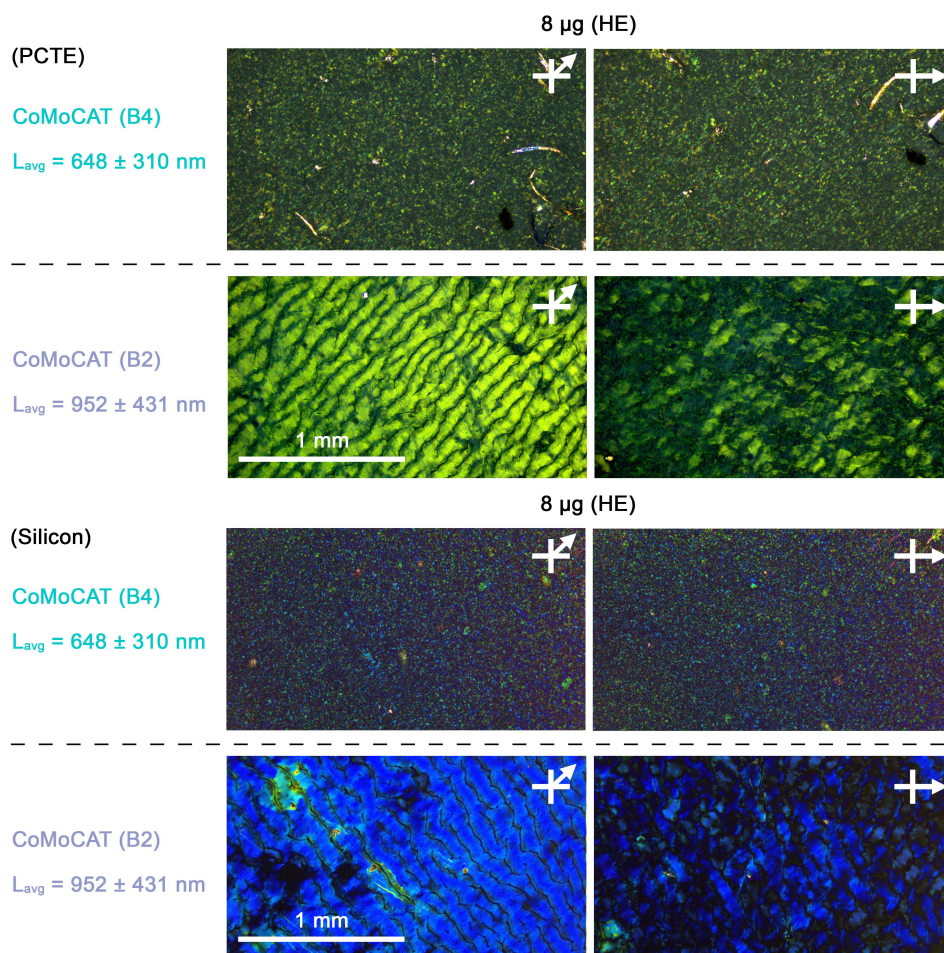


Figure A.45.: Cross-polarized light microscopy images of CoMoCAT films from 8 μg of the length-sorted fractions B4 and B2 in the bright (45°) and dark (0°) orientation and with the use of hot embossed membranes. Images were recorded both on the membrane (top) and after transfer (bottom) of the SWCNT film to silicon. Figure reproduced from [3].

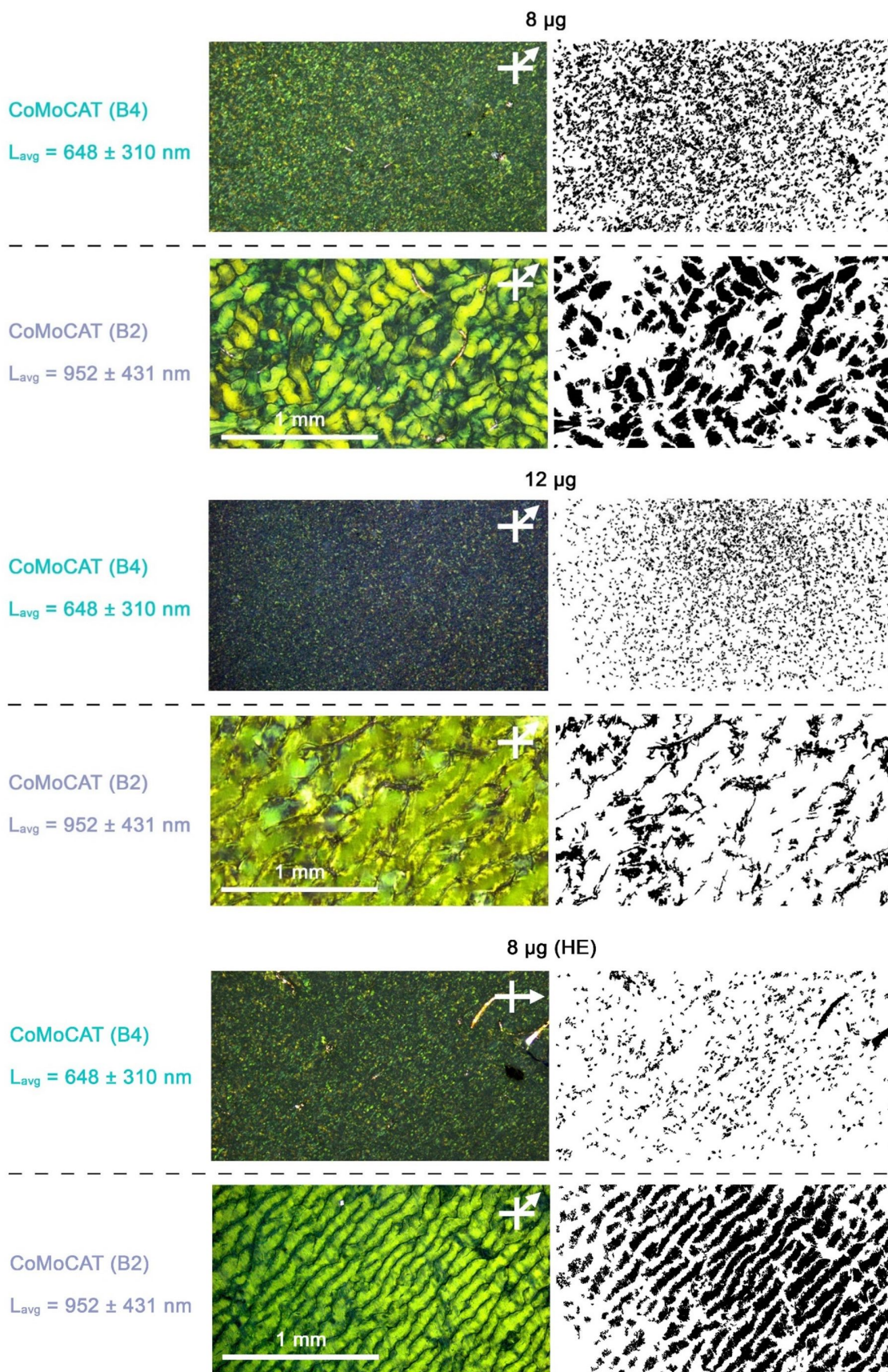


Figure A.46.: Cross polarized microscopy of CoMoCAT films from length sorted fractions B4 and B2 in the bright (45°) orientation and maps of the detected grains or grain boundaries (B2, 12 μg) using machine vision. Figure reproduced from [3].

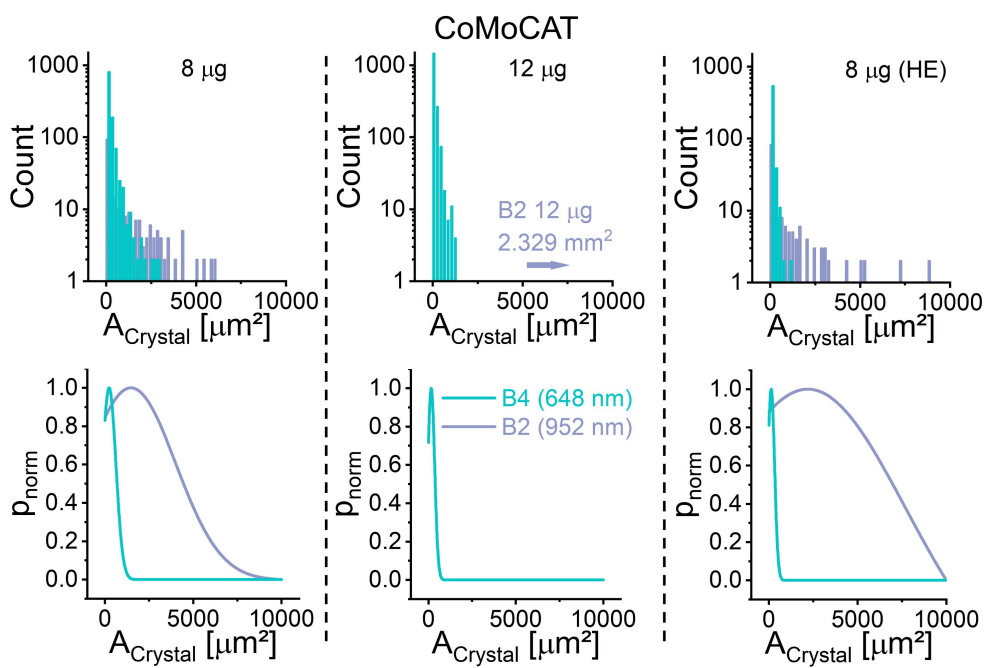


Figure A.47.: SWCNT domain size in CoMoCAT films from the length sorted fractions B4 and B2 as determined by machine-vision. Figure reproduced from [3].

CoMoCAT B2 (952 nm)



Figure A.48.: SEM images taken of the B2 CoMoCAT fraction filtered onto a hot-embossed 80 nm membrane shown in Figure 3.26 and Figure A.45. Figure reproduced from [3].

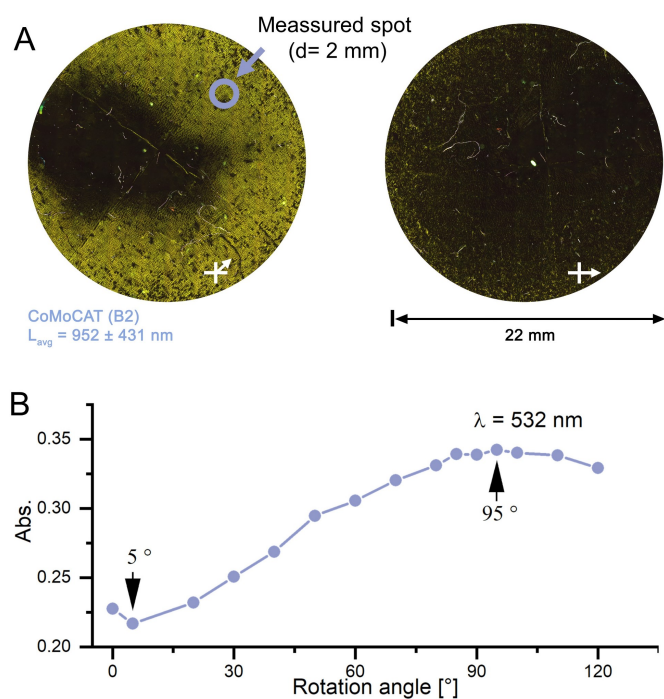


Figure A.49.: (A) CoMoCAT (B2) SWCNTs transferred from an HE membrane to an ITO-coated glass substrate, measured in transmittance using scanning cross-polarized light microscopy. The 2 mm beam spot for the angular dependent measurement shown in (B) is marked by a blue circle. The maximal and minimal absorption were measured at 5° and 95° using a wavelength of $\lambda = 532$ nm. Figure reproduced from [3].

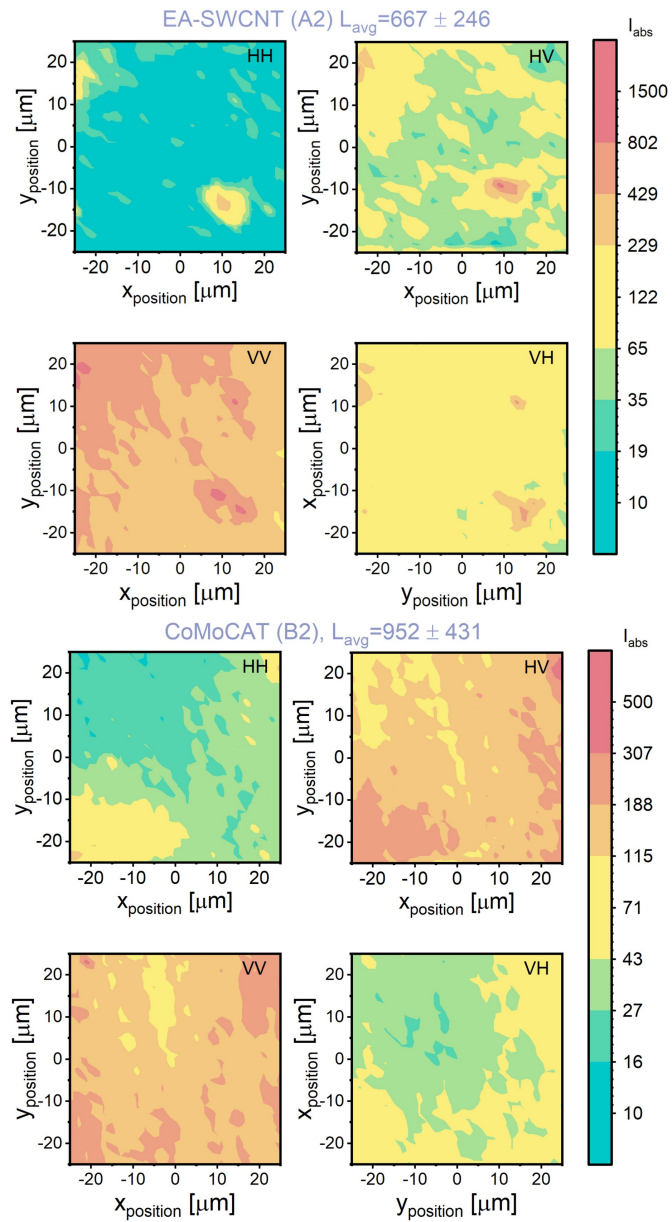


Figure A.50.: I_{HH} , I_{HV} , I_{VV} and I_{VH} measured to calculate the S_{2D} values shown in Figure 3.27 for films made with EA-SWCNT (A2) and CoMoCAT (B2). Figure reproduced from [3].

A.7. Derjaguin, Landau, Verwey, Overbeek Calculations for Unsorted SWCNTs

List of parameters for the DLVO calculations used for the unsorted EA-SWCNTS dispersed in either DOC or CTAB onto hot-embossed (HE), uncoated (UC) and PVP coated membranes (PVP)

$a = 1.4$ nm, average EA-SWCNT diameter.

$A = 9.81 \times 10^{-21}$ J, Hamaker constant.[180]

$L_{EA-SWCNT(DOC)} = 346$ nm, half the nanotube length , determined in Figure 3.2 (C).

$L_{EA-SWCNT(CTAB)} = 422$ nm, half the nanotube length, determined in Figure 3.2 (D).

$R = 0.04$ nm, thickness of the cylinder wall and approximated by the thickness of graphene.

$\kappa^{-1} = 2.9$ nm, Debye-length (inverse Debye-Hückel parameter) for $I = 0.01$ mol L⁻¹ , $T = 298$ K.

$\epsilon_0 \epsilon_r$: permittivity of water at $T = 298$ K.

$N_A = 6.022e23$: Avogadro number.

$k = 1.38066 \times 10^{-23}$ J K⁻¹: Boltzmann constant.

γ_1 : approximated by the zeta potential of the unsorted EA-SWCNTs ($\zeta_{CTAB} = 72$ mV and $\zeta_{DOC} = -14$ mV) , Figure 3.2 (A) and (B)

γ_2 : surface charge of the membrane, approximated by zeta potential of the membrane (Ranges between $\zeta_{surf} = -120$ mV and -10 mV, Figure 3.1 (A) and (B) show the zeta potentials used for the specific 80 nm membranes ($\zeta_{HE} = -42$ mV, $\zeta_{PVP} = -67$ mV, $\zeta_{UC} = -110$ mV)

$\nu = 1$, valence.

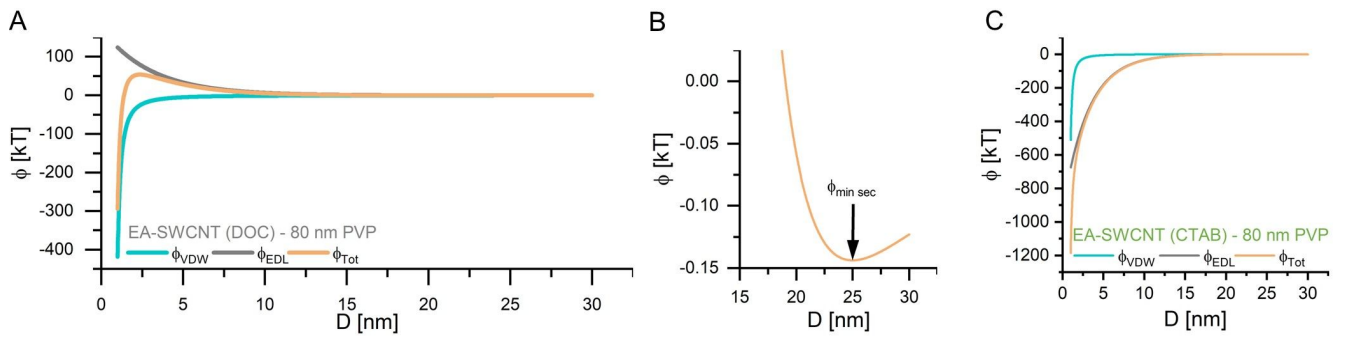


Figure A.51.: (A) Total potential Φ_{TOT} derived from the attractive van der Waals potential Φ_{VDW} and the repulsive electronic double layer potential Φ_{EDL} for an individual EA-SWCNT dispersed in DOC ($\zeta_{0.04 \text{ wt\% } DOC} = -14 \text{ mV}$) close to the surface of an 80 nm membrane ($\zeta_{m \text{ 80nm}} = -67 \text{ mV}$). The shallow secondary minimum is depicted in (B). Total potential Φ_{TOT} derived for an individual EA-SWCNT dispersed in CTAB ($\zeta_{0.02 \text{ wt\% } DOC} = 72 \text{ mV}$). Figure reproduced from [1].

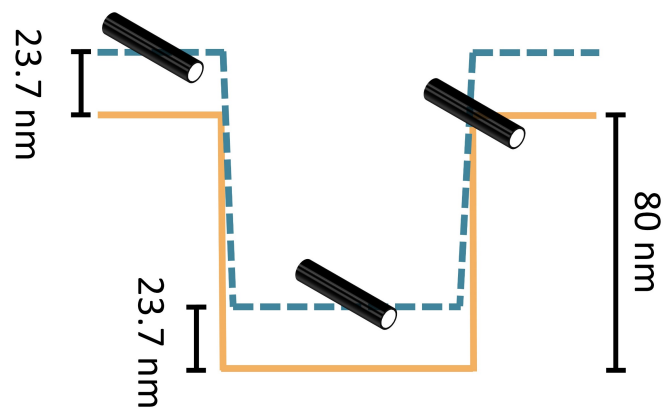


Figure A.52.: Schematic of SWCNTs circumventing the potential barrier at the edge of an artificial groove on a textured surface. Without flow, a SWCNT will be 23.7 nm away from the surface, both on a ridge and in a valley, however, due to a discontinuity at the edge in its position, an adsorption on the edges as observed in 3.11 (E) can occur. Figure reproduced from [1].

A.8. Derjaguin, Landau, Verwey, Overbeek Calculations for Sorted SWCNTs

List of parameters for the DLVO calculations used for the length-sorted EA-SWCNTS dispersed DOC onto a PVP-coated PCTE membranes.

$d_{t\ EA-SWCNT} = 1.4\text{ nm}$, average EA-SWCNT diameter.

$d_{t\ CoMoCAT} = 0.76\text{ nm}$, average CoMoCAT diameter.

$A = 9.81 \times 10^{-21}\text{ J}$, Hamaker constant.[180]

$L_{EA-SWCNT(DOC)} = 346\text{ nm}$, half the nanotube length , determined in Figure 3.2 (C).

$L_{EA-SWCNT(CTAB)} = 422\text{ nm}$, half the nanotube length, determined in Figure 3.2 (D).

$R = 0.04\text{ nm}$, thickness of the cylinder wall and approximated by the thickness of graphene.

$\kappa^{-1} = 2.9\text{ nm}$, Debye-length (inverse Debye-Hückel parameter) for $I = 0.01\text{ mol L}^{-1}$, $T = 298\text{ K}$.

$\epsilon_0\epsilon_r$: permittivity of water at $T = 298\text{ K}$.

$N_A = 6.022 \times 10^{23}$: Avogadro number.

$k = 1.38066 \times 10^{-23}\text{ J K}^{-1}$: Boltzmann constant.

γ_1 : approximated by the zeta potential of the length-sorted EA- and CoMoCAT-SWCNTs and unsorted EA-SWCNTs (Figure 3.13 (A) and A.21 (B) , $\zeta_{EA-SWCNT\ unsorted} = -14\text{ mV}$)

γ_2 : surface charge of the membrane, approximated by zeta potential of the 80 nm Figure 3.1 (A) and (B) show the zeta potentials used for the specific 80 nm membranes ($\zeta_{PVP} = -60\text{ mV}$ at pH=7, Figure 3.1 (B))

$\nu = 1$, valence.

Parameters for SWCNT length L and d_t dependence calculation Figure 3.30 (C,D):

Range of diameter of the SWCNT d_t : 0.5 nm to 2.75 nm, 0.05 nm intervals

Range of distance to the surface, z : 1 nm to 50 nm, 0.25 nm intervals

Range of length L : 50 nm to 5000 nm, 10 nm intervals

Range of the surface potential of the SWCNT, γ_1 : -10 mV to -40 mV , -10 mV intervals

Threshold for secondary minimum: -0.075 kT ($I = 0.01\text{ mol L}^{-1}$)

Fitting parameters for the L and d_t relationship are based on the inverse length plot shown in Figure 3.30 (D). The linear fit can be written as:

$$L^{-1} = m_{\zeta\ SWCNT}d_t + b_{\zeta\ SWCNT} \quad (\text{A.3})$$

$$L = \frac{1}{m_{\zeta\ SWCNT}d_t + b_{\zeta\ SWCNT}} \quad (\text{A.4})$$

All fits had fitting errors below 1 %. The slope and intercept vary with the zeta potential of the SWCNT as shown below:

$$m_{\zeta_{SWCNT=-40\text{ mV}}} = 1.541 \times 10^{12} \text{ m}^{-2}, b_{\zeta_{SWCNT=-40\text{ mV}}} = -0.083 \times 10^3 \text{ m} \quad (\text{A.5})$$

$$m_{\zeta_{SWCNT=-30\text{ mV}}} = 1.633 \times 10^{12} \text{ m}^{-2}, b_{\zeta_{SWCNT=-30\text{ mV}}} = -0.089 \times 10^3 \text{ m} \quad (\text{A.6})$$

$$m_{\zeta_{SWCNT=-20\text{ mV}}} = 1.786 \times 10^{12} \text{ m}^{-2}, b_{\zeta_{SWCNT=-20\text{ mV}}} = -0.098 \times 10^3 \text{ m} \quad (\text{A.7})$$

$$m_{\zeta_{SWCNT=-10\text{ mV}}} = 2.122 \times 10^{12} \text{ m}^{-2}, b_{\zeta_{SWCNT=-10\text{ mV}}} = -0.119 \times 10^3 \text{ m} \quad (\text{A.8})$$

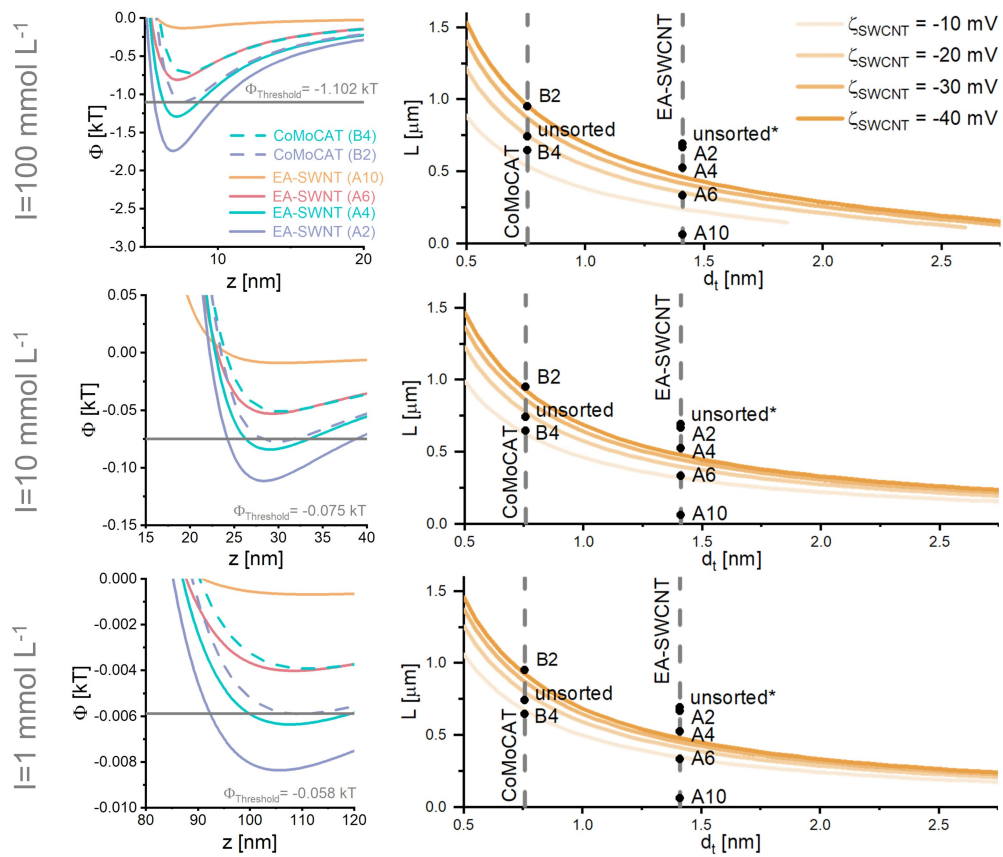
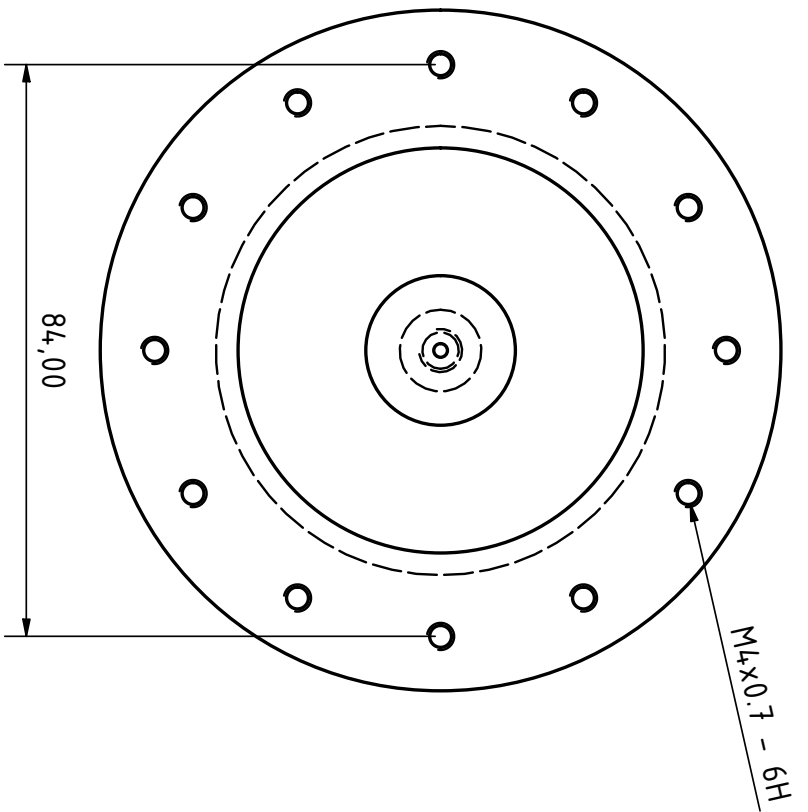
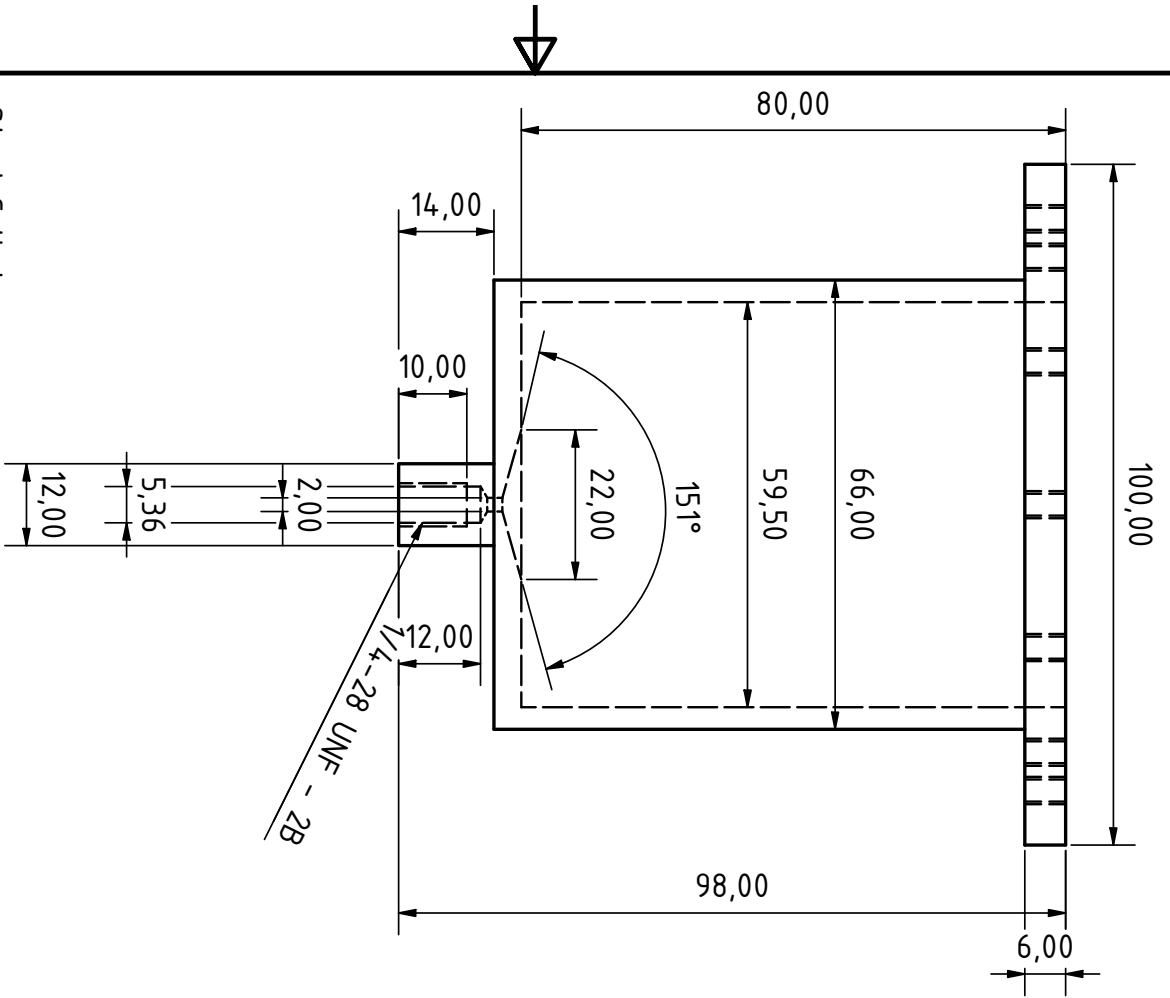


Figure A.53.: DLVO calculations for a variation of the ionic strength from bulk DOC (0.04 wt% DOC, $I = 1 \text{ mmol L}^{-1}$) to $I = 100 \text{ mmol L}^{-1}$ with corresponding potential thresholds being defined as the secondary minimum of CoMoCAT (B2). Due to the enrichment of surfactant close to the membrane surface the real ionic concentration during filtration is unknown, but it can be seen that the $L(d)$ curves shown on the right, only differ for zeta potentials far away from the zeta potentials measured for the SWCNTs (cf. Figure 3.19, Figure 3.20). Figure reproduced from [3].

A.9. Construction plans: Frame of the Microfluidic Filtration Setup

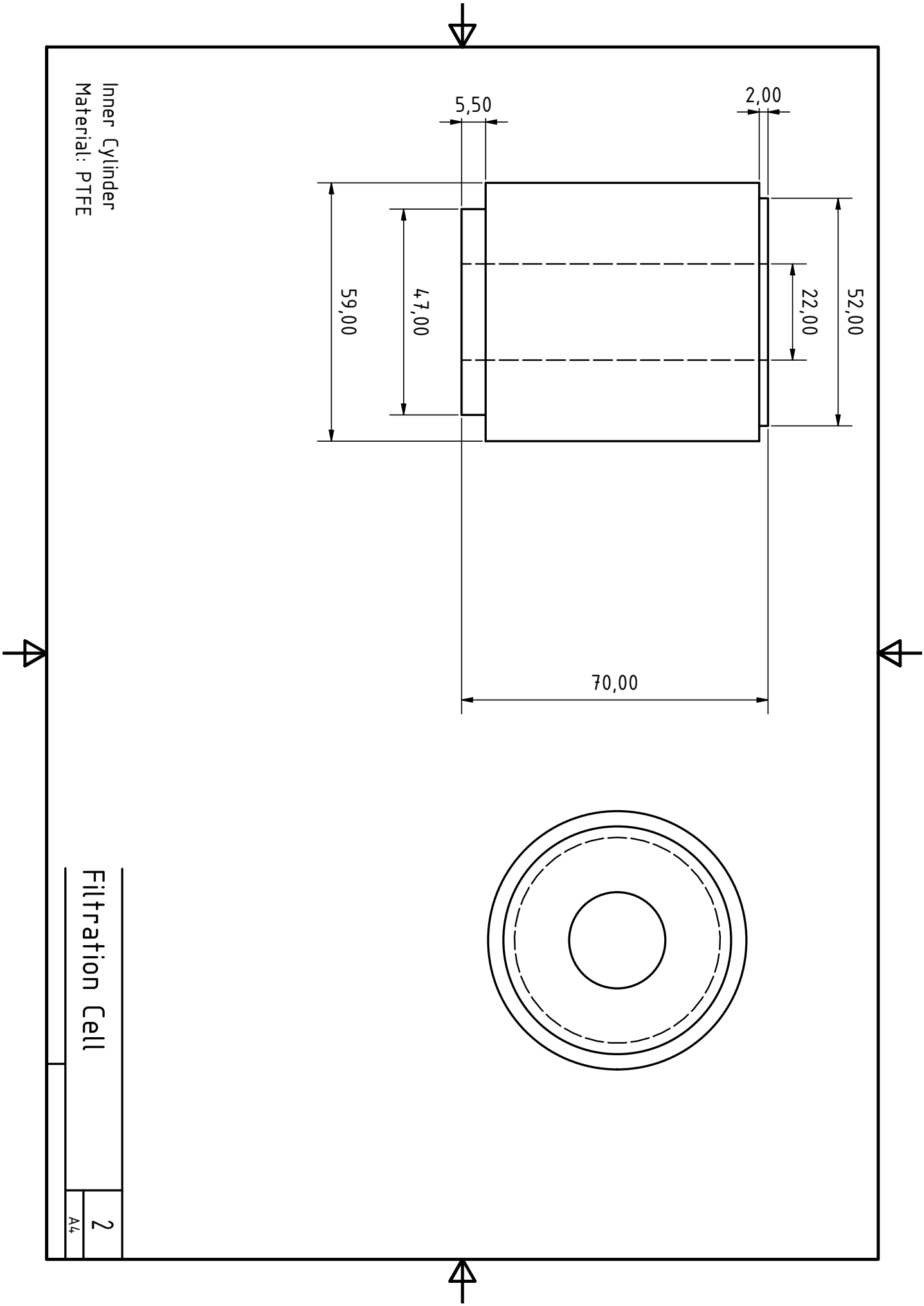
In the following section, the construction plans of the setup are shown. These encompass only the parts, that have to be ordered to the specifications as shown below. Commercially available parts will hence not be listed in the plans. Thereby the custom-made filtration cell is detailed first, followed by the frame. If not stated otherwise, stainless chrom-alloy steel should be used. Since some of the schematics require DIN A3 pages to represent the details needed, they are split into two DIN A4 pages instead.

Steel Cylinder
Material: 1.4571



Filtration Cell

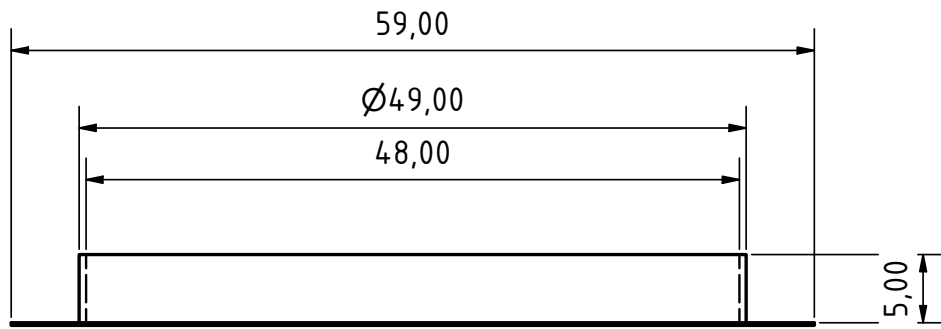
1
A4



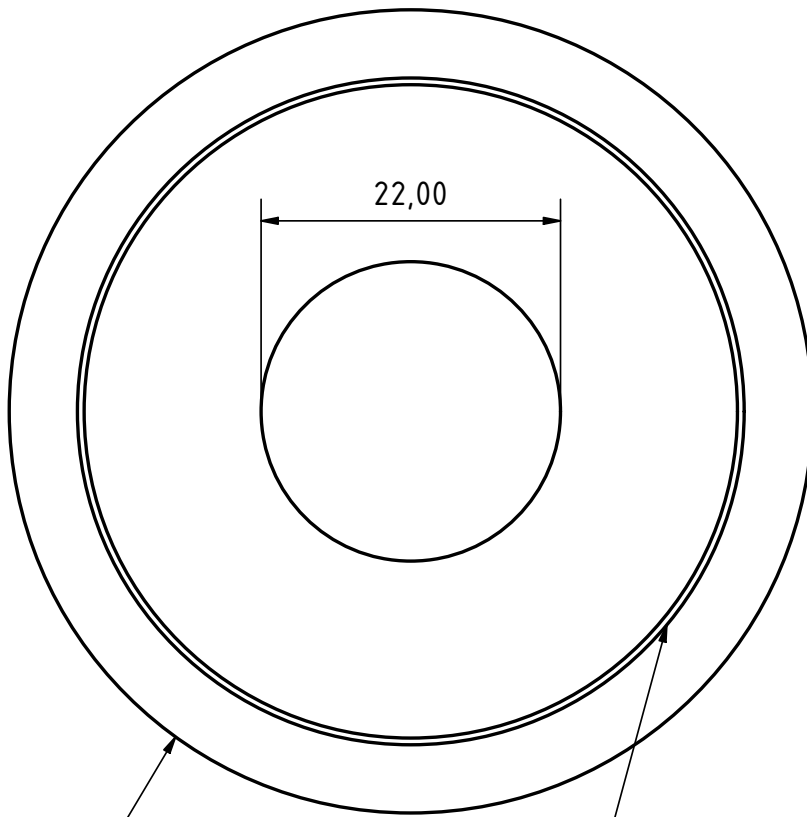
Inner Cylinder
Material: PTFE

Filtration Cell

2
A4



Blechstapel: 0,1 Blech, Drahtgitter, 0,1 Blech



Rand geschweißt

Ring angeheftet und geschweißt

Werkstoff: 1.4301 + Drahtgitter

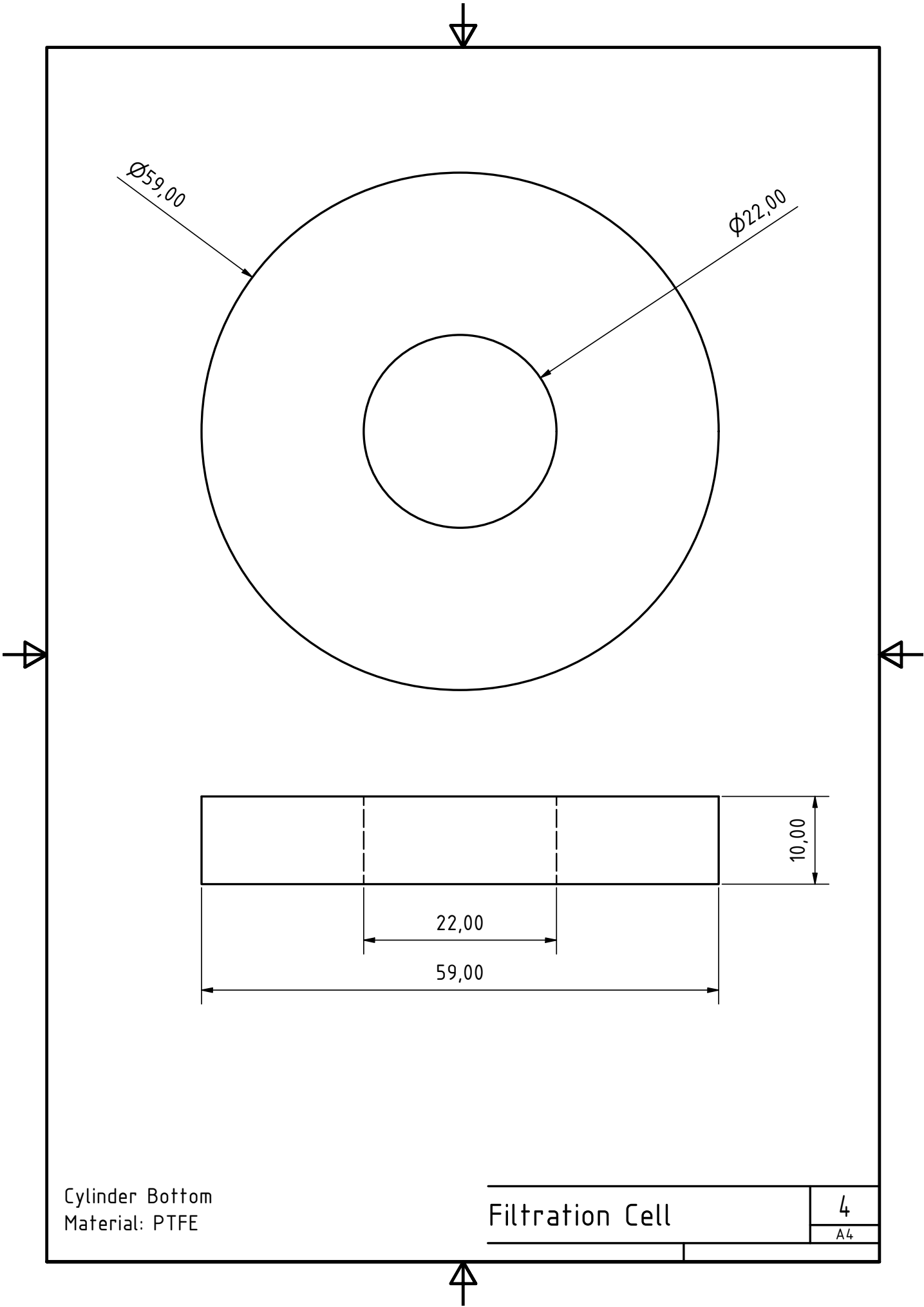
Sieve Holder
 Material: 1.4301; Wire Mesh (300)

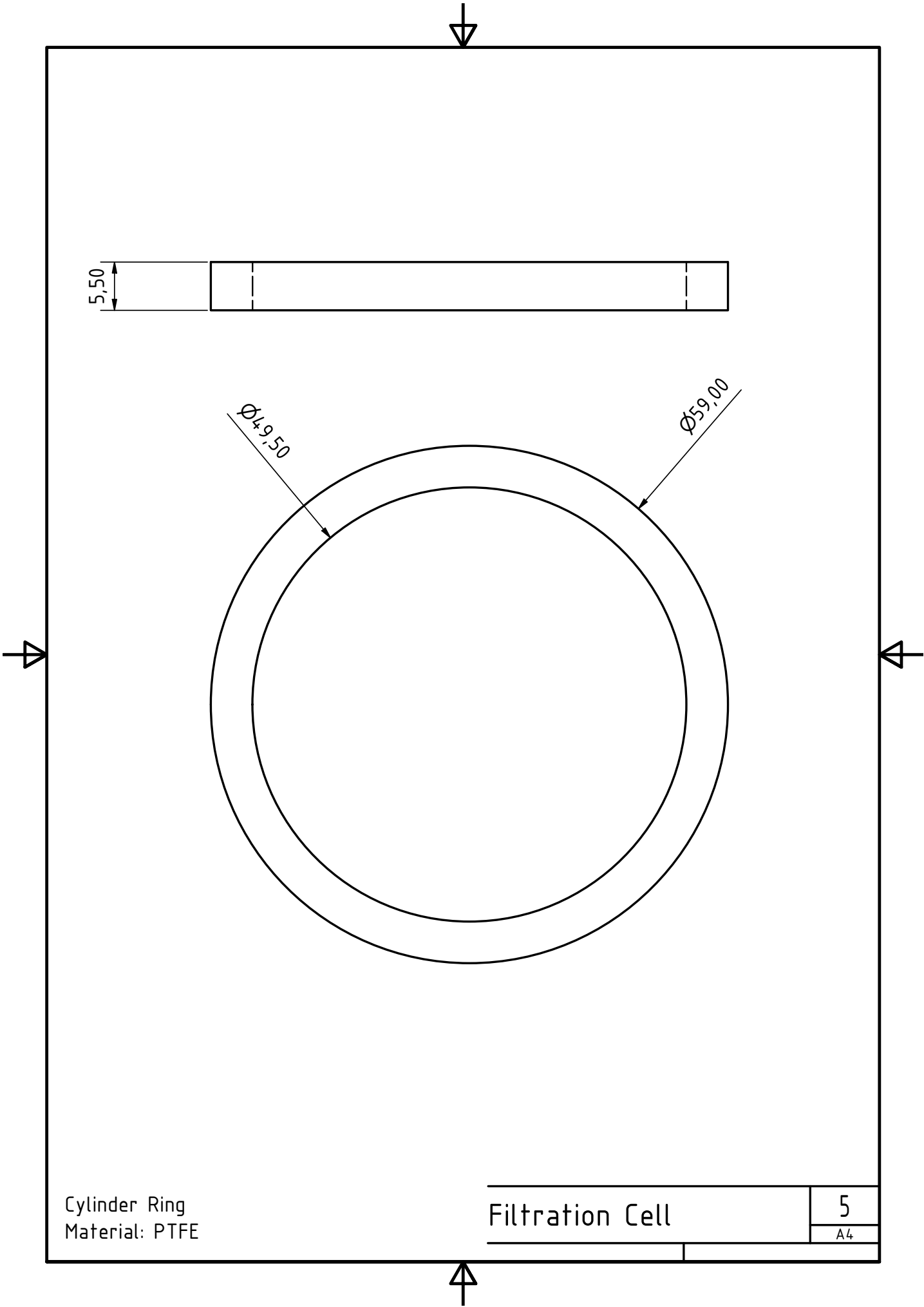
Filtration Cell

3

A4





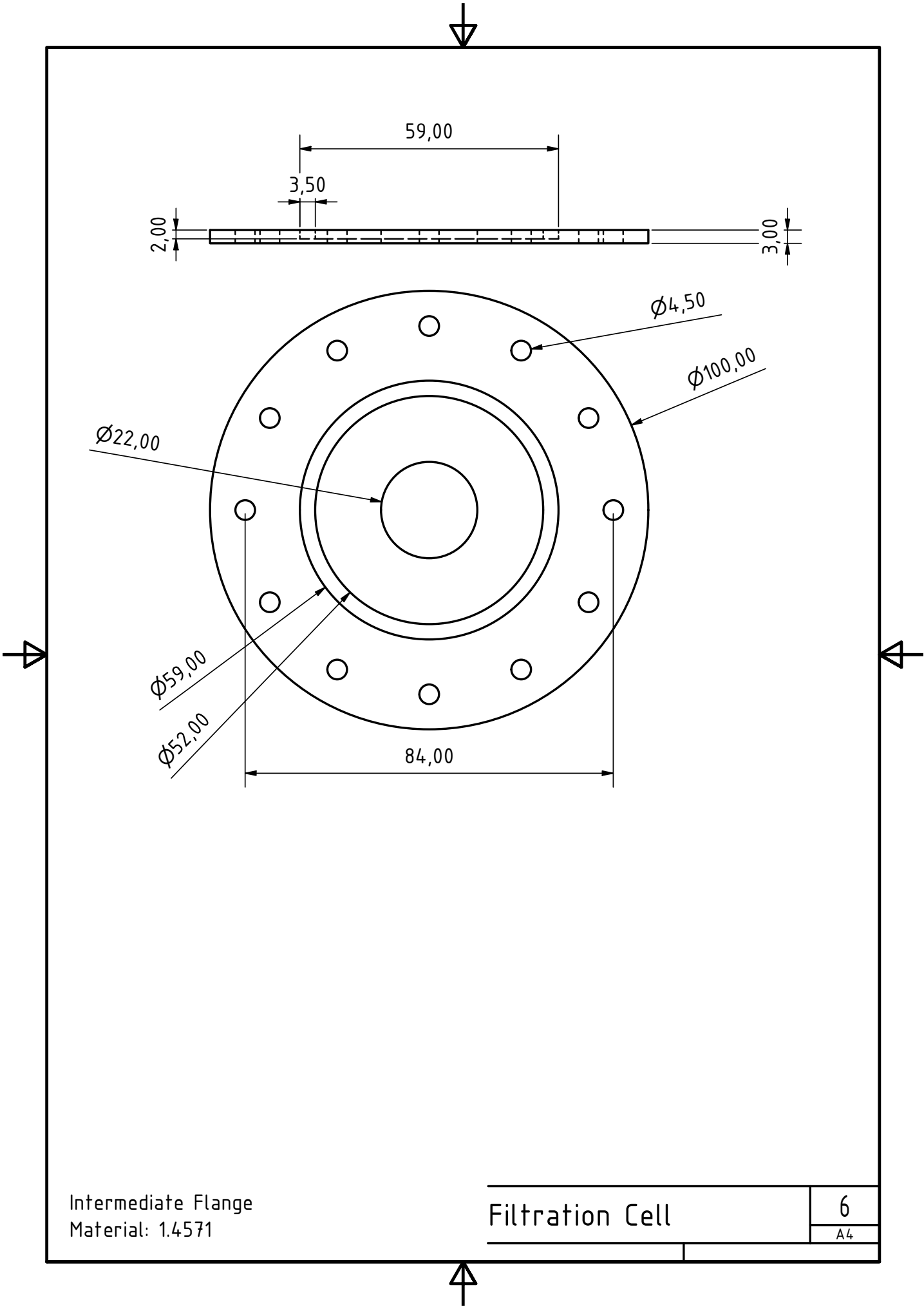


Cylinder Ring
Material: PTFE

Filtration Cell

5

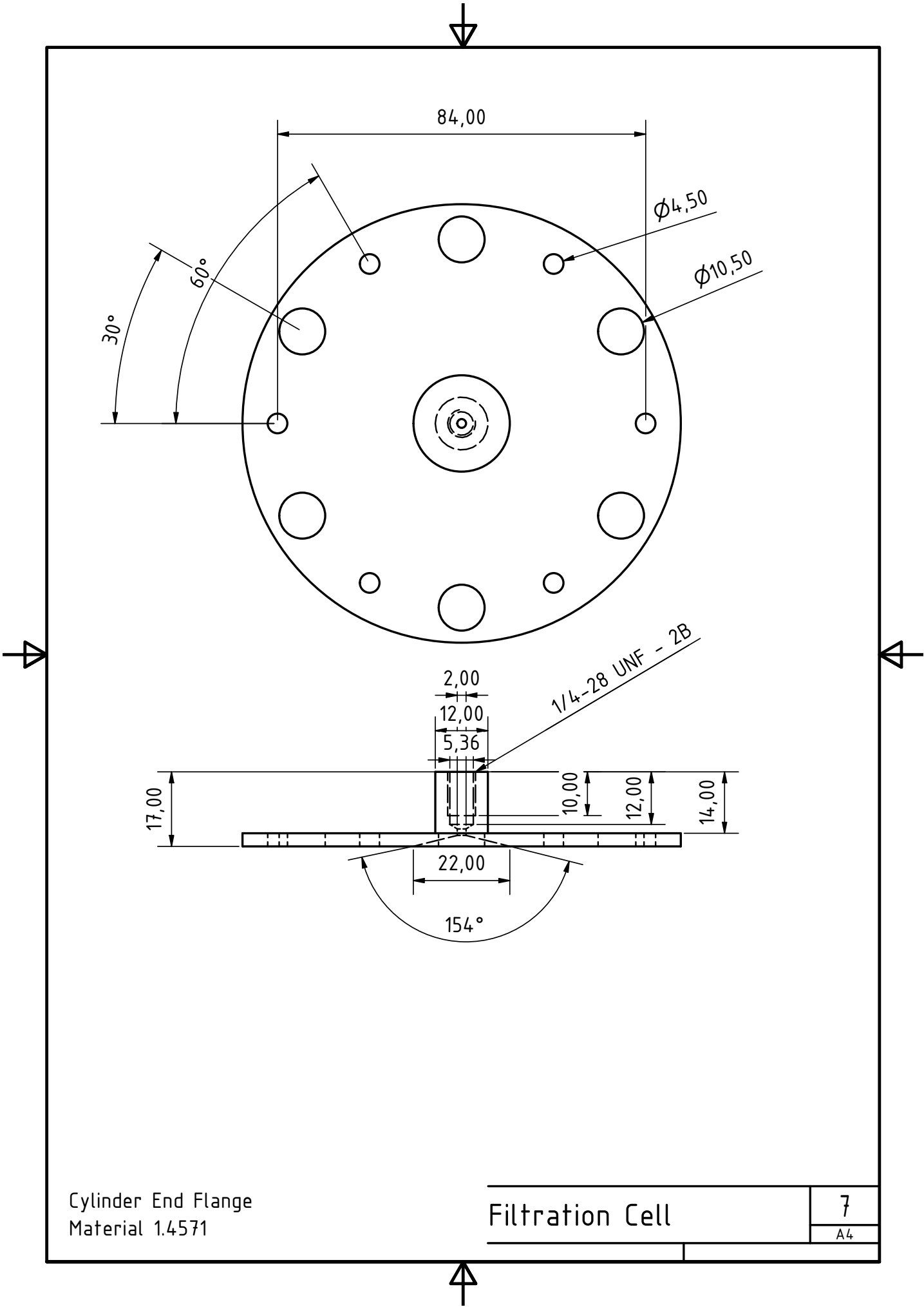
A4



Intermediate Flange
 Material: 1.4571

Filtration Cell

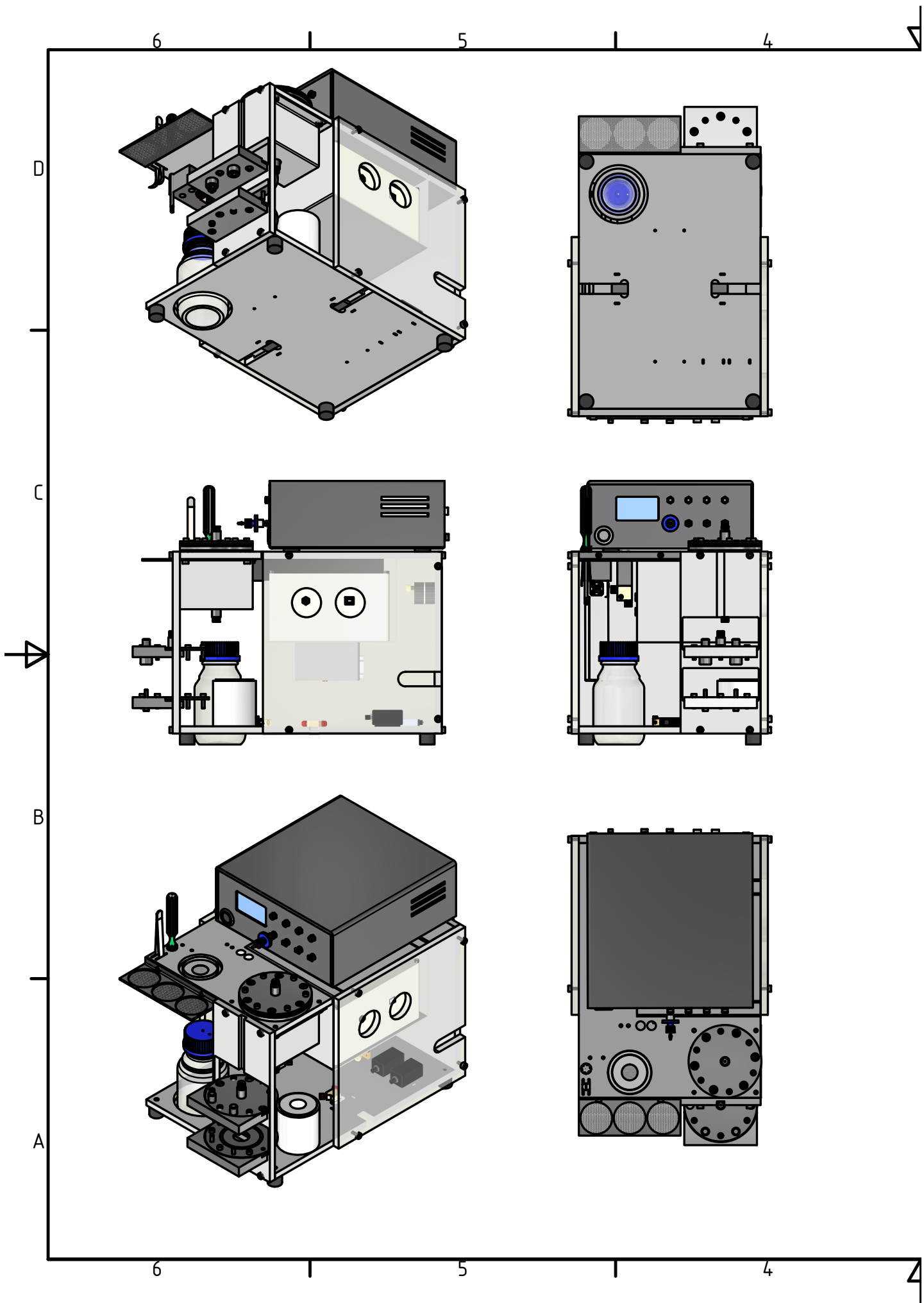
6
A4

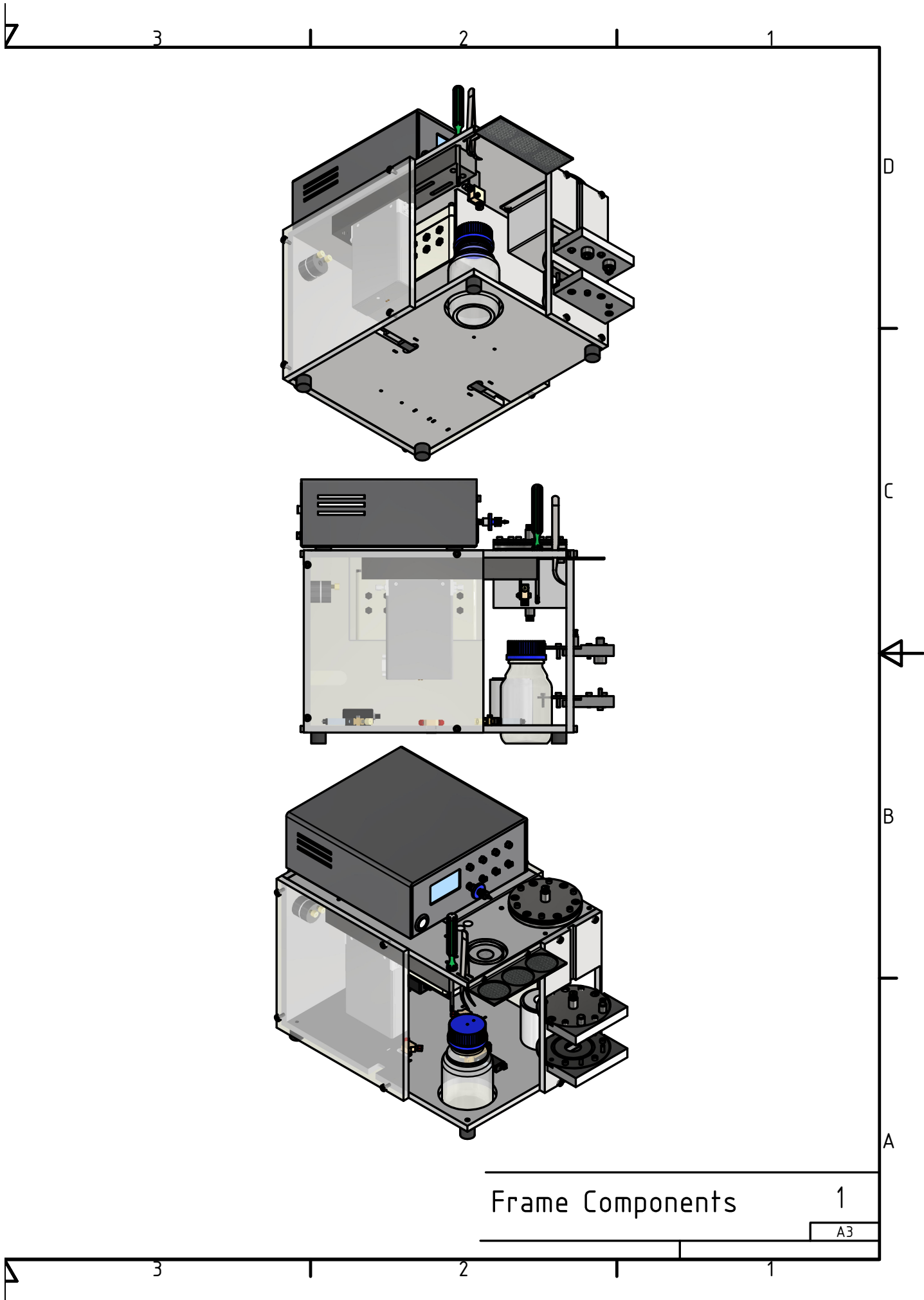


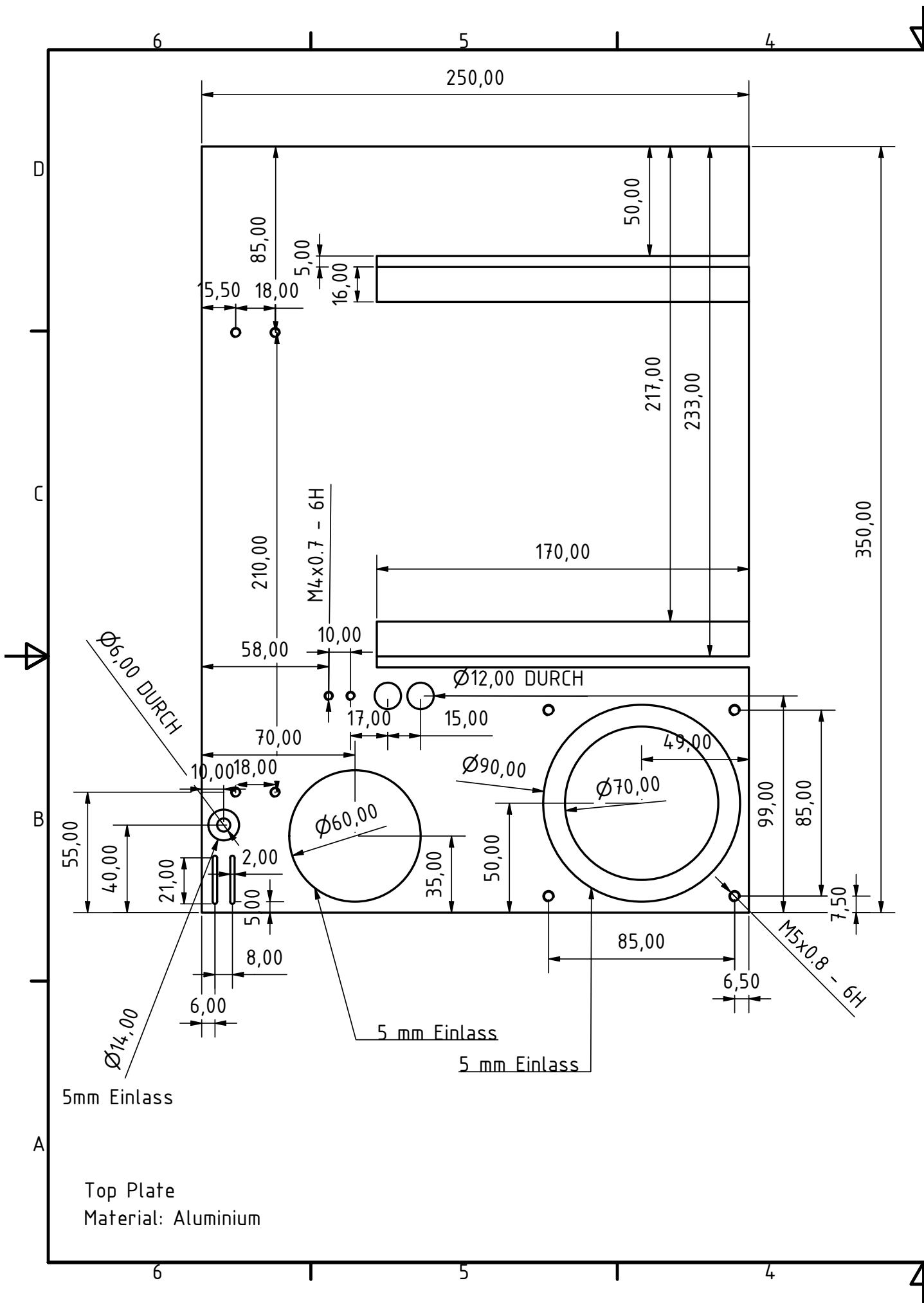
Cylinder End Flange
Material 1.4571

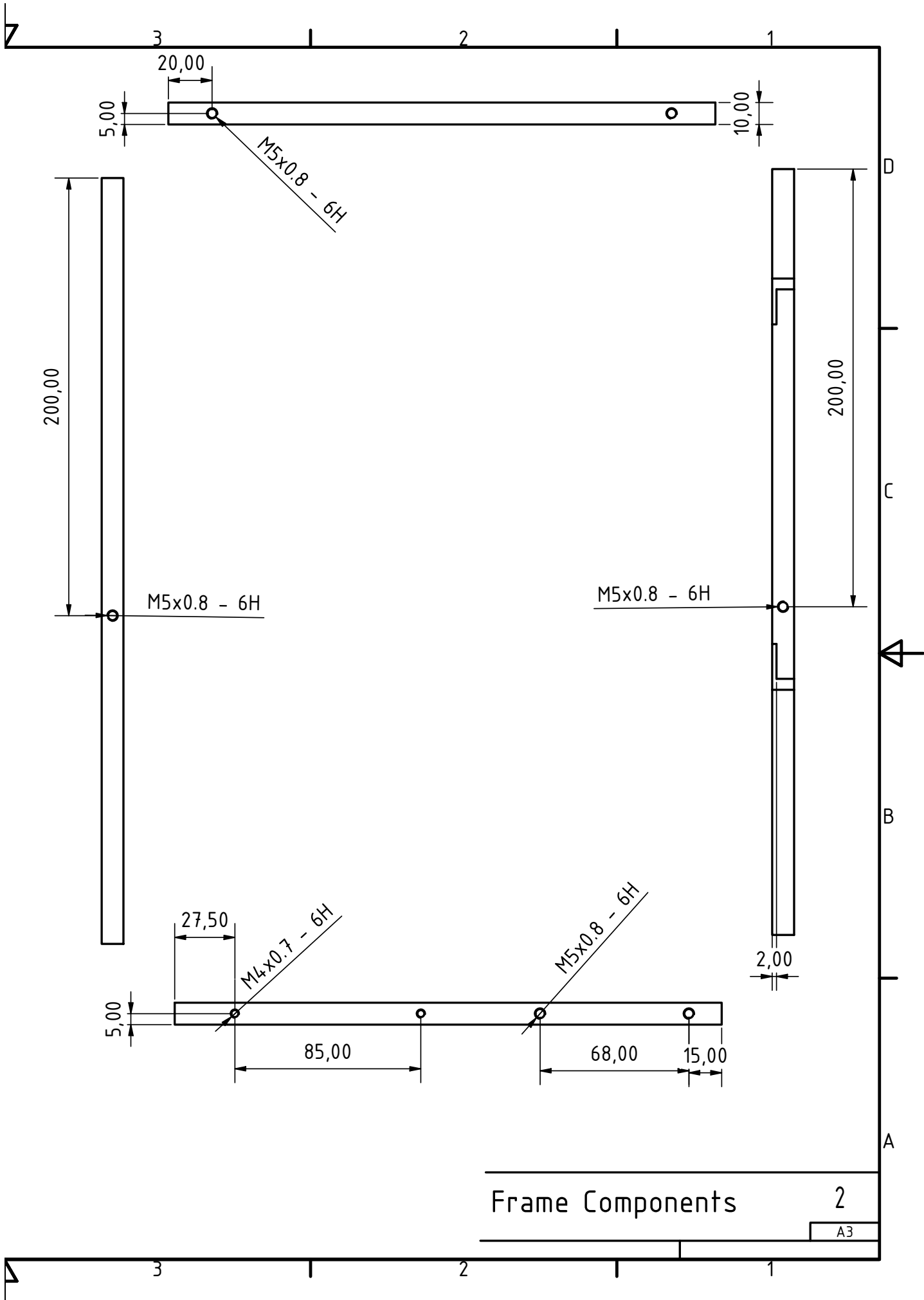
Filtration Cell

7
A4





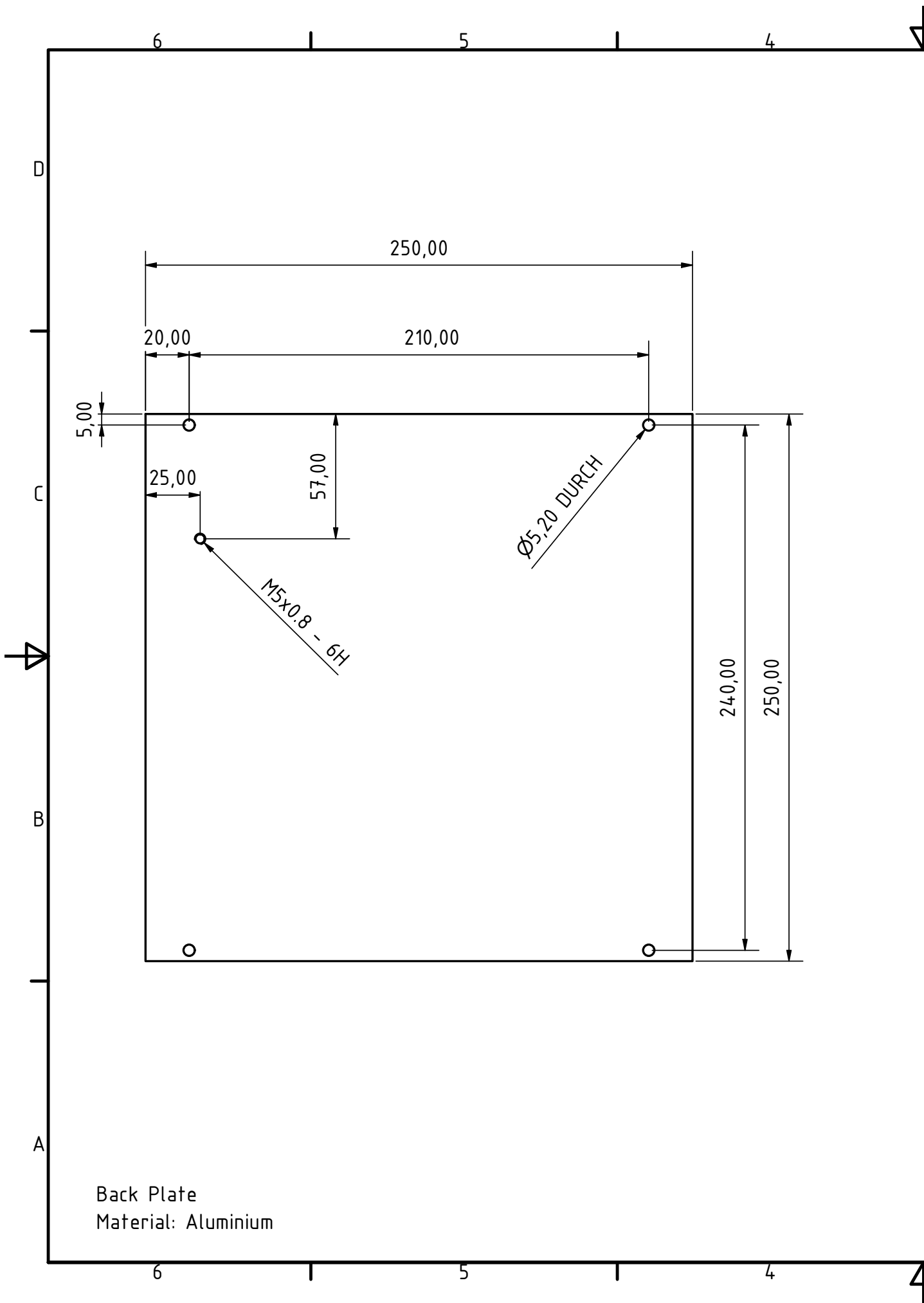




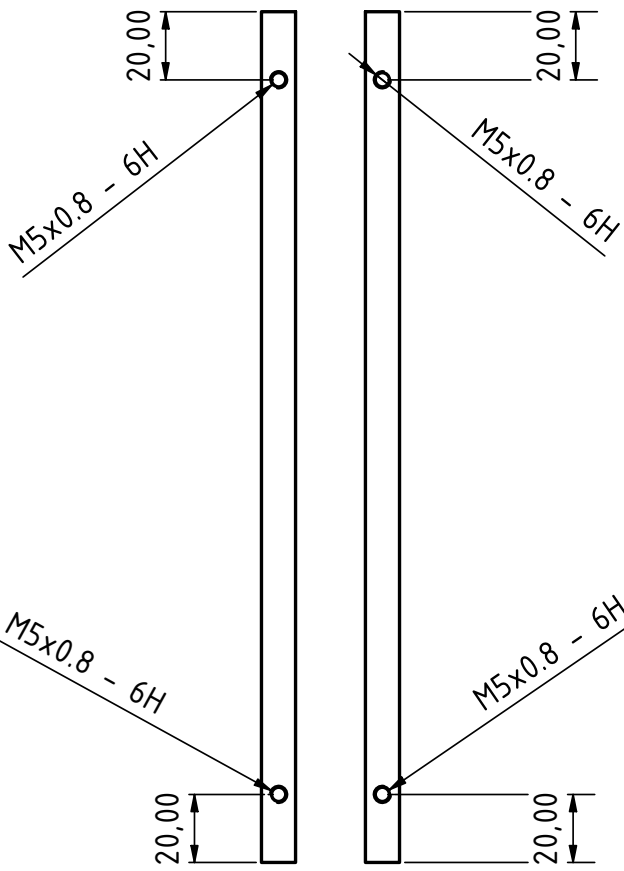
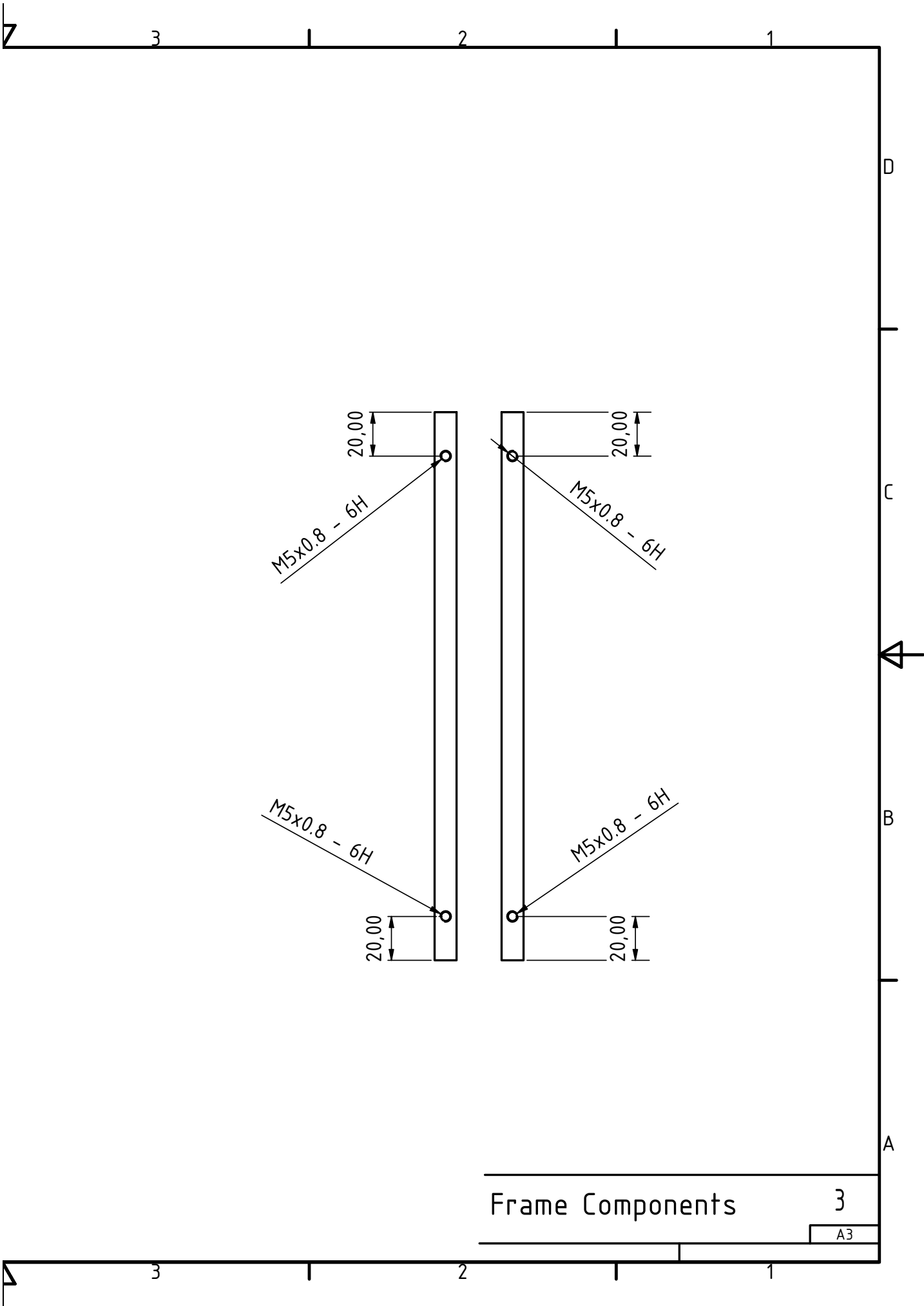
Frame Components

2

A3



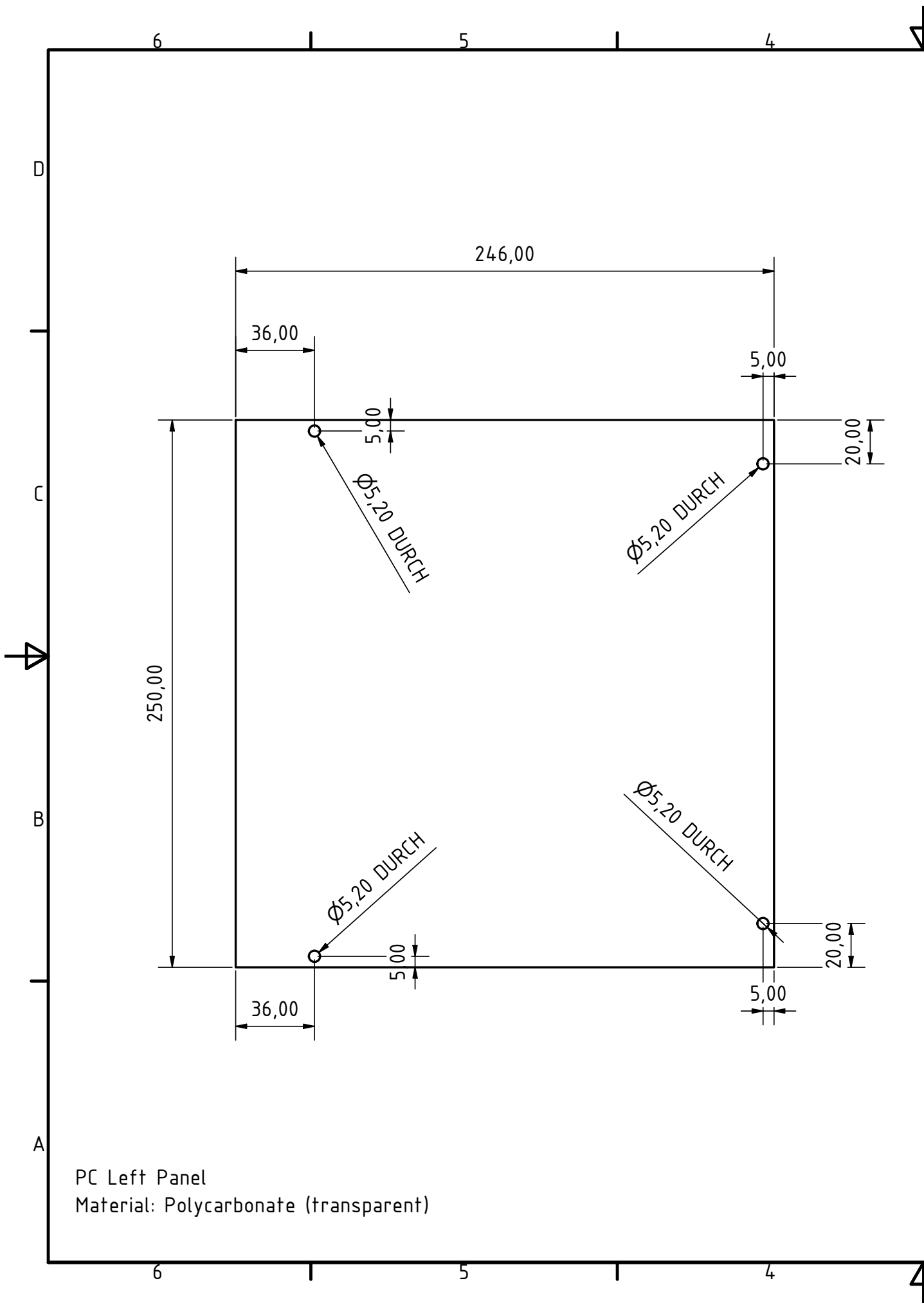
Back Plate
Material: Aluminium



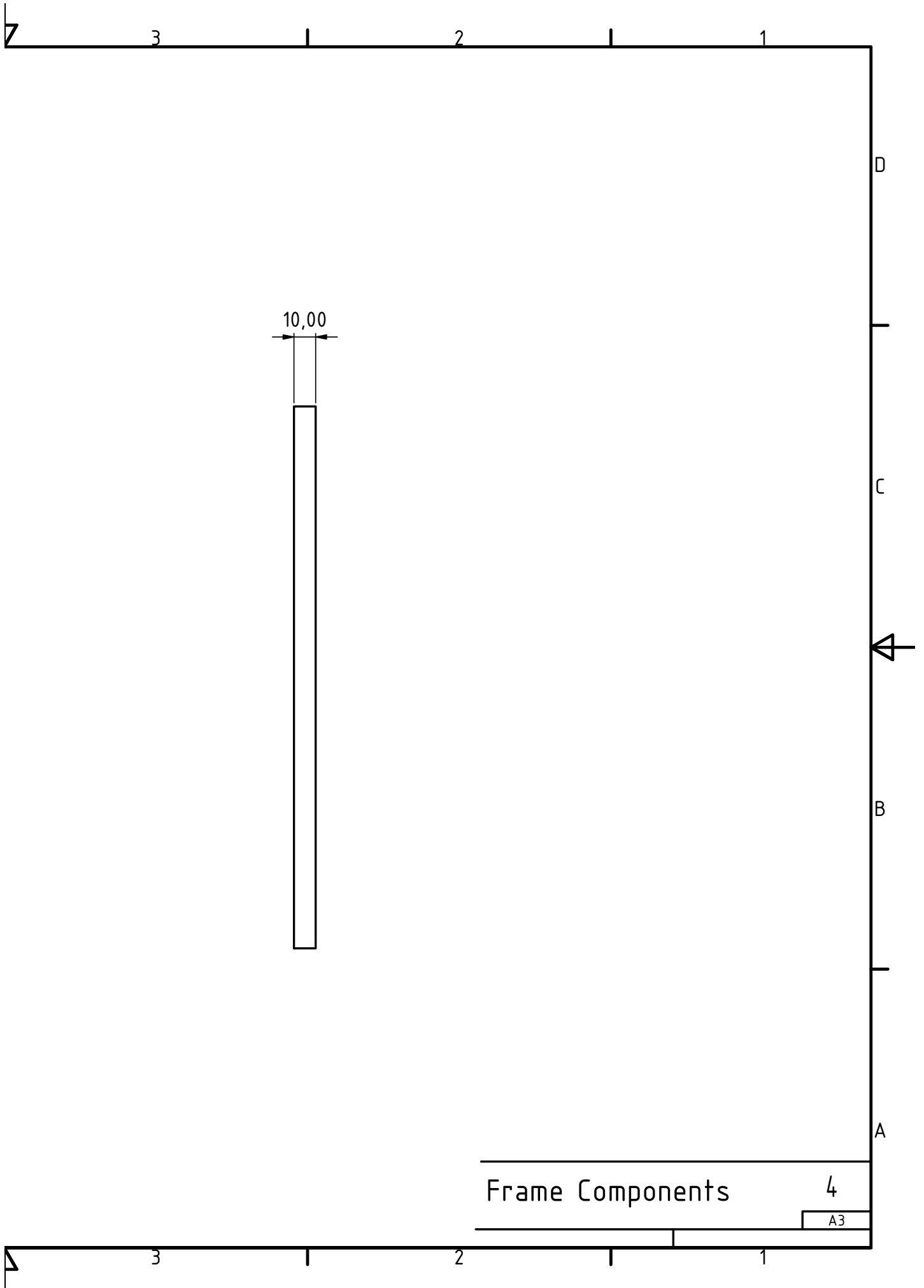
Frame Components

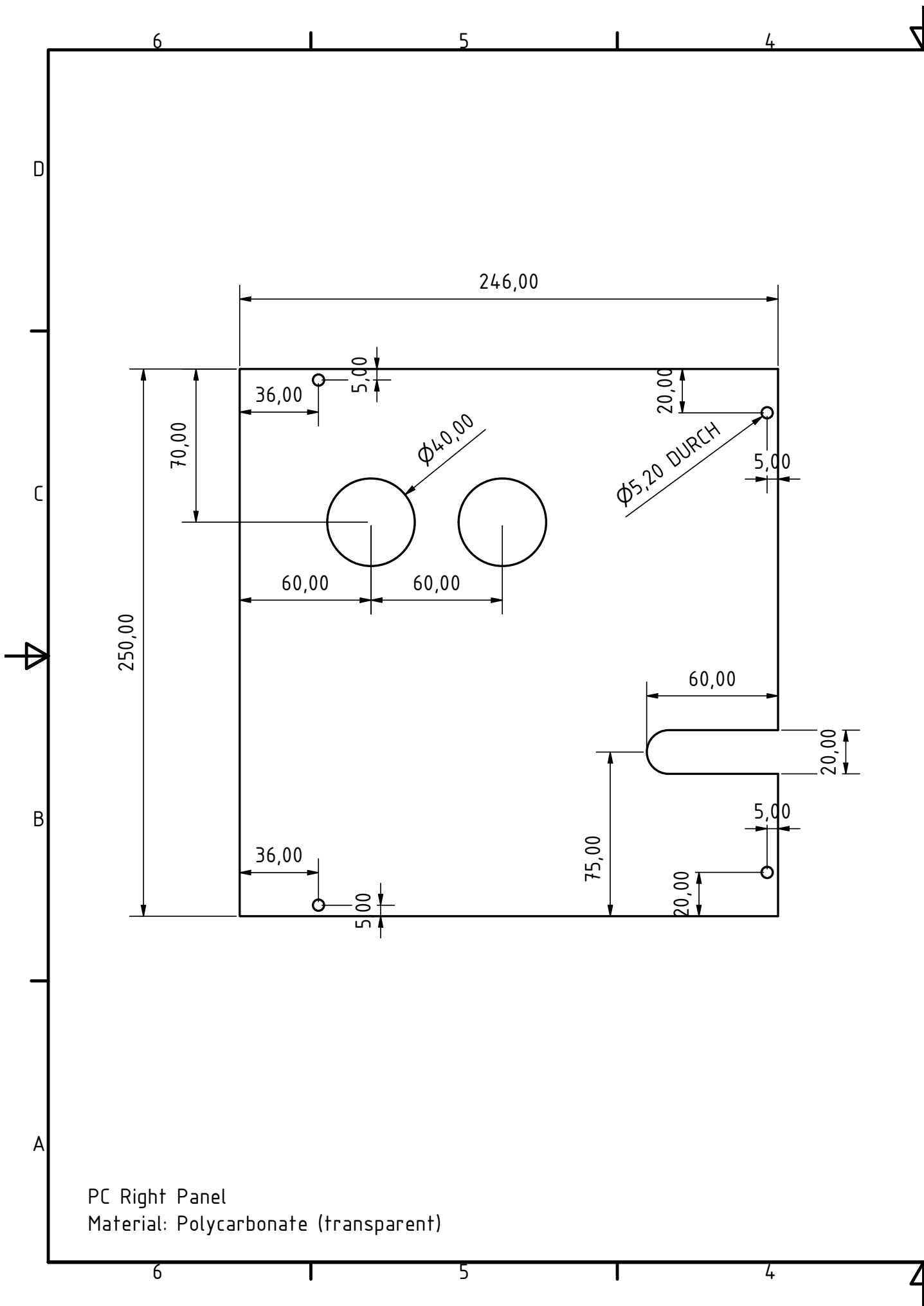
3

A3

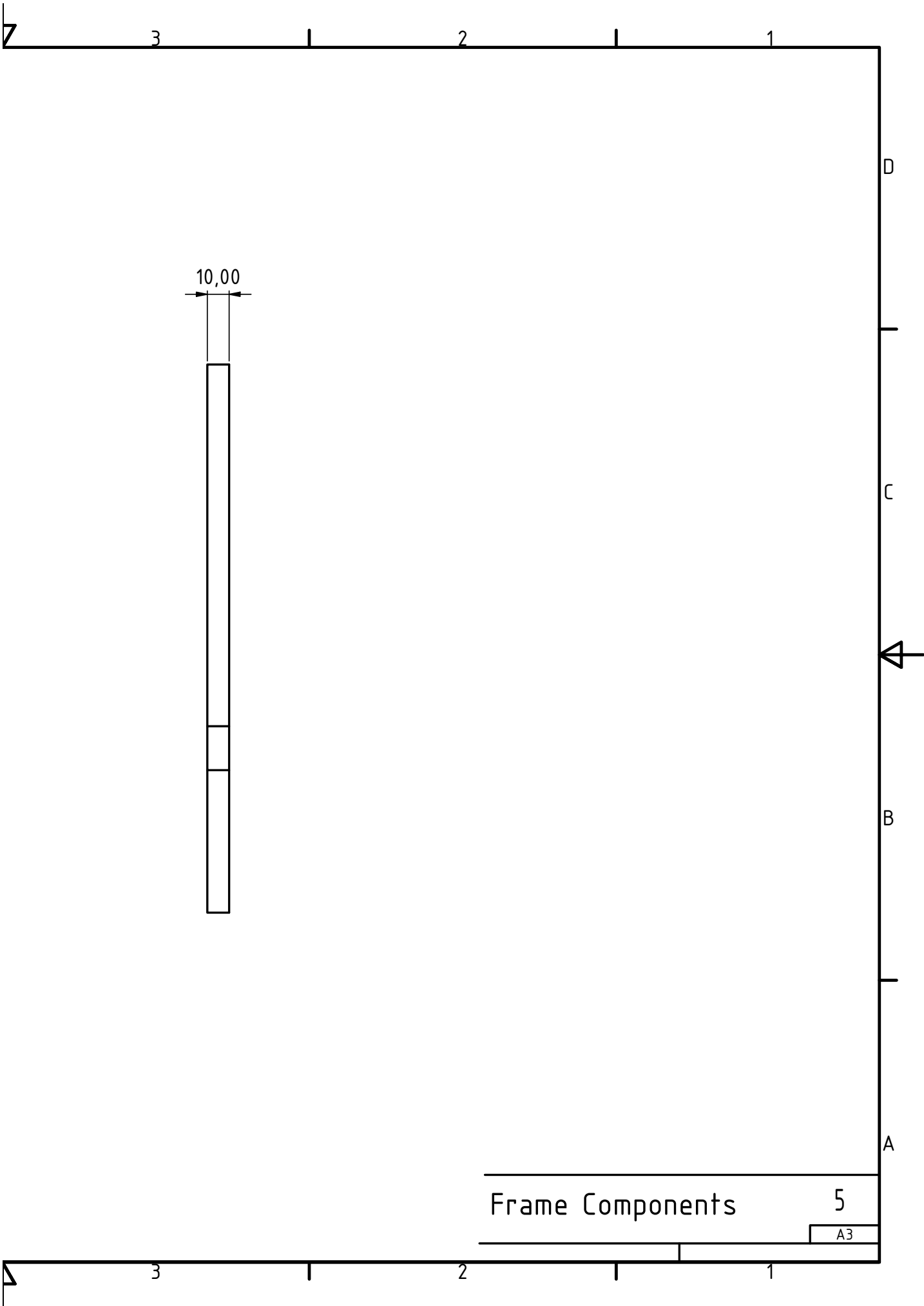


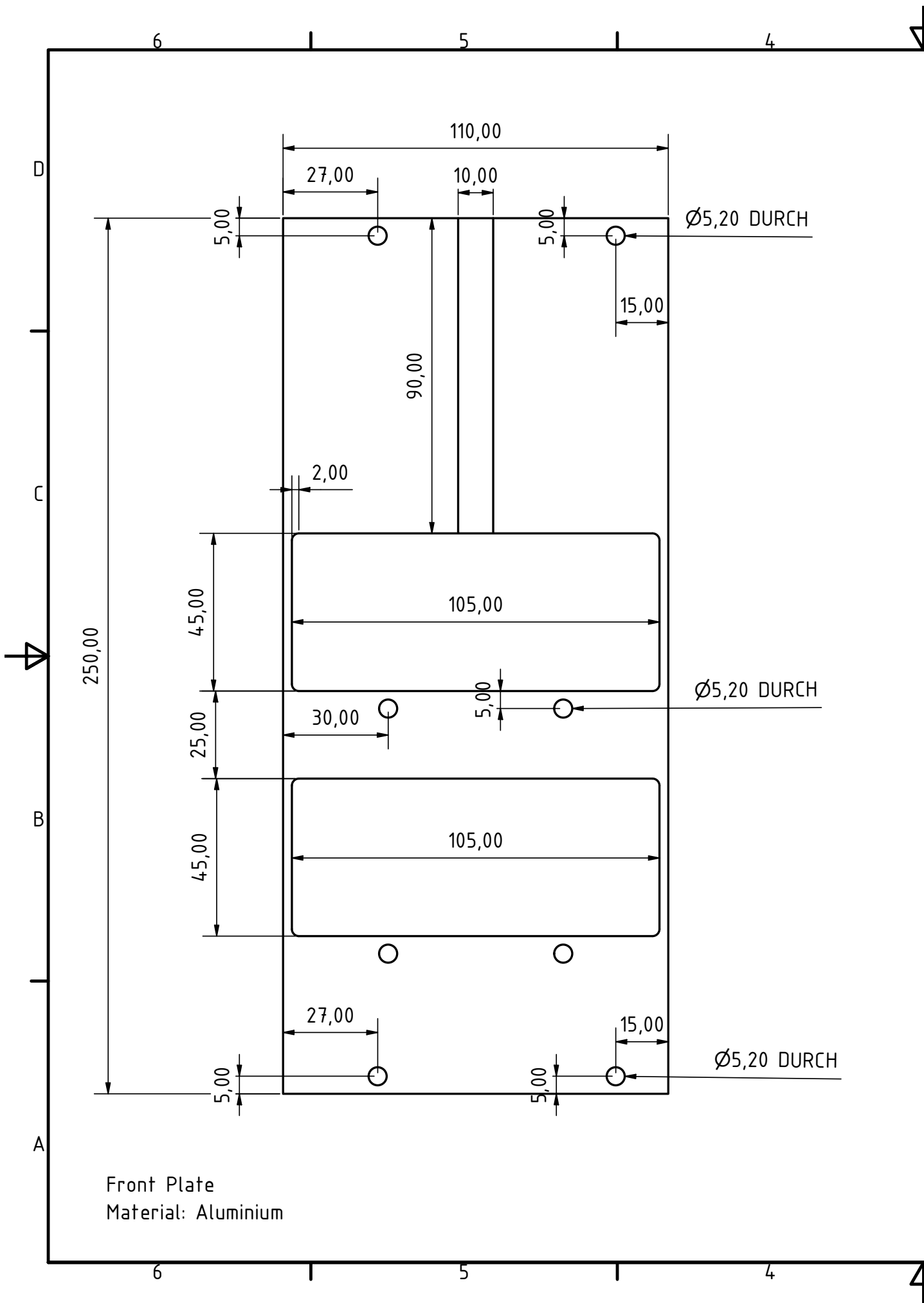
PC Left Panel
 Material: Polycarbonate (transparent)

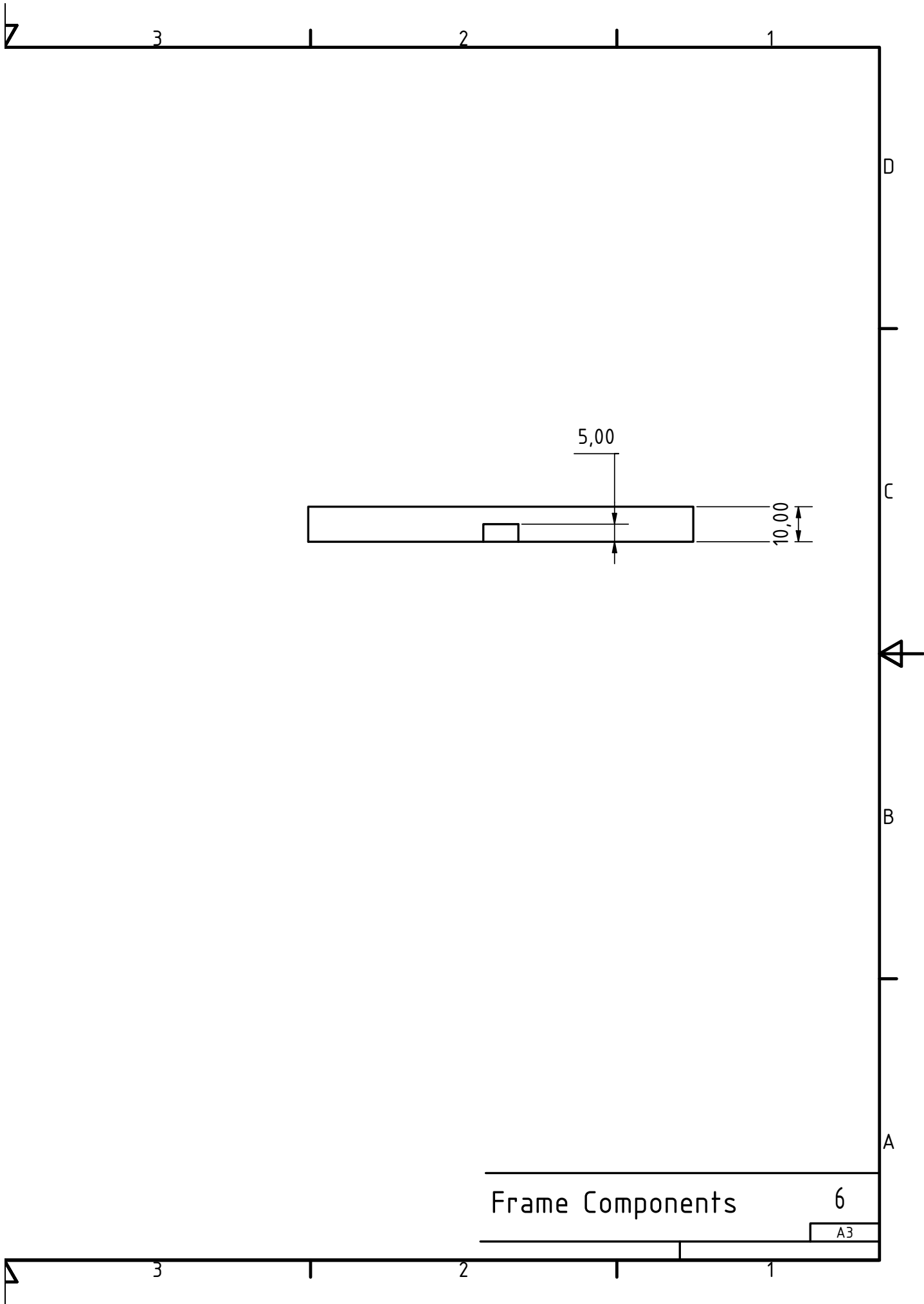




PC Right Panel
 Material: Polycarbonate (transparent)



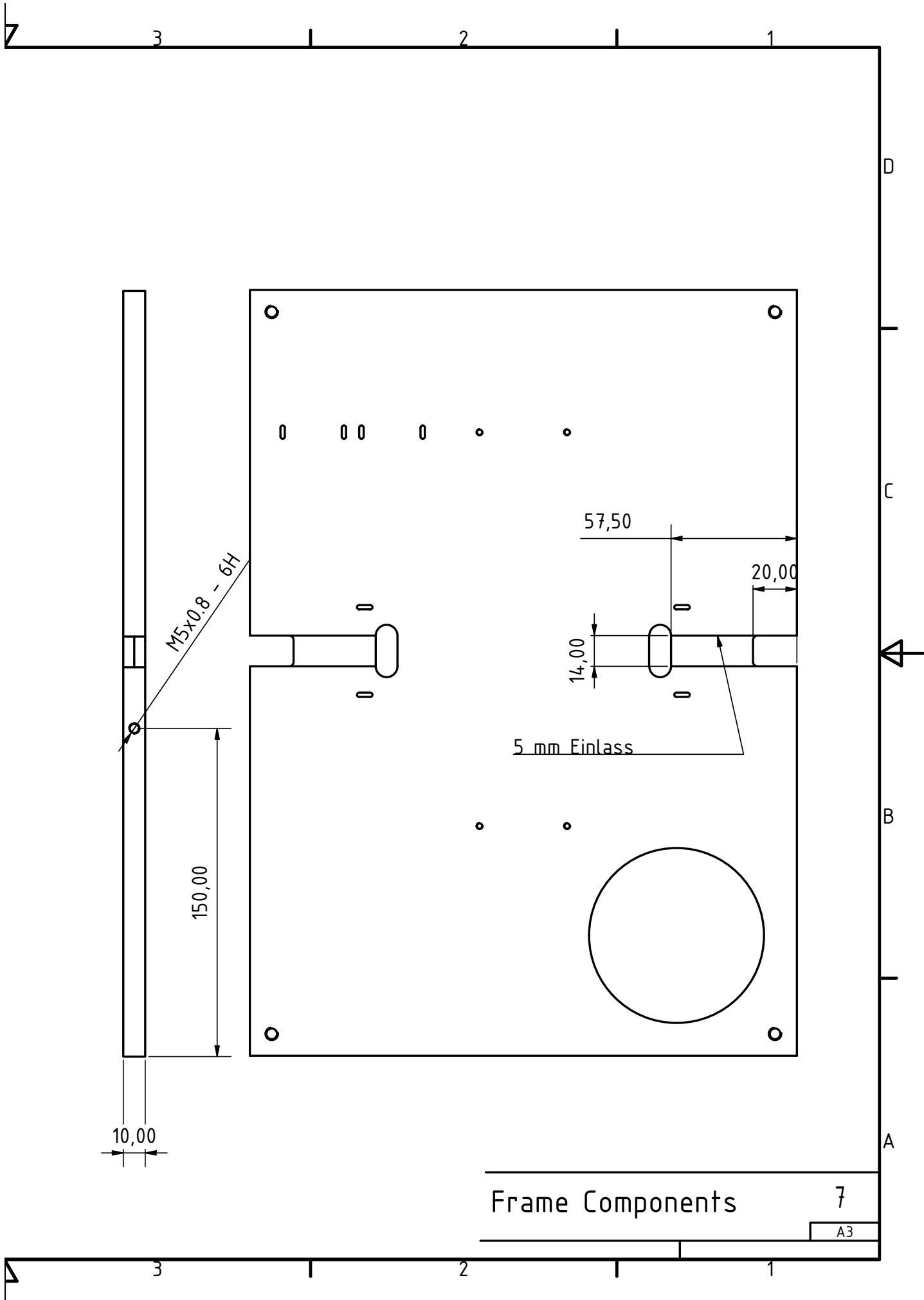


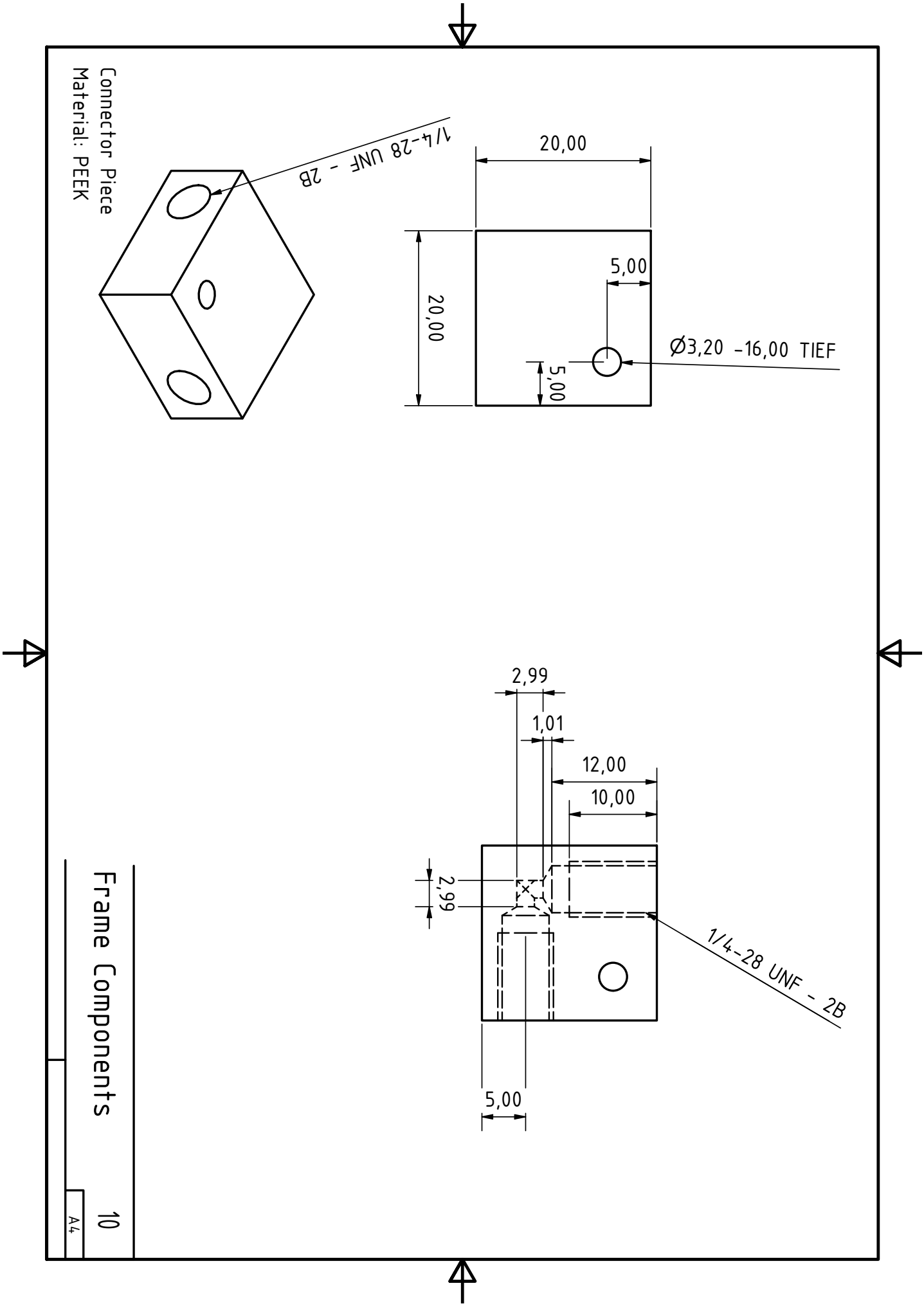


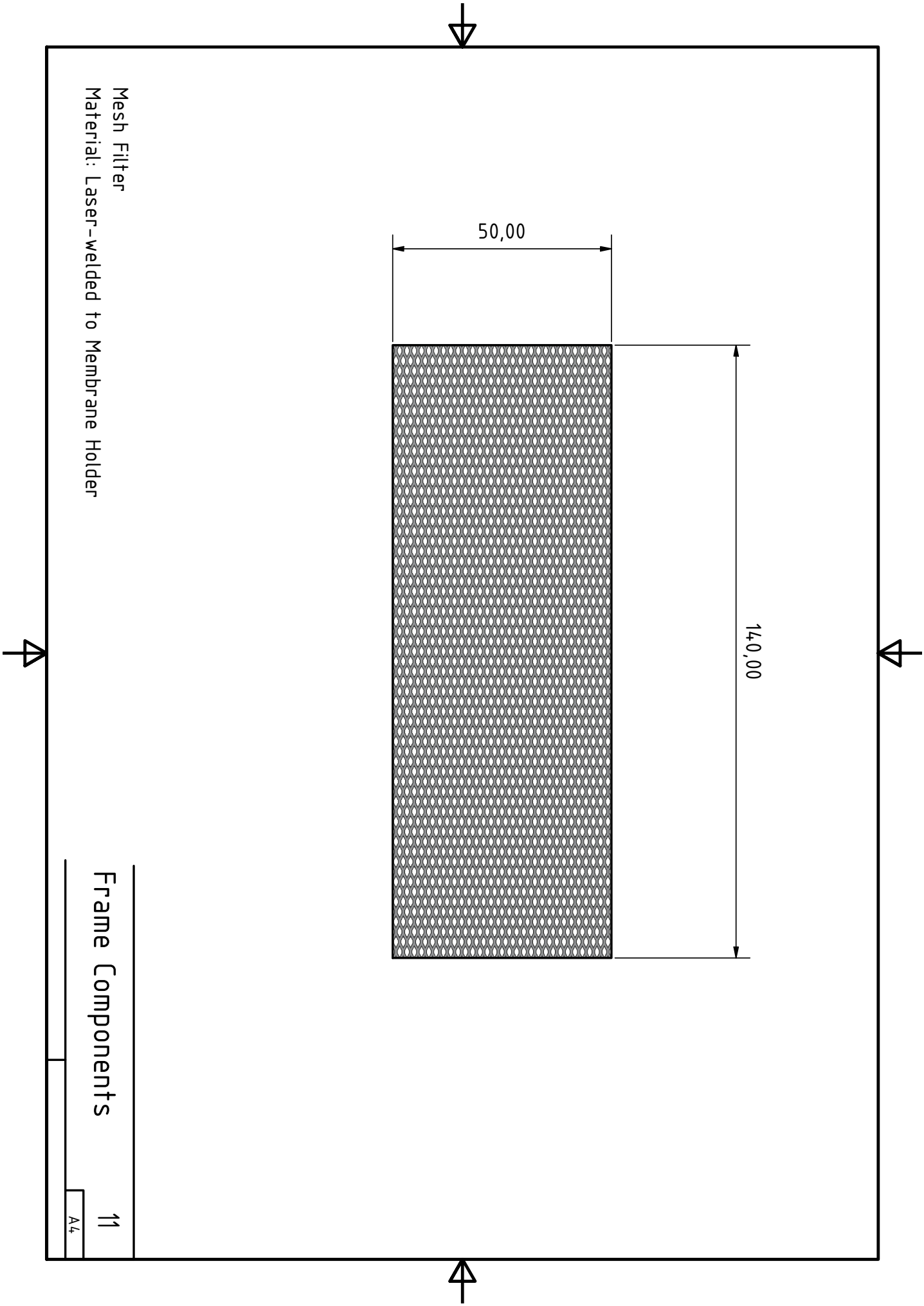
Frame Components

6

A3







Mesh Filter
Material: Laser-welded to Membrane Holder

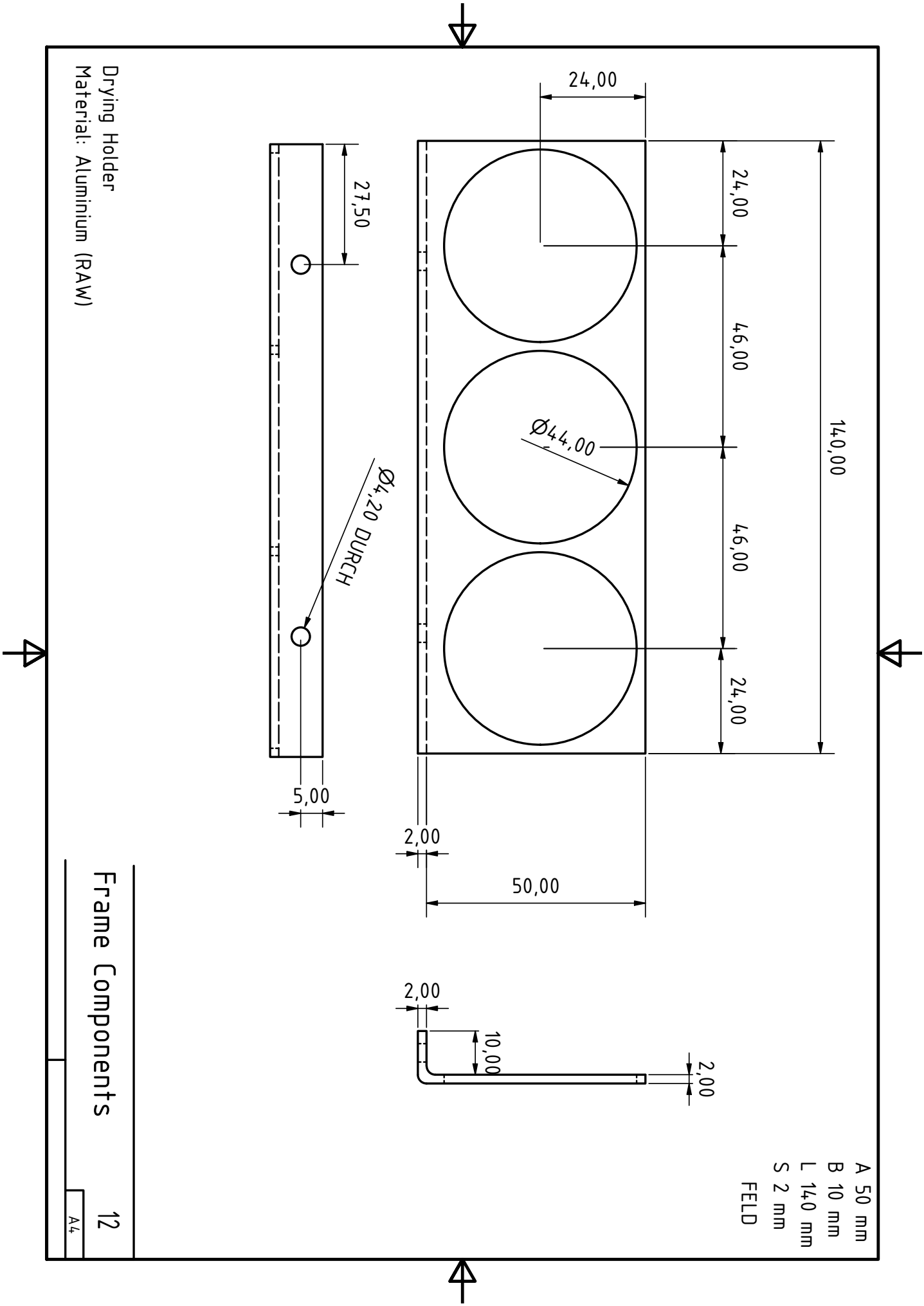
50,00

140,00

Frame Components

11

A4

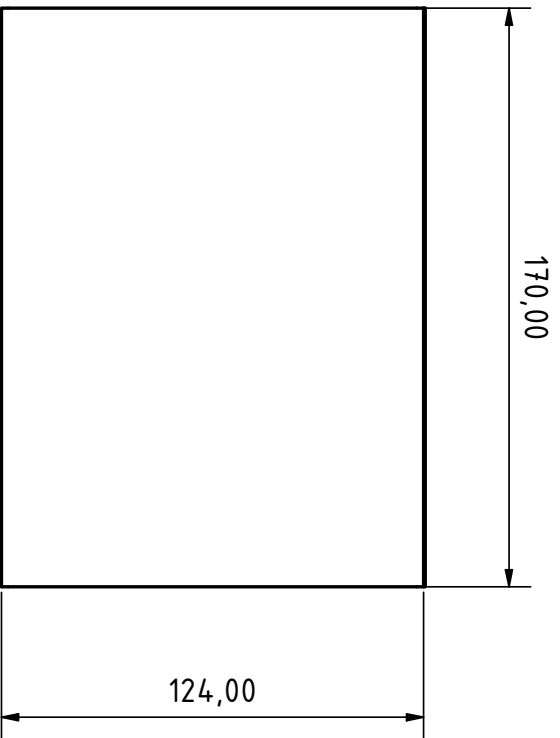
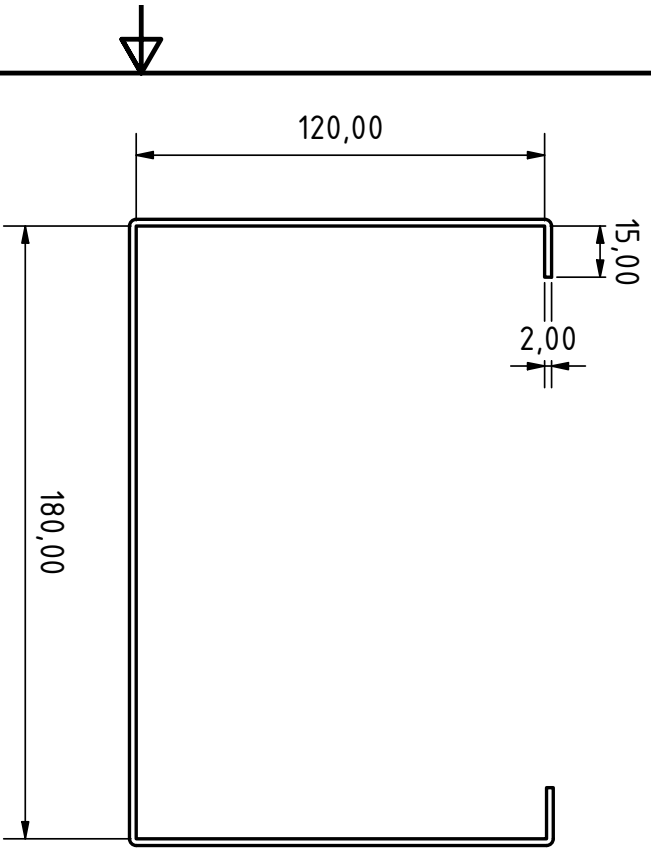


Drying Holder
 Material: Aluminium (RAW)

Frame Components

12
 A4

A 50 mm
 B 10 mm
 L 140 mm
 S 2 mm
 FIELD



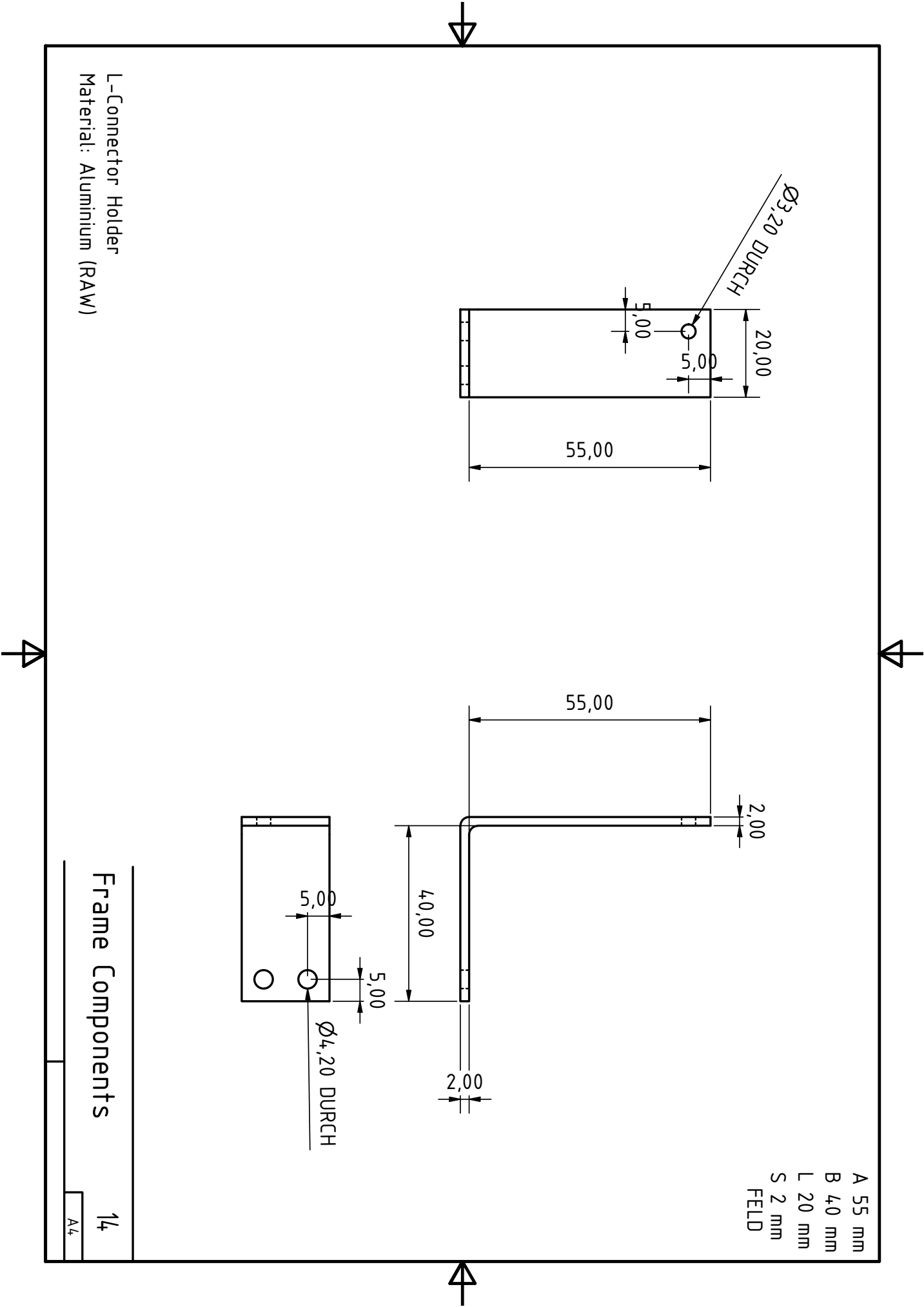
- A 15 mm
- B 120 mm
- C 180 mm
- L 170 mm
- S 2 mm
- FELD

Arduino Box Holder
Material: Aluminium (RAW)

Frame Components

13

A4



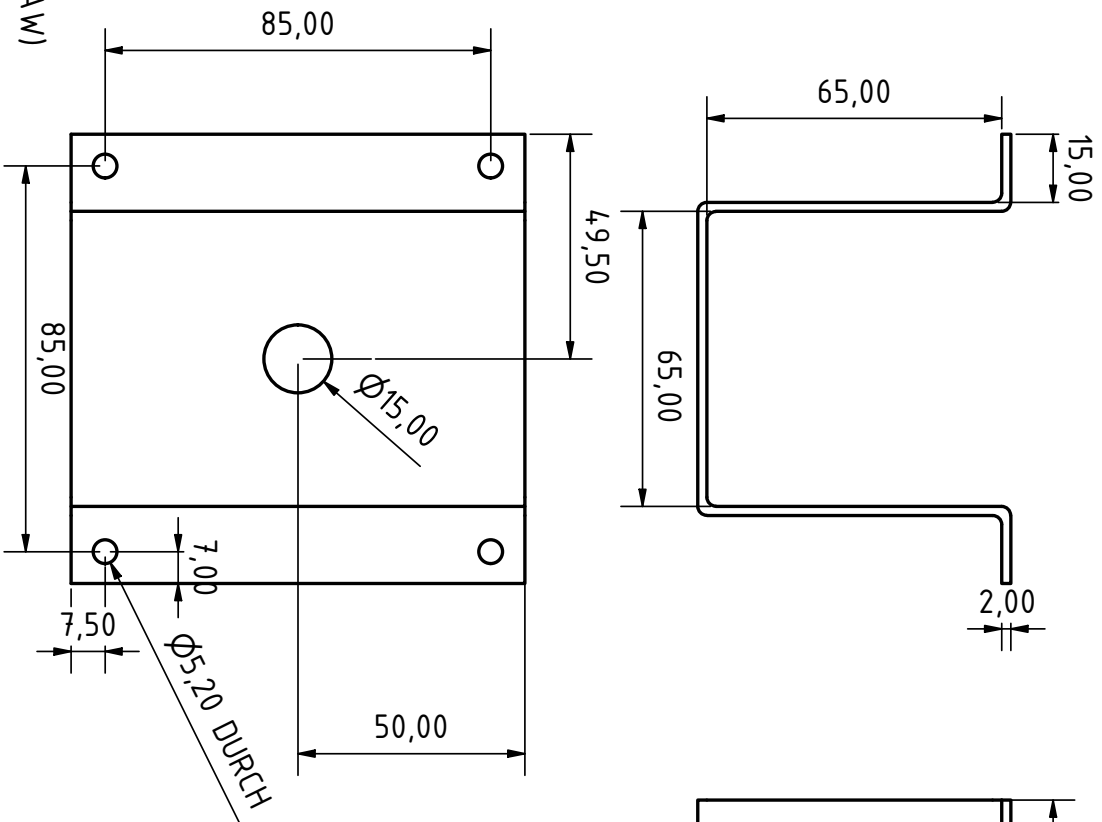
L-Connector Holder
 Material: Aluminium (RAW)

Frame Components

14
 A4

A 55 mm
 B 40 mm
 L 20 mm
 S 2 mm
 FIELD

Holder for Filter
Material: Aluminium (RAW)

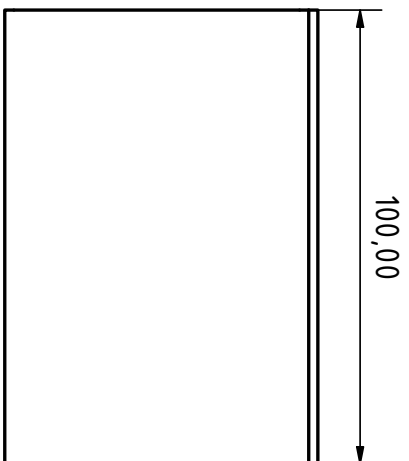


Frame Components

15

A4

A 15 mm
B 65 mm
C 65 mm
L 100 mm
S 2 mm
FELD



- This page is left blank intentionally. -

Bibliography

- ¹C. Rust, H. Li, G. Gordeev, M. Spari, M. Guttman, Q. Jin, S. Reich, and B. S. Flavel, “Global alignment of carbon nanotubes via high precision microfluidic dead-end filtration”, *Advanced Functional Materials* **32**, 2107411 (2022).
- ²C. Rust, E. Schill, O. Garrity, M. Spari, H. Li, A. Bacher, M. Guttman, S. Reich, and B. S. Flavel, “Radial alignment of carbon nanotubes via dead-end filtration”, *Small* (2023).
- ³C. Rust, P. Shapturenka, M. Spari, Q. Jin, H. Li, A. Bacher, M. Guttman, M. Zheng, T. Adel, A. R. H. Walker, J. A. Fagan, and B. S. Flavel, “The impact of carbon nanotube length and diameter on their global alignment by dead-end filtration”, *Small* **1**, 2206774 (2023).
- ⁴L. Wieland, H. Li, C. Rust, J. Chen, and B. S. Flavel, “Carbon nanotubes for photovoltaics: from lab to industry”, *Advanced Energy Materials* **11**, 2002880 (2021).
- ⁵L. Wieland, C. Rust, H. Li, M. Jakoby, I. Howard, F. Li, J. Shi, J. Chen, and B. Flavel, “The potential of swcnts to extend the ir-absorption of silicon solar cells”, *Carbon* **184**, 828–835 (2021).
- ⁶E. Schill, “Impact of carbon nanotube film structure on strain sensing”, Bachelor’s Thesis (Karlsruhe Institute of Technology, 2022).
- ⁷S. Iijima, “Helical microtubules of graphitic carbon”, *nature* **354**, 56–58 (1991).
- ⁸M. Pfohl, D. D. Tune, A. Graf, J. Zaumseil, R. Krupke, and B. S. Flavel, “Fitting single-walled carbon nanotube optical spectra”, *ACS omega* **2**, 1163–1171 (2017).
- ⁹M. S. Strano, V. C. Moore, M. K. Miller, M. J. Allen, E. H. Haroz, C. Kittrell, R. H. Hauge, and R. Smalley, “The role of surfactant adsorption during ultrasonication in the dispersion of single-walled carbon nanotubes”, *Journal of nanoscience and nanotechnology* **3**, 81–86 (2003).
- ¹⁰A. Jorio, G. Dresselhaus, and M. S. Dresselhaus, *Carbon nanotubes: advanced topics in the synthesis, structure, properties and applications*, Vol. 111 (Springer, 2008).
- ¹¹L. Wieland, H. Li, C. Rust, J. Chen, and B. S. Flavel, “Carbon nanotubes for photovoltaics: from lab to industry”, *Advanced Energy Materials* **11**, 2002880 (2021).
- ¹²G. Dresselhaus, M. S. Dresselhaus, and R. Saito, *Physical properties of carbon nanotubes* (World scientific, 1998).

-
- ¹³M. S. Arnold, J. L. Blackburn, J. J. Crochet, S. K. Doorn, J. G. Duque, A. Mohite, and H. Telg, “Recent developments in the photophysics of single-walled carbon nanotubes for their use as active and passive material elements in thin film photovoltaics”, *Physical Chemistry Chemical Physics* **15**, 14896–14918 (2013).
- ¹⁴H. Hu, S. Wang, X. Feng, M. Pauly, G. Decher, and Y. Long, “In-plane aligned assemblies of 1d-nanoobjects: recent approaches and applications”, *Chemical Society Reviews* **49**, 509–553 (2020).
- ¹⁵B. Su, Y. Wu, and L. Jiang, “The art of aligning one-dimensional (1d) nanostructures”, *Chemical Society Reviews* **41**, 7832–7856 (2012).
- ¹⁶R. Saito, M. S. Ukhtary, S. Wang, and Y. Iwasaki, “Circular dichroism of doped carbon nanotubes”, *Journal of Applied Physics* **128**, 164301 (2020).
- ¹⁷A. Baydin, N. Komatsu, F. Tay, S. Ghosh, T. Makihara, G. T. Noe, and J. Kono, “Giant terahertz polarization rotation in ultrathin films of aligned carbon nanotubes”, *Optica* **8**, 760–764 (2021).
- ¹⁸L. Ren, C. L. Pint, T. Arikawa, K. Takeya, I. Kawayama, M. Tonouchi, R. H. Hauge, and J. Kono, “Broadband terahertz polarizers with ideal performance based on aligned carbon nanotube stacks”, *Nano letters* **12**, 787–790 (2012).
- ¹⁹Z. Li, K. R. Jinkins, D. Cui, M. Chen, Z. Zhao, M. S. Arnold, and C. Zhou, “Air-stable n-type transistors based on assembled aligned carbon nanotube arrays and their application in complementary metal-oxide-semiconductor electronics”, *Nano Research* (2021).
- ²⁰L. Zhang, G. Zhang, C. Liu, and S. Fan, “High-density carbon nanotube buckypapers with superior transport and mechanical properties”, *Nano letters* **12**, 4848–4852 (2012).
- ²¹D. Wang, P. Song, C. Liu, W. Wu, and S. Fan, “Highly oriented carbon nanotube papers made of aligned carbon nanotubes”, *Nanotechnology* **19**, 075609 (2008).
- ²²S. J. Kang, C. Kocabas, T. Ozel, M. Shim, N. Pimparkar, M. A. Alam, S. V. Rotkin, and J. A. Rogers, “High-performance electronics using dense, perfectly aligned arrays of single-walled carbon nanotubes”, *Nature nanotechnology* **2**, 230–236 (2007).
- ²³M. D. Lynch and D. L. Patrick, “Organizing carbon nanotubes with liquid crystals”, *Nano letters* **2**, 1197–1201 (2002).
- ²⁴A. Peigney, E. Flahaut, C. Laurent, F. Chastel, and A. Rousset, “Aligned carbon nanotubes in ceramic-matrix nanocomposites prepared by high-temperature extrusion”, *Chemical Physics Letters* **352**, 20–25 (2002).

-
- ²⁵Q. Cao, S.-j. Han, G. S. Tulevski, Y. Zhu, D. D. Lu, and W. Haensch, “Arrays of single-walled carbon nanotubes with full surface coverage for high-performance electronics”, *Nature nanotechnology* **8**, 180–186 (2013).
- ²⁶X. Li, Y. Jung, K. Sakimoto, T.-H. Goh, M. A. Reed, and A. D. Taylor, “Improved efficiency of smooth and aligned single walled carbon nanotube/silicon hybrid solar cells”, *Energy and Environmental Science* **6**, 879–887 (2013).
- ²⁷M. S. Arnold, S. I. Stupp, and M. C. Hersam, “Enrichment of single-walled carbon nanotubes by diameter in density gradients”, *Nano Letters* **5**, 713–718 (2005).
- ²⁸X. Huang, R. S. McLean, and M. Zheng, “High-resolution length sorting and purification of dna-wrapped carbon nanotubes by size-exclusion chromatography”, *Analytical Chemistry* **77**, 6225–6228 (2005).
- ²⁹H. Li, G. Gordeev, S. Wasserroth, V. S. K. Chakravadhanula, S. K. C. Neelakandhan, F. Hennrich, A. Jorio, S. Reich, R. Krupke, and B. S. Flavel, “Inner-and outer-wall sorting of double-walled carbon nanotubes”, *Nature nanotechnology* **12**, 1176–1182 (2017).
- ³⁰K. E. Moore, M. Pfohl, F. Hennrich, V. S. K. Chakradhanula, C. Kuebel, M. M. Kappes, J. G. Shapter, R. Krupke, and B. S. Flavel, “Separation of double-walled carbon nanotubes by size exclusion column chromatography”, *ACS nano* **8**, 6756–6764 (2014).
- ³¹M. S. Arnold, A. A. Green, J. F. Hulvat, S. I. Stupp, and M. C. Hersam, “Sorting carbon nanotubes by electronic structure using density differentiation”, *Nature Nanotechnology* **1**, 60 (2006).
- ³²H. Gui, J. K. Streit, J. A. Fagan, A. R. Hight Walker, C. Zhou, and M. Zheng, “Redox sorting of carbon nanotubes”, *Nano Letters* **15**, 1642–1646 (2015).
- ³³C. Y. Khripin, J. A. Fagan, and M. Zheng, “Spontaneous partition of carbon nanotubes in polymer-modified aqueous phases”, *Journal of the American Chemical Society* **135**, 6822–6825 (2013).
- ³⁴M. Zheng, A. Jagota, M. S. Strano, A. P. Santos, P. Barone, S. G. Chou, B. A. Diner, M. S. Dresselhaus, R. S. Mclean, and G. B. Onoa, “Structure-based carbon nanotube sorting by sequence-dependent dna assembly”, *Science* **302**, 1545–1548 (2003).
- ³⁵H. Liu, D. Nishide, T. Tanaka, and H. Kataura, “Large-scale single-chirality separation of single-wall carbon nanotubes by simple gel chromatography”, *Nature communications* **2**, 1–8 (2011).
- ³⁶H. Li, G. Gordeev, O. Garrity, S. Reich, and B. S. Flavel, “Separation of small-diameter single-walled carbon nanotubes in one to three steps with aqueous two-phase extraction”, *ACS nano* **13**, 2567–2578 (2019).

-
- ³⁷X. Wei, T. Tanaka, T. Hirakawa, Y. Yomogida, and H. Kataura, “Determination of enantiomeric purity of single-wall carbon nanotubes using flavin mononucleotide”, *Journal of the American Chemical Society* **139**, 16068–16071 (2017).
- ³⁸H. Li, G. Gordeev, O. Garrity, N. A. Peyyety, P. B. Selvasundaram, S. Dehm, R. Krupke, S. Cambré, W. Wenseleers, and S. Reich, “Separation of specific single-enantiomer single-wall carbon nanotubes in the large-diameter regime”, *ACS nano* **14**, 948–963 (2019).
- ³⁹L. Jin, C. Bower, and O. Zhou, “Alignment of carbon nanotubes in a polymer matrix by mechanical stretching”, *Applied physics letters* **73**, 1197–1199 (1998).
- ⁴⁰X. W. He, W. L. Gao, L. J. Xie, B. Li, Q. Zhang, S. D. Lei, J. M. Robinson, E. H. Haroz, S. K. Doorn, W. P. Wang, R. Vajtai, P. M. Ajayan, W. W. Adams, R. H. Hauge, and J. Kono, “Wafer-scale monodomain films of spontaneously aligned single-walled carbon nanotubes”, *Nature Nanotechnology* **11**, 633–+ (2016).
- ⁴¹J. S. Walker, J. A. Fagan, A. J. Biacchi, V. A. Kuehl, T. A. Searles, A. R. Hight Walker, and W. D. Rice, “Global alignment of solution-based single-wall carbon nanotube films via machine-vision controlled filtration”, *Nano Letters* **19**, 7256–7264 (2019).
- ⁴²A. Hirsch, “The era of carbon allotropes”, *Nature Materials* **9**, 868–871 (2010).
- ⁴³H. W. Kroto, J. R. Heath, S. C. O’Brien, R. F. Curl, and R. E. Smalley, “C₆₀: buckminsterfullerene”, *Nature* **318**, 162–163 (1985).
- ⁴⁴K. S. Novoselov, A. K. Geim, S. V. Morozov, D. Jiang, Y. Zhang, S. V. Dubonos, I. V. Grigorieva, and A. A. Firsov, “Electric field effect in atomically thin carbon films”, *Science* **306**, 666–669 (2004).
- ⁴⁵S. Reich, C. Thomsen, and J. Maultzsch, *Carbon nanotubes: basic concepts and physical properties* (John Wiley & Sons, 2004).
- ⁴⁶M. J. Allen, V. C. Tung, and R. B. Kaner, “Honeycomb carbon: a review of graphene”, *Chemical Reviews* **110**, 132–145 (2010).
- ⁴⁷W. L. Gao and J. Kono, “Science and applications of wafer-scale crystalline carbon nanotube films prepared through controlled vacuum filtration”, *Royal Society Open Science* **6** (2019).
- ⁴⁸D.-M. Chen, P. M. Shenai, and Y. Zhao, “Tight binding description on the band gap opening of pyrene-dispersed graphene”, *Physical Chemistry Chemical Physics* **13**, 1515–1520 (2011).

-
- ⁴⁹C. Thomsen and S. Reich, “Raman scattering in carbon nanotubes”, in *Light scattering in solid ix*, edited by M. Cardona and R. Merlin (Springer Berlin Heidelberg, Berlin, Heidelberg, 2007), pp. 115–234.
- ⁵⁰M. S. Dresselhaus, G. Dresselhaus, and P. C. Eklund, *Science of fullerenes and carbon nanotubes: their properties and applications* (Elsevier, 1996).
- ⁵¹R. B. Pipes, S. Frankland, P. Hubert, and E. Saether, “Self-consistent properties of carbon nanotubes and hexagonal arrays as composite reinforcements”, *Composites Science and Technology* **63**, 1349–1358 (2003).
- ⁵²M. V. Kharlamova, “Advances in tailoring the electronic properties of single-walled carbon nanotubes”, *Progress in Materials Science* **77**, 125–211 (2016).
- ⁵³A. H. Castro Neto, F. Guinea, N. M. R. Peres, K. S. Novoselov, and A. K. Geim, “The electronic properties of graphene”, *Reviews of Modern Physics* **81**, 109–162 (2009).
- ⁵⁴L. Van Hove, “The occurrence of singularities in the elastic frequency distribution of a crystal”, *Physical Review* **89**, 1189 (1953).
- ⁵⁵R. Saito and H. Kataura, “Optical properties and raman spectroscopy of carbon nanotubes”, in *Carbon nanotubes* (Springer, 2001), pp. 213–247.
- ⁵⁶H. Kataura, Y. Kumazawa, Y. Maniwa, I. Umezumi, S. Suzuki, Y. Ohtsuka, and Y. Achiba, “Optical properties of single-wall carbon nanotubes”, *Synthetic Metals* **103**, 2555–2558 (1999).
- ⁵⁷N. Anzar, R. Hasan, M. Tyagi, N. Yadav, and J. Narang, “Carbon nanotube - a review on synthesis, properties and plethora of applications in the field of biomedical science”, *Sensors International* **1**, 100003 (2020).
- ⁵⁸C. Journet, M. Picher, and V. Jourdain, “Carbon nanotube synthesis: from large-scale production to atom-by-atom growth”, *Nanotechnology* **23**, 142001 (2012).
- ⁵⁹N. Arora and N. N. Sharma, “Arc discharge synthesis of carbon nanotubes: comprehensive review”, *Diamond and Related Materials* **50**, 135–150 (2014).
- ⁶⁰P. Bernier, D. Laplaze, J. Auriol, L. Barbedette, G. Flamant, M. Lebrun, A. Brunelle, and S. Della-Negra, “Production of fullerenes from solar energy”, *Synthetic Metals* **70**, 1455–1456 (1995).
- ⁶¹D. Laplaze, P. Bernier, W. Maser, G. Flamant, T. Guillard, and A. Loiseau, “Carbon nanotubes: the solar approach”, *Carbon* **36**, 685–688 (1998).

-
- ⁶²T. Guo, P. Nikolaev, A. Thess, D. T. Colbert, and R. E. Smalley, “Catalytic growth of single-walled nanotubes by laser vaporization”, *Chemical Physics Letters* **243**, 49–54 (1995).
- ⁶³M. Kumar and Y. Ando, “Chemical vapor deposition of carbon nanotubes: a review on growth mechanism and mass production”, *Journal of nanoscience and nanotechnology* **10**, 3739–3758 (2010).
- ⁶⁴S. Sinnott, R. Andrews, D. Qian, A. M. Rao, Z. Mao, E. Dickey, and F. Derbyshire, “Model of carbon nanotube growth through chemical vapor deposition”, *Chemical Physics Letters* **315**, 25–30 (1999).
- ⁶⁵R. Baker, M. Barber, P. Harris, F. Feates, and R. Waite, “Nucleation and growth of carbon deposits from the nickel catalyzed decomposition of acetylene”, *Journal of catalysis* **26**, 51–62 (1972).
- ⁶⁶M. J. Bronikowski, P. A. Willis, D. T. Colbert, K. Smith, and R. E. Smalley, “Gas-phase production of carbon single-walled nanotubes from carbon monoxide via the hipco process: a parametric study”, *Journal of Vacuum Science & Technology A: Vacuum, Surfaces, and Films* **19**, 1800–1805 (2001).
- ⁶⁷D. Resasco, W. Alvarez, F. Pompeo, L. Balzano, J. Herrera, B. Kitiyanan, and A. Borgna, “A scalable process for production of single-walled carbon nanotubes (swnts) by catalytic disproportionation of CO on a solid catalyst”, *Journal of Nanoparticle Research* **4**, 131–136 (2002).
- ⁶⁸J. R. Sanchez-Valencia, T. Dienel, O. Gröning, I. Shorubalko, A. Mueller, M. Jansen, K. Amsharov, P. Ruffieux, and R. Fasel, “Controlled synthesis of single-chirality carbon nanotubes”, *Nature* **512**, 61–64 (2014).
- ⁶⁹F. Yang, X. Wang, D. Zhang, J. Yang, D. Luo, Z. Xu, J. Wei, J.-Q. Wang, Z. Xu, and F. Peng, “Chirality-specific growth of single-walled carbon nanotubes on solid alloy catalysts”, *Nature* **510**, 522–524 (2014).
- ⁷⁰P. Ajayan and S. Iijima, “Smallest carbon nanotube”, *Nature* **358**, 23–23 (1992).
- ⁷¹S. W. Kim, T. Kim, Y. S. Kim, H. S. Choi, H. J. Lim, S. J. Yang, and C. R. Park, “Surface modifications for the effective dispersion of carbon nanotubes in solvents and polymers”, *Carbon* **50**, 3–33 (2012).
- ⁷²Z. Wang, M. D. Shirley, S. T. Meikle, R. L. D. Whitby, and S. V. Mikhalovsky, “The surface acidity of acid oxidised multi-walled carbon nanotubes and the influence of in-situ generated fulvic acids on their stability in aqueous dispersions”, *Carbon* **47**, 73–79 (2009).
- ⁷³D. Nepal, J.-I. Sohn, W. K. Aicher, S. Lee, and K. E. Geckeler, “Supramolecular conjugates of carbon nanotubes and DNA by a solid-state reaction”, *Biomacromolecules* **6**, 2919–2922 (2005).
- ⁷⁴H. Pan, L. Liu, Z.-X. Guo, L. Dai, F. Zhang, D. Zhu, R. Czerw, and D. L. Carroll, “Carbon nanotubols from mechanochemical reaction”, *Nano letters* **3**, 29–32 (2003).

-
- ⁷⁵N. Pierard, A. Fonseca, Z. Konya, I. Willems, G. Van Tendeloo, and J. B. Nagy, “Production of short carbon nanotubes with open tips by ball milling”, *Chemical physics letters* **335**, 1–8 (2001).
- ⁷⁶T. Okpalugo, P. Papakonstantinou, H. Murphy, J. Mclaughlin, and N. Brown, “Oxidative functionalization of carbon nanotubes in atmospheric pressure filamentary dielectric barrier discharge (apdbd)”, *Carbon* **43**, 2951–2959 (2005).
- ⁷⁷M. E. Sullivan, D. Klosterman, and G. R. Palmese, “Electron beam modification and functionalization of mwnt for covalent dispersion into polymeric systems”, *Nuclear Instruments and Methods in Physics Research Section B: Beam Interactions with Materials and Atoms* **265**, 352–355 (2007).
- ⁷⁸K. J. Ziegler, Z. Gu, H. Peng, E. L. Flor, R. H. Hauge, and R. E. Smalley, “Controlled oxidative cutting of single-walled carbon nanotubes”, *Journal of the American Chemical Society* **127**, 1541–1547 (2005).
- ⁷⁹A. Kuznetsova, I. Popova, J. Yates John T., M. J. Bronikowski, C. B. Huffman, J. Liu, R. E. Smalley, H. H. Hwu, and J. G. Chen, “Oxygen-containing functional groups on single-wall carbon nanotubes: Raman and vibrational spectroscopic studies”, *Journal of the American Chemical Society* **123**, 10699–10704 (2001).
- ⁸⁰D. D. Tune, A. J. Blanch, C. J. Shearer, K. E. Moore, M. Pfohl, J. G. Shapter, and B. S. Flavel, “Aligned carbon nanotube thin films from liquid crystal polyelectrolyte inks”, *ACS Applied Materials and Interfaces* **7**, 25857–25864 (2015).
- ⁸¹V. Skakalova, A. Kaiser, U. Dettlaff-Weglikowska, K. Hrnčarikova, and S. Roth, “Effect of chemical treatment on electrical conductivity, infrared absorption, and raman spectra of single-walled carbon nanotubes”, *The Journal of Physical Chemistry B* **109**, 7174–7181 (2005).
- ⁸²W. Zhao, C. Song, and P. E. Pehrsson, “Water-soluble and optically pH-sensitive single-walled carbon nanotubes from surface modification”, *Journal of the American Chemical Society* **124**, 12418–12419 (2002).
- ⁸³M. Yang, V. Koutsos, and M. Zaiser, “Interactions between polymers and carbon nanotubes: a molecular dynamics study”, *The Journal of Physical Chemistry B* **109**, 10009–10014 (2005).
- ⁸⁴A. Nish, J.-Y. Hwang, J. Doig, and R. J. Nicholas, “Highly selective dispersion of single-walled carbon nanotubes using aromatic polymers”, *Nature nanotechnology* **2**, 640–646 (2007).
- ⁸⁵A. Graf, Y. Zakharko, S. P. Schießl, C. Backes, M. Pfohl, B. S. Flavel, and J. Zaumseil, “Large scale, selective dispersion of long single-walled carbon nanotubes with high photoluminescence quantum yield by shear force mixing”, *Carbon* **105**, 593–599 (2016).

-
- ⁸⁶S. K. Samanta, M. Fritsch, U. Scherf, W. Gomulya, S. Z. Bisri, and M. A. Loi, “Conjugated polymer-assisted dispersion of single-wall carbon nanotubes: the power of polymer wrapping”, *Accounts of chemical research* **47**, 2446–2456 (2014).
- ⁸⁷S. Liang, H. Li, B. S. Flavel, and A. Adronov, “Effect of single-walled carbon nanotube (swcnt) composition on polyfluorene-based swcnt dispersion selectivity”, *Chemistry–A European Journal* **24**, 9799–9806 (2018).
- ⁸⁸Y. Joo, G. J. Brady, M. S. Arnold, and P. Gopalan, “Dose-controlled, floating evaporative self-assembly and alignment of semiconducting carbon nanotubes from organic solvents”, *Langmuir* **30**, 3460–3466 (2014).
- ⁸⁹T. Lei, I. Pochorovski, and Z. Bao, “Separation of semiconducting carbon nanotubes for flexible and stretchable electronics using polymer removable method”, *Accounts of chemical research* **50**, 1096–1104 (2017).
- ⁹⁰D. J. Bindl, A. J. Ferguson, M.-Y. Wu, N. Kopidakis, J. L. Blackburn, and M. S. Arnold, “Free carrier generation and recombination in polymer-wrapped semiconducting carbon nanotube films and heterojunctions”, *The Journal of Physical Chemistry Letters* **4**, 3550–3559 (2013).
- ⁹¹C. Richard, F. Balavoine, P. Schultz, T. W. Ebbesen, and C. Mioskowski, “Supramolecular self-assembly of lipid derivatives on carbon nanotubes”, *Science* **300**, 775–778 (2003).
- ⁹²H. Li, C. M. Sims, R. Kang, F. Biedermann, J. A. Fagan, and B. S. Flavel, “Isolation of the (6,5) single-wall carbon nanotube enantiomers by surfactant-assisted aqueous two-phase extraction”, *Carbon* **204**, 475–483 (2023).
- ⁹³C. Zhang, P. Wang, B. Barnes, J. Fortner, and Y. Wang, “Cleanly removable surfactant for carbon nanotubes”, *Chemistry of Materials* **33**, 4551–4557 (2021).
- ⁹⁴B. White, S. Banerjee, S. O’Brien, N. J. Turro, and I. P. Herman, “Zeta-potential measurements of surfactant-wrapped individual single-walled carbon nanotubes”, *The Journal of Physical Chemistry C* **111**, 13684–13690 (2007).
- ⁹⁵B. Dan, A. W. K. Ma, E. H. Hároz, J. Kono, and M. Pasquali, “Nematic-like alignment in swnt thin films from aqueous colloidal suspensions”, *Industrial & Engineering Chemistry Research* **51**, 10232–10237 (2012).

-
- ⁹⁶J. W. Jo, J. W. Jung, J. U. Lee, and W. H. Jo, “Fabrication of highly conductive and transparent thin films from single-walled carbon nanotubes using a new non-ionic surfactant via spin coating”, *ACS Nano* **4**, 5382–5388 (2010).
- ⁹⁷F. Mirri, A. W. K. Ma, T. T. Hsu, N. Behabtu, S. L. Eichmann, C. C. Young, D. E. Tsentalovich, and M. Pasquali, “High-performance carbon nanotube transparent conductive films by scalable dip coating”, *ACS Nano* **6**, 9737–9744 (2012).
- ⁹⁸K. K. S. Lau, J. Bico, K. B. K. Teo, M. Chhowalla, G. A. J. Amaratunga, W. I. Milne, G. H. McKinley, and K. K. Gleason, “Superhydrophobic carbon nanotube forests”, *Nano Letters* **3**, 1701–1705 (2003).
- ⁹⁹J. L. Blackburn, A. J. Ferguson, C. Cho, and J. C. Grunlan, “Carbon-nanotube-based thermoelectric materials and devices”, *Advanced Materials* **30**, 1704386 (2018).
- ¹⁰⁰A. Ismach, D. Kantorovich, and E. Joselevich, “Carbon nanotube graphoepitaxy: highly oriented growth by faceted nanosteps”, *Journal of the American Chemical Society* **127**, 11554–11555 (2005).
- ¹⁰¹Y. Ji, Y. Y. Huang, R. Rungsawang, and E. M. Terentjev, “Dispersion and alignment of carbon nanotubes in liquid crystalline polymers and elastomers”, *Advanced Materials* **22**, 3436–3440 (2010).
- ¹⁰²A. R. Tao, J. Huang, and P. Yang, “Langmuir–blodgett of nanocrystals and nanowires”, *Accounts of chemical research* **41**, 1662–1673 (2008).
- ¹⁰³L. Xu, A. R. Tetreault, H. H. Khaligh, I. A. Goldthorpe, S. D. Wettig, and M. A. Pope, “Continuous langmuir–blodgett deposition and transfer by controlled edge-to-edge assembly of floating 2d materials”, *Langmuir* **35**, 51–59 (2019).
- ¹⁰⁴H. Li, T. C. Hain, A. Muzha, F. Schöppler, and T. Hertel, “Dynamical contact line pinning and zipping during carbon nanotube coffee stain formation”, *ACS nano* **8**, 6417–6424 (2014).
- ¹⁰⁵M. Engel, J. P. Small, M. Steiner, M. Freitag, A. A. Green, M. C. Hersam, and P. Avouris, “Thin film nanotube transistors based on self-assembled, aligned, semiconducting carbon nanotube arrays”, *ACS nano* **2**, 2445–2452 (2008).
- ¹⁰⁶G. J. Brady, Y. Joo, S. Singha Roy, P. Gopalan, and M. S. Arnold, “High performance transistors via aligned polyfluorene-sorted carbon nanotubes”, *Applied Physics Letters* **104**, 083107 (2014).
- ¹⁰⁷Y. Joo, G. J. Brady, C. Kanimozhi, J. Ko, M. J. Shea, M. T. Strand, M. S. Arnold, and P. Gopalan, “Polymer-free electronic-grade aligned semiconducting carbon nanotube array”, *ACS applied materials & interfaces* **9**, 28859–28867 (2017).

-
- ¹⁰⁸K. R. Jenkins, J. Chan, G. J. Brady, K. K. Gronski, P. Gopalan, H. T. Evensen, A. Berson, and M. S. Arnold, “Nanotube alignment mechanism in floating evaporative self-assembly”, *Langmuir* **33**, 13407–13414 (2017).
- ¹⁰⁹R. Krupke, F. Hennrich, H. V. Lohneysen, and M. M. Kappes, “Separation of metallic from semiconducting single-walled carbon nanotubes”, *Science* **301**, 344–347 (2003).
- ¹¹⁰C. Zamora-Ledezma, C. Blanc, M. Maugey, C. Zakri, P. Poulin, and E. Anglaret, “Anisotropic thin films of single-wall carbon nanotubes from aligned lyotropic nematic suspensions”, *Nano Letters* **8**, 4103–4107 (2008).
- ¹¹¹P. Kim, S. Baik, and K. Y. Suh, “Capillarity-driven fluidic alignment of single-walled carbon nanotubes in reversibly bonded nanochannels”, *Small* **4**, 92–95 (2008).
- ¹¹²J. Li, Q. Zhang, Y. Yan, S. Li, and L. Chen, “Fabrication of carbon nanotube field-effect transistors by fluidic alignment technique”, *IEEE transactions on nanotechnology* **6**, 481–484 (2007).
- ¹¹³K. R. Jenkins, J. Chan, R. M. Jacobberger, A. Berson, and M. S. Arnold, “Substrate-wide confined shear alignment of carbon nanotubes for thin film transistors”, *Advanced Electronic Materials* **5**, 1800593 (2019).
- ¹¹⁴L. Qiu, X. Wang, G. Su, D. Tang, X. Zheng, J. Zhu, Z. Wang, P. M. Norris, P. D. Bradford, and Y. Zhu, “Remarkably enhanced thermal transport based on a flexible horizontally-aligned carbon nanotube array film”, *Scientific Reports* **6**, 21014 (2016).
- ¹¹⁵D. Zhang, K. Ryu, X. Liu, E. Polikarpov, J. Ly, M. E. Tompson, and C. Zhou, “Transparent, conductive, and flexible carbon nanotube films and their application in organic light-emitting diodes”, *Nano letters* **6**, 1880–1886 (2006).
- ¹¹⁶E. Bekyarova, M. E. Itkis, N. Cabrera, B. Zhao, A. Yu, J. Gao, and R. C. Haddon, “Electronic properties of single-walled carbon nanotube networks”, *Journal of the American Chemical Society* **127**, 5990–5995 (2005).
- ¹¹⁷Q. Cao, H.-s. Kim, N. Pimparkar, J. P. Kulkarni, C. Wang, M. Shim, K. Roy, M. A. Alam, and J. A. Rogers, “Medium-scale carbon nanotube thin-film integrated circuits on flexible plastic substrates”, *Nature* **454**, 495–500 (2008).
- ¹¹⁸Z. Wu, Z. Chen, X. Du, J. M. Logan, J. Sippel, M. Nikolou, K. Kamaras, J. R. Reynolds, D. B. Tanner, A. F. Hebard, and A. G. Rinzler, “Transparent, conductive carbon nanotube films”, *Science* **305**, 1273–1276 (2004).

-
- ¹¹⁹N. Rouhi, D. Jain, and P. J. Burke, “High-performance semiconducting nanotube inks: progress and prospects”, *ACS Nano* **5**, 8471–8487 (2011).
- ¹²⁰M. B. Jakubinek, M. A. White, G. Li, C. Jayasinghe, W. Cho, M. J. Schulz, and V. Shanov, “Thermal and electrical conductivity of tall, vertically aligned carbon nanotube arrays”, *Carbon* **48**, 3947–3952 (2010).
- ¹²¹X. Wang, Z. Zhong, and J. Xu, “Noncontact thermal characterization of multiwall carbon nanotubes”, *Journal of Applied Physics* **97**, 064302 (2005).
- ¹²²T. Tong, A. Majumdar, Y. Zhao, A. Kashani, L. Delzeit, and M. Meyyappan, “Indium assisted multiwalled carbon nanotube array thermal interface materials”, in *Thermal and thermomechanical proceedings 10th intersociety conference on phenomena in electronics systems, 2006. itherm 2006.* (2006), pp. 1406–1411.
- ¹²³A. A. Balandin, “Thermal properties of graphene and nanostructured carbon materials”, *Nature materials* **10**, 569–581 (2011).
- ¹²⁴P. Kim, L. Shi, A. Majumdar, and P. L. McEuen, “Thermal transport measurements of individual multi-walled nanotubes”, *Physical review letters* **87**, 215502 (2001).
- ¹²⁵A. M. Marconnet, M. A. Panzer, and K. E. Goodson, “Thermal conduction phenomena in carbon nanotubes and related nanostructured materials”, *Reviews of Modern Physics* **85**, 1295 (2013).
- ¹²⁶J. Cao, X. Yan, Y. Xiao, and J. Ding, “Thermal conductivity of zigzag single-walled carbon nanotubes: role of the umklapp process”, *Physical Review B* **69**, 073407 (2004).
- ¹²⁷Y. Wang, L. Huang, Y. Liu, D. Wei, H. Zhang, H. Kajiura, and Y. Li, “Minimizing purification-induced defects in single-walled carbon nanotubes gives films with improved conductivity”, *Nano Research* **2**, 865–871 (2009).
- ¹²⁸F. L. Ltd., *Fujitsu laboratories develops pure carbon-nanotube sheets with world’s top heat-dissipation performance*, (2017) <https://www.fujitsu.com/global/about/resources/news/press-releases/2017/1130-01.html> (visited on 12/19/2022).
- ¹²⁹P. Yeh, “A new optical model for wire grid polarizers”, *Optics Communications* **26**, 289–292 (1978).
- ¹³⁰S.-W. Ahn, K.-D. Lee, J.-S. Kim, S. H. Kim, J.-D. Park, S.-H. Lee, and P.-W. Yoon, “Fabrication of a 50 nm half-pitch wire grid polarizer using nanoimprint lithography”, *Nanotechnology* **16**, 1874 (2005).

-
- ¹³¹Y. Chen, Y. Lin, Y. Liu, J. Doyle, N. He, X. Zhuang, J. Bai, and W. J. Blau, “Carbon nanotube-based functional materials for optical limiting”, *Journal of Nanoscience and Nanotechnology* **7**, 1268–1283 (2007).
- ¹³²V. M. Gubarev, V. Y. Yakovlev, M. G. Sertsu, O. F. Yakushev, V. M. Krivtsun, Y. G. Gladush, I. A. Ostanin, A. Sokolov, F. Schäfers, V. V. Medvedev, and A. G. Nasibulin, “Single-walled carbon nanotube membranes for optical applications in the extreme ultraviolet range”, *Carbon* **155**, 734–739 (2019).
- ¹³³X. He, X. Wang, S. Nanot, K. Cong, Q. Jiang, A. A. Kane, J. E. M. Goldsmith, R. H. Hauge, F. Léonard, and J. Kono, “Photothermoelectric p–n junction photodetector with intrinsic broadband polarimetry based on macroscopic carbon nanotube films”, *ACS Nano* **7**, 7271–7277 (2013).
- ¹³⁴S. Matano, H. Takahashi, N. Komatsu, Y. Shimura, K. Nakagawa, J. Kono, and H. Maki, “Electrical generation of polarized broadband radiation from an on-chip aligned carbon nanotube film”, *ACS Materials Letters*, 626–633 (2022).
- ¹³⁵M. S. Shaffer, X. Fan, and A. Windle, “Dispersion and packing of carbon nanotubes”, *Carbon* **36**, 1603–1612 (1998).
- ¹³⁶C. Jiang, A. Saha, C. Xiang, C. C. Young, J. M. Tour, M. Pasquali, and A. A. Martí, “Increased solubility, liquid-crystalline phase, and selective functionalization of single-walled carbon nanotube polyelectrolyte dispersions”, *ACS nano* **7**, 4503–4510 (2013).
- ¹³⁷J. P. F. Lagerwall and G. Scalia, “Carbon nanotubes in liquid crystals”, *Journal of Materials Chemistry* **18**, 2890–2898 (2008).
- ¹³⁸B. King and B. Panchapakesan, “Vacuum filtration based formation of liquid crystal films of semiconducting carbon nanotubes and high performance transistor devices”, *Nanotechnology* **25**, 175201 (2014).
- ¹³⁹N. Komatsu, M. Nakamura, S. Ghosh, D. Kim, H. Chen, A. Katagiri, Y. Yomogida, W. Gao, K. Yanagi, and J. Kono, “Groove-assisted global spontaneous alignment of carbon nanotubes in vacuum filtration”, *Nano Letters* **20**, 2332–2338 (2020).
- ¹⁴⁰Y. Yomogida, T. Tanaka, M. Tsuzuki, X. Wei, and H. Kataura, “Automatic sorting of single-chirality single-wall carbon nanotubes using hydrophobic cholates: implications for multicolor near-infrared optical technologies”, *ACS Applied Nano Materials* **3**, 11289–11297 (2020).
- ¹⁴¹Z. Bi, Z. Zhang, F. Xu, Y. Qian, and J. Yu, “Wettability, oil recovery, and interfacial tension with an sdb-s-dodecane-kaolin system”, *Journal of colloid and interface science* **214**, 368–372 (1999).

-
- ¹⁴²P.-H. Ho, D. B. Farmer, G. S. Tulevski, S.-J. Han, D. M. Bishop, L. M. Gignac, J. Bucchignano, P. Avouris, and A. L. Falk, “Intrinsically ultrastrong plasmon–exciton interactions in crystallized films of carbon nanotubes”, *Proceedings of the National Academy of Sciences* **115**, 12662–12667 (2018).
- ¹⁴³J. Hermia, “Constant pressure blocking filtration laws - application to power-law non-newtonian fluids”, *Transactions of the Institution of Chemical Engineers* **60**, 183–187 (1982).
- ¹⁴⁴J. S. Walker, Z. J. Macdermid, J. A. Fagan, A. Kolmakov, A. J. Biacchi, T. A. Searles, A. R. H. Walker, and W. D. Rice, “Dependence of single-wall carbon nanotube alignment on the filter membrane interface in slow vacuum filtration”, *Small* **18**, 2105619 (2022).
- ¹⁴⁵K. Yanagi, R. Okada, Y. Ichinose, Y. Yomogida, F. Katsutani, W. Gao, and J. Kono, “Intersubband plasmons in the quantum limit in gated and aligned carbon nanotubes”, *Nature Communications* **9**, 1121 (2018).
- ¹⁴⁶K.-C. Chiu, A. L. Falk, P.-H. Ho, D. B. Farmer, G. Tulevski, Y.-H. Lee, P. Avouris, and S.-J. Han, “Strong and broadly tunable plasmon resonances in thick films of aligned carbon nanotubes”, *Nano Letters* **17**, 5641–5645 (2017).
- ¹⁴⁷W. Gao, C. F. Doiron, X. Li, J. Kono, and G. V. Naik, “Macroscopically aligned carbon nanotubes as a refractory platform for hyperbolic thermal emitters”, *ACS Photonics* **6**, 1602–1609 (2019).
- ¹⁴⁸F. Katsutani, W. Gao, X. Li, Y. Ichinose, Y. Yomogida, K. Yanagi, and J. Kono, “Direct observation of cross-polarized excitons in aligned single-chirality single-wall carbon nanotubes”, *Physical Review B* **99**, 035426 (2019).
- ¹⁴⁹P. Bacchin, A. Marty, P. Duru, M. Meireles, and P. Aimar, “Colloidal surface interactions and membrane fouling: investigations at pore scale”, *Advances in Colloid and Interface Science* **164**, 2–11 (2011).
- ¹⁵⁰P. Bacchin, P. Aimar, and R. W. Field, “Critical and sustainable fluxes: theory, experiments and applications”, *Journal of Membrane Science* **281**, 42–69 (2006).
- ¹⁵¹Y. Bessiere, N. Abidine, and P. Bacchin, “Low fouling conditions in dead-end filtration: evidence for a critical filtered volume and interpretation using critical osmotic pressure”, *Journal of Membrane Science* **264**, 37–47 (2005).
- ¹⁵²B. Espinasse, P. Bacchin, and P. Aimar, “On an experimental method to measure critical flux in ultrafiltration”, *Desalination* **146**, 91–96 (2002).
- ¹⁵³B. Espinasse, P. Bacchin, and P. Aimar, “Filtration method characterizing the reversibility of colloidal fouling layers at a membrane surface: analysis through critical flux and osmotic pressure”, *Journal of Colloid and Interface Science* **320**, 483–490 (2008).

-
- ¹⁵⁴W. Wagner and A. Pruß, “The iapws formulation 1995 for the thermodynamic properties of ordinary water substance for general and scientific use”, *Journal of physical and chemical reference data* **31**, 387–535 (2002).
- ¹⁵⁵S. Chellam and N. G. Cogan, “Colloidal and bacterial fouling during constant flux microfiltration: comparison of classical blocking laws with a unified model combining pore blocking and eps secretion”, *Journal of Membrane Science* **382**, 148–157.
- ¹⁵⁶K. Nakamura, T. Orime, and K. Matsumoto, “Response of zeta potential to cake formation and pore blocking during the microfiltration of latex particles”, *Journal of Membrane Science* **401-402**, 274–281 (2012).
- ¹⁵⁷G. B. van den Berg and C. A. Smolders, “The boundary-layer resistance model for unstirred ultrafiltration. a new approach”, *Journal of Membrane Science* **40**, 149–172 (1989).
- ¹⁵⁸G. B. van den Berg and C. A. Smolders, “Concentration polarization phenomena during dead-end ultrafiltration of protein mixtures. the influence of solute-solute interactions”, *Journal of Membrane Science* **47**, 1–24 (1989).
- ¹⁵⁹Q.-F. Liu and S.-H. Kim, “Evaluation of membrane fouling models based on bench-scale experiments: a comparison between constant flowrate blocking laws and artificial neural network (anns) model”, *Journal of Membrane Science* **310**, 393–401 (2008).
- ¹⁶⁰E. Iritani, N. Katagiri, T. Takenaka, and Y. Yamashita, “Membrane pore blocking during cake formation in constant pressure and constant flux dead-end microfiltration of very dilute colloids”, *Chemical Engineering Science* **122**, 465–473 (2015).
- ¹⁶¹P. H. Hermans and H. L. Bredée, “Zur kenntnis der filtrationsgesetze”, *Recueil des Travaux Chimiques des Pays-Bas* **54**, 680–700 (1935).
- ¹⁶²H. P. Grace, “Structure and performance of filter media”, *Aiche Journal* **2**, 307–336 (1956).
- ¹⁶³M. Hlavacek and F. Bouchet, “Constant flowrate blocking laws and an example of their application to dead-end microfiltration of protein solutions”, *Journal of Membrane Science* **82**, 285–295 (1993).
- ¹⁶⁴E. Iritani, “A review on modeling of pore-blocking behaviors of membranes during pressurized membrane filtration”, *Drying Technology* **31**, 146–162 (2013).
- ¹⁶⁵G. Trefalt and M. Borkovec, “Overview of dlvo theory”, (2014).
- ¹⁶⁶J. N. Israelachvili, *Intermolecular and surface forces* (Academic press, 2011).

-
- ¹⁶⁷B. Derjaguin, “A theory of interaction of particles in presence of electric double layers and the stability of lyophobic colloids and disperse systems”, *Progress in Surface Science* **43**, 1–14 (1993).
- ¹⁶⁸B. V. Deraguin and L. Landau, “Theory of the stability of strongly charged lyophobic sols and of the adhesion of strongly charged particles in solution of electrolytes”, *Acta Physicochim: USSR* **14**, 633–662 (1941).
- ¹⁶⁹E. Verwey and J. T. G. Overbeek, “Theory of the stability of lyophobic colloids. elsevier, amsterdam”, Elsevier, Amsterdam., 216 pp. (1948).
- ¹⁷⁰R. F. Rajter, R. Podgornik, V. A. Parsegian, R. H. French, and W. Ching, “Van der waals–london dispersion interactions for optically anisotropic cylinders: metallic and semiconducting single-wall carbon nanotubes”, *Physical Review B* **76**, 045417 (2007).
- ¹⁷¹R. H. French, V. A. Parsegian, R. Podgornik, R. F. Rajter, A. Jagota, J. Luo, D. Asthagiri, M. K. Chaudhury, Y.-m. Chiang, and S. Granick, “Long range interactions in nanoscale science”, *Reviews of Modern Physics* **82**, 1887 (2010).
- ¹⁷²A. R. Petosa, D. P. Jaisi, I. R. Quevedo, M. Elimelech, and N. Tufenkji, “Aggregation and deposition of engineered nanomaterials in aquatic environments: role of physicochemical interactions”, *Environmental science and technology* **44**, 6532–6549 (2010).
- ¹⁷³D. Tabor and W. R.H.S, “The direct measurement of normal and retarded van der waals forces”, *Proceedings of the Royal Society of London. A. Mathematical and Physical Sciences* **312**, 435–450 (1969).
- ¹⁷⁴E. Blagov, G. Klimchitskaya, and V. Mostepanenko, “Van der waals interaction between a microparticle and a single-walled carbon nanotube”, *Physical Review B* **75**, 235413 (2007).
- ¹⁷⁵L. A. Girifalco, M. Hodak, and R. S. Lee, “Carbon nanotubes, buckyballs, ropes, and a universal graphitic potential”, *Physical Review B* **62**, 13104 (2000).
- ¹⁷⁶A. I. Zhbanov, E. G. Pogorelov, and Y.-C. Chang, “Van der waals interaction between two crossed carbon nanotubes”, *Acs Nano* **4**, 5937–5945 (2010).
- ¹⁷⁷A. N. Volkov and L. V. Zhigilei, “Mesoscopic interaction potential for carbon nanotubes of arbitrary length and orientation”, *The Journal of Physical Chemistry C* **114**, 5513–5531 (2010).
- ¹⁷⁸R. Nap and I. Szleifer, “Control of carbon nanotube– surface interactions: the role of grafted polymers”, *Langmuir* **21**, 12072–12075 (2005).

-
- ¹⁷⁹G. S. Manning, “The molecular theory of polyelectrolyte solutions with applications to the electrostatic properties of polynucleotides”, *Quarterly reviews of biophysics* **11**, 179–246 (1978).
- ¹⁸⁰L. Wu, B. Gao, Y. Tian, R. Munoz-Carpena, and K. J. Zigler, “Dlvo interactions of carbon nanotubes with isotropic planar surfaces”, *Langmuir* **29**, 3976–3988 (2013).
- ¹⁸¹J. Gregory, “Interaction of unequal double layers at constant charge”, *Journal of colloid and interface science* **51**, 44–51 (1975).
- ¹⁸²H. Du, X. Lin, Z. Xu, and D. Chu, “Electric double-layer transistors: a review of recent progress”, *Journal of Materials Science* **50**, 5641–5673 (2015).
- ¹⁸³H. H. v. U. einige Gesetze, “Der vertheilung elektrischer ströme in körperlichen leitern mit anwendung auf die thierisch-elektrischen versuche”, *Annalender Physik und Chemie* **89**, 211–233 (1853).
- ¹⁸⁴O. Stern, “Zur theorie der elektrolytischen doppelschicht”, *Zeitschrift für Elektrochemie und angewandte physikalische Chemie* **30**, 508–516 (1924).
- ¹⁸⁵K. Weber and W. Stahl, “Improvement of filtration kinetics by pressure electrofiltration”, *Separation and Purification Technology* **26**, 69–80 (2002).
- ¹⁸⁶K. N. Vasista, S. K. Mehta, S. Pati, and S. Sarkar, “Electroosmotic flow of viscoelastic fluid through a microchannel with slip-dependent zeta potential”, *Physics of Fluids* **33**, 123110 (2021).
- ¹⁸⁷W. Techonology, *Electrophoretic light scattering theory*, <https://www.wyatt.com/library/theory/electrophoretic-light-scattering-theory.html> (visited on 12/19/2022).
- ¹⁸⁸C. Tanford, *Physical chemistry of macromolecules* (Wiley, 1961).
- ¹⁸⁹A. P. Group, *Manual for streaming potential measurementns*, Journal Article.
- ¹⁹⁰A. P. Minton, “Recent applications of light scattering measurement in the biological and biopharmaceutical sciences”, *Analytical Biochemistry* **501**, 4–22 (2016).
- ¹⁹¹R. W. O’Brien, D. W. Cannon, and W. N. Rowlands, “Electroacoustic determination of particle size and zeta potential”, *Journal of Colloid and Interface Science* **173**, 406–418 (1995).
- ¹⁹²D. McMullan, “Scanning electron microscopy 1928–1965”, *Scanning* **17**, 175–185 (1995).
- ¹⁹³R. García, *Amplitude modulation atomic force microscopy* (John Wiley & Sons, 2011).
- ¹⁹⁴P. Arenas-Guerrero, M. L. Jiménez, K. Scott, and K. J. Donovan, “Electric birefringence of carbon nanotubes: single-vs double-walled”, *Carbon* **126**, 77–84 (2018).

-
- ¹⁹⁵S. Inoué, “Polarization microscopy”, *Current Protocols in Cell Biology* **13**, 4.9.1–4.9.27 (2002).
- ¹⁹⁶R. L. Weaver, “Rediscovering polarized light microscopy”, *American Laboratory* **35**, 55–61 (2003).
- ¹⁹⁷W. Freitas, C. R. Cena, D. C. Alves, and A.-M. B. Goncalves, “Arduino-based experiment demonstrating malus’s law”, *Physics Education* **53**, 035034 (2018).
- ¹⁹⁸Ossila, *Sheet resistance theory*, <https://www.ossila.com/en-eu/pages/sheet-resistance-theory> (visited on 01/26/2023).
- ¹⁹⁹G. Stando, S. Han, B. Kumanek, D. Łukowiec, and D. Janas, “Tuning wettability and electrical conductivity of single-walled carbon nanotubes by the modified hummers method”, *Scientific Reports* **12**, 4358 (2022).
- ²⁰⁰M. Jouni, P. Fedorko, C. Celle, D. Djurado, P. Chenevier, and J. Faure-Vincent, “Conductivity vs functionalization in single-walled carbon nanotube films”, *SN Applied Sciences* **4**, 132 (2022).
- ²⁰¹C. Huang, J. A. Wippold, D. Stratis-Cullum, and A. Han, “Eliminating air bubble in microfluidic systems utilizing integrated in-line sloped microstructures”, *Biomedical Microdevices* **22**, 76 (2020).
- ²⁰²I. Pereiro, A. Fomitcheva Khartchenko, L. Petrini, and G. V. Kaigala, “Nip the bubble in the bud: a guide to avoid gas nucleation in microfluidics”, *Lab Chip* **19**, 2296–2314 (2019).
- ²⁰³X. H. Sun, D. M. Kanani, and R. Ghosh, “Characterization and theoretical analysis of protein fouling of cellulose acetate membrane during constant flux dead-end microfiltration”, *Journal of Membrane Science* **320**, 372–380 (2008).
- ²⁰⁴J. Haneveld, T. S. J. Lammerink, M. J. de Boer, R. G. P. Sanders, A. Mehendale, J. C. Lötters, M. Dijkstra, and R. J. Wiegerink, “Modeling, design, fabrication and characterization of a micro coriolis mass flow sensor”, *Journal of Micromechanics and Microengineering* **20**, 125001 (2010).
- ²⁰⁵D. E. Rivera, M. Morari, and S. Skogestad, “Internal model control: pid controller design”, *Industrial & Engineering Chemistry Process Design and Development* **25**, 252–265 (1986).
- ²⁰⁶H. Li, G. Gordeev, D. Toroz, D. Di Tommaso, S. Reich, and B. S. Flavel, “Endohedral filling effects in sorted and polymer-wrapped single-wall carbon nanotubes”, *The Journal of Physical Chemistry C* **125**, 7476–7487 (2021).
- ²⁰⁷J. Campo, S. Cambré, B. Botka, J. Obrzut, W. Wenseleers, and J. A. Fagan, “Optical property tuning of single-wall carbon nanotubes by endohedral encapsulation of a wide variety of dielectric molecules”, *ACS Nano* **15**, 2301–2317 (2021).

-
- ²⁰⁸J. Campo, Y. Piao, S. Lam, C. M. Stafford, J. K. Streit, J. R. Simpson, A. R. Hight Walker, and J. A. Fagan, “Enhancing single-wall carbon nanotube properties through controlled endohedral filling”, *Nanoscale Horizons* **1**, 317–324 (2016).
- ²⁰⁹J. A. Fagan, “Aqueous two-polymer phase extraction of single-wall carbon nanotubes using surfactants”, *Nanoscale Advances* **1**, 3307–3324 (2019).
- ²¹⁰C. Y. Khripin, X. Tu, J. M. Heddleston, C. Silvera-Batista, A. R. Hight Walker, J. Fagan, and M. Zheng, “High-resolution length fractionation of surfactant-dispersed carbon nanotubes”, *Analytical Chemistry* **85**, 1382–1388 (2013).
- ²¹¹F. L. Sebastian, N. F. Zorn, S. Settele, S. Lindenthal, F. J. Berger, C. Bendel, H. Li, B. S. Flavel, and J. Zaumseil, “Absolute quantification of sp³ defects in semiconducting single-wall carbon nanotubes by raman spectroscopy”, *The Journal of Physical Chemistry Letters* **13**, PMID: 35420437, 3542–3548 (2022).
- ²¹²N. Komatsu, M. Nakamura, S. Ghosh, D. Kim, H. Chen, A. Katagiri, Y. Yomogida, W. Gao, K. Yanagi, and J. Kono, “Groove-assisted global spontaneous alignment of carbon nanotubes in vacuum filtration”, *Nano Letters* **20**, 2332–2338 (2020).
- ²¹³R. H. Perry and D. W. Green, *Perry’s chemical engineers’ handbook: seventh edition* (1999).
- ²¹⁴S. Geissler and U. Werner, “Dynamic model of crossflow microfiltration in flat-channel systems under laminar flow conditions”, *Filtration & Separation* **32**, 533–537 (1995).
- ²¹⁵N. Kuehn, H.-J. Jacobasch, and K. Lunkenheimer, “Zum zusammenhang zwischen dem kontaktwinkel zwischen wasser und festen polymeren und ihrem zeta-potential gegenüber wäßrigen lösungen”, *Acta Polymerica* **37**, 394–396 (1986).
- ²¹⁶C. Werner, U. König, A. Augsburg, C. Arnhold, H. Körber, R. Zimmermann, and H.-J. Jacobasch, “Electrokinetic surface characterization of biomedical polymers — a survey”, *Colloids and Surfaces A: Physicochemical and Engineering Aspects* **159**, 519–529 (1999).
- ²¹⁷D. J. Miller, S. Kasemset, D. R. Paul, and B. D. Freeman, “Comparison of membrane fouling at constant flux and constant transmembrane pressure conditions”, *Journal of Membrane Science* **454**, 505–515 (2014).
- ²¹⁸J. I. Calvo, A. Bottino, G. Capannelli, and A. Hernández, “Comparison of liquid–liquid displacement porosimetry and scanning electron microscopy image analysis to characterise ultrafiltration track-etched membranes”, *Journal of Membrane Science* **239**, 189–197 (2004).

-
- ²¹⁹K. Suttiponparnit, J. Jiang, M. Sahu, S. Suvachittanont, T. Charinpanitkul, and P. Biswas, “Role of surface area, primary particle size, and crystal phase on titanium dioxide nanoparticle dispersion properties”, *Nanoscale Res Lett* **6**, 27 (2010).
- ²²⁰F. Yang, W. Wu, S. Chen, and W. Gan, “The ionic strength dependent zeta potential at the surface of hexadecane droplets in water and the corresponding interfacial adsorption of surfactants”, *Soft Matter* **13**, 638–646 (2017).
- ²²¹S. Alamri, A. I. Aguilar-Morales, and A. F. Lasagni, “Controlling the wettability of polycarbonate substrates by producing hierarchical structures using direct laser interference patterning”, *European Polymer Journal* **99**, 27–37 (2018).
- ²²²P. van der Wal and U. Steiner, “Super-hydrophobic surfaces made from teflon”, *Soft Matter* **3**, 426–429 (2007).
- ²²³A. Díaz Lantada, N. Mazarío Picazo, M. Guttman, M. Wissmann, M. Schneider, M. Worgull, S. Hengsbach, F. Rupp, K. Bade, and G. R. Plaza, “Soft-lithography of polyacrylamide hydrogels using microstructured templates: towards controlled cell populations on biointerfaces”, *Materials* **13**, 1586 (2020).
- ²²⁴W. Zou, J. Sackmann, A. Striegel, M. Worgull, and W. K. Schomburg, “Comparison of hot embossing micro structures with and without ultrasound”, *Microsystem Technologies* **25**, 4185–4195 (2019).
- ²²⁵E. M. Frohlich, J. L. Alonso, J. T. Borenstein, X. Zhang, M. A. Arnaout, and J. L. Charest, “Topographically-patterned porous membranes in a microfluidic device as an in vitro model of renal reabsorptive barriers”, *Lab on a Chip* **13**, 2311–2319 (2013).
- ²²⁶J. S. Walker, Z. J. Macdermid, J. A. Fagan, A. Kolmakov, A. J. Biacchi, T. A. Searles, A. R. H. Walker, and W. D. Rice, “Dependence of single-wall carbon nanotube alignment on the filter membrane interface in slow vacuum filtration”, *Small* **18**, 2105619 (2022).
- ²²⁷W. Gao, X. Li, M. Bamba, and J. Kono, “Continuous transition between weak and ultrastrong coupling through exceptional points in carbon nanotube microcavity exciton–polaritons”, *Nature Photonics* **12**, 362–367 (2018).
- ²²⁸R. S. McLean, X. Huang, C. Khripin, A. Jagota, and M. Zheng, “Controlled two-dimensional pattern of spontaneously aligned carbon nanotubes”, *Nano Letters* **6**, 55–60 (2006).
- ²²⁹A. M. Donald, A. H. Windle, and S. Hanna, *Liquid crystalline polymers* (Cambridge University Press, 2006).

-
- ²³⁰L. Onsager, “The effects of shape on the interaction of colloidal particles”, *Annals of the New York Academy of Sciences* **51**, 627–659 (1949).
- ²³¹V. A. Davis, L. M. Ericson, A. N. G. Parra-Vasquez, H. Fan, Y. Wang, V. Prieto, J. A. Longoria, S. Ramesh, R. K. Saini, C. Kittrell, W. E. Billups, W. W. Adams, R. H. Hauge, R. E. Smalley, and M. Pasquali, “Phase behavior and rheology of swnts in superacids”, *Macromolecules* **37**, 154–160 (2004).
- ²³²A. Mehta, J. D. Brown, P. Srinivasan, R. C. Rumpf, and E. G. Johnson, “Spatially polarizing autocloned elements”, *Opt. Lett.* **32**, 1935–1937 (2007).